Journal of
Mechanics of
Materials and Structures

◆ mathematical sciences publishers

A WAVE-BASED DAMAGE INDEX FOR THE ANALYSIS OF THE FILTERED RESPONSE OF DAMAGED BEAMS

NICOLE APETRE, MASSIMO RUZZENE, SATHYANARAYA HANAGUD AND S. GOPALAKRISHNAN

This paper introduces a wave propagation-based damage index which relies on the evaluation of the strain energy distribution associated with propagating waves. The presence of localized damages typically distorts the wavefield by causing reflections and diffractions. The evaluation of such distortions, in reference to the wavefield corresponding to the undamaged structure, can be used as an indicator which potentially locates, quantifies and classifies the damage.

The damage index formulation is first illustrated through a numerical model of a beam with a small notch, modeled as a localized thickness reduction. The beam's wave propagation response is simulated through the combined application of perturbation techniques and the spectral finite element method. The perturbation approach and a first order model for the beam capture the coupling between bending and axial behavior caused by the damage, and allow the prediction of mode conversion phenomena. The perturbation solution allows direct comparison between undamaged and damaged strain energy contributions, which are directly associated with perturbation solutions of different orders. The resulting damage index locates the damage along the beam length and estimates its severity.

Experimentally, the damage index is implemented by considering full wavefield measurements obtained through a scanning laser vibrometer. The undamaged reference response is derived directly from measurements on the damaged component, through the application of a filtering procedure operating in the wavenumber/frequency domain.

1. Introduction

The objective of a structural health monitoring (SHM) system is to identify anomalies or damages such as cracks, delaminations, and disbonds in structures. The term identification includes the determination of the existence of damages, their location, and their size as accurately as possible. In the literature, the amount of information that can be obtained regarding a damaged structure is typically classified into five levels: (1) identification of the presence of damage, (2) determination of the location of the damage, (3) classification of the type of damage, (4) quantification of its extent, and (5) estimation of the remaining life of the component under investigation. The definition of an effective measure of damage responds to the requirements of the first 4 stages, and ideally provides inputs to step (5). Damage indices proposed in the literature from an SHM perspective are meant to identify and locate the damage, and, in some cases, to provide an indication regarding the extent of the damage and its progression.

Many SHM techniques developed over the years are based on the detection of changes in the modal behavior of the monitored components. A valuable review of the state-of-the-art in modal-based SHM can be found in [Doebling et al. 1996]. The existing techniques vary on the basis of the type of dynamic response signals used for the analysis, and on the features or parameters considered as damage indicators. Examples include techniques based on changes in modal frequencies [Ostachowicz and Krawczuk 1991; Kim and Stubbs 2003], in measured mode shapes and their spatial derivatives (curvatures) [Pandey et al. 1991; Lestari 2001; Luo and Hanagud 1997; Ho and Ewins 1999], in calculated mean modal strain energies [Sharma et al. 2006; Choi and Stubbs 2004; Cornwell et al. 1999] and in measured flexibility coefficients. Although effective, these methods generally are not sensitive enough to to detect small damages, and often require comparisons with baseline measurements on undamaged specimens. Their lack in sensitivity and their inability to discriminate damage from changes in the operating conditions of modal-based methods can be overcome through the application of guided ultrasonic waves (GUWs) inspections [Staszewski et al. 2004; Rose 2002; Raghavan and Cesnik 2007]. Guided waves, such as Lamb waves, show sensitivity to a variety of damage types and have the ability to travel relatively long distances within the structure under investigation. For this reason, GUWs are particularly suitable for SHM applications, which may employ a built-in sensor/actuator network to interrogate and assess the state of health of the structure [Staszewski et al. 2004; Rose 2002; Giurgiutiu et al. 2003; Giurgiutiu 2005; 2008]. Alternatively, full wavefield measurements can be obtained through scanning laser vibrometers, which allow the implementation of strain energy-based damage index [Sharma et al. 2006], and of frequency/wavenumber filtering techniques for improved damage visualization [Ruzzene 2007]. Interaction of the ultrasonic waves with various scatterers that represent arbitrary thickness variation was study by experimental techniques and was validated with analytical and numerical models such as hybrid boundary element method [Cho and Rose 1996; Cho 2000], finite difference method and finite element method [Kazys et al. 2006; Basri and Chiu 2004], local interaction simulation approach [Ruzzene et al. 2005] and acoustic wavefield imaging [Michaels et al. 2005].

This paper extends the approach in [Ruzzene 2007], by introducing a wave propagation-based damage index which relies on the estimation of the strain energy associated with waves reflected by damage. The approach is illustrated through numerically simulated data which are obtained from the model of a notched beam. The model considers damage as a small, localized thickness reduction, which allows the application of perturbation techniques [Apetre et al. 2008; Lestari 2001]. The resulting perturbation equations are solved in the frequency domain using the spectral finite element method (SFEM) [Doyle 1997; Lee et al. 2000]. SFEM, developed from matrix structural methods [Przemieniecki 1968], is using a discrete Fourier transform to translate a problem to the frequency domain where an exact solution can be found.

In the field of SHM, the SFEM has been previously used for example in [Kumar et al. 2004] to describe the behavior of a first-order shear deformable beam with a transverse crack. Also, the SFE model of a cracked Timoshenko beam is presented in [Krawczuk et al. 2003], where a massless spring, with bending and shear flexibilities computed using Castigliano's theorem and the laws of fracture mechanics is used to model the crack. A review of damage detection using SFEM is presented in [Ostachowicz 2008]. The perturbation approach applied herein leads to a set of linear equations for increasing order of the perturbation parameter. In this context, the separation between the response of the undamaged structure (zero order perturbation solution) and the changes introduced by damage (first order perturbation

solution) is immediate. The proposed damage index formulation is defined as the ratio of the strain energy distribution associated with perturbations due to damage and the strain energy of the undamaged structure, which in the numerical model respectively correspond to the first order and zero order solutions. The formulation can be easily extended for the analysis of full-field experimental data according to procedures outlined in [Ruzzene 2007].

   The paper is organized as follows. Section 2 describes the numerical model of the notched beam, while Section 3 presents the damage index formulation and a set of illustrative numerical examples. The experimental implementation of the concept with the simultaneous application of frequency/wavenumber filtering procedures are presented in Section 4. A summary of the main results of the work is finally presented in Section 5.

2. Wave propagation model for notched beams

Damage description. A detailed derivation of the governing differential equations for a notched Euler-Bernoulli beam is presented in [Apetre et al. 2008]. Here for completeness, a short summary of the derivation is given. The dynamic behavior of the notched beam shown in Figure 1 is described by a set of governing equations derived through the Hamilton principle. The defect is modeled as a reduction in thickness of depth h_d, extending over a length Δl, placed at the distance x_d. As seen in the figure, $x \in [0, L]$ denotes the horizontal coordinate, whereas the vertical coordinate z varies in the interval

$$z \in \left[-\frac{h}{2}, \; \frac{h}{2}(1 - 2\varepsilon\gamma_d(x)) \right], \tag{2-1}$$

where $\varepsilon = h_d / h$, and where $\gamma_d(x) = H(x - (x_d - \Delta l)) - H(x - x_d)$ is a damage function with H denoting the Heaviside function. Both the stiffness and the mass loss due to the edge notch are considered. The moment of inertia at the damage location is truncated at ε order as

$$I_d = I(1 - \varepsilon)^3 \approx I(1 - 3\varepsilon), \tag{2-2}$$

where I is the moment of inertia of the undamaged beam. Thus the expressions for the stiffness and mass distribution along the beam are [Lestari 2001]

$$EI_d(x) = EI[1 - 3\varepsilon\gamma_d(x)] \quad \text{and} \quad m_d(x) = m[1 - \varepsilon\gamma_d(x)], \tag{2-3}$$

where EI and m are the stiffness and the mass of the undamaged beam.
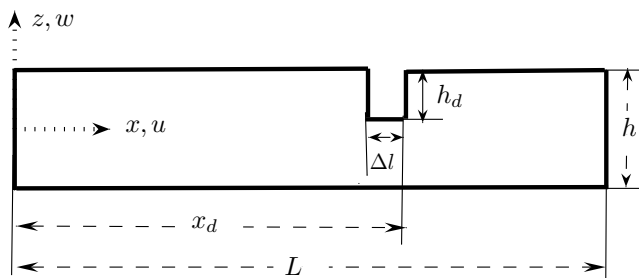
Figure 1. Beam geometry.

Perturbation equations. The governing equations for the notched beam and the appropriate set of boundary conditions are derived using Hamilton's Principle. The required kinetic and strain energies, and the work of external forces are formulated using the first-order approximation

$$\mathbf{u}(x, z, t) = u(x, t) - z\frac{\partial w}{\partial x}, \quad \mathbf{w}(x, z, t) = w(x, t), \tag{2-4}$$

where $u(x, t)$ and $w(x, t)$ are the axial and transverse displacements in the reference plane $z = 0$, respectively. Application of Hamilton's Principle yields the following set of differential equations:

$$\left[EAu_{,x} + \left(-u_{,x} + w_{,xx}\frac{h}{2}\right)EA\gamma_d(x)\varepsilon\right]_{,x} - m\left[1 - \varepsilon\gamma_d(x)\right]\ddot{u} - \frac{mh}{2}\varepsilon\gamma_d(x)\dot{w}_{,xx} = f_1(x, t), \tag{2-5}$$

$$\left[-EIw_{,xx} + \left(-u_{,x} + w_{,xx}\frac{h}{2}\right)E\frac{Ah}{2}\gamma_d(x)\varepsilon\right]_{,xx} + \frac{mh}{2}\left[\ddot{u}\varepsilon\gamma_d(x)\right]_{,x} - m\left[1 - \varepsilon\gamma_d(x)\right]\ddot{w} = f_2(x, t), \tag{2-6}$$

where E is the Young's modulus, A is the lateral area, h is beam thickness, m is the mass per unit length, and $f_1(x, t)$, $f_2(x, t)$ denote the applied distributed generalized loads, assumed for simplicity to be applied along the reference plane $z = 0$. The important feature of equations (2-5), (2-6) is the coupling between the axial and transverse displacement resulting from the damage description considered. It is noted that in the absence of damage, the small parameter ε becomes zero and equations (2-5), (2-6) reduce to the classical uncoupled equations governing bending and axial behavior of a symmetric beam.

The governing equations can be conveniently expressed in the frequency domain through the application of the Fourier transform, by letting the applied generalized loads $f_j(x, t)$ (with $j = 1, 2$) be

$$f_j(x, t) = \sum_k \hat{f}_{jk}(x, \omega_k)e^{i\omega_k t}, \tag{2-7}$$

where $i = \sqrt{-1}$, and $\hat{f}_{jk}(x, \omega_k)$ denotes the harmonic component of the generalized load at frequency ω_k [Doyle 1997]. Accordingly, the beam's axial and transverse displacements can be written as

$$u(x, t) = \sum_k \hat{u}_k(x, \omega_k)e^{i\omega_k t}, \quad w(x, t) = \sum_k \hat{w}_k(x, \omega_k)e^{i\omega_k t}, \tag{2-8}$$

where $\hat{u}_k(x, \omega_k)$, $\hat{w}_k(x, \omega_k)$ are the displacements corresponding to the kth harmonic component. In the remainder of the paper, the subscript k is dropped to simplify notation, so that $\omega_k = \omega$, $\hat{u}_k(x, \omega_k) = \hat{u}(x, \omega)$, $\hat{w}_k(x, \omega) = \hat{w}(x, \omega)$.

Next, the axial and vertical displacements of the beam in the reference plane are expanded as perturbations (in terms of a small parameter ε) of the axial and vertical displacement of the undamaged beam

$$\hat{\mathbf{u}}(x, \omega) = \hat{\mathbf{u}}^{(0)}(x, \omega) - \varepsilon\hat{\mathbf{u}}^{(1)}(x, \omega) - \mathbb{O}(\varepsilon^2), \tag{2-9}$$

where $\hat{\mathbf{u}} = \{\hat{u} \; \hat{w}\}^T$. Substituting (2-8), (2-9) into the differential system (2-5), (2-6) and collecting the coefficients of ε^0 and ε^1 results in the set of differential equations

$$\varepsilon^0 : \mathbf{M}\hat{\mathbf{u}}^{(0)}(x, \omega) + \mathbf{E}_1\hat{\mathbf{u}}^{(0)}_{,xx}(x, \omega) + \mathbf{E}_2\hat{\mathbf{u}}^{(0)}_{,4x}(x, \omega) = \hat{\mathbf{f}}^{(0)}(x, \omega), \tag{2-10}$$

$$\varepsilon^1 : \mathbf{M}\hat{\mathbf{u}}^{(1)}(x, \omega) + \mathbf{E}_1\hat{\mathbf{u}}^{(1)}_{,xx}(x, \omega) + \mathbf{E}_2\hat{\mathbf{u}}^{(1)}_{,4x}(x, \omega) = \hat{\mathbf{f}}^{(1)}(x, \omega), \tag{2-11}$$

where

$$\mathbf{M} = \begin{bmatrix} m\omega^2 & 0 \\ 0 & m\omega^2 \end{bmatrix}, \quad \mathbf{E}_1 = \begin{bmatrix} EA & 0 \\ 0 & 0 \end{bmatrix}, \quad \mathbf{E}_2 = \begin{bmatrix} 0 & 0 \\ 0 & -EI \end{bmatrix}, \tag{2-12}$$

where $A = bh$ and $I = bh^3/12$. In (2-11), $\hat{\mathbf{f}}^{(1)}(x, \omega)$ is the load on the first order perturbation equation, which is a function of the zero order displacement $\hat{\mathbf{u}}^{(0)}$ and is responsible for the axial-bending coupling. Its explicit expression can be found in [Apetre et al. 2008].

Spectral finite element discretization. The equation for the ε^0 term corresponds to the uncoupled governing equation for the undamaged beam in the frequency domain, while the first order perturbation equation has the same form, with an applied generalized load that is a function of $\hat{\mathbf{u}}^{(0)}$. A common strategy for the solution of the equations (2-10), (2-11) is based on their formally identical form. Each of the equations can in fact be written in matrix form as

$$\mathbf{M}\hat{\mathbf{u}}(x, \omega) + \mathbf{E}_1\hat{\mathbf{u}}_{,xx}(x, \omega) + \mathbf{E}_2\hat{\mathbf{u}}_{,4x}(x, \omega) = \mathbf{q}(x, \omega), \tag{2-13}$$

where coefficients are 2×2 matrices. We assume that the beam can be divided into finite elements where an element j of length L_j connects two nodes (Figure 2). The behavior of each node is described by 3 degrees of freedom, so that the element's vector of degrees of freedom is defined as $\mathbf{d}_j = \{\hat{u}_{1j}, \; \hat{w}_{1j}, \; \hat{w}_{1j,x}, \; \hat{u}_{2j}, \; \hat{w}_{2j}, \; \hat{w}_{2j,x}\}^T$. The displacement $\hat{\mathbf{u}}(x, \omega)$ within element j is obtained as an interpolation of the nodal degrees of freedom $\mathbf{d}_j$

$$\hat{\mathbf{u}}(x, \omega) = \mathbf{N}_j(x, \omega)\mathbf{d}_j(\omega), \tag{2-14}$$

where $\mathbf{N}_j(x, \omega)$ is the matrix of dynamic shape functions, which are obtained from the solution of the homogeneous governing equation [Doyle 1997]. The application of the dynamic shape functions as interpolation functions is the main feature of the SFEM, which otherwise maintains the formalism of conventional FEs as demonstrated by the theoretical description of this section. Accordingly, the dynamic shape functions $\mathbf{N}_j(x, \omega)$ provide a description of the displacement variation within an element, which is as exact as the homogeneous distributed parameter model used for the description of the problem at hand [Doyle 1997]. In the case considered here, it can be shown that the generalized load in the first order (ε^1) perturbation equations reduces to a concentrated nodal load if a node is placed at the damage location. Then, the solution of the homogeneous beam equations and the proper description of nodal loads corresponding to the presence of damage based on the formulation presented above can be used to obtain exact dynamic shape functions and accurate representations of the beam's displacements in the frequency range corresponding to the applied load. This approach can also be applied when loads are generally distributed along the element length. In this case the dynamic shape functions do not reproduce exactly the displacement field within the element, and some approximation is introduced. The
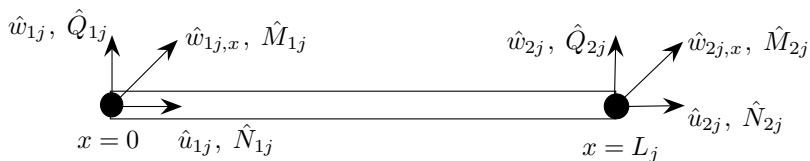
Figure 2. Spectral finite element with nodal displacements and loads.

application of nodes at damage and load locations do not cause a dramatic increase in the computational cost, since only a node needs to be added at each damage and loading site, as opposed to the highly refined meshes that are required for the accurate simulation of wave propagation phenomena with FEs based on the polynomial interpolation of the nodal degrees of freedom. Therefore, the presented modeling approach still represents an efficient tool for the analysis of wave propagation in the considered class of damaged structures. Refinements of the formulation, allowing the accurate representation of general load distributions and of damage locations within the element will be discussed in a forthcoming paper.

Based on the weak formulation of the governing equations (2-13), we can derive the equation

$$\mathbf{K}_j(\omega)\mathbf{d}_j(\omega) = \mathbf{f}_j(\omega), \tag{2-15}$$

where $\mathbf{K}_j(\omega)$ is the element stiffness matrix at frequency ω, defined as

$$\mathbf{K}_j(\omega) = \int_0^{L_j} \left\{ \mathbf{N}_j^T(x, \omega)\mathbf{M}\mathbf{N}_j(x, \omega) - \mathbf{N}_{j,x}^T(x, \omega)\mathbf{E}_1\mathbf{N}_{j,x}(x, \omega) + \mathbf{N}_{j,xx}^T(x, \omega)\mathbf{E}_1\mathbf{N}_{j,xx}(x, \omega) \right\} dx, \tag{2-16}$$

and where $\mathbf{f}_j$ is the vector of applied nodal loads

$$\mathbf{f}_j(\omega) = \int_0^{L_j} \mathbf{N}_j^T(x, \omega)\mathbf{q}(x, \omega) dx, \tag{2-17}$$

Numerical results. The numerical model is used to simulate the response of beams with notches, and specifically to illustrate mode conversion phenomena captured by the model considered. The results are obtained by first transforming the time history of the applied load in the frequency domain through the application of the fast Fourier transform (FFT) algorithm. The nodal displacements corresponding to the various harmonic components are then computed through inversion of the dynamic stiffness matrix of the structure according to (2-17). At each frequency, the displacements' variation along the elements' length is obtained through interpolation using the dynamic shape functions (2-14). Final application of the inverse FFT provides the displacements' variation in time.

An aluminum (Young's modulus $E = 70\,\text{GPa}$, density $\rho = 2750\,\text{kg/m}^3$) beam of length $L = 1\,\text{m}$, thickness $h = 1 \times 10^{-2}\,\text{m}$ and width $b = 5 \times 10^{-2}\,\text{m}$ is considered in the simulations. The beam has a notch of length $\Delta l = 1 \times 10^{-2}\,\text{m}$ and depth h_d, located at $x_d = 3L/4$. The beam is modeled using two spectral elements for a total of nine degrees of freedom (Figure 3). The applied load is a longitudinal tip force whose variation in time is described by a Hanning modulated sine burst at 500 kHz (Figure 4).

Figure 5 shows the variation of the displacements in time and space, while Figure 6 shows snapshots of the beam's deformed configuration at three instants in time. The longitudinal wave generated by the applied load propagates from the tip of the beam and gets partially reflected and converted when it reaches the notch at $x_D = 3L/4$. Mode conversion phenomena such as the one illustrated in this example are
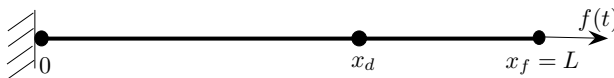
Figure 3. Schematic of the clamped-free beam with a longitudinal tip load, modeled using two spectral elements.
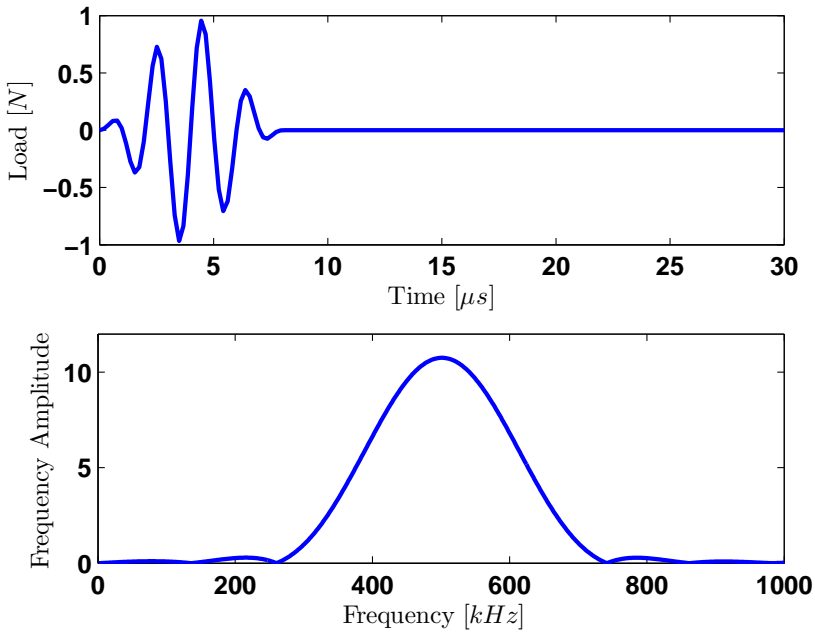
Figure 4. Modulated sinusoidal pulse load in time and frequency domain.
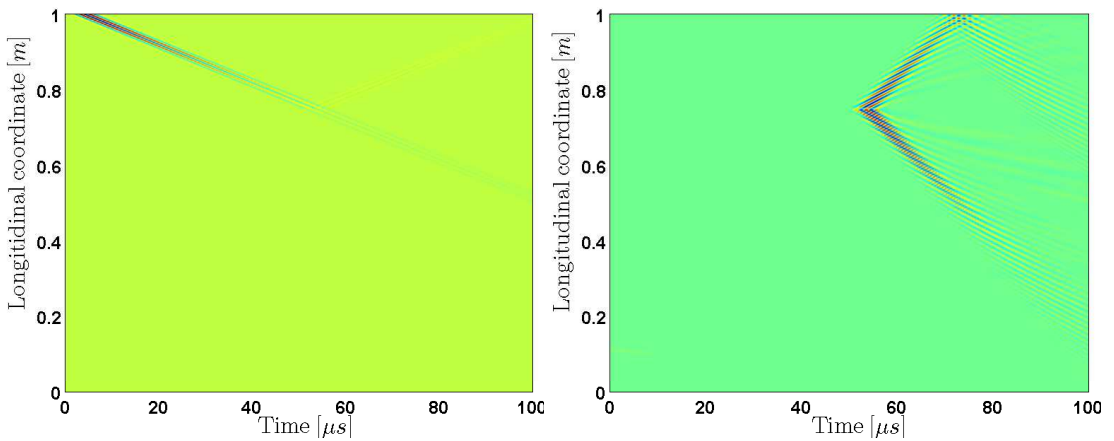
Figure 5. Longitudinal (left) and transverse (right) displacement as functions of time and longitudinal coordinate. Notch length $\Delta l = 0.001$ m.

very important as they may be exploited to increase the sensitivity of damage detection and interpretation techniques.

3. Wave-based damage index formulation

Theoretical background. The perturbation analysis is used to define a damage index (DI) which locates the notch and estimates its severity. The definition is such that the DI has value 1 at undamaged locations,
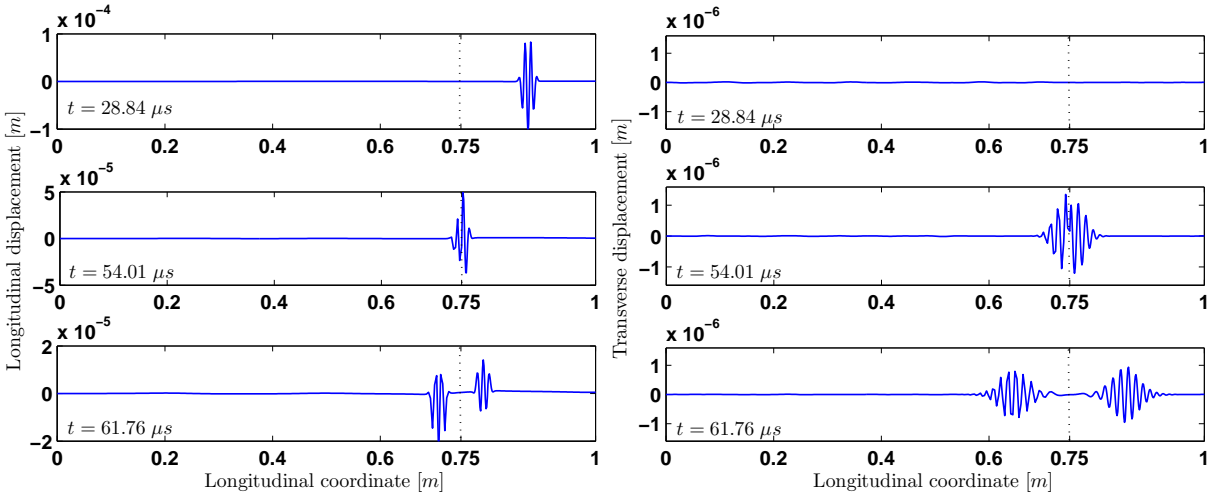
Figure 6. Longitudinal (left) and transversal (right) displacements as function of longitudinal coordinate, for three instants in time.

while it deviates from unity in the vicinity of the notch. The formulation is based on the estimation of the distribution of strain energy associated with propagating and reflected waves. In the proposed approach, which follows procedures previously applied on modal curvature data of notched plates [Sharma et al. 2006], the beam is divided into N segments, over which the strain energy is evaluated through integration over the segment length. At a given instant of time t, the strain energy over segment p, defined by $x \in [x_p, x_{p+1}]$, is obtained by summing contributions from axial and bending deformations

$$\Delta U_p(t) = U(x_{p+1}, t) - U(x_p, t) = \frac{1}{2} \int_{x_p}^{x_{p+1}} \left[EAu_{,x}^2(x, t) + EI w_{,xx}^2(x, t) \right] dx, \tag{3-1}$$

where u and w can be considered as superpositions of the solutions obtained for various orders of the perturbation parameter of (2-9). Substituting the displacement expansions and truncating at the second order yields the following approximate expression for the strain energy of the damaged beam

$$\Delta U_p(t) \approx \Delta U_p^{(0)}(t) - \varepsilon \Delta U_p^{(1)}(t) - O(\varepsilon^2), \tag{3-2}$$

where

$$\Delta U_p^{(0)}(t) = \frac{1}{2} \int_{x_p}^{x_{p+1}} \left[EA[u_{,x}^{(0)}(x, t)]^2 + EI[w_{,xx}^{(0)}(x, t)]^2 \right] dx \tag{3-3}$$

corresponds to the strain energy of the undamaged beam, and where

$$\Delta U_p^{(1)}(t) = \int_{x_p}^{x_{p+1}} \left[EA u_{,x}^{(0)}(x, t) u_{,x}^{(1)}(x, t) + EI w_{,xx}^{(0)}(x, t) w_{,xx}^{(1)}(x, t) \right] dx \tag{3-4}$$

is the contribution due to damage. In preparation for the analysis of experimental data, the integrals are estimated numerically by using a set of spline functions. This leads to continuous strain energy functions $\Delta U^{(0)}(x, t)$ and $\Delta U(x, t)$. Based on (3-4) and the numerical results presented in the previous section, displacement perturbations occur only when waves reach the notch location. Accordingly, the

corresponding strain energy perturbation $\Delta U_p^{(1)}(x, t)$ originates at the damage location, where it reaches its maximum value [Sharma et al. 2006], to progressively decrease in value as the secondary wave produced by the damage propagates away from the damage. The damage index can be thus defined as a ratio between the strain energies associated with the 1st order perturbation, to the strain energy of the undamaged beam, as quantified by the zero order solution

$$d(x, t) = \frac{\Delta U(x, t)}{\Delta U^{(0)}(x, t)} \approx 1 - \varepsilon \frac{\Delta U^{(1)}(x, t)}{\Delta U^{(0)}(x, t)}. \tag{3-5}$$

Equation (3-5) explicitly shows how the deviation from unity of the DI is directly proportional to the perturbation parameter ε which defines the notch depth. The location of damage along the beam length is instead identified by a peak of the $\Delta U^{(1)}(x, t)/\Delta U^{(0)}(x, t)$ function occurring at the damage site.

The above damage index is time-dependent, and it is convenient to consider its cumulative value over a selected time interval

$$d_c(x) = \int_t \left| d(x, t) \right| dt \tag{3-6}$$

to obtain a function depending uniquely on the spatial coordinate.

Numerical examples. Three examples are presented to demonstrate the effectiveness of the proposed damage index formulation as a damage locator and estimator. In all the cases, the beam is simply supported and is excited at a given point by a 5-cycle sinusoidal load. The beam is made of aluminum with Young's modulus $E = 70$ GPa and density $\rho = 2750$ kg/m^3 and has length of $L = 1$ m, thickness $h = 1 \times 10^{-2}$ m and width $b = 5 \times 10^{-2}$ m. The simulation is performed over a time interval which corresponds to the time required for the injected pulse to reach the boundary. The corresponding cumulative DIs are calculated according to (3-6), and plotted in Figure 7. As expected, damage is highlighted by a clear deviation from unity at the damage site. It is important to note how the DI values increase with the notch depth h_D and also shows a monotonic dependence upon the damage width Δl.

The first configuration considers a 5-cycle sinusoidal load applied in the longitudinal direction at $x_f = 0.6L$ and a notch located at $x_f = 0.4L$. According to this load configuration, $w^{(0)} \equiv 0$, and the damage index reduces to

$$d(x, t) = 1 - \varepsilon \frac{\int u_{,x}^{(0)} u_{,x}^{(1)} dx}{\int (u_{,x}^{(0)})^2 dx}. \tag{3-7}$$

Figure 7, top left, shows that for a given notch depth h_D, the DI increases with the damage width Δl.

The results for a transverse load shown in the top right part of the same figure also confirm the damage index behavior. In this last case, the DI can be approximated as

$$d(x, t) = 1 - \varepsilon \frac{\int w_{,xx}^{(0)} w_{,xx}^{(1)} dx}{\int (w_{,xx}^{(0)})^2 dx}, \tag{3-8}$$

since $u^{(0)} \equiv 0$. The graph shows that for a given damage width Δl, the DI increases with the notch depth h_D.

In these two cases, the coupling between longitudinal and transverse displacements due to the damage is of order $\mathbb{O}(\varepsilon^2)$ so it is neglected. To include coupling at $\mathbb{O}(\varepsilon)$, the third configuration considers a 5-cycle sinusoidal load applied in both longitudinal and direction at $x_f = L/2$ and a notch located at $x_f = L/4$.
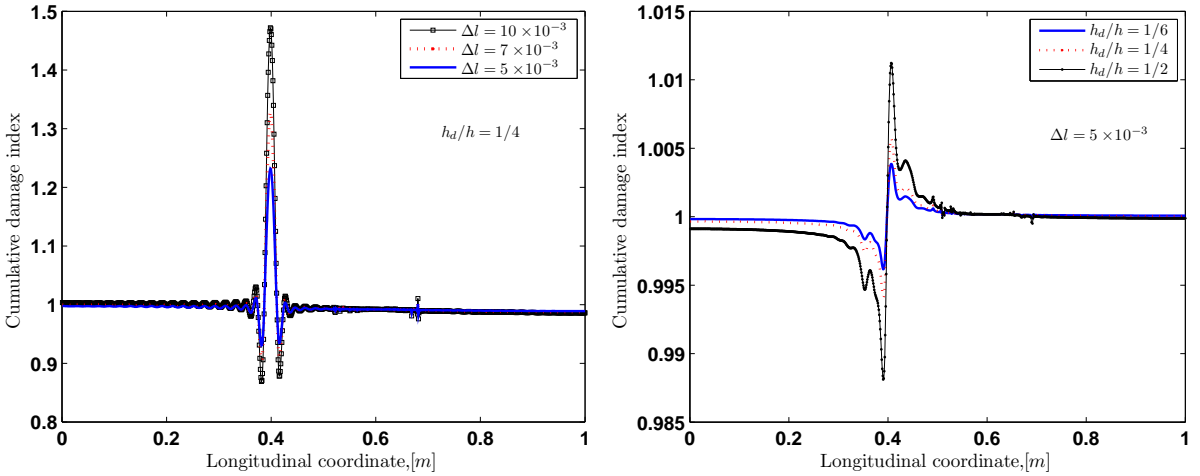
Figure 7. Cumulative damage index results for (left) a horizontal applied load, with $h_d/h = 1/4$ and varying damage length ($\Delta l = 0.005, 0.007, 0.01$ m); and (right) a vertical applied load, with $\Delta l = 0.005$ m and varying damage depth ($h_d/h = 1/6, 1/4, 1/2$).
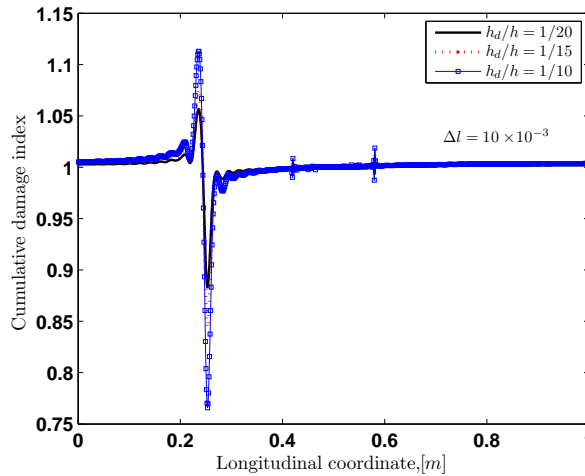
Figure 8. Cumulative damage index results for both horizontal and vertical applied loads, with $\Delta l = 0.01$ m and varying damage depth ($h_d/h = 1/20, 1/15, 1/10$).

Both zero order longitudinal and transverse displacements are present and the DI is given by (3-6). The resulting DI is plotted in Figure 8 for a given damage width Δl and for various notch depths h_D. Once more we see that the DI increases as h_D increases.

4. Experimental implementation

This section presents the extension of the DI concept to the analysis of experimental data. The presented results demonstrate the effectiveness of the DI as a damage indicator, and show its practicality as an inspection tool. The case of a homogeneous plate with a transverse notch is considered. The results in

this section therefore cannot be directly compared with those obtained analytically as the analytical results are obtained for an Euler-Bernoulli beam. Refinements of the analytical formulation to include Lamb modes thus allowing the accurate simulation of the experiments presented here are under development and will be discussed in future papers. However, the objective is to illustrate the application of the concept in a practical setting and to demonstrate how it may be applied to correctly identify the presence of damage.

Experimental evaluation of the DI requires information regarding the undamaged response of the component under investigation and of the perturbation of its response due to the presence of damage. While in the numerical model such information was directly obtained as a by-product of the adopted numerical approach, the effective analysis of experimental data requires the ability to separate these two pieces of information. Preferably, this should be done without need to rely on historical data on the undamaged part. This is here achieved through the application of simple filtering strategies in the wavenumber/frequency domain, which are enabled by the elevated spatial resolution provided by scanning devices such as a scanning laser Doppler vibrometer [Ruzzene 2007]. A summary of this filtering approach, used to remove the reflections due to damage, is presented in the next section, which is followed by the illustration of how the filtering procedure can be used in conjunction with the DI to detect damage in a structure.

Filtering procedure for the estimation of undamaged response. The basic concept behind the filtering technique under consideration is illustrated here for the case of propagating waves in a one-dimensional rod. The data is obtained based on SFE model described in Section 2. Additional details, including the application to two dimensional problems and a more in-depth description can be found in [Ruzzene 2007]. It is assumed that the clamped-free rod is excited at its free end by a modulated harmonic load, which generates a wave. The injected wave interacts with the damage located at $x_d = L/2$, again modeled as a thickness reduction corresponding to $h_d/h = 0.1$, where it is reflected.

The graphs on the left on Figure 9 are snapshots of the rod response at instants of time before, during and after the wave interaction with the notch. After the reflection, the rod's displacement is given by

$$u(x, t) = u^{(i)}(x, t) + u^{(r)}(x, t), \tag{4-1}$$

where one can consider $u^{(i)}(x, t)$ as the 0th order term in the perturbation solution. The two-dimensional FFT in space and time of the rod response is also given by the superposition of contributions from incident and reflected waves

$$\hat{u}(k, \omega) = \hat{u}^{(i)}(k, \omega) + \hat{u}^{(r)}(k, \omega). \tag{4-2}$$

Its representation in the frequency/wavenumber domain shown on the right in Figure 9 highlights the presence of the main pulse propagating along the $x > 0$ direction, and of the reflected pulse propagating in the opposite direction ($x < 0$). As a result, the two corresponding peaks of the two-dimensional FFT appear centered at $\omega = \omega_0$, $k = \pm k_0$. In particular, the reflected pulse has lower amplitude, it is characterized by the same frequency, and appears in the $k > 0$ region of the wavenumber/frequency domain. The two-dimensional representation hence effectively separates incident and reflected wave components. This allows the application of simple filtering strategies, which remove the reflected wave from the recorder signal, thus providing an approximation of the response of the structure in the absence of the damage. For example, a two-dimensional Hanning window can be used to eliminate the reflected
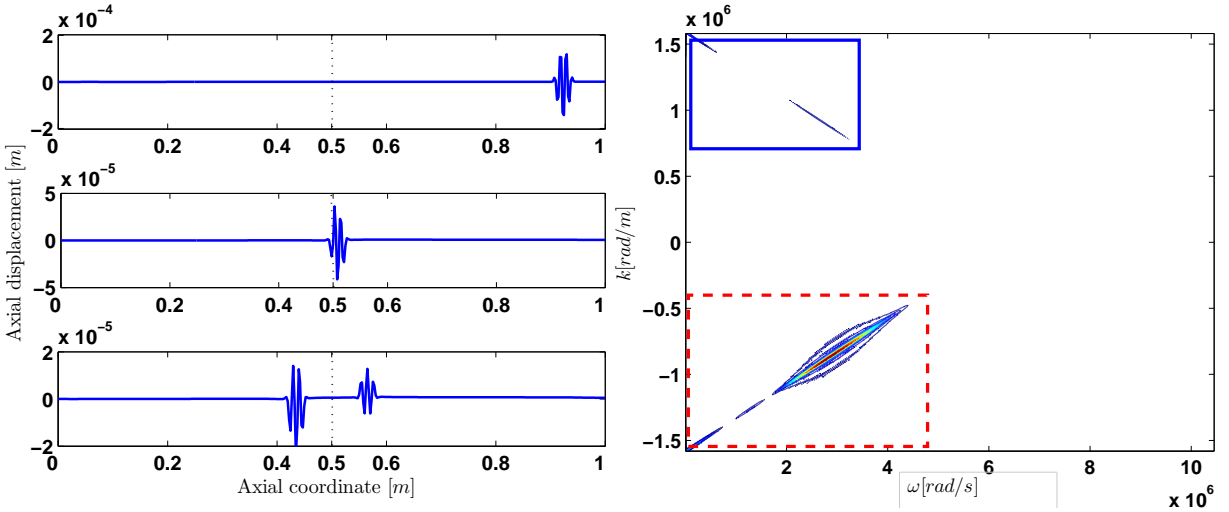
Figure 9. Left: Snapshots of rod deformed configuration at three instants of time. Right: 2D frequency/wavenumber domain representation; the solid box highlights the reflected component, and the dashed box the incident component.

wave and to obtain the frequency/wavenumber spectrum shown in Figure 10, left. Mathematically, the windowing process can be simply expressed as a function product between the wave's two-dimensional FFT and a two-dimensional window function

$$\hat{u}^{(i)}(k, \omega) \approx \left[1 - H(k - k_0, \omega - \omega_0)\right]\hat{u}(k, \omega), \tag{4-3}$$
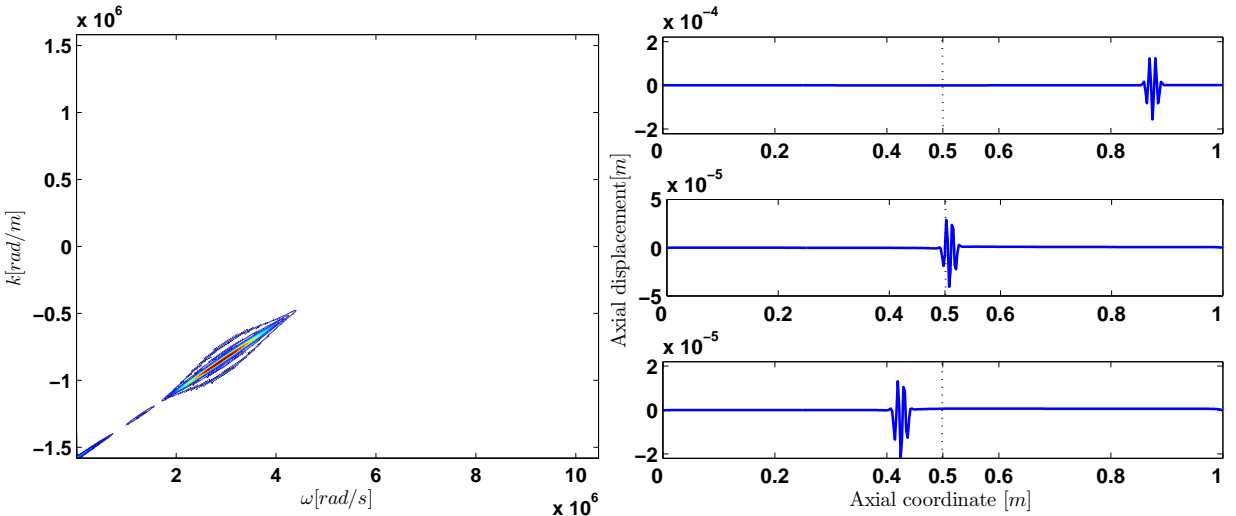
Figure 10. Representation of filtered (incident) axial displacement in the two-dimensional frequency domain (left), and the corresponding deformed configurations at three instants of time (right).
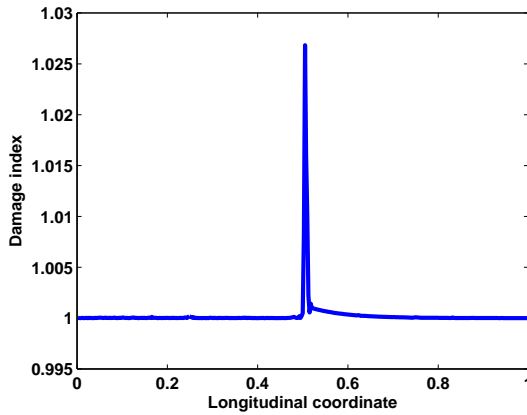
Figure 11. Damage index in a rod.

where $H(k - k_0, \omega - \omega_0)$ denotes the windowing function centered at k_0, ω_0. The incident space-time domain signal can then be reconstructed through inverse Fourier transformation. The incident signal obtained upon filtering at the same instant considered in the left half of Figure 9 is shown in the right half of Figure 10, to demonstrate how the windowing procedure removes the reflected propagating pulse while leaving the response corresponding to the undamaged beam practically unaltered. The separated incident and the total signals can be used for the damage index estimation according to the definition provided above. The result in terms of cumulative damage index for the simple case discussed in this section is plotted in Figure 11.

Experimental set-up for wavefield measurements. A schematic of the set-up is shown in Figure 12. The experimental results are obtained using piezoceramic discs as actuators and a scanning laser Doppler
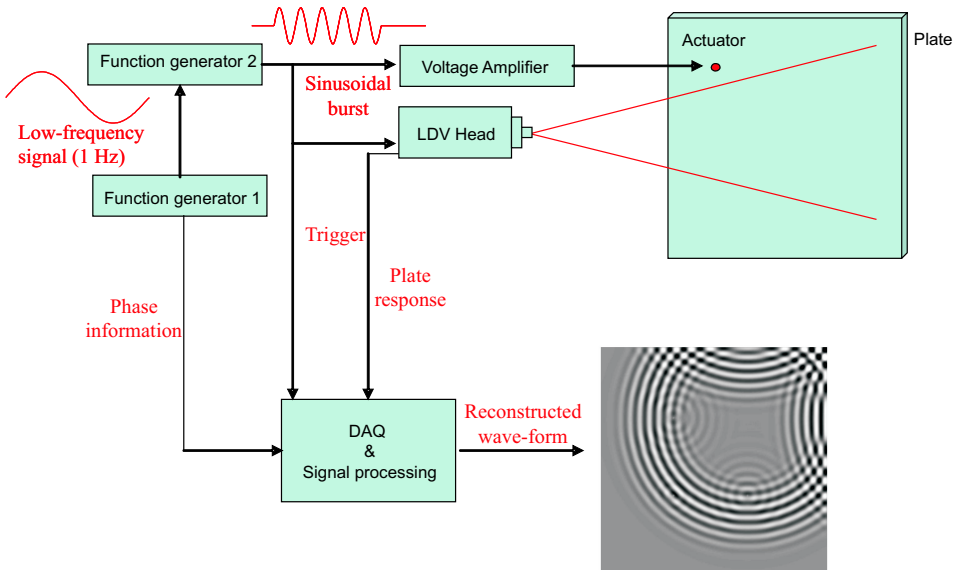
Figure 12. Schematic of experimental set-up for wavefield measurement.

vibrometer (SLDV) as a sensor. The SLDV (Polytec PI, Model PSV400M2) allows frequency sampling up to 1 MHz, which enables GUWs detection and visualization. In the wave propagation tests, the piezodiscs are driven by a sinusoidal burst generated by a signal generator. The resulting elastic waves are recorded at the measurement grid points defined on the scanning system. The operation of the SLDV requires the generation of a pulse at each grid point in order to record the corresponding response. Phase information is retained by triggering the excitation signal through a low frequency signal (10 Hz), which also defines the scanning rate. Upon completion of measurements at all grid points, the recorded responses are postprocessed to obtain full images of the propagating wavefield within the region of inspection.

Shown on the right is a detail top view of a typical test specimen: in this case, an aluminum plate of dimensions $0.76 \, \text{m} \times 0.76 \, \text{m} \times 3.05 \times 10^{-3} \, \text{m}$. The damage is a $27 \times 10^{-3} \, \text{m}$ long and $1 \times 10^{-3} \, \text{m}$ deep grove which was cut in the plate at the location shown. The figure also shows a typical line of measurement points (in the case presented below the number of points is 69). The wave is generated by a surface bonded piezotransducer excited by a 5-cycle, 110 kHz sinusoidal pulse. The responses at the grid points is recorded, stored, and converted for postprocessing. In particular, the responses are interpolated using spline functions, which can be conveniently differentiated for strain energy evaluation.
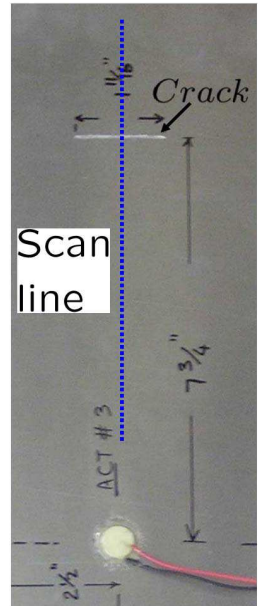
Experimental results. The time-spatial variation of the plate response shows the presence of a low amplitude S_0 mode, which propagates faster than the A_0 mode (Figure 13). The significant difference in amplitude recorded for the two modes is related to their polarization (S_0 is mostly in-plane, while A_0 is mostly out-of-plane) and to the limitation of the currently available SLDV which only measures out-of-plane displacement or velocity components. When the S_0 mode reaches the crack location, it is partially converted into A_0, as well as reflected and transmitted. The detailed spatial information obtained
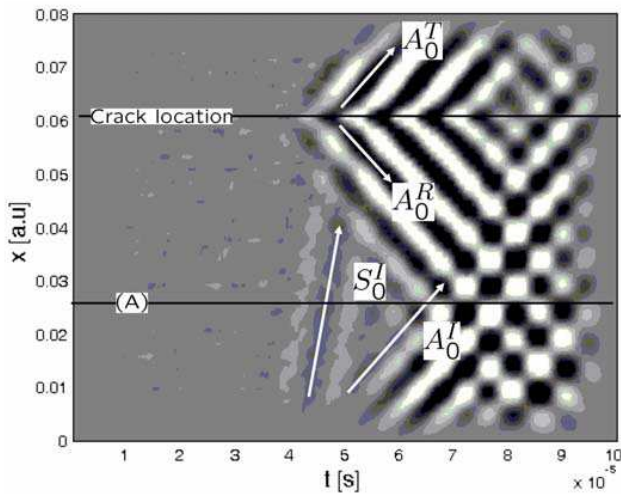
Figure 13. Space-time variation of recorded response showing multimodal wave propagation, mode conversion and reflection at crack location.
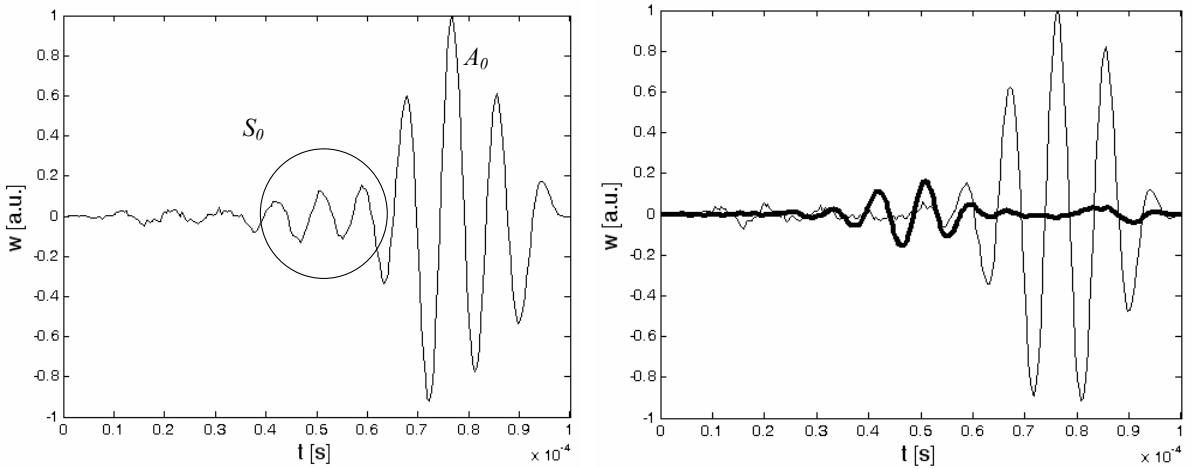
Figure 14. Left: Response at location A of Figure 13. Right: Filtered S_0 response (thick line) and reflected A_0 mode (thin line).

from the SLDV can be used to effectively separate the S_0 mode from the A_0 mode through filtering in the frequency/wavenumber domain. Proper design of the filtering window allows in fact the separation of incident and reflected waves as well as the decoupling of different modes propagating at the same frequency. Figure 14, left shows the time response recorded at location A, while the right half of the same figure compares the two reconstructed signals corresponding to the S_0 mode and the reflected A_0 mode.

Figure 15 shows the variation of the plate incident and reflected responses in time and space as colormap plots. Both responses contain both S_0 and A_0 modes.
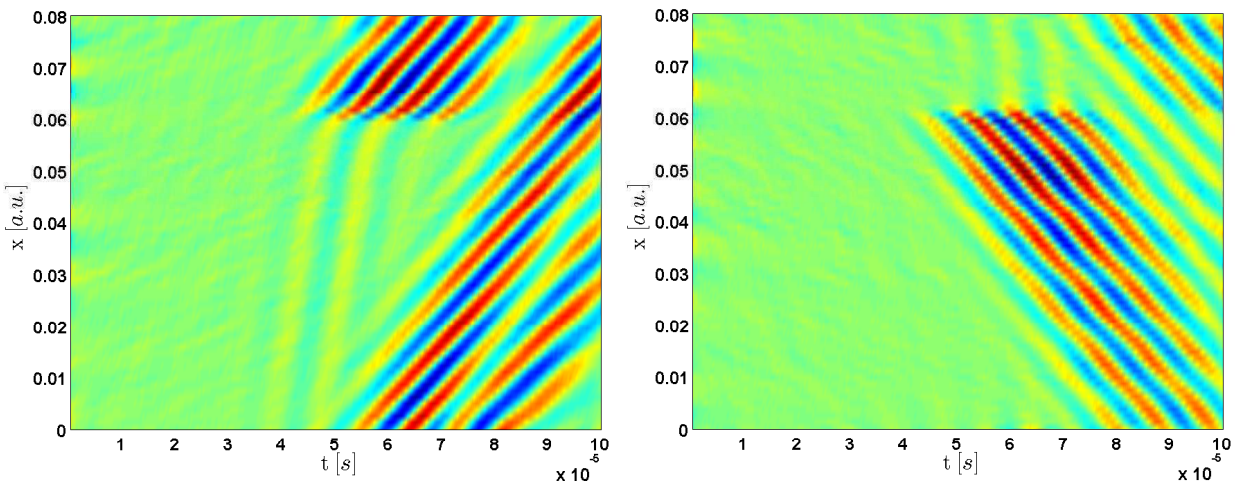
Figure 15. Filtered incident (left) and reflected (right) response as function of time and longitudinal coordinate.
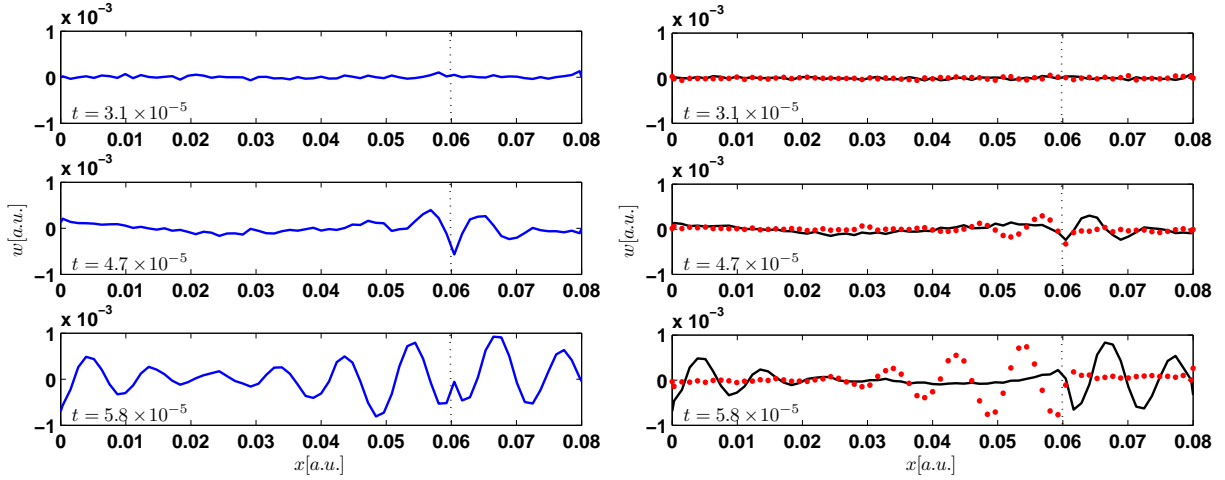
Figure 16. Left: Raw test data (transverse displacement) as function of longitudinal co-ordinate at three instants. Right: Filtered incident (dotted line) and reflected (continuous line) waves as function of longitudinal coordinate at the same three moments.

Figure 16 shows snapshots of the displacements' variation along the beam at three instants of time as raw data and also as filtered data. A very clear separation between the incident and the reflected waves is presented in Figure 16, right.

Analytically the damage index was defined as the ratio of strain energies associated with damaged and undamaged beams. Due to the mode conversion phenomena, the damage index obtained from the experimental data is defined as the ratio of strain energies associated with the damaged beam and with the incident S_0 mode denoted by S_0^I (Figure 14, left)

$$d(x,t) = \frac{\Delta U(x,t)}{\Delta U^{(S_0^I)}(x,t)}, \tag{4-4}$$

where the stain energy associated with S_0^I is defined as

$$\Delta U^{(S_0^I)}(x,t) = \int \left[w_{,xx}^{(S_0^I)}(x,t) \right]^2 dx \tag{4-5}$$

and where $w^{(S_0^I)}$ is the displacement associated with the S_0^I. As in the analytically defined damage measure of (3-6), a cumulative damage index is considered and the result is plotted in Figure 17. Due to the significant difference in amplitude recorded for the two modes the ratio $d(x,t)$ gives very large values. But the ratio still has a peak at the location of the damage (Figure 17). Refinements of the proposed DI will be further investigated and in future papers.

5. Conclusions and future work

This paper presents a wave-based damage index and illustrates the model by applying it to both analytical and experimental data. The formulation is first supported by a numerical method which simulates the effects of a notch damage on a propagating elastic wave. The numerical technique combines the SFEM
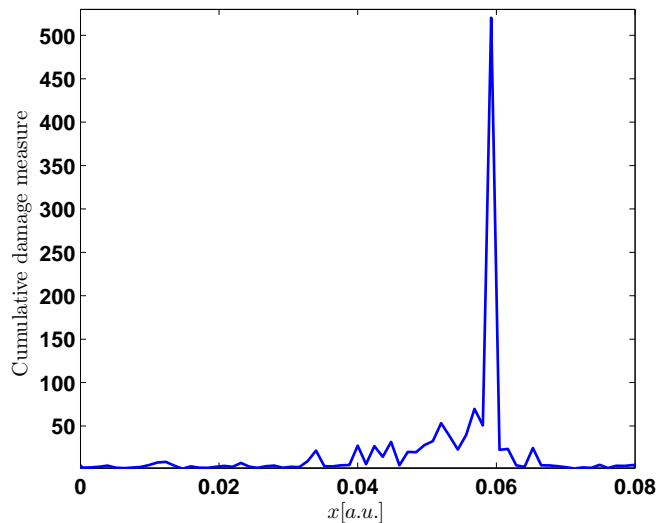
Figure 17. Cumulative damage index of experimental data.

and perturbation techniques and allows the prediction of reflections and mode conversion phenomena associated with wave/damage interactions.

The damage index formulation is based on the distribution of strain energy within the structure. The technique is implemented by estimating the undamaged response through a filtering process that operates in the frequency/wavenumber domain to separate wave components propagating in opposite directions. Numerical results, based on the developed numerical model, as well as experimental data, obtained through a scanning laser vibrometer show the effectiveness of the proposed formulation and its potentials for implementation as a practical inspection tool for detection of the damage location. Future work will include results for the quantification of the damage that are missing in the current development. Also a similar concept will be developed for the case of multimodal signals.

The objective of the paper is to illustrate the effectiveness of the damage index for both analytical and experimental data. The experimental data cannot be validated with the present numerical model, due to the model's limitation to describe higher Lamb modes. Future work includes extensions of the analytical formulation, allowing accurate simulation of the experiments.

Future work will also extend the concept to practical aerospace structures in the presence of structural features such as holes, rivets, or localized impedance changes which complicate the wavefield and its interpretation, and make the identification of the presence of damage much more challenging. The authors are already successful in applying the same tool for two dimensional data in the presence of multiple scatterers. In future work, the authors will demonstrate how multiple scatterers contributions to the scattered field can be resolved to obtain the characterization of the individual scatterers.

References

[Apetre et al. 2008] N. Apetre, M. Ruzzene, S. Hanagud, and S. Gopalakrishnan, "Spectral and perturbation analysis of first-order beams with notch damage", *J. Appl. Mech.* (*ASME*) **75**:3 (2008), 031019.

[Basri and Chiu 2004] R. Basri and W. K. Chiu, "Numerical analysis on the interaction of guided Lamb waves with a local elastic stiffness reduction in quasi-isotropic composite plate structures", *Compos. Struct.* **66**:1–4 (2004), 87–99.

[Cho 2000] Y. Cho, "Estimation of ultrasonic guided wave mode conversion in a plate with thickness variation", *IEEE Trans. Ultrason. Ferroelectr. Freq. Control* **47**:3 (2000), 591–603.

[Cho and Rose 1996] Y. Cho and J. L. Rose, "A boundary element solution for a mode conversion study on the edge reflection of Lamb waves", *J. Acoust. Soc. Am.* **99**:4 (1996), 2097–2109.

[Choi and Stubbs 2004] S. Choi and N. Stubbs, "Damage identification in structures using the time-domain response", *J. Sound Vib.* **275**:3–5 (2004), 577–590.

[Cornwell et al. 1999] P. Cornwell, S. W. Doebling, and C. R. Farrar, "Application of the strain energy damage detection method to plate-like structures", *J. Sound Vib.* **224**:2 (1999), 359–374.

[Doebling et al. 1996] S. W. Doebling, C. R. Farrar, M. B. Prime, and D. W. Shevitz, "Damage identification and health monitoring of structural and mechanical systems from changes in their vibration characteristics: a literature review", Technical report LA-13070-MS, Los Alamos National Laboratory, 1996, Available at http://www.lanl.gov/projects/ei/shm/pubs/lit_review.pdf.

[Doyle 1997] J. F. Doyle, *Wave propagation in structures: spectral analysis using fast discrete Fourier transforms*, 2nd ed., Springer, New York, 1997.

[Giurgiutiu 2005] V. Giurgiutiu, "Tuned Lamb wave excitation and detection with piezoelectric wafer active sensor of structural health monitoring", *J. Intell. Mater. Syst. Struct.* **16**:4 (2005), 291–305.

[Giurgiutiu 2008] V. Giurgiutiu, *Structural health monitoring with piezoelectric wafer active sensors*, Academic Press, Amsterdam, 2008.

[Giurgiutiu et al. 2003] V. Giurgiutiu, J. Bao, and W. Zhao, "Piezoelectric wafer active sensor embedded ultrasonics in beams and plates", *Exp. Mech.* **43**:4 (2003), 428–449.

[Ho and Ewins 1999] Y. K. Ho and D. J. Ewins, "Numerical evaluation of the damage index", pp. 995–1011 in *Structural health monitoring 2000* (Stanford, CA, 1999), edited by F.-K. Chang, Technomic, Lancaster, PA, 1999.

[Kazys et al. 2006] R. Kazys, L. Mazeika, R. Barauskas, R. Raisutis, V. Cicenas, and A. Demcenko, "3D analysis of interaction of Lamb waves with defects in loaded steel plates", *Ultrasonics* **44**:Supplement 1 (2006), e1127–e1130.

[Kim and Stubbs 2003] J. T. Kim and N. Stubbs, "Crack detection in beam type structures using frequency data", *J. Sound Vib.* **259**:1 (2003), 146–160.

[Krawczuk et al. 2003] M. Krawczuk, M. Palacz, and M. Ostachowicz, "The dynamic analysis of a cracked Timoshenko beam by the spectral element method", *J. Sound Vib.* **264**:5 (2003), 1139–1153.

[Kumar et al. 2004] D. S. Kumar, D. R. Mahapatra, and S. Gopalakrishnan, "A spectral finite element for wave propagation and structural diagnostic analysis of composite beam with transverse crack", *Finite Elem. Anal. Des.* **40**:13–14 (2004), 1729–1751.

[Lee et al. 2000] U. Lee, J. Kim, and A. Y. T. Leung, "The spectral element method in structural dynamics", *Shock Vib. Digest* **32**:6 (2000), 451–465.

[Lestari 2001] W. Lestari, *Damage of composite structures: detection technique, dynamic response and residual strength*, Ph.D. thesis, Georgia Institute of Technology, 2001.

[Luo and Hanagud 1997] H. Luo and S. Hanagud, "An integral equation for changes in the structural dynamics characteristics of damaged stuctures", *Int. J. Solids Struct.* **34**:35-36 (1997), 4557–4579.

[Michaels et al. 2005] T. E. Michaels, J. E. Michaels, B. Mi, and M. Ruzzene, "Damage detection in plate structures using sparse transducer arrays and acoustic wavefield imaging", pp. 938–945 in *Review of progress in quantitative nondestructive evaluation*, vol. 24A, edited by D. O. Thompson and D. E. Chimenti, American Institute of Physics, Melville, NY, 2005.

[Ostachowicz 2008] M. Ostachowicz, "Damage detection of structures using spectral finite element method", *Comput. Struct.* **86**:3–5 (2008), 454–462.

[Ostachowicz and Krawczuk 1991] M. Ostachowicz and M. Krawczuk, "Analysis of the effect of cracks on the natural frequencies of a cantilever beam", *J. Sound Vib.* **150**:2 (1991), 191–201.

[Pandey et al. 1991] A. K. Pandey, M. Biswas, and M. M. Samman, "Damage detection from changes in curvature mode shapes", *J. Sound Vib.* **145**:2 (1991), 321–332.

[Przemieniecki 1968] J. S. Przemieniecki, *Theory of matrix structural analysis*, McGraw-Hill, New York, 1968.

[Raghavan and Cesnik 2007] A. Raghavan and C. E. S. Cesnik, "Review of guided-wave structural health monitoring", *Shock Vib. Digest* **39**:2 (2007), 91–114.

[Rose 2002] J. L. Rose, "A baseline and vision of ultrasonic guided wave inspection potential", *J. Pressure Vessel Technol. (ASME)* **124**:3 (2002), 273–282.

[Ruzzene 2007] M. Ruzzene, "Frequency-wavenumber domain filtering for improved damage visualization", *Smart Mater. Struct.* **16** (2007), 2116–2129.

[Ruzzene et al. 2005] M. Ruzzene, S. M. Jeong, T. E. Michaels, J. E. Michaels, and B. Mi, "Simulation and measurement of ultrasonic waves in elastic plates using laser vibrometry", pp. 172–179 in *Review of progress in quantitative nondestructive evaluation*, vol. 24A, edited by D. O. Thompson and D. E. Chimenti, American Institute of Physics, Melville, NY, 2005.

[Sharma et al. 2006] V. Sharma, M. Ruzzene, and S. Hanagud, "Damage index estimation in beams and plates using laser vibrometry", *AIAA J.* **44**:4 (2006), 919–923.

[Staszewski et al. 2004] W. J. Staszewski, C. Boller, and G. Tomlinson (editors), *Health monitoring of aerospace structures: smart sensor technologies and signal processing*, Wiley, West Sussex, 2004.

NICOLE APETRE: nicole.apetre@gatech.edu
School of Aerospace Engineering, Georgia Institute of Technology, 270 Ferst Drive, Atlanta, GA 30332, United States

MASSIMO RUZZENE: ruzzene@ae.gatech.edu
School of Aerospace Engineering, Georgia Institute of Technology, 270 Ferst Drive, Atlanta, GA 30332, United States
http://www.ae.gatech.edu/people/mruzzene/

SATHYANARAYA HANAGUD: hanagud@aerospace.gatech.edu
School of Aerospace Engineering, Georgia Institute of Technology, 270 Ferst Drive, Atlanta, GA 30332, United States

S. GOPALAKRISHNAN: krishnan@aero.iisc.ernet.in
Department of Aerospace Engineering, Indian Institute of Science, Bangalore, 560012, India
http://www.aero.iisc.ernet.in/~krishnan

GENERALIZED PLANE STRAIN FINITE-ELEMENT FORMULATION FOR THERMAL AND ELECTRICAL BUCKLING ANALYSIS OF PIEZO COMPOSITE BEAM

R. JEROME AND N. GANESAN

We develop a generalized plane strain (GPS) finite element formulation to predict the critical buckling voltage and temperature of a piezo composite beam in more generality than the cases characterized by plane strain and plane stress assumptions.

This generalized plane strain formulation represents the two-dimensional finite element model as closely as possible to the three-dimensional finite element model. It is similar to the plane strain formulation that reduces a three-dimensional stress-strain relation to a two-dimensional one, but in contrast with most GPS formulations in the literature, it does not include out of plane degrees of freedom. In our formulation the reduced two-dimensional stress-strain relation incorporates the effect of allowed/applied strain ε_0 in the dimension not included in the two-dimensional model. Further, since the goal is to deal with thermal and electrical buckling analysis, an initial strain vector is incorporated in the formulation.

A finite element solver based on an eight-node quadrilateral element was developed under the new formulation, and its results show good agreement with those reported by Varelis and Saravanos (2004) and those obtained with ANSYS. The critical electrical and thermal buckling loads for examples other than those characterized by plane stress and plane strain were analyzed, and it was found that they are significantly influenced by α, the parameter controlling the out-of-plane strains.

1. Introduction

Finite element analysis of smart structures has attracted much attention in recent years due to its wide range of applications. A significant amount of research has gone into the analysis of piezo composite structures. A number of finite element (FE) models have been proposed for the analysis of smart structures; and a detailed survey is given in [Benjeddou 2000]. One of the main problems addressed is the buckling analysis of smart structures.

Three-dimensional beam models can be simulated using two-dimensional in-plane elements by considering only the longitudinal cross-section of the three-dimensional beam model. The boundary conditions and the loading conditions can be simulated more accurately in this two-dimensional model than in the one-dimensional beam element model. Still, the two-dimensional analysis of the beam is based on either the plane stress or plane strain assumption, and cases outside these assumptions cannot be handled by two-dimensional in-plane elements. The generalized plane strain formulation can be used to model cases other than plane stress and plane strain at the cost of additional degrees of freedom.

The generalized plane strain formulation has been discussed extensively in the literature and has been used for several applications. Most composite problems are generalized plane strain in nature, and they

are often solved using three-dimensional finite element analysis. Lin and Yi [1991] used the generalized plane strain formulation for the analysis of interlaminar stresses in viscoelastic composites. Krueger et al. [2002] have critically compared the two-dimensional finite element modeling assumptions with results from three-dimensional finite element analysis for composite skin-stiffener debonding. They have proposed a method for analyzing the composite using one layer of brick elements instead of using plane elements. Hu and Pagano [1997] presented a new method of solving generalized plane strain problems by introducing out-of-plane thermal strains in a two-dimensional finite element analysis with the plane strain model. They have done their proposed two-dimensional FE analysis using ANSYS and compared the results and computation time with those of the three-dimensional FE models.

In most of the literature, a plate element has been used to model the piezo composite plate as well as piezo composite beams for buckling analysis. Varelis and Saravanos [2002] developed a nonlinear mechanics to describe piezoelectric laminated plates, including nonlinear effects due to large displacements and rotations, and carried out a linear buckling analysis of plates by neglecting the nonlinear stiffness matrix. Varelis and Saravanos [2004] carried out pre- and post-buckling analysis of plates. Giannopoulos et al. [2007] presented a coupled formulation between thermal, electrical, and mechanical fields incorporating nonlinearity due to large displacements, and solved for linear buckling by neglecting the nonlinear stiffness matrix.
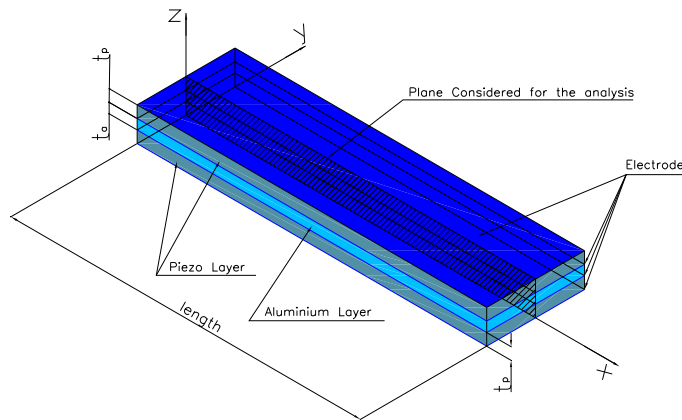
Figure 1. The three-dimensional piezo composite beam.
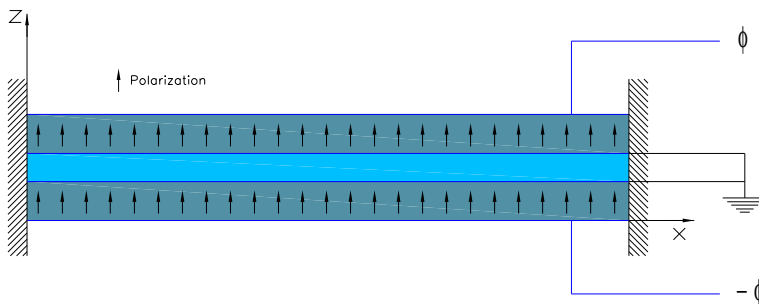
Figure 2. The plane of the finite element model used for thermal and electrical buckling analysis, with electrical boundary conditions and kinematic constraints. For thermal buckling analysis, the applied voltage is zero.

This paper presents a generalized plane strain FE formulation for thermal and electrical buckling of a piezo composite beam (Figure 1). The two-dimensional model is a cross-sectional one, as shown in Figure 2. This contrasts with the plate finite elements generally used to model a piezo composite beam [Varelis and Saravanos 2002; 2004; Giannopoulos et al. 2007]. Our generalized plane strain formulation is similar to the standard plane strain formulation (which reduces a three-dimensional stress-strain relation to a two-dimensional stress-strain relation), in that it does not include out-of-plane degrees of freedom. Therefore, it has fewer degrees of freedom than the conventional generalized plane strain formulation. As we shall see, however, this does not compromise its performance.

Our formulation includes the effect of out-of-plane strain (that is, in the direction not included in the two-dimensional FE model) via a parameter α, which intervenes in the stress-strain relationship of the beam. The effect of the out-of-plane strain is included in the formulation through the constitutive relations.

We compare the performance of the plane strain model, the plane stress model and the newly developed generalized plane strain model in calculating the critical buckling voltage and critical buckling temperature of a piezo composite beam. It turns out that the present model simulates the three-dimensional FE model more closely than the conventional plane stress or plane strain two-dimensional FE model for the same number of degrees of freedom.

The present formulation can be used to analyze beams inside a gap or a slot which constrains expansion of the beam in the direction not included in the two-dimensional FE model.

List of symbols

$\varepsilon_{xx}, \varepsilon_{yy}, \varepsilon_{zz}$	Strains in the x, y and z directions
$\sigma_{xx}, \sigma_{yy}, \sigma_{zz}$	Stresses in the x, y and z directions
$\varepsilon_{x0}, \varepsilon_{y0}, \varepsilon_{z0}$	Initial strains in the x, y and z directions
ε_{yy}^0	Free expansion strain in y direction
$\sigma_{yy}^{\mathrm{PS}}$	Stress in the y direction for plane strain case
σ_{yy}^G	Stress in the y direction for generalized plane strain
ε^0	allowed/applied strain in the z direction
$\alpha = \varepsilon^0/\varepsilon_{yy}^0$	Ratio between allowed/applied strain to the free expansion strain in the z direction
$\{T\}$	Stress vector
$\{S\}$	Stain vector
$\{S_0\}$	Initial strain vector
$\{E\}$	Electric field vector
$\{D\}$	Electric displacement vector
$[c]$, $[s]$	Elastic constants matrices
$[\varepsilon]$	Dielectric constants matrix
$[d]$, $[e]$	Piezoelectric constants matrix
$[\bar{c}]$, $[\bar{s}]$	two-dimensional reduced elastic constants matrices
$[\bar{\varepsilon}]$	two-dimensional reduced dielectric constants matrix
$[\bar{d}]$, $[\bar{e}]$	two-dimensional reduced piezoelectric constants matrix
$\{u_e\}$	Elemental structural displacement degrees of freedom
$\{\varphi_e\}$	Elemental electric potential degrees of freedom

$[N_u]$ Shape function matrix for structural displacement
$[N_\varphi]$ Shape function matrix for electric potential
$[B_u]$ Shape function derivative matrix for structural strain
$[B_\phi]$ Shape function derivative matrix for electric field
$[M]$ Elemental mass matrix
$[K_{uu}]$ Elemental structural stiffness matrix
$[K_{u\varphi}]$ Elemental piezostructure coupling matrix
$[K_{\varphi\varphi}]$ Elemental capacitance matrix
$\{f_e\}$ Elemental external mechanical force
$\{g_e\}$ Elemental electrical charge
$[K_\sigma]$ Elemental geometric nonlinear matrix
s Elemental stress matrix
$[M]$ Assembled mass matrix
$[\boldsymbol{K}_{uu}]$ Assembled structural stiffness matrix
$[\boldsymbol{K}_{u\varphi}]$ Assembled piezostructure coupling matrix
$[\boldsymbol{K}_{\varphi\varphi}]$ Assembled capacitance matrix
$[\boldsymbol{K}_\sigma]$ Assembled geometric nonlinear matrix
$\{\boldsymbol{f}\}$ Assembled external mechanical force
$[\boldsymbol{K}_{\mathrm{eq}}]$ Assembled equivalent capacitance matrix

2. Formulation

Generalized plane strain FE formulation.   The three-dimensional stress-strain relation is given by

$$\varepsilon_{xx} = s_{11}\sigma_{xx} + s_{12}\sigma_{yy} + s_{13}\sigma_{zz} + \varepsilon_{x0}, \tag{1}$$

$$\varepsilon_{yy} = s_{21}\sigma_{xx} + s_{22}\sigma_{yy} + s_{23}\sigma_{zz} + \varepsilon_{y0}, \tag{2}$$

$$\varepsilon_{zz} = s_{31}\sigma_{xx} + s_{32}\sigma_{yy} + s_{33}\sigma_{zz} + \varepsilon_{z0}, \tag{3}$$

where ε_{xx}, ε_{yy} and ε_{zz} are the strains in the x, y and z directions and σ_{xx}, σ_{yy} and σ_{zz} are the stresses in the x, y and z directions. The strains ε_{x0}, ε_{y0} and ε_{z0} are the initial strains. Consider a plane strain case where $\varepsilon_{yy} = \gamma_{xy} = \gamma_{yz} = 0$. Because of the assumption $\varepsilon_{yy} = 0$, Equation (3) becomes $\varepsilon_{yy} = s_{21}\sigma_{xx} + s_{22}\sigma_{yy} + s_{23}\sigma_{zz} + \varepsilon_{y0} = 0$, which gives

$$\sigma_{yy} = -\frac{s_{21}}{s_{22}}\sigma_{xx} - \frac{s_{23}}{s_{22}}\sigma_{zz} - \frac{\varepsilon_{y0}}{s_{22}}. \tag{4}$$

This σ_{yy} is required to resist the y direction strain ε_{yy}^0 caused by the stresses σ_{xx} and σ_{zz}. Therefore, σ_{yy} produces a strain equal to ε_{yy}^0 but in the opposite direction, so the net strain in the y direction is maintained at zero.

Based on this argument, Equation (4) can be recast as

$$s_{22}\sigma_{yy} = -\varepsilon_{yy}^0 = -s_{21}\sigma_{xx} - s_{23}\sigma_{zz} - \varepsilon_{y0}. \tag{5}$$

Substituting σ_{yy} from (4) into (1) and (2) for the plane strain case implies, from (5), that we are incorporating the effect of $-\varepsilon_{yy}^0$ in the two-dimensional stress-strain relation. The stress-strain relationship then

becomes

$$
\begin{Bmatrix} \varepsilon_{xx} \\ \varepsilon_{zz} \\ \gamma_{xz} \end{Bmatrix} = \begin{bmatrix} s_{11} - s_{12}^2/s_{22} & s_{13} - s_{12}s_{23}/s_{22} & 0 \\ s_{13} - s_{12}s_{23}/s_{22} & s_{33} - s_{23}^2/s_{22} & 0 \\ 0 & 0 & s_{55} \end{bmatrix} \begin{Bmatrix} \sigma_{xx} \\ \sigma_{zz} \\ \tau_{xz} \end{Bmatrix} + \begin{Bmatrix} \varepsilon_{x0} - (s_{12}/s_{22})\varepsilon_{y0} \\ \varepsilon_{z0} - (s_{23}/s_{22})\varepsilon_{y0} \\ \gamma_{xz0} \end{Bmatrix}, \tag{6}
$$

which enforces the condition $\varepsilon_{yy} = 0$.

Now consider the case where $\varepsilon_{yy} = \varepsilon_{yy}^0$ but $\gamma_{xy} = \gamma_{yz} = 0$, that is, the y direction is allowed to expand freely, as shown in Figure 3. In this case the effect of ε_{yy}^0 caused by the stresses σ_{xx} and σ_{zz} has to be incorporated into the two-dimensional stress-strain relation. From (5), it is clear that to produce positive strain ε_{yy}^0, the stress σ_{yy} should be in the opposite direction of the plane strain case. From (5) we get

$$
s_{22}\sigma_{yy}^G = s_{22}\left(-\sigma_{yy}^{PS}\right) = \varepsilon_{yy}^0 = s_{21}\sigma_{xx} + s_{23}\sigma_{zz} + \varepsilon_{y0}, \tag{7}
$$

$$
\sigma_{yy}^G = \left(-\sigma_{yy}^{PS}\right) = \frac{s_{21}}{s_{22}}\sigma_{xx} + \frac{s_{23}}{s_{22}}\sigma_{zz} + \frac{\varepsilon_{y0}}{s_{22}}, \tag{8}
$$

where σ_{yy}^G and σ_{yy}^{PS} are the stresses in the y direction for the case $\varepsilon_{yy} = \varepsilon_{yy}^0$ and for the plane strain case, respectively.

By substituting σ_{yy}^G from (8) into (1) and (2), we obtain for the stress-strain relationship the equation

$$
\begin{Bmatrix} \varepsilon_{xx} \\ \varepsilon_{zz} \\ \gamma_{xz} \end{Bmatrix} = \begin{bmatrix} s_{11} + s_{12}^2/s_{22} & s_{13} + s_{12}s_{23}/s_{22} & 0 \\ s_{13} + s_{12}s_{23}/s_{22} & s_{33} + s_{23}^2/s_{22} & 0 \\ 0 & 0 & s_{55} \end{bmatrix} \begin{Bmatrix} \sigma_{xx} \\ \sigma_{zz} \\ \tau_{xz} \end{Bmatrix} + \begin{Bmatrix} \varepsilon_{x0} + (s_{12}/s_{22})\varepsilon_{y0} \\ \varepsilon_{z0} + (s_{23}/s_{22})\varepsilon_{y0} \\ \gamma_{xz0} \end{Bmatrix}, \tag{9}
$$

which enforces the condition $\varepsilon_{yy} = \varepsilon_{yy}^0$.

Before enforcing this condition, however, the condition $\varepsilon_{yy} = 0$ has to be enforced, which means that before applying the strain ε_{yy}^0, there should not be any strain in the y direction. By enforcing the
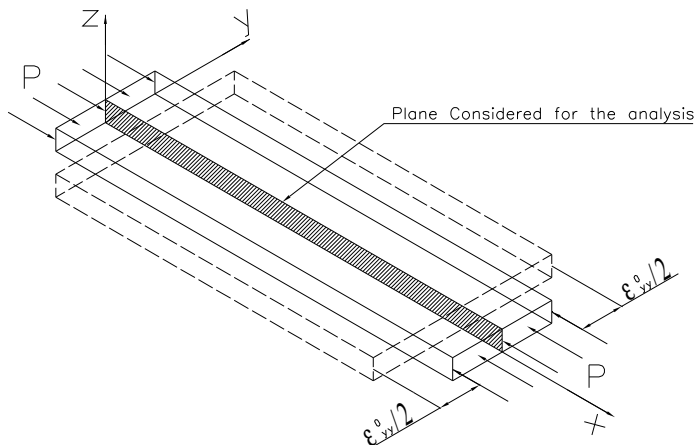
Figure 3. The beam is allowed to expand freely in y direction.

condition $\varepsilon_{yy} = 0$, the stress-strain relation becomes (6). Introducing the quantities

$$s'_{11} = s_{11} - \frac{s_{12}^2}{s_{22}}, \quad s'_{13} = s_{13} - \frac{s_{12}s_{23}}{s_{22}}, \quad s'_{33} = s_{33} - \frac{s_{23}^2}{s_{22}}, \quad \varepsilon'_{x0} = \varepsilon_{x0} - \frac{s_{12}}{s_{22}}\varepsilon_{y0}, \quad \varepsilon'_{z0} = \varepsilon_{z0} - \frac{s_{23}}{s_{22}}\varepsilon_{y0}, \quad (10)$$

we can recast (6) as

$$\begin{Bmatrix} \varepsilon_{xx} \\ \varepsilon_{zz} \\ \gamma_{xz} \end{Bmatrix} = \begin{bmatrix} s'_{11} & s'_{13} & 0 \\ s'_{13} & s'_{33} & 0 \\ 0 & 0 & s_{55} \end{bmatrix} \begin{Bmatrix} \sigma_{xx} \\ \sigma_{zz} \\ \tau_{xz} \end{Bmatrix} + \begin{Bmatrix} \varepsilon'_{x0} \\ \varepsilon'_{z0} \\ \gamma_{xz0} \end{Bmatrix}. \quad (11)$$

Next, the condition $\varepsilon_{yy} = \varepsilon_{yy}^0$ has to be enforced on the y direction for the strain-free ($\varepsilon_{yy} = 0$) stress-strain relation. By enforcing the condition $\varepsilon_{yy} = \varepsilon_{yy}^0$, the stress-strain relation becomes (9) . Now the stress-strain relation becomes

$$\begin{Bmatrix} \varepsilon_{xx} \\ \varepsilon_{zz} \\ \gamma_{xz} \end{Bmatrix} = \begin{bmatrix} s'_{11} + s_{12}^2/s_{22} & s'_{13} + s_{12}s_{23}/s_{22} & 0 \\ s'_{13} + s_{12}s_{23}/s_{22} & s'_{33} + s_{23}^2/s_{22} & 0 \\ 0 & 0 & s_{55} \end{bmatrix} \begin{Bmatrix} \sigma_{xx} \\ \sigma_{zz} \\ \tau_{xz} \end{Bmatrix} + \begin{Bmatrix} \varepsilon'_{x0} + (s_{12}/s_{22})\varepsilon_{y0} \\ \varepsilon'_{z0} + (s_{23}/s_{22})\varepsilon_{y0} \\ \gamma_{xz0} \end{Bmatrix} \quad (12)$$

The two conditions $\varepsilon_{yy} = 0$ and $\varepsilon_{yy} = \varepsilon_{yy}^0$ can be enforced in any order; this is just a superposition of one condition over the other. The condition $\varepsilon_{yy} = 0$ enforces zero strain in the y direction, and $\varepsilon_{yy} = \varepsilon_{yy}^0$ says the beam can expand freely in the y direction. By superimposing these two conditions, the beam is forced to expand exactly the same amount as that of free expansion in the y direction. The derivation for generalized plane strain is carried out based on this analogy.

For the generalized plane strain case we have $\varepsilon_{yy} = \varepsilon^0$ but $\gamma_{xy} = \gamma_{yz} = 0$. In this case, ε^0 is the allowed/applied strain in the y direction. If ε^0 is specified as a multiple of ε_{yy}^0, its effect can be taken into account in the two-dimensional stress-strain relation.

Let the allowed/applied strain be $\varepsilon^0 = \alpha\varepsilon_{yy}^0$, as shown in Figures 4 and 5. The reduced two-dimensional stress-strain relation, incorporating the effect of ε^0, becomes

$$\begin{Bmatrix} \varepsilon_{xx} \\ \varepsilon_{zz} \\ \gamma_{xz} \end{Bmatrix} = \begin{bmatrix} s'_{11} + \alpha s_{12}^2/s_{22} & s'_{13} + \alpha s_{12}s_{23}/s_{22} & 0 \\ s'_{13} + \alpha s_{12}s_{23}/s_{22} & s'_{33} + \alpha s_{23}^2/s_{22} & 0 \\ 0 & 0 & s_{55} \end{bmatrix} \begin{Bmatrix} \sigma_{xx} \\ \sigma_{zz} \\ \tau_{xz} \end{Bmatrix} + \begin{Bmatrix} \varepsilon'_{x0} + \alpha(s_{12}/s_{22})\varepsilon_{y0} \\ \varepsilon'_{z0} + \alpha(s_{23}/s_{22})\varepsilon_{y0} \\ \gamma_{xz0} \end{Bmatrix}, \quad (13)$$

where s'_{11}, s'_{12}, and s'_{22} are given by (10) .

If α in (13) is 0, then (13) reduces to (6), which is a stress-strain relation for the plane strain case. If the α in (13) is 1, then (13) reduces to (12), which is a stress-strain relation for the condition $\varepsilon_{yy} = \varepsilon_{yy}^0$. By substituting (10) into (12) , the stress-strain relation for the condition $\varepsilon_{yy} = \varepsilon_{yy}^0$ becomes

$$\begin{Bmatrix} \varepsilon_{xx} \\ \varepsilon_{zz} \\ \gamma_{xz} \end{Bmatrix} = \begin{bmatrix} s_{11} & s_{13} & 0 \\ s_{13} & s_{33} & 0 \\ 0 & 0 & s_{55} \end{bmatrix} \begin{Bmatrix} \sigma_{xx} \\ \sigma_{zz} \\ \tau_{xz} \end{Bmatrix} + \begin{Bmatrix} \varepsilon_{x0} \\ \varepsilon_{z0} \\ \gamma_{xz0} \end{Bmatrix}. \quad (14)$$

This is a simple two-dimensional stress-strain relation which completely does not constrain the strain ε_{yy}^0, caused by the stresses σ_{xx} and σ_{zz}.
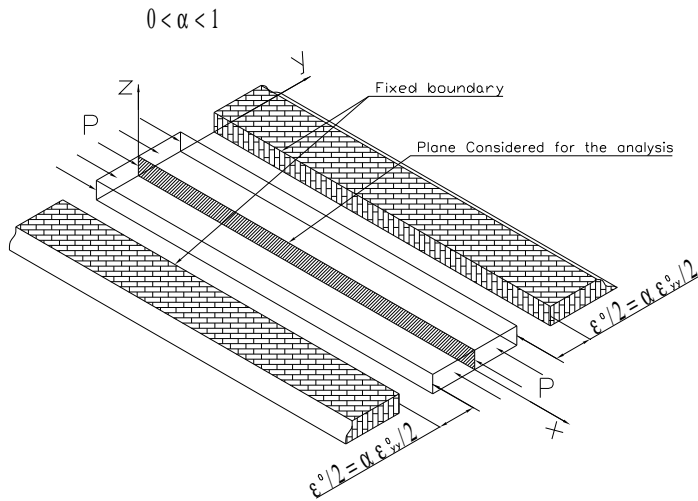
Figure 4. Beam is not allowed to undergo full free expansion in the y direction.
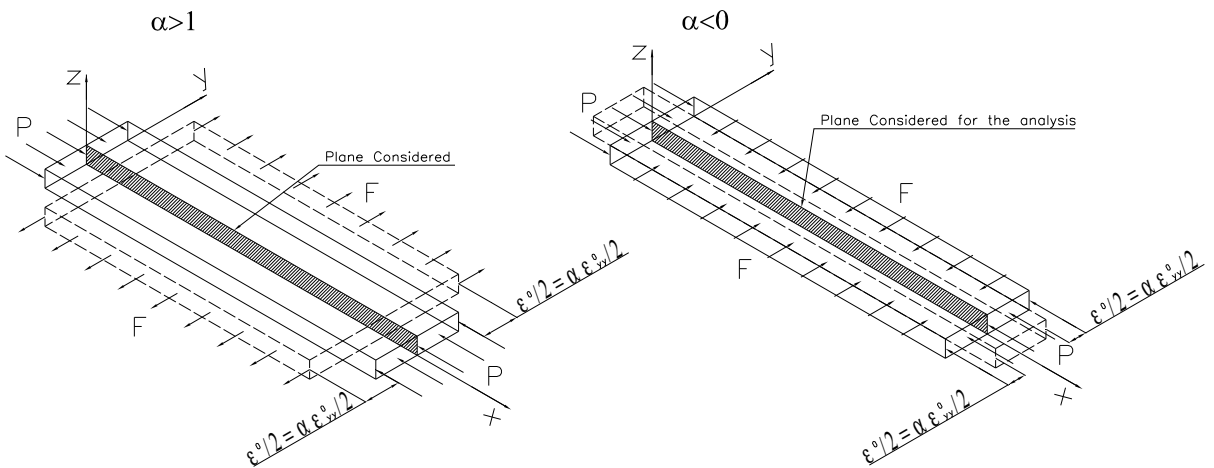
Figure 5. Left: Beam expands more than the free expansion in the y direction by the external load. Right: Beam gets compressed in the y direction by the external load.

The generalized plane strain stress-strain relations of (13) can be extended to generalized plane strain two-dimensional piezostructure coupled stress-strain relations. The constitutive equations for a piezo-electric material are

$$\{T\} = [c^E]\big(\{S\} - \{S_0\}\big) - [e]^T\{E\}, \quad \{D\} = [e]\{S\} + [\varepsilon^S]\{E\}, \tag{15}$$

where $\{T\}$ is the stress vector, $\{S\}$ the stain vector, $\{S_0\}$ the initial strain vector, $\{E\}$ the electric field vector, $\{D\}$ the electric displacement vector, $[c]$ and $[s]$ the elastic constants matrices, $[\varepsilon]$ the dielectric constants matrix, and $[d]$ and $[e]$ the piezoelectric constants matrix, and where superscript E and S indicate that the specified values are evaluated at constant E and S.

Equation (15) can be written in strain form as

$$\{S\} = [s^E]\{T\} + [d]^T\{E\} + \{S_0\}, \quad \{D\} = [d]\{T\} + [\varepsilon^E]\{E\}, \tag{16}$$

where

$$[e] = [d][c^E], \quad [c^E] = [s^E]^{-1}. \tag{17}$$

Equation (16) can be recast as

$$\begin{Bmatrix} \{S\} \\ \{D\} \end{Bmatrix} = \begin{bmatrix} [s^E] & [d]^T \\ [d] & [\varepsilon^E] \end{bmatrix} \begin{Bmatrix} \{T\} \\ \{E\} \end{Bmatrix} + \begin{Bmatrix} \{S_0\} \\ \{0\} \end{Bmatrix}. \tag{18}$$

This in turn can be expanded for the case where the polarization direction is the positive z axis as follows:

$$\begin{Bmatrix} S_1 \\ S_2 \\ S_3 \\ S_4 \\ S_5 \\ S_6 \\ D_1 \\ D_2 \\ D_3 \end{Bmatrix} = \begin{bmatrix} s_{11} & s_{12} & s_{13} & 0 & 0 & 0 & 0 & 0 & d_{31} \\ s_{12} & s_{22} & s_{23} & 0 & 0 & 0 & 0 & 0 & d_{32} \\ s_{13} & s_{23} & s_{33} & 0 & 0 & 0 & 0 & 0 & d_{33} \\ 0 & 0 & 0 & s_{44} & 0 & 0 & 0 & d_{24} & 0 \\ 0 & 0 & 0 & 0 & s_{55} & 0 & d_{15} & 0 & 0 \\ 0 & 0 & 0 & 0 & 0 & s_{66} & 0 & 0 & 0 \\ 0 & 0 & 0 & 0 & d_{15} & 0 & \varepsilon_{11} & 0 & 0 \\ 0 & 0 & 0 & d_{24} & 0 & 0 & 0 & \varepsilon_{22} & 0 \\ d_{31} & d_{32} & d_{33} & 0 & 0 & 0 & 0 & 0 & \varepsilon_{33} \end{bmatrix} \begin{Bmatrix} T_1 \\ T_2 \\ T_3 \\ T_4 \\ T_5 \\ T_6 \\ E_1 \\ E_2 \\ E_3 \end{Bmatrix} + \begin{Bmatrix} S_{10} \\ S_{20} \\ S_{30} \\ S_{40} \\ S_{50} \\ S_{60} \\ 0 \\ 0 \\ 0 \end{Bmatrix}. \tag{19}$$

In the piezostructure coupled two-dimensional case, the xz plane is considered for analysis as shown in Figure 2, and the y direction is the be the out-of-plane direction. Now consider the plane strain case, where

$$S_2 = S_4 = S_6 = 0, \tag{20}$$

$$D_2 = E_2 = 0. \tag{21}$$

By substituting (20) into (19), the second row of (19) becomes $S_2 = s_{12}T_1 + s_{22}T_2 + s_{23}T_3 + d_{32}E_3 + S_{20} = 0$, which gives

$$T_2 = -\frac{s_{12}}{s_{22}}T_1 - \frac{s_{23}}{s_{22}}T_3 - \frac{d_{32}}{s_{22}}E_3 - \frac{S_{20}}{s_{22}}. \tag{22}$$

Substituting (22) into (19) and using (20) and (21), we obtain the reduced stress-strain relationship in the plane strain case in the form

$$\begin{Bmatrix} S_1 \\ S_3 \\ S_5 \\ D_1 \\ D_3 \end{Bmatrix} = \begin{bmatrix} s'_{11} & s'_{13} & 0 & 0 & d'_{31} \\ s'_{13} & s'_{33} & 0 & 0 & d'_{33} \\ 0 & 0 & s_{55} & d_{15} & 0 \\ 0 & 0 & d_{15} & \varepsilon_{11} & 0 \\ d'_{31} & d'_{33} & 0 & 0 & \varepsilon'_{33} \end{bmatrix} \begin{Bmatrix} T_1 \\ T_3 \\ T_5 \\ E_1 \\ E_3 \end{Bmatrix} + \begin{Bmatrix} S'_{10} \\ S'_{30} \\ S_{50} \\ 0 \\ 0 \end{Bmatrix}, \tag{23}$$

where

$$s'_{11} = s_{11} - \frac{s_{12}^2}{s_{22}}, \quad s'_{13} = s_{13} - \frac{s_{12}s_{23}}{s_{22}}, \quad s'_{33} = s_{33} - \frac{s_{23}^2}{s_{22}}, \tag{24}$$

$$d'_{31} = d_{31} - \frac{s_{12}d_{32}}{s_{22}}, \quad d'_{33} = d_{33} - \frac{s_{23}d_{32}}{s_{22}}, \quad \varepsilon'_{33} = \varepsilon_{33} - \frac{d_{32}^2}{s_{22}}, \tag{25}$$

$$S'_{10} = S_{10} - \frac{s_{12}}{s_{22}}S_{20}, \quad S'_{30} = S_{30} - \frac{s_{23}}{s_{22}}S_{20}. \tag{26}$$

The arguments given for the pure elastic generalized plane strain case can be extended for the piezo-structure coupled generalized plane strain case. The reduced two-dimensional piezostructure coupled stress-strain relationship for the generalized plane strain case is given by

$$\begin{Bmatrix} S_1 \\ S_3 \\ S_5 \\ D_1 \\ D_3 \end{Bmatrix} = \begin{bmatrix} s'_{11}+\alpha s_{12}^2/s_{22} & s'_{13}+\alpha s_{12}s_{23}/s_{22} & 0 & 0 & d'_{31}+\alpha s_{12}d_{32}/s_{22} \\ s'_{13}+\alpha s_{12}s_{23}/s_{22} & s'_{33}+\alpha s_{23}^2/s_{22} & 0 & 0 & d'_{33}+\alpha s_{23}d_{32}/s_{22} \\ 0 & 0 & s_{55} & d_{15} & 0 \\ 0 & 0 & d_{15} & \varepsilon_{11} & 0 \\ d'_{31}+\alpha s_{12}d_{32}/s_{22} & d'_{33}+\alpha s_{23}d_{32}/s_{22} & 0 & 0 & \varepsilon'_{33}+\alpha d_{32}^2/s_{22} \end{bmatrix} \begin{Bmatrix} T_1 \\ T_3 \\ T_5 \\ E_1 \\ E_3 \end{Bmatrix} + \begin{Bmatrix} S'_{10}-\alpha s_{12}S_{20}/s_{22} \\ S'_{30}-\alpha s_{23}S_{20}/s_{22} \\ S_{50} \\ 0 \\ 0 \end{Bmatrix},$$

which can be recast as

$$\begin{Bmatrix} \{S\} \\ \{D\} \end{Bmatrix} = \begin{bmatrix} [\bar{s}] & [\bar{d}]^T \\ [\bar{d}] & [\bar{\varepsilon}] \end{bmatrix} \begin{Bmatrix} \{T\} \\ \{E\} \end{Bmatrix} + \begin{Bmatrix} \{\bar{S}_0\} \\ \{0\} \end{Bmatrix}, \quad \{S\} = [\bar{s}]\{T\} + [\bar{d}]^T\{E\} + \{\bar{S}_0\}, \quad \{D\} = [\bar{d}]\{T\} + [\bar{\varepsilon}]\{E\}.$$

Using (17) , this can further be rewritten in stress form as

$$\{T\} = [\bar{c}]\left(\{S\} - \{\overline{S_0}\}\right) - [\bar{e}]^T\{E\}, \quad \{D\} = [\bar{e}]\{S\} + [\bar{\varepsilon}]\{E\}.$$

Finite element formulation. In order to model the piezo composite beam, an eight-node quadrilateral element was developed. The finite element model of the piezo composite beam is shown in Figure 6. Each node has three degrees of freedom: axial displacement (u_1), transverse displacement (u_3) and electric potential (ϕ). The elemental degrees of freedom are

$$\{u_e\} = \left\{u_1^1, u_3^1, u_1^2, u_3^2, u_1^3, u_3^3, \ldots, u_1^8, u_3^8\right\}^T, \quad \{\varphi_e\} = \{\varphi_1, \varphi_2, \varphi_3, \ldots, \varphi_8\}^T. \tag{27}$$
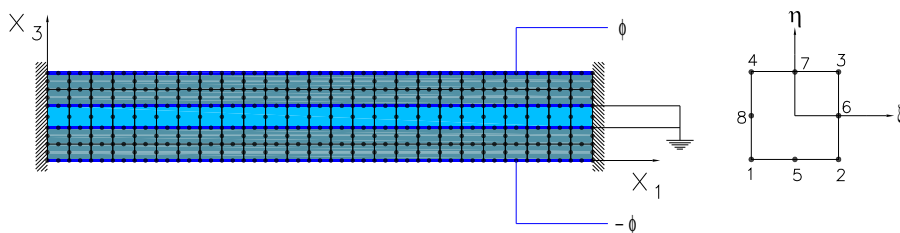
Figure 6. Finite element model of the piezo composite beam with kinematic constraints and electrical boundary conditions for electrical buckling analysis and (with zero applied voltage) for thermal buckling analysis.

The displacement $\{u\} = \{u_1, u_3\}^T$ and electric potential (ϕ) within the element can be expressed in terms of element shape functions as

$$\{u\} = [N_u]\{u_e\}, \quad \{\varphi\} = [N_\varphi]\{\varphi_e\},$$

where

$$[N_u] = \begin{bmatrix} N_1 & 0 & N_2 & 0 & \dots & N_8 & 0 \\ 0 & N_1 & 0 & N_2 & \dots & 0 & N_8 \end{bmatrix}, \quad [N_\varphi] = [N_1 \ N_2 \ N_3 \ \dots \ N_8],$$

$N_1, N_2, \dots, N_8$ being the shape functions.

The strain displacement relation can be expressed as

$$\{S\} = \begin{Bmatrix} S_1 \\ S_3 \\ S_5 \end{Bmatrix} = \begin{Bmatrix} \partial u_1/\partial x_1 \\ \partial u_3/\partial x_3 \\ \partial u_1/\partial x_3 + \partial u_3/\partial x_1 \end{Bmatrix} = [B_u]\{u_e\},$$

where $[B_u]$ is the shape function derivative matrix:

$$[B_u] = \begin{bmatrix} \partial N_1/\partial x_1 & 0 & \partial N_2/\partial x_1 & 0 & \dots & \partial N_8/\partial x_1 & 0 \\ 0 & \partial N_1/\partial x_3 & 0 & \partial N_2/\partial x_3 & \dots & 0 & \partial N_8/\partial x_3 \\ \partial N_1/\partial x_3 & \partial N_1/\partial x_1 & \partial N_2/\partial x_3 & \partial N_2/\partial x_1 & \dots & \partial N_8/\partial x_3 & \partial N_8/\partial x_1 \end{bmatrix}$$

The electric field-potential relation can be expressed as

$$\{E\} = \begin{Bmatrix} E_1 \\ E_3 \end{Bmatrix} = \begin{Bmatrix} -\partial\varphi/\partial x_1 \\ -\partial\varphi/\partial x_3 \end{Bmatrix} = [B_\varphi]\{\varphi_e\},$$

where $[B_\phi]$ is the shape function derivative matrix:

$$[B_\varphi] = \begin{bmatrix} \partial N_1/\partial x_1 & \partial N_2/\partial x_1 & \partial N_3/\partial x_1 & \dots & \partial N_8/\partial x_1 \\ \partial N_1/\partial x_3 & \partial N_2/\partial x_3 & \partial N_3/\partial x_3 & \dots & \partial N_8/\partial x_3 \end{bmatrix}.$$

After application of the variational principle, the coupled finite element matrix equation becomes (see [Allik and Hughes 1970; Lerch 1990; Tzou and Tseng 1990])

$$[M]\{\ddot{u}_e\} + [K_{uu}]\{u_e\} + [K_{u\varphi}]\{\varphi_e\} = \{f_e\}, \quad [K_{\varphi u}]\{u_e\} + [K_{\varphi\varphi}]\{\varphi_e\} = \{g_e\}, \tag{28}$$

where $[M] = \int_V \rho[N]^T[N]\,dV$ is the element mass,

$$[K_{uu}] = \int_V [B_u]^T[\bar{c}^E][B_u]\,dV, \quad [K_{u\varphi}] = [K_{\varphi u}]^T = \int_V [B_u]^T[\bar{e}]^T[B_\varphi]\,dV, \quad [K_{\varphi\varphi}] = \int_V [B_\varphi]^T[\bar{\varepsilon}][B_\varphi]\,dV$$

are the stiffness, piezoelectric coupling and capacitance matrices, and

$$\{f_e\} = \int_V [B_u]^T[\bar{c}^E]\{S_0\}\,dV + \int_V [N]^T\{P_b\}\,dV + \int_{\Omega_1} [N]^T\{P_s\}d\Omega_1 + [N]^T\{P_c\}, \tag{29}$$

$$\{g_e\} = -\int_{\Omega_2} [N]^T P\,d\Omega_2 - [N]^T Q \tag{30}$$

are the external mechanical force and electrical charge. The first term in (29) is the element load vector due to initial strains, and the other terms are body, surface, and point forces, respectively [Cook et al. 2003].

In order to do the buckling analysis, the geometric nonlinear matrix can be computed as [Cook et al. 2003]

$$[K_\sigma] = \int_V [G]^T \begin{bmatrix} s & 0 \\ 0 & s \end{bmatrix} [G] \, dV,$$

where

$$s = \begin{bmatrix} \sigma_{x0} & \tau_{xz0} \\ \tau_{xz0} & \sigma_{z0} \end{bmatrix} \quad \text{and} \quad [G] = \begin{bmatrix} \partial N_1/\partial x_1 & 0 & \partial N_2/\partial x_1 & 0 & \dots & \partial N_8/\partial x_1 & 0 \\ \partial N_1/\partial x_3 & 0 & \partial N_2/\partial x_3 & 0 & \dots & \partial N_8/\partial x_3 & 0 \\ 0 & \partial N_1/\partial x_1 & 0 & \partial N_2/\partial x_1 & \dots & 0 & \partial N_8/\partial x_1 \\ 0 & \partial N_1/\partial x_3 & 0 & \partial N_2/\partial x_3 & \dots & 0 & \partial N_8/\partial x_3 \end{bmatrix}$$

are the stress and shape function derivative matrices.

For static analysis and for the case where only a mechanical load exists, Equation (28) becomes, after assembling the stiffness matrices,

$$[K_{uu}]\{u\} + [K_{u\varphi}]\{\phi\} = \{f\}, \quad [K_{\varphi u}]\{u\} + [K_{\varphi\varphi}]\{\phi\} = 0; \tag{31}$$

the assembled geometric nonlinear matrix is $[K_\sigma]$.

In the case of thermal buckling analysis, since only the thermal load exists, the right-hand side of $(31)_1$ is simply

$$\{f\} = \sum \int_V [B_u]^T [\bar{c}^E]\{S_0\} \, dV,$$

and the assembled buckling eigenequation is

$$\big([K_{uu}] + \lambda [K_\sigma] \big)\{\delta u\} = \{0\}. \tag{32}$$

In the case of electrical buckling analysis, the right-hand side of (31) is $\{f\} = \{0\}$ and the known quantities are only the voltages on the electrodes. Therefore, for electrical buckling, (31) becomes

$$[K_{uu}]\{u\} + [K_{u\varphi}]\{\phi\} = \{0\}, \quad [K_{\varphi u}]\{u\} + [K_{\varphi\varphi}]\{\phi\} = \{0\}. \tag{33}$$

Since the FE model is a cross section model, as shown in Figure 6, the voltages are known only at the electrodes. There are other nodes in the piezo layer whose potentials have to be evaluated, and this in a coupled way. To evaluate the voltages applied in the piezolayer in a coupled way, Equation $(33)_1$ is solved for $\{u\}$ and it is substituted into $(33)_2$ to get an equivalent stiffness matrix

$$[K_{\text{eq}}] = [K_{\varphi\varphi}] + [K_{\varphi u}][K_{uu}]^{-1}(-[K_{u\varphi}].)$$

Now $[K_{\text{eq}}]$ is a coupled capacitance matrix because the effect of the first equation of $(33)_1$ has been incorporated into the second equation of $(33)_2$ and the unknown potentials can be evaluated using the equation

$$[K_{\text{eq}}]\{\phi\} = \{0\}. \tag{34}$$

The unknown potentials in the piezolayers have been determined by taking the known potentials to the right-hand side and solving (34), which is similar to the process of solving thermal problems where one

knows temperatures on some nodes and the temperatures on the other nodes are evaluated. Once all the potentials are known, $(33)_1$ can be used to determine the displacements. The buckling eigenequation is (32).

3. Results and discussion

A finite element solver was written implementing the formulation above. In this section we discuss some validation tests and then new example calculations involving a system where neither plane stress nor plain strain conditions are assumed.

Validation. The code was validated for electric buckling by comparison with the results in [Varelis and Saravanos 2004]. The same example was also subjected to a three-dimensional FE computation in ANSYS; due to the limitations of ANSYS, a thermal analog of the linear electrical buckling problem [Dong and Meng 2006] was solved as a proxy.

The example beam of Varelis and Saravanos is a three-layer [pzt/Al/pzt] composite with length 200 mm, width 20 mm, thickness of each piezo layer $t_p = 0.25$ mm, and aluminum layer thickness $t_a = 0.5$ mm. In the case $\alpha = 1$ (the beam is allowed to expand freely in the y direction), we obtain these values for the critical electrical buckling voltage:

$$
\begin{aligned}
&\text{present approach} &&189.6\,\text{V} \\
&\text{ANSYS 3D model} &&188.8\,\text{V} \\
&\text{[Varelis and Saravanos 2004]} &&188\;\;\text{V}
\end{aligned}
\tag{35}
$$

We observe good agreement between all three results.

For thermal buckling validation, we took an example beam from [Giannopoulos et al. 2007]: a three-layer [pzt/Al/pzt] composite with length 70 mm and width 5 mm. The thickness of each piezo layer is $t_p = 0.191$ mm and that of the aluminium layer is $t_a = 0.070$ mm. The beam is subjected to a uniform temperature rise above the ambient temperature, and again we take $\alpha = 1$. These are the values obtained for the critical thermal buckling temperature:

$$
\begin{aligned}
&\text{present approach} &&29.7^\circ\text{C} \\
&\text{ANSYS 3D model} &&28.3^\circ\text{C}
\end{aligned}
\tag{36}
$$

No direct comparison is possible with the calculations in [Giannopoulos et al. 2007], since that reference only contains the thermal buckling analysis of plates. However, we performed a three-dimensional analysis in ANSYS for the same problem solved by these authors, and it was found that the ANSYS result and their result agree very well.

Further examples. We next performed the thermal and electrical buckling analysis for an example structure taken from [Giannopoulos et al. 2007], using different assumptions for the parameter α. In the particular cases of plane stress assumptions and plane strain assumptions, the results obtained are compared with those obtained with ANSYS; however, the more general case (neither plane stress nor plane strain) has also been studied.

The beam is a three layer [pzt/Al/pzt] composite with length 70 mm and width 5 mm. The thickness t_p of each piezo layer is 0.191 mm and the aluminium layer thickness t_a is 0.070 mm.

Electrical buckling. An equal voltage was applied to the piezolayers in the corresponding direction as shown in Figure 6, so that pure compression is developed in the structure due to the kinematic constraints imposed by the boundary conditions. The results obtained for the buckling voltage with our FE solver under assumptions of plane stress, plane strain, and free expansion ($\alpha = 1$) are shown here along with those obtained from an ANSYS solution of the thermal analog [Dong and Meng 2006] to our problem:

	free expansion	plane stress	plane strain	
ANSYS (3D/2D/2D)	98.3 V	102.7 V	78.4 V	(37)
present approach	97.5 V	102.3 V	78.2 V	

This shows good agreement between the ANSYS results and those from the present analysis; in particular, our critical buckling voltage calculated using $\alpha = 1$ (free expansion) matches closely the one obtained using a three-dimensional analysis in ANSYS.

It is also clear that the calculated critical buckling voltage varies greatly with the constraints assumed. This dependence was explored further by varying the value of α in the calculation using the present approach. For $\alpha = 1$ (free expansion), as we have seen, we obtained 97.5 V, then 91.8 V for $\alpha = 0.75$, and 86.7 V for $\alpha = 0.5$, 82.2 V for $\alpha = 0.25$, and finally 78.2 V, for $\alpha = 0$ (plane strain assumption). The decrease in the critical buckling voltage with α can be rationalized by observing that as α is reduced, compressive stress is increased in the y direction (perpendicular to the plane of the FE model), which in turn increases the voltage produced in the piezo layer. The developed voltage is such that it causes the piezo layer to expand in the other two directions (in the plane of the FE model). This expansion causes additional compressive stress due to the imposed kinematic constrains on the boundary, which in turn makes the structure buckle at lower voltages.

We extended the computation to $\alpha < 0$, meaning that external strain is applied in compression (Figure 5, right), and to $\alpha > 1$, meaning that external strain is applied in tension (Figure 5, left). When $\alpha < 0$ the trend just discussed still holds true: the calculated critical buckling voltage decreases in tandem with α. Thus for $\alpha < 0$ we have 74.6 V at $\alpha = -0.25$ and 71.3 V at $\alpha = -0.5$. When $\alpha > 1$ the critical buckling voltage increases (103.9 V at $\alpha = 1.25$ and 111.3 V at $\alpha = 1.5$); this is because the expansion in the y direction produces voltage in such a way that the piezo layer contracts in the xz plane. Due to the kinematic constraints imposed by the boundary condition, this produces tensile stress opposed to the compressive stress produced by electrical actuation, resulting in an increase in the buckling voltage.

Thermal buckling. The analysis carried out in the preceding paragraphs was repeated for thermal buckling. Here the setup as the same as in Figure 6, but there is no applied voltage. Instead, the beam is subjected to a uniform temperature rise above the ambient temperature. The buckling temperatures obtained in the calculations under various assumptions are as follows:

	free expansion	plane stress	plane strain	
ANSYS (3D/2D/2D)	28.30 °C	29.62 °C	22.56 °C	(38)
present approach	29.66 °C	29.66 °C	22.44 °C	

Again we see good agreement between the ANSYS calculations and those based on the present approach. Further, the calculations yield the same critical buckling temperature using the plane stress assumption or using $\alpha = 1$ (free expansion). This is because the thermal expansion mechanism is given by the initial

strain vector $\{S_0\}$, which is not reduced under the plane stress assumption. More precisely, when the three-dimensional stress-strain relation (1) is reduced to a two-dimensional stress-strain relation based on the plane stress assumption ($T_2 = T_4 = T_6 = 0$, $D_2 = E_2 = 0$), the initial strain vector $\{S_0\}$ is unchanged.

Here are the results given by the present approach for various values of α:

$\alpha = -0.5$	$19.9529°C$	$\alpha = 0.25$	$23.9296°C$	$\alpha = 1$	$29.6673°C$
$\alpha = -0.25$	$21.1288°C$	$\alpha = 0.75$	$27.4970°C$	$\alpha = 1.5$	$35.1063°C$
$\alpha = 0$	$22.4481°C$	$\alpha = 0.5$	$25.6004°C$	$\alpha = 1.25$	$32.1751°C$

We see that the critical buckling temperature increases with α. This is because, as α decreases, the compressive stress in the direction perpendicular to the FE model increases, which makes the material expand in the other two directions due to the Poisson effect. This expansion causes additional compressive stress in the beam due to the kinematic constraints imposed by the boundary condition, reducing the critical buckling temperature. The influence of α on the critical buckling temperature is similar to that of the influence in critical buckling voltage as discussed earlier.

Combined thermal and electrical buckling. In the combined thermal and electrical buckling analysis, the critical electrical buckling voltage was predicted for different uniform temperature increases in the beam. All analyses carried out for electrical and thermal buckling were also repeated for combined thermal and electrical buckling. The results obtained under different assumptions are presented in Figure 7 (comparison with ANSYS calculation performed on the thermal analog [Dong and Meng 2006]) and in Figure 8 (dependence on α). The results are similar to those just discussed.
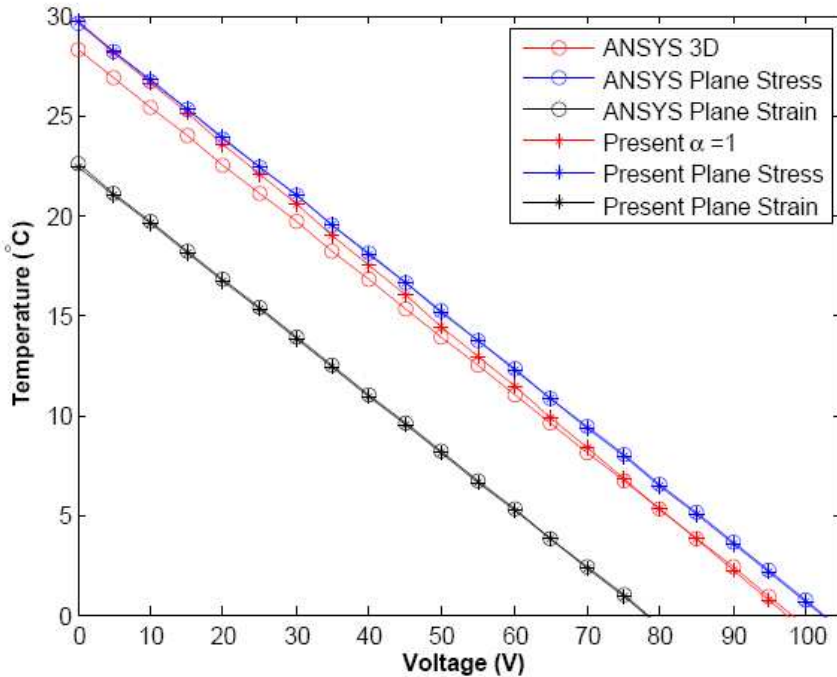
Figure 7. Values of critical buckling voltage obtained with the present approach and with ANSYS [Varelis and Saravanos 2004].
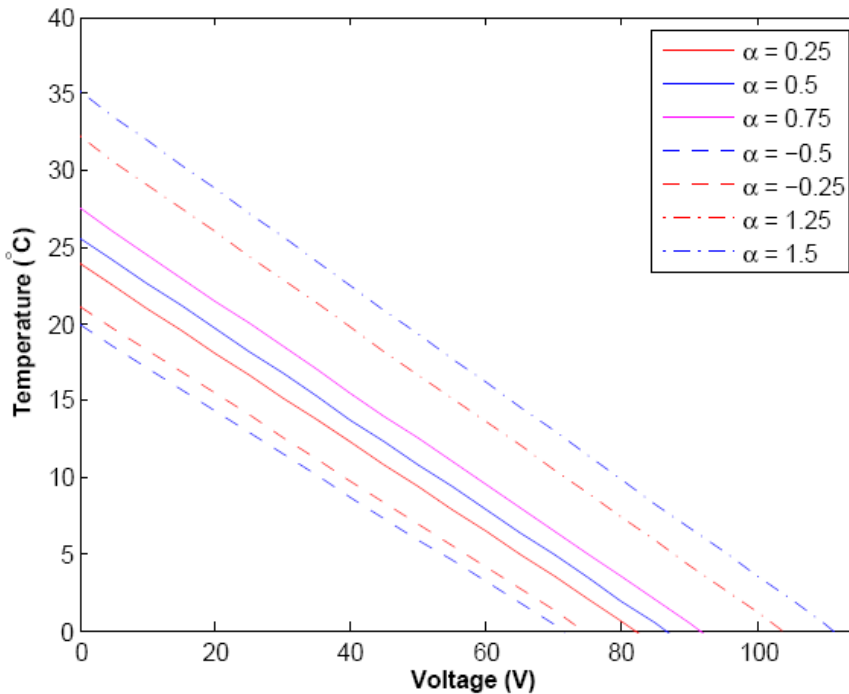
Figure 8. Influence of α on the combined thermal and electrical buckling analysis.

4. Conclusion

A generalized plane strain FE formulation was developed to predict the critical buckling voltage and critical buckling temperature of a piezo composite beam for cases other than those characterized by plane strain and plane stress assumptions. The two-dimensional FE formulation presented in this paper is capable of describing the strain ε^0 allowed/applied in the direction which is not included in the two-dimensional FE model, (here the y direction) if the strain ε^0 is specified in terms of the free expansion strain ε_{yy}^0. An eight-node quadrilateral element was developed based on the new formulation, and the FE solver results were validated by comparison to the results in [Varelis and Saravanos 2004] and those obtained with ANSYS. These results are in good agreement with each other. The critical electrical and thermal buckling load for the cases other than those characterized by plane stress and plane strain, which can be handled by the present two-dimensional FE solver, was analyzed, and it was found that the influence of α on the critical buckling voltage as well as the critical buckling temperature is significant. Since the present formulation varies only in the constitutive equation matrix reduction, this formulation can be easily incorporated into the existing piezostructure coupled FE solvers.

Acknowledgment

References

[Allik and Hughes 1970] H. Allik and T. J. R. Hughes, "Finite element method for piezoelectric vibration", *Int. J. Numer. Methods Eng.* **2**:2 (1970), 151–157.

[Benjeddou 2000] A. Benjeddou, "Advances in piezoelectric finite element modeling of adaptive structural elements: a survey", *Comput. Struct.* **76**:1-3 (2000), 347–363.

[Cook et al. 2003] R. D. Cook, D. S. Malkus, M. E. Plesha, and R. J. Witt, *Concepts and applications of finite element analysis*, Wiley, New York, 2003.

[Dong and Meng 2006] X.-J. Dong and G. Meng, "Dynamic analysis of structures with piezoelectric actuators based on thermal analogy method", *Int. J. Adv. Manuf. Tech.* **27**:9-10 (2006), 841–844.

[Giannopoulos et al. 2007] G. Giannopoulos, F. Santafe, J. Monreal, and J. Vantomme, "Thermal, electrical, mechanical coupled mechanics for initial buckling analysis of smart plates and beams using discrete layer kinematics", *Int. J. Solids Struct.* **44**:14-15 (2007), 4707–4722.

[Hu and Pagano 1997] S. Hu and N. J. Pagano, "On the use of a plane-strain model to solve generalized plane-strain problems", *J. Appl. Mech.*(*ASME*) **64**:1 (1997), 236 – 238.

[Krueger et al. 2002] R. Krueger, I. L. Paris, T. K. O'Brien, and P. J. Minguet, "Comparison of 2D finite element modeling assumptions with results from 3D analysis for composite skin-stiffener debonding", *Compos. Struct.* **57**:1-4 (2002), 161–168.

[Lerch 1990] R. Lerch, "Simulation of piezoelectric devices by two- and three-dimensional finite elements", *IEEE Trans. Ultrason. Ferroelectr. Freq. Control* **37**:3 (1990), 233–247.

[Lin and Yi 1991] K. Y. Lin and S. Yi, "Analysis of interlaminar stresses in viscoelastic composites", *Int. J. Solids Struct.* **27**:7 (1991), 929–945.

[Tzou and Tseng 1990] H. S. Tzou and C. I. Tseng, "Distributed piezoelectric sensor/actuator design for dynamic measurement/control of distributed parameter systems: a piezoelectric finite element approach", *J. Sound Vib.* **138**:1 (1990), 17–34.

[Varelis and Saravanos 2002] D. Varelis and D. A. Saravanos, "Nonlinear coupled mechanics and initial buckling of composite plates with piezoelectric actuators and sensors", *Smart Mater. Struct.* **11**:3 (2002), 330–336.

[Varelis and Saravanos 2004] D. Varelis and D. A. Saravanos, "Coupled buckling and postbuckling analysis of active laminated piezoelectric composite plates", *Int. J. Solids Struct.* **41**:5-6 (2004), 1519–1538.

R. JEROME: jerrome_r@hotmail.com

Department of Mechanical Engineering, Machine Design Section, Room No. 403, Indian Institute of Technology Madras, Chennai 600 036, India

N. GANESAN: nganesan@iitm.ac.in

Department of Mechanical Engineering, Machine Design Section, Room No. 405, Indian Institute of Technology Madras, Chennai 600 036, India

THREE-DIMENSIONAL NONLINEAR ANALYSES OF SCARF REPAIR IN COMPOSITE LAMINATES AND SANDWICH PANELS

MANABENDRA DAS, ERDOGAN MADENCI AND DAMODAR R. AMBUR

A special-purpose analysis tool based on the finite element method is presented for parametric design studies of composite laminates and sandwich panels with scarf repairs. This design tool provides the complete three-dimensional stress and strain fields in scarf-repaired panels without any requirements on the nature of the lamination and the type of loading. The adherends are modeled using a plate element based on a higher-order single-layer theory, and the adhesive is modeled using a solid element. The higher-order nature of the plate theory makes it suitable for analyzing thick laminates and sandwich panels comprised of numerous plies. The model takes into account geometric nonlinearity in the adherends and assumes a bilinear stress-strain relationship for the adhesive. The responses of composite laminates with single- and double-sided repairs and sandwich panels with both full and partial repairs of the top face sheets are investigated.

1. Introduction

Bonded joints and repairs, in a variety of forms such as lap, step, and scarf, have become the most common types of repairs for composite laminated and sandwich panels. The objective of a scarf repair is to restore the static strength and durability of a composite structure that contains damage due to unexpected impact loading on the structure, crack occurrence within the structure after longtime use, and environmental reasons. Panels with scarf joints do not experience excessive secondary bending and the magnitude of transverse shear and peel stress concentration is not as severe as in lap and step joints. In fact in the case of homogeneous adherends, the stress variation inside the adhesive remains fairly uniform. In the case of panels made of composite laminates, however, a nonuniform stress variation inside the adhesive has been observed [Johnson 1989]. Therefore, a detailed analysis of composite laminates for the accurate prediction of the stress and strain fields becomes critical for failure analysis. Moreover, geometric nonlinearity due to adherend bending and material nonlinearity of the adhesive should be taken into account for realistic predictions. With the increasing use of sandwich panels in aircraft structures, the development of repair methods and analysis tools to investigate the responses of these panels with scarf repair has become very important [Tomblin et al. 2004].

Analytical and numerical methods have been used in the past to examine scarf joints [Hart-Smith 1973; Erdogan and Ratwani 1971]. These methods are two dimensional in nature and the scarf repair is analyzed based on a representative scarf joint. In a scarf joint, the entire load is transferred through the adhesive bond, as opposed to both the undamaged base material and the repair sharing the load in the case of a scarf repair. The two dimensional scarf joint model over-predicts the stresses inside the adhesive and therefore underestimates the strength of the repaired panel [Soutis and Hu 1997]. Moreover,

---

the adherends are assumed to be homogeneous, and arbitrary boundary conditions and loading cannot be imposed. More recently, Mortensen and Thomsen [1997] employed the classical plate theory to model the adherends and a nonlinear material model for the adhesive. The analysis permits adherend bending as well as arbitrary load and boundary conditions. Finite element analysis can be employed to overcome the limitations of the analytical methods. While comparing different finite element models for scarf repair analysis, Odi and Friend [2002] noticed that although a considerable amount of work had been done on bonded joints, the number of numerical analysis methods devoted to bonded repair was inadequate. Johnson [1989] carried out a finite element analysis of scarf joints to investigate the nonuniform stress variation in nonhomogeneous laminated composites. It was observed that due to discontinuity in adherend stiffness, the stress variation had an oscillating trend with peaks in the vicinity of the 0° plies. Similar characteristics were observed by Harman and Wang [2006], who carried out both analytical and finite element analyses to investigate the influence of a varying scarf angle on the shear stress distribution. Gunnion and Herszberg [2006] conducted two- and three-dimensional finite element analyses and investigated the influence of various parameters on the average and peak values of shear and peel stress. Their work was later extended to accommodate the elastic-plastic nature of the adhesive [Wang and Gunnion 2008]. Baker et al. [1999] carried out a combined experimental and computational analysis where a detailed three-dimensional finite element model was created and the tapered scarf was modeled as a series of steps. In several studies finite element models have been used to investigate the effect of scarf angle and stacking sequence on the failure load of panels with scarf repair [Du et al. 2004; Kumar et al. 2006; Campilho et al. 2007]. Very often, instead of discretizing each layer of the laminate, average material properties are utilized to represent a specific stacking sequence [Soutis and Hu 1997; Kumar et al. 2006]. This approach reduces the size of the model considerably but the oscillating variation of the stress field inside the adhesive layer is not captured. Although detailed three-dimensional finite element analyses of scarf joints using solid elements can be used to provide accurate results, these models tend to be computationally expensive due to the presence of the thin adhesive layer and the numerous layers of plies in the laminate or the face sheet of a sandwich panel. Mesh refinement can be significant, especially in the case of nonlinear analysis where a fine mesh might be required for convergence. Moreover, difficulties associated with parameterizing the meshing process requires extra effort in creating a new mesh every time a panel with a different number of plies, adhesive thicknesses, or panel dimensions is to be analyzed.

An alternative to this approach is to use an element based on a single-layer theory, which utilizes a modest number of degrees of freedom for the entire FE model and provides accurate results. The current analysis utilizes one such plate element [Das et al. 2005; Das et al. 2006] for the adherents and a separate solid element for the adhesive layer in between the adherents. The tapered scarf is modeled as a stepped joint with numerous steps in order to replicate the taper as closely as possible. The analysis incorporates geometric and material nonlinearity in the adherent and adhesive elements, respectively. A bilinear stress strain relationship is used for the material model and geometric nonlinearity is incorporated based on the total Lagrangian formulation. The model accounts for finite boundaries, the presence of a cutout or grind-out in the skin, general loading conditions, material anisotropy, different thicknesses of the repair patch and skin, and different repair and parent materials. The material properties are input for each ply without any limitation on refinement in the thickness direction. While it is computationally robust and fast, it leads to accurate stress predictions in each specific ply and the adhesive layer.
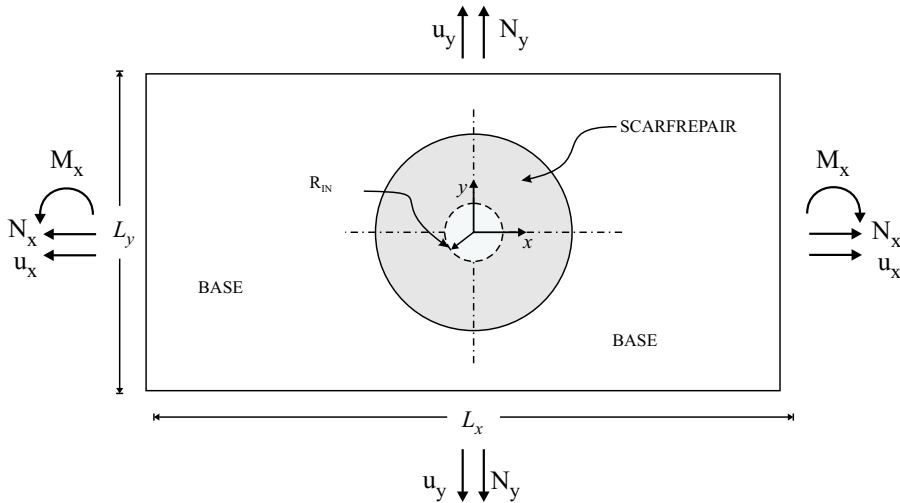
Figure 1. Top view of a panel with scarf repair under arbitrary loading conditions.

2. Problem definition

This study concerns the analysis of scarf repairs of composite laminates and sandwich panels. The top view of a composite laminate, or sandwich panel, with a scarf repair is illustrated in Figure 1. The panels have a rectangular geometry with length L_x and width L_y. As shown in Figure 1, the panel is subjected to forces, moments, and prescribed displacements at the edges. The composite laminate is made of several plies with orthotropic material properties. The laminate can have either a single-sided repair or a double-sided repair, as shown in Figures 2a and 2b. The sandwich panel can have either the full top face sheet or only a portion of it under the repair as shown in Figures 2c and 2d. The face sheets, as well as the core, can be composed of homogeneous, elastic, and orthotropic material layers. The problem posed herein concerns the determination of the complete three-dimensional stress and strain fields in the base and repair adherend and in the thin adhesive layer.

3. Present approach

The tapered scarf is modeled as a series of steps and each step consists of the adhesive layer in between the repair and base adherend. Plate elements, based on the {3,2}-order theory, and solid elements are utilized to model each step along the scarf repair. As shown in Figure 3, the base and repair adherends are represented through separate plate elements, through the thickness. The adhesive layer on the other hand is modeled using a solid element. Since all the plate elements are required to have a constant thickness, a fictitious material with a very low stiffness value is used in the region where the adherent does not occupy any space, as shown in Figure 3. A similar approach was adopted by Bair et al. [1991] for their FE model based on shell elements.

Since the nodes of the plate elements are placed along the mid-surface, they are not aligned with the nodes of the adhesive element. Hence, the nodes of the adhesive elements are offset to the mid-surface of the adherend elements so that they coincide with the nodes of the adherend element [Carpenter 1973]. The
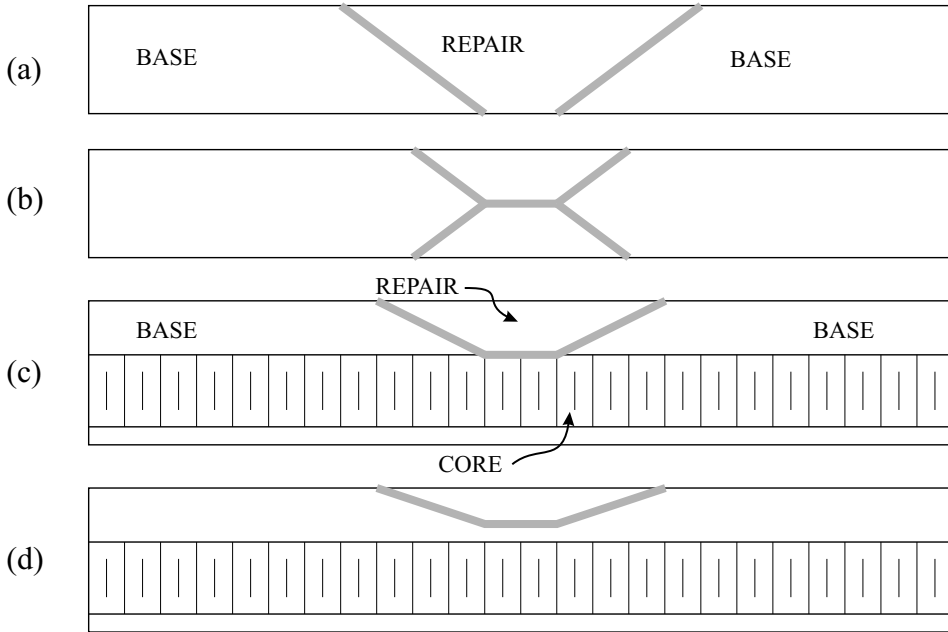
Figure 2. Side view of a composite panel with (a) single- and (b) double-sided repairs and a sandwich panel with (c) full repair of the top face sheet and (d) partial repair of the top face sheet.

details of the element formulation for the plate and solid elements are given in subsequent sections. The stiffness matrix and the unknown displacement vector of the super element, comprised of the adhesive and adherends, have the following forms

$$\boldsymbol{K}_{\text{SCARF}} = \begin{bmatrix} \boldsymbol{K}_b^P + \boldsymbol{K}_{bb}^S & \boldsymbol{K}_{br}^S \\ \boldsymbol{K}_{rb}^S & \boldsymbol{K}_r^P + \boldsymbol{K}_{rr}^S \end{bmatrix}_{78 \times 78}, \qquad \boldsymbol{v}_{\text{SCARF}}^T = \left\{ \boldsymbol{v}_b^T \ \ \boldsymbol{v}_r^T \right\}, \tag{1}$$
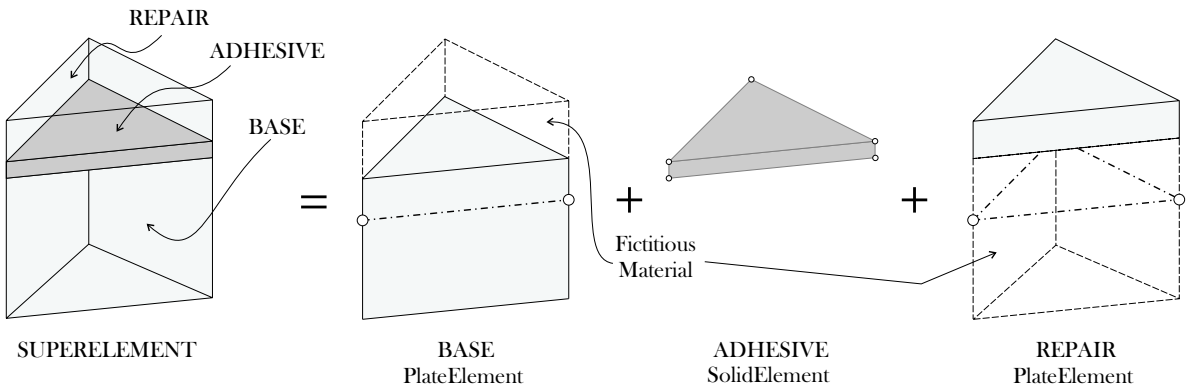
Figure 3. The scarf super element comprised of the two adherend plate elements with the solid adhesive element in between them.
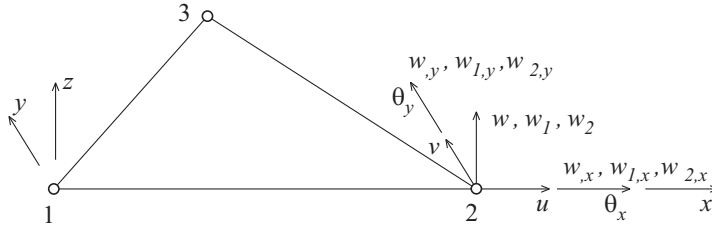
Figure 4. A triangular plate element with three nodes having 13 degrees of freedom at each node.

where $\boldsymbol{K}_b^P$ and $\boldsymbol{K}_r^P$ are the stiffness matrix of the base and repair adherend plate elements, respectively, and $\boldsymbol{K}^S$ corresponds to the stiffness matrix of the adhesive element. The displacement vector consists of the nodal unknowns, $\boldsymbol{v}_b$ and $\boldsymbol{v}_r$, that correspond to the base and repair plate elements, respectively. The region outside the repair zone is modeled using a single layer of plate elements.

4. Plate element

The plate element for the adherends is based on the {3,2}-order single-layer theory [Cook and Tessler 1998; Barut et al. 2001]. The triangular element contains 13 degrees of freedom at each node, as shown in Figure 4. These degrees of freedom consist of two in-plane displacements, (u, v), two out-of-plane rotations, (θ_x, θ_y), and three transverse nodal displacements, (w, w_1, w_2), and their derivatives, $(w_{,x}, w_{,y}, w_{1,x}, w_{1,y}, w_{2,x}, w_{2,y})$. The weighted-average in-plane displacement components in the x- and y-directions are denoted by u and v, respectively. The weighted-average transverse displacement is denoted by w. The weighted-average bending rotations about the negative x- and positive y-axes are denoted by θ_x and θ_y, respectively. Their positive sign convention is shown in Figure 4. The transverse displacements, not weighted-averaged, (w_1, w_2), represent the symmetric and antisymmetric expansion modes through the thickness of the element.

As shown by Barut et al. [2001], the displacement components of the plate are defined as

$$
\begin{aligned}
u_x(x, y, z) = u(x, y) + h\zeta\theta_y(x, y) + \left(\frac{1}{6} - \frac{\zeta^2}{2}\right)hw_{1,x}(x, y) \\
+ h\left(\frac{\zeta}{5} - \frac{\zeta^3}{3}\right)\left[\frac{5}{4}(\theta_y(x, y) + w_{,x}(x, y)) + w_{2,x}(x, y)\right],
\end{aligned}
\tag{2a}
$$

$$
\begin{aligned}
u_y(x, y, z) = v(x, y) + h\zeta\theta_x(x, y) + \left(\frac{1}{6} - \frac{\zeta^2}{2}\right)hw_{1,y}(x, y) \\
+ h\left(\frac{\zeta}{5} - \frac{\zeta^3}{3}\right)\left[\frac{5}{4}(\theta_x(x, y) + w_{,y}(x, y)) + w_{2,y}(x, y)\right],
\end{aligned}
\tag{2b}
$$

$$
u_z(x, y, z) = w(x, y) + w_1(x, y)\zeta + w_2(x, y)(\zeta^2 - 1/5),
\tag{2c}
$$

where $\zeta = z/h$ is the normalized thickness and varies in the range $-1 \leq \zeta \leq 1$. In accordance with the {3,2} plate theory, the in-plane displacement components vary cubically and the transverse displacement

component varies quadratically across the thickness of the panel. At any point in the panel, the in-plane displacement components in the x- and y-directions are represented by $u_x(x, y, z)$ and $u_y(x, y, z)$, respectively, and the transverse displacement component by $u_z(x, y, z)$.

The definitions of the stress and moment resultants and the form of the resultant strain and curvatures are provided in [Barut et al. 2001]. The resultant stresses and moments are expressed in terms of the strain and curvature components as

$$\begin{Bmatrix} N \\ M \\ Q \end{Bmatrix} = \begin{bmatrix} A & B & 0 \\ B^T & D & 0 \\ 0 & 0 & G \end{bmatrix} \begin{Bmatrix} \epsilon \\ \kappa \\ \gamma \end{Bmatrix}, \tag{3}$$

where

$$N^T = \{N_{xx0}, N_{yy0}, N_{zz0}, N_{xy0}, N_{xx1}, N_{yy1}, N_{xy1}\}, \tag{4a}$$

$$M^T = \{M_{xx0}, M_{yy0}, M_{zz0}, M_{xy0}, M_{xx1}, M_{yy1}, M_{xy1}\}, \tag{4b}$$

$$Q^T = \{Q_{yz0}, Q_{xz0}\}, \tag{4c}$$

$$\epsilon^T = \{\varepsilon_{xx0}, \varepsilon_{yy0}, \varepsilon_{zz0}, \gamma_{xy0}, \varepsilon_{xx1}, \varepsilon_{yy1}, \gamma_{xy1}\}, \tag{4d}$$

$$\kappa^T = \{\kappa_{xx0}, \kappa_{yy0}, \kappa_{zz0}, \kappa_{xy0}, \kappa_{xx1}, \kappa_{yy1}, \kappa_{xy1}\}, \tag{4e}$$

$$\gamma^T = \{\gamma_{yz0}, \gamma_{xz0}\}. \tag{4f}$$

The explicit forms of A, B, D, and G are given in [Barut et al. 2001]. This constitutive relation can also be expressed in terms of the compliance matrix C in the form $E = CS$, where $E^T = \{\epsilon^T \; \kappa^T \; \gamma^T\}$ and $S^T = \{N^T \; M^T \; Q^T\}$. The governing equations concerning the equilibrium equations and continuity of interelement displacements along the element edges are derived utilizing the principle of virtual work. The resulting equations of equilibrium and boundary conditions are derived in [Barut et al. 2001]. The kinematic continuity conditions are imposed not only on the weighted-average displacements and slopes, $(u, v, w, \theta_x, \theta_y)$, but also on the derivatives of the higher-order displacement modes, (w_1, w_2), in the transverse direction. Therefore, the finite element implementation of the equilibrium equations requires at least C^1 interelement continuity for the out-of-plane displacement modes of w, w_1, and w_2. Because of this requirement, the finite element implementation of the total potential energy functional in terms of the assumed displacement field becomes rather difficult. The hybrid energy functional formulation overcomes the difficulty of the C^1 interelement continuity requirement because the displacements, as well as the slopes, are independently assumed only along element boundaries, which can be rendered identical along the common boundaries of adjacent elements. However, the kinematic compatibility between the displacements and slopes along the element boundaries is preserved in order to avoid a possible shear-locking phenomenon. Also, as part of the hybrid energy functional formulation, the stress and moment resultants within the element are selected such that they satisfy the equilibrium equations.

The hybrid energy functional for an element, Π_H, is defined as

$$\Pi_H = \frac{1}{2} \int_{A_e} S^T C S \, dA - \int_{\Gamma_e} T_b^T u_b \, d\Gamma, \tag{5}$$

in which the element boundary is denoted by Γ_e and its area by A_e. The vectors $\boldsymbol{T}_b$ and $\boldsymbol{u}_b$ include the components of the boundary forces and boundary displacements, respectively. In accordance with the hybrid energy formulation, the resultant stress vector, $\boldsymbol{S}$, must satisfy the equilibrium equations identically. The derivation of the resultant stress vector, $\boldsymbol{S}$, satisfying the equilibrium equations is presented in [Das et al. 2005]. Also, the boundary displacement vector, $\boldsymbol{u}_b^{(k)}$, containing the assumed boundary displacement components, and the boundary stress vector, $\boldsymbol{T}_b^{(k)}$, containing the resultant stresses and moments corresponding to the boundary displacement vector $\boldsymbol{u}_b^{(k)}$, are given in [Das et al. 2005]. Substituting for the stress vector, the boundary displacement and boundary stress vectors in the hybrid energy functional result in

$$\Pi_H = \tfrac{1}{2}\boldsymbol{b}^T \boldsymbol{H}\boldsymbol{b} + \boldsymbol{\lambda}^T \boldsymbol{c}\boldsymbol{b} + \boldsymbol{R}_b^T \boldsymbol{b} - \boldsymbol{R}_v^T \boldsymbol{v} - \boldsymbol{b}^T \boldsymbol{G}\boldsymbol{v} + \Pi_0, \tag{6}$$

where

$$\boldsymbol{H} = \int_{A_e} \boldsymbol{P}^T \boldsymbol{C}\boldsymbol{P}\, dA, \qquad \boldsymbol{G} = \sum_k \int_{\Gamma_{(k)}} \boldsymbol{P}^T \boldsymbol{B}_s^{(k)} \boldsymbol{B}_b^{(k)} \boldsymbol{L}^{(k)}\, d\Gamma,$$

$$\boldsymbol{R}_b = \int_{A_e} \boldsymbol{S}_0^T \boldsymbol{C}\boldsymbol{P}\, dA, \qquad \boldsymbol{R}_v = \sum_{k=1}^{3} \int_{\Gamma_{(k)}} \boldsymbol{S}_0^T \boldsymbol{B}_s^{(k)} \boldsymbol{B}_b^{(k)} \boldsymbol{L}^{(k)}\, d\Gamma, \qquad \Pi_0 = \frac{1}{2}\int_{A_e} \boldsymbol{S}_0^T \boldsymbol{C}\boldsymbol{S}_0\, dA, \tag{7}$$

in which the explicit definition of each of the matrices and vectors is given in [Das et al. 2005]. In matrix form, the hybrid energy functional, Π_H, can be rewritten as

$$\Pi_H = \tfrac{1}{2}\hat{\boldsymbol{b}}^T \hat{\boldsymbol{H}}\hat{\boldsymbol{b}} + \hat{\boldsymbol{R}}_b^T \hat{\boldsymbol{b}} - \boldsymbol{R}_v^T \boldsymbol{v} + \hat{\boldsymbol{b}}^T \hat{\boldsymbol{G}}\boldsymbol{v} + \Pi_0, \tag{8}$$

where

$$\hat{\boldsymbol{b}}^T = \{\boldsymbol{b}^T, \boldsymbol{\lambda}^T\}, \qquad \hat{\boldsymbol{H}} = \begin{bmatrix} \boldsymbol{H} & \boldsymbol{c}^T \\ \boldsymbol{c} & \boldsymbol{0} \end{bmatrix}, \qquad \hat{\boldsymbol{R}}_b^T = \{\boldsymbol{R}_b^T, \boldsymbol{0}^T\}, \qquad \hat{\boldsymbol{G}} = \begin{bmatrix} \boldsymbol{G} \\ \boldsymbol{0} \end{bmatrix}.$$

In accordance with the concept of energy minimization, the first variation of the hybrid energy functional with respect to the unknown vector $\hat{\boldsymbol{b}}$ of generalized coordinates yields

$$\delta\hat{\boldsymbol{b}}^T \left(\hat{\boldsymbol{H}}\hat{\boldsymbol{b}} + \hat{\boldsymbol{R}}_b - \hat{\boldsymbol{G}}\boldsymbol{v}\right) = \boldsymbol{0} \qquad \text{or} \qquad \hat{\boldsymbol{b}} = \hat{\boldsymbol{H}}^{-1}\left(\hat{\boldsymbol{G}}\boldsymbol{v} - \hat{\boldsymbol{R}}_b\right). \tag{9}$$

With this explicit solution form, the hybrid energy functional becomes

$$\Pi_H = -\tfrac{1}{2}\boldsymbol{v}^T \boldsymbol{k}_L \boldsymbol{v} + \boldsymbol{f}_0^T \boldsymbol{v} + \Pi_0, \tag{10}$$

in which the linear stiffness matrix $\boldsymbol{k}_L$ and the resultant force (load) vector $\boldsymbol{f}_0$ are defined as

$$\boldsymbol{k}_L = \hat{\boldsymbol{G}}^T \hat{\boldsymbol{H}}^{-1} \hat{\boldsymbol{G}} \qquad \text{and} \qquad \boldsymbol{f}_0^T = \hat{\boldsymbol{R}}_b^T \hat{\boldsymbol{H}}^{-1} \hat{\boldsymbol{G}} - \hat{\boldsymbol{R}}_v^T. \tag{11}$$

Finally, the element equilibrium equation is obtained by requiring the first variation of the hybrid energy functional to vanish

$$\delta\Pi_H = \delta\boldsymbol{v}^T (\boldsymbol{k}_L \boldsymbol{v} - \boldsymbol{f}_0) = 0. \tag{12}$$

For arbitrary variation of $\delta\boldsymbol{v}$, the element equilibrium equations become

$$\boldsymbol{k}_L \boldsymbol{v} = \boldsymbol{f}_0. \tag{13}$$

The nonlinear analysis is based on the total Lagrangian formulation. The principle of virtual work in the total Lagrangian formulation is given by

$$\int_{0V} \sum_k {}^{t+\Delta t}_0 S^{(k)} \delta_0 E^{(k)} d^0 V = \delta^{t+\Delta t} \mathfrak{R}. \tag{14}$$

In this expression, the left subscript indicates the configuration by which the quantity is measured and the left superscript refers to the configuration of the body at a specific time. The right superscript refers to the kth component of the Piola-Kirchoff stress, $\boldsymbol{S}$, and Green strain, $\boldsymbol{E}$, resultant vector. The right-hand side of Equation (14) represents the virtual work done by the conservative external forces on the virtual displacements. The Piola-Kirchoff stress are decomposed between times t and $t + \Delta t$ as

$$^{t+\Delta t}_0 S^{(k)} = {}^t_0 S^{(k)} + {}_0 S^{(k)}. \tag{15}$$

The incremental Piola-Kirchoff stress vector, ${}_0 S^{(k)}$, represents the incremental loading between $t + \Delta t$ and t, and ${}^t_0 S^{(k)}$ represents the known component from time t. The Green strain at any state $t + \Delta t$ can be written in terms of linear and nonlinear components as

$$^{t+\Delta t}_0 E^{(k)} = {}^{t+\Delta t}_0 E^{(k)}_L + {}^{t+\Delta t}_0 E^0_{NL}. \tag{16}$$

This expression can be written in terms of the unknown displacement as

$$^{t+\Delta t}_0 E^{(k)} = \boldsymbol{B}_L^{(k)^T} \left({}^t\boldsymbol{v} + \boldsymbol{v}\right) + \tfrac{1}{2}\left({}^t\boldsymbol{v} + \boldsymbol{v}\right)^T \boldsymbol{B}_{NL}^{(k)} \left({}^t\boldsymbol{v} + \boldsymbol{v}\right), \tag{17}$$

where $\boldsymbol{B}_L^{(k)}$ and $\boldsymbol{B}_{NL}^{(k)}$ are the linear and nonlinear strain-displacement relationship vector and matrix, respectively, corresponding to the kth strain resultant component. Based on the hybrid formulation, the linear strain-displacement relationship matrix can be expressed as

$$\boldsymbol{B}_L = \boldsymbol{C} \boldsymbol{P} \hat{\boldsymbol{H}}^{-1} \hat{\boldsymbol{G}}. \tag{18}$$

The matrix $\boldsymbol{B}_{NL}^{(k)}$ is obtained based on von Karman assumptions and therefore the current analysis is applicable only for small rotations. The incremental strain ${}_0 E^{(k)}$ can be obtained by finding the difference between the strain at state $t + \Delta t$ and t

$$_0 E^{(k)} = {}^{t+\Delta t}_0 E^{(k)} - {}^t_0 E^{(k)} = \boldsymbol{B}_L^{(k)^T} \boldsymbol{v} + {}^t\boldsymbol{v}^T \boldsymbol{B}_{NL}^{(k)} \boldsymbol{v} + \tfrac{1}{2} \boldsymbol{v}^T \boldsymbol{B}_{NL}^{(k)} \boldsymbol{v}. \tag{19}$$

The virtual strain increment can be expressed as

$$\delta_0 E^{(k)} = \boldsymbol{B}_L^{(k)^T} \delta\boldsymbol{v} + {}^t\boldsymbol{v}^T \boldsymbol{B}_{NL}^{(k)} \delta\boldsymbol{v} + \boldsymbol{v}^T \boldsymbol{B}_{NL}^{(k)} \delta\boldsymbol{v}. \tag{20}$$

Based on Equations (15) and (19), the expression for stress can now be written in terms of the unknown displacements as

$$^{t+\Delta t}_0 S^{(k)} = {}^t_0 S^{(k)} + \sum_j C^{-1}_{jk} E^{(j)} = {}^t_0 S^{(k)} + \sum_j C^{-1}_{jk} \left(\boldsymbol{B}_L^{(j)^T} \boldsymbol{v} + {}^t\boldsymbol{v}^T \boldsymbol{B}_{NL}^{(j)} \boldsymbol{v} + \tfrac{1}{2} \boldsymbol{v}^T \boldsymbol{B}_{NL}^{(j)} \boldsymbol{v}\right), \tag{21}$$

where C^{-1}_{jk} represents the linear relationship between the resultant stresses and strains. Substituting the expressions for virtual incremental strain and total stress from Equations (20) and (21) into the virtual

work expression and neglecting the higher order terms results in

$$\left(\int_{0V}\left(\sum_k\sum_j \boldsymbol{B}_L^{(k)}C_{jk}^{-1}\boldsymbol{B}_L^{(k)^T}+\sum_k\sum_j \boldsymbol{B}_L^{(k)}C_{jk}^{-1t}\boldsymbol{v}^T\boldsymbol{B}_{NL}^{(k)}+\sum_k \boldsymbol{B}_{NL}^{(k)\,t}\boldsymbol{v}C_{jk}^{-1t}\boldsymbol{B}_L^{(k)^T}\right.\right.$$

$$\left.\left.+\sum_k \boldsymbol{B}_{NL}^{(k)\,t}\boldsymbol{v}C_{jk}^{-1t}\boldsymbol{v}^T\boldsymbol{B}_{NL}^{(k)}+\sum_k {}_0^t S^{(k)}\boldsymbol{B}_{NL}^{(k)}\right)d^0V\right)\boldsymbol{v}=\boldsymbol{f}_e-\sum_k {}_0^t S^{(k)}\boldsymbol{B}_L^{(k)}-\sum_k {}_0^t S^{(k)}\boldsymbol{B}_{NL}^{(k)\,t}\boldsymbol{v}. \quad (22)$$

The final nonlinear system of finite element equations can be written as

$$\boldsymbol{K}^P\boldsymbol{v}=\boldsymbol{F}^P, \qquad (23)$$

where $\boldsymbol{K}^P=\boldsymbol{k}_L+\boldsymbol{k}_v+\boldsymbol{k}_\sigma$ and ${}^P\boldsymbol{F}=\boldsymbol{f}_e-\boldsymbol{f}_i$. The matrices $\boldsymbol{k}_L$, $\boldsymbol{k}_v$, and $\boldsymbol{k}_\sigma$ are the linear, initial displacement, and geometric stiffness matrices, respectively, and $\boldsymbol{f}_i$ and $\boldsymbol{f}_e$ are the internal and external force vectors, respectively. The explicit form of these matrices and vectors is as follows

$$\boldsymbol{k}_L=\int_{0V}\left(\sum_k\sum_j \boldsymbol{B}_L^{(k)}C_{jk}^{-1}\boldsymbol{B}_L^{(k)^T}\right)d^0V, \qquad (24a)$$

$$\boldsymbol{k}_v=\int_{0V}\left(\sum_k\sum_j \boldsymbol{B}_L^{(k)}C_{jk}^{-1}\boldsymbol{v}^T\boldsymbol{B}_{NL}^{(k)}+\sum_k \boldsymbol{B}_{NL}^{(k)\,t}\boldsymbol{v}C_{jk}^{-1t}\boldsymbol{B}_L^{(k)^T}+\sum_k \boldsymbol{B}_{NL}^{(k)\,t}\boldsymbol{v}C_{jk}^{-1t}\boldsymbol{v}^T\boldsymbol{B}_{NL}^{(k)}\right)d^0V, \quad (24b)$$

$$\boldsymbol{k}_\sigma=\int_{0V}\left(\sum_k {}_0^t S^{(k)}\boldsymbol{B}_{NL}^{(k)}\right)d^0V, \qquad (24c)$$

$$\boldsymbol{f}_i=\int_{0V}\left(\sum_k {}_0^t S^{(k)}\boldsymbol{B}_L^{(k)}+\sum_k {}_0^t S^{(k)}\boldsymbol{B}_{NL}^{(k)\,t}\boldsymbol{v}\right)d^0V. \qquad (24d)$$

Note that by combining the linear strain-displacement relationship matrix given in Equation (18) with Equation (24a), the linear stiffness matrix obtained from the hybrid formulation, Equation (11), can be reproduced.

5. Adhesive element

A solid element with six nodes is used for the adhesive layer. Unlike the plate element, the adhesive element is based on a displacement formulation and each node has three degrees of freedom. The displacement field varies linearly both in the in-plane and transverse directions. Therefore, the displacement field inside the adhesive can be expressed as

$$\boldsymbol{u}^S=\begin{bmatrix}N_{\eta+} & \boldsymbol{0}\\ \boldsymbol{0} & N_{\eta-}\end{bmatrix}\begin{bmatrix}N_{xy} & \boldsymbol{0}\\ \boldsymbol{0} & N_{xy}\end{bmatrix}\begin{Bmatrix}\boldsymbol{v}_{\text{bot}}^S\\ \boldsymbol{v}_{\text{top}}^S\end{Bmatrix}, \qquad (25)$$

where $\boldsymbol{u}^S=\{u_x^S\ u_y^S\ u_z^S\}^T$ and $\boldsymbol{v}_{\text{bot}}^S$ and $\boldsymbol{v}_{\text{top}}^S$ consist of the nodal displacements corresponding to the bottom and top surfaces, respectively. As mentioned earlier, the nodes of the solid element do not coincide with the nodes of the adherend plate element. Therefore, in order to enforce continuity, the nodes of the adhesive elements are offset to the mid-surface of the adherend elements. The displacements at the nodes of the solid element are expressed in terms of the nodal displacements of the plate element, as
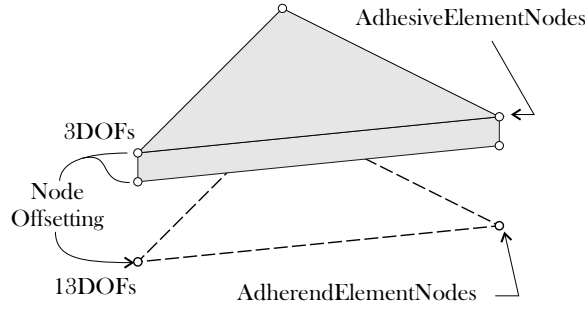
Figure 5. Offset nodes of the solid element for the adhesive.

shown in Figure 5, based on the following transformation

$$
\left\{ \begin{matrix} \boldsymbol{v}^S_{\text{bot}} \\ \boldsymbol{v}^S_{\text{top}} \end{matrix} \right\} = \begin{bmatrix} \boldsymbol{T}_b & \boldsymbol{0} \\ \boldsymbol{0} & \boldsymbol{T}_r \end{bmatrix} \left\{ \begin{matrix} \boldsymbol{v}^P_b \\ \boldsymbol{v}^P_r \end{matrix} \right\},
\tag{26}
$$

where $\boldsymbol{v}^P_b$ and $\boldsymbol{v}^P_r$ are nodal displacements of the base and repair plate element, and $\boldsymbol{T}_b$ and $\boldsymbol{T}_r$ are transformation matrices. The transformation matrices are constructed based on the definition of through-the-thickness variation of the displacement field inside the adherend plate, as given in Equation (2). Combining Equations (25) and (26), the displacement field inside the adhesive element can now be expressed in terms of the degrees of freedom associated with the plate elements as

$$
\boldsymbol{u}^S = \begin{bmatrix} \boldsymbol{N}_{\eta+} & \boldsymbol{0} \\ \boldsymbol{0} & \boldsymbol{N}_{\eta-} \end{bmatrix} \begin{bmatrix} \boldsymbol{N}_{xy} & \boldsymbol{0} \\ \boldsymbol{0} & \boldsymbol{N}_{xy} \end{bmatrix} \begin{bmatrix} \boldsymbol{T}^{(i)} & \boldsymbol{0} \\ \boldsymbol{0} & \boldsymbol{T}^{(j)} \end{bmatrix} \left\{ \begin{matrix} \boldsymbol{v}^P_b \\ \boldsymbol{v}^P_r \end{matrix} \right\}.
\tag{27}
$$

Using the displacement variation given in Equation (27), the strain field inside the element takes the form

$$
\boldsymbol{\varepsilon}^S = \boldsymbol{B}^S \left\{ \begin{matrix} \boldsymbol{v}^P_b \\ \boldsymbol{v}^P_r \end{matrix} \right\},
\tag{28}
$$

where $\boldsymbol{B}^S$ is the strain-displacement transformation matrix. Instead of using a typical shear lag model, the adhesive layer takes into account the presence of all six components of strain such that

$$
\boldsymbol{\varepsilon}^S = \{\varepsilon_{xx} \ \ \varepsilon_{yy} \ \ \varepsilon_{zz} \ \ \gamma_{yz} \ \ \gamma_{xz} \ \ \gamma_{xy}\}^T.
\tag{29}
$$

The stiffness matrix is therefore defined as

$$
\boldsymbol{K}^S = \int_{S_V} \boldsymbol{B}^{S^T} \boldsymbol{D}^S \boldsymbol{B}^S \, dV = \begin{bmatrix} \boldsymbol{K}^S_{bb} & \boldsymbol{K}^S_{br} \\ \boldsymbol{K}^S_{rb} & \boldsymbol{K}^S_{rr} \end{bmatrix}_{78 \times 78},
\tag{30}
$$

where $\boldsymbol{D}^S$ is the stress-strain relationship matrix. The isotropic adhesive material has a bilinear relation between the effective transverse shear stress, τ_{eff}, and effective transverse shear strain, γ_{eff}. The effective transverse shear stress and strain in the adhesive are defined as

$$
\tau_{\text{eff}} = \sqrt{\tau_{xz}^2 + \tau_{yz}^2}
\tag{31a}
$$
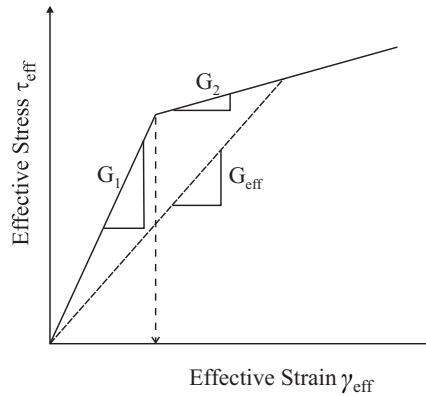
Figure 6. Bilinear relationship between effective stress and strain.

and

$$\gamma_{\text{eff}} = \sqrt{\gamma_{xz}^2 + \gamma_{yz}^2}. \tag{31b}$$

As shown in Figure 6, the initial shear modulus of the bilinear adhesive behavior is denoted by G_1, and it reduces to G_2 when the effective transverse shear strain, γ_{eff}, reaches the critical shear strain, γ_c. For a given value of effective shear strain, the effective shear stress can be obtained from Figure 6. Thereafter, the effective shear modulus can be obtained as

$$G_{\text{eff}} = \tau_{\text{eff}}/\gamma_{\text{eff}}. \tag{32}$$

Moreover, the effective Young's modulus can be expressed as

$$E_{\text{eff}} = 2G_{\text{eff}}(1 + \nu). \tag{33}$$

Note that due to the dependence of the effective modulus on the effective strain, the system of equations become nonlinear.

6. Results and discussion

The current analysis tool is validated against an analytical solution and the commercial finite element analysis software ANSYS. Although both two-dimensional and three-dimensional models were created using ANSYS, only the three-dimensional results are reported here. In the ANSYS model, two layers of elements were used for each ply in the adherends and the adhesive was divided into three layers of elements. PLANE 42 and SOLID 45 elements were used for the two-dimensional and three-dimensional model, respectively. Similar to the approximation made in the current analysis tool, a series of steps were used to represent the scarf, instead of modeling it as a smooth taper. The adhesive along with each ply in the laminate was divided into multiple steps and one layer of solid element was used for every step.

The first problem involves the linear analysis of a two-dimensional scarf joint previously considered by [Erdogan and Ratwani 1971]. The scarf joint is subjected to in-plane stress, and its geometry is shown in Figure 7. The first adherend is made of aluminum with an elastic modulus $E = 1.0 \times 10^7$ psi and Poisson's ratio $\nu = 0.3$. The second adherend is made of boron-epoxy with elastic moduli $E_x = 3.24 \times 10^7$ psi and $E_z = 3.5 \times 10^6$ psi, shear modulus $G = 1.23 \times 10^6 \, psi$, and Poisson's ratio $\nu_x = 0.23$. An epoxy
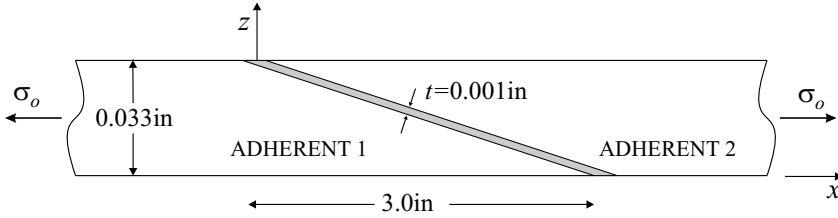
Figure 7. Schematics of the scarf joint.

material with elastic modulus $E = 4.45 \times 10^5$ psi and shear modulus $G = 1.65 \times 10^5$ psi is used for the thin adhesive layer. Since the analytical analysis does not permit the adherends to bend, for this problem, the bending deformations were suppressed in the finite element analysis as well. The transverse shear stress variation inside the adhesive layer is shown in Figure 8. Unlike a lap or step joint, the scarf joint has a fairly uniform variation of shear stress inside the adhesive. The difference in the results from the analytical and current finite element analysis is due to the presence of stress-free boundary condition at the edges. The current finite element solution tries to satisfy the stress boundary condition whereas the analytical results do not capture this feature.

The nonuniform variation of adhesive stress in a composite laminated joint is investigated next. The two-dimensional joint has a stacking sequence of $(45/90/-45/0)_5$, and each ply has a thickness of 0.0072 in. The total length of the panel is 12.32 in, and the scarf ratio is 30.0. The material properties of the plies in the base and repair adherends are given in Table 1. The 0.01-inch-thick adhesive has linear material properties with shear modulus $G = 6.0 \times 10^4$ psi and Poisson's ratio $\nu = 0.3$. The panel is subjected to an in-plane force of $N_x = 1000.0$ lbs/in; the stresses in the adhesive are shown in Figure 9. Unlike the homogeneous adherends, the stress distribution in the laminated joints has an oscillating trend and locations of the peaks are in the vicinity of the $0°$ degree plies. The transverse shear stress,
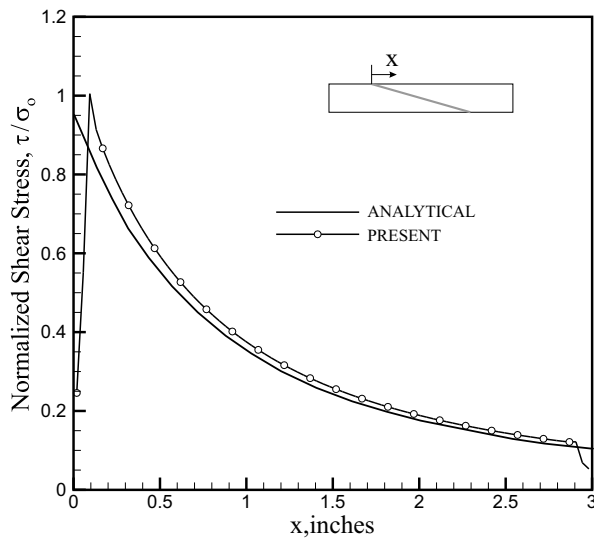
Figure 8. Shear stress variation inside the adhesive layer of a scarf joint.
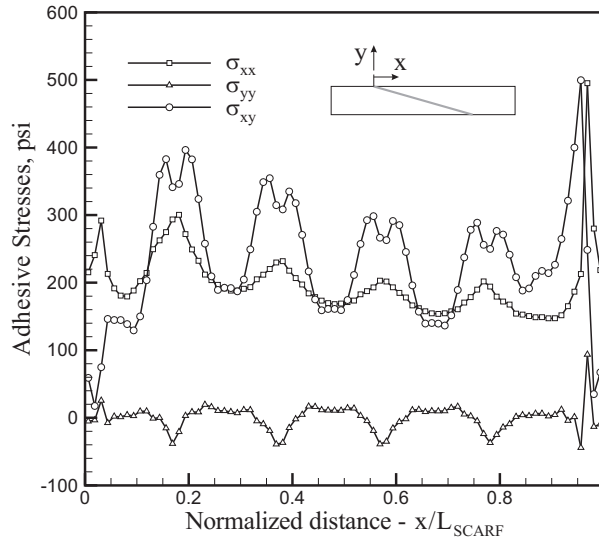
Figure 9. Stress variation inside the adhesive layer of a scarf joint.

σ_{xy}, is the dominant component whereas the magnitude of transverse normal stress, σ_{yy}, is much smaller even though the laminate has an unsymmetrical stacking sequence. Since the adhesive element is not based on a typical shear-lag-type model, the in-plane normal stress, σ_{xx}, can also be computed using the current analysis; the results are shown in Figure 9.

The next problem involves the three-dimensional scarf repair analysis of a composite laminate with a single-sided repair. The panel has length and width of 40 in and 28 in, respectively. The inner radius of the scarf repair is 0.25 in, and the scarf ratio is 30.0. The laminate has a stacking sequence of $(45/90/-45/0)_{5s}$, and each ply has a thickness of 0.0072 in. The adhesive thickness and material properties of the base, repair, and adhesive are the same as the scarf joint discussed earlier. The linear and geometrically nonlinear responses of the repaired laminate under two loading conditions have been analyzed. In the first case, a moment of $M_x = 10.0$ lbs-in/in is applied at the edges of the panel. The

	Base	Repair	Core
E_1(psi)	1.85×10^7	1.58×10^7	1.50×10^2
E_2(psi)	1.00×10^6	8.50×10^5	7.50×10^1
E_3(psi)	1.00×10^6	8.50×10^5	2.00×10^5
G_{12}(psi)	5.20×10^5	4.40×10^5	1.00×10^3
G_{13}(psi)	5.20×10^5	4.40×10^5	1.00×10^3
G_{23}(psi)	3.30×10^5	2.80×10^5	4.00×10^4
ν_{12}	0.34	0.34	1.20
ν_{13}	0.34	0.34	1.00×10^{-5}
ν_{23}	0.53	0.53	1.00×10^{-5}

Table 1. Material properties for the base, repair, and core
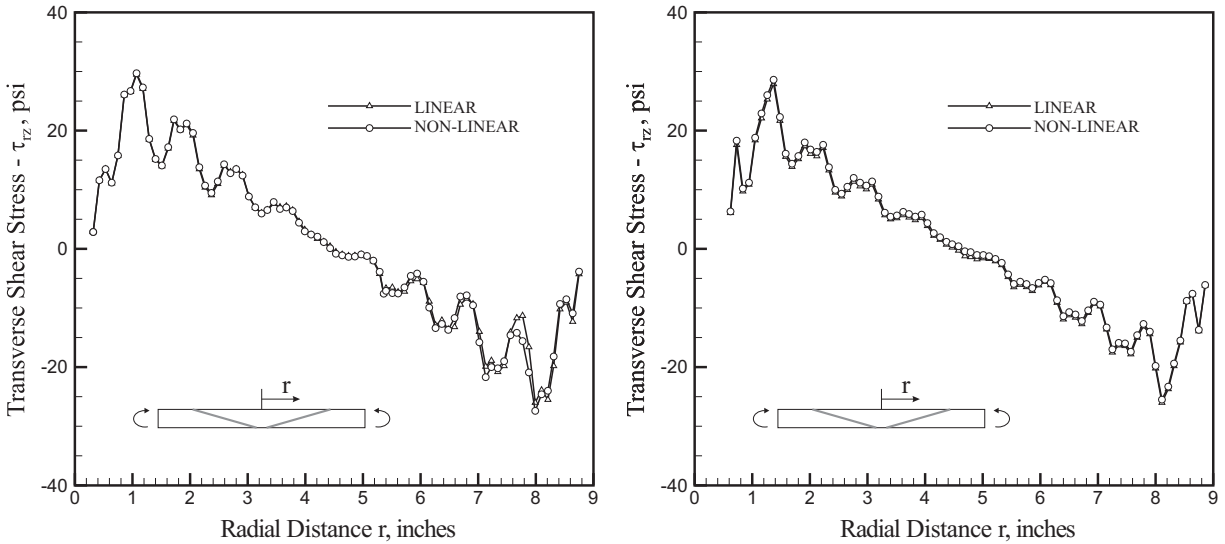
Figure 10. Shear stress, τ_{rz}, variation obtained from (a) the current analysis and (b) ANSYS for a composite panel with a single-sided repair under moment loading.

transverse shear stress inside the adhesive along the x-axis is shown in Figure 10a. The deformations due to the applied loading are not significant enough and therefore there is hardly any difference between the results from the linear and nonlinear analyses. The variation of the transverse shear stress obtained from ANSYS is shown in Figure 10b; the results are in good agreement with the current analysis. In the second case, the laminate is subjected to a moment of $M_x = 10.0$ lbs-in/in along with an in-plane force of $N_x = 100.0$ lbs/in. Even though the panel does not experience large deformations, there is a considerable difference between the solutions obtained from the linear and nonlinear analyses, as shown in Figure 11a. This is due the presence of in-plane forces that introduce the stress stiffening effect, which is not considered in the linear analysis. The results obtained from ANSYS are shown in Figure 11b; they match the results obtained form the current analysis.

A composite laminate with a double-sided repair is considered next. The geometry, stacking sequence, and material properties are same as the previous problem, which involved a laminate with a single-sided repair. The panel is subjected to an in-plane force of $N_x = 1000.0$ lbs/in. The stress variations inside the adhesive along lines that are $0°$, $30°$, $60°$, and $90°$ from the x-axis are shown in Figures 12a and 12b. Since both the stacking sequence and the nature of the repair are symmetrical, the variations of shear stresses τ_{rz} and $\tau_{\theta z}$ are shown only inside the adhesive layer between the top repair and the base. A dominant peak is observed at the inner edge of the repair, which is also the location where two $0°$ plies exist. As expected the shear stress, τ_{rz}, is dominant along the direction of loading, that is, the x-axis, whereas the $\tau_{\theta z}$ component has significant stress concentration in the $30°$–$60°$ region.

A sandwich panel with full repair of the top face sheet is considered next. The panel has length and width of 40 in and 28 in, respectively. The inner radius of the scarf repair is 0.25 inch, and the scarf ratio is 30.0. The top face sheet has 40 plies with a stacking sequence of $(45/90/-45/0)_{5s}$ and the bottom face sheet has 8 plies with a stacking sequence of $(45/90/-45/0)_2$. Each ply has a thickness of 0.0072 in, and the core is 1.0 in thick. The material properties of the undamaged top and bottom face
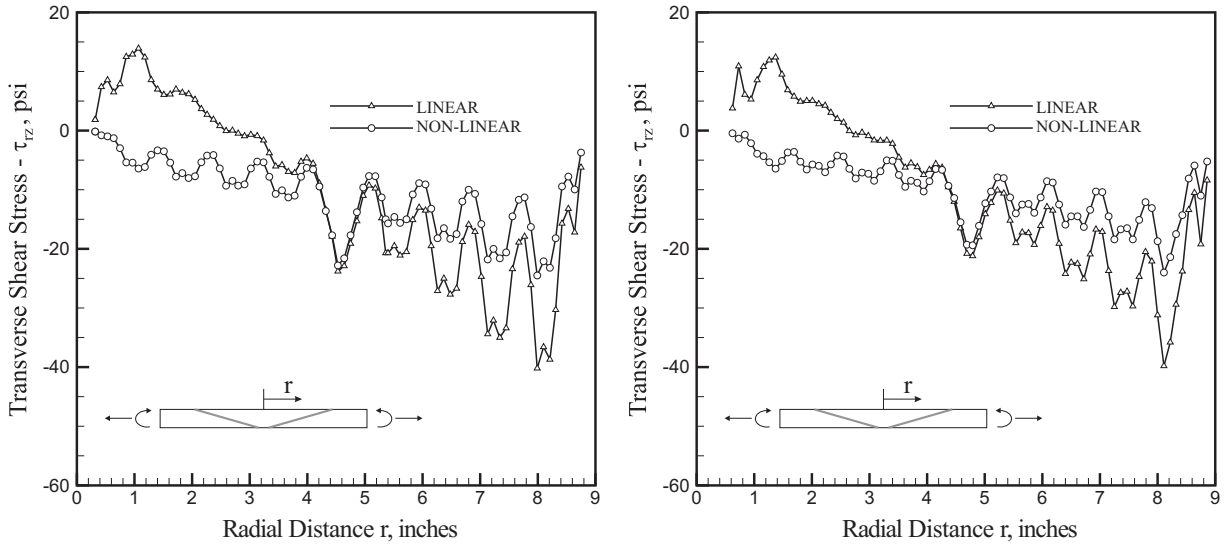
Figure 11. Shear stress, τ_{rz}, variation obtained from (a) the current analysis and (b) ANSYS for a composite panel with a single-sided repair under combined moment and in-plane loading.

sheets correspond to the base material in Table 1. The material properties of the repair and core are also given in Table 1. The adhesive, which is 0.01 in thick, has a bilinear stress-strain relationship. The shear moduli of the adhesive are $G_1 = 6.0 \times 10^4$ psi and $G_2 = 6.0 \times 10^2$ psi, and the Poisson's ratio is $\nu = 0.3$. The adhesive has a critical shear strain values of $\gamma_c = 0.04$. The edge of the sandwich panel
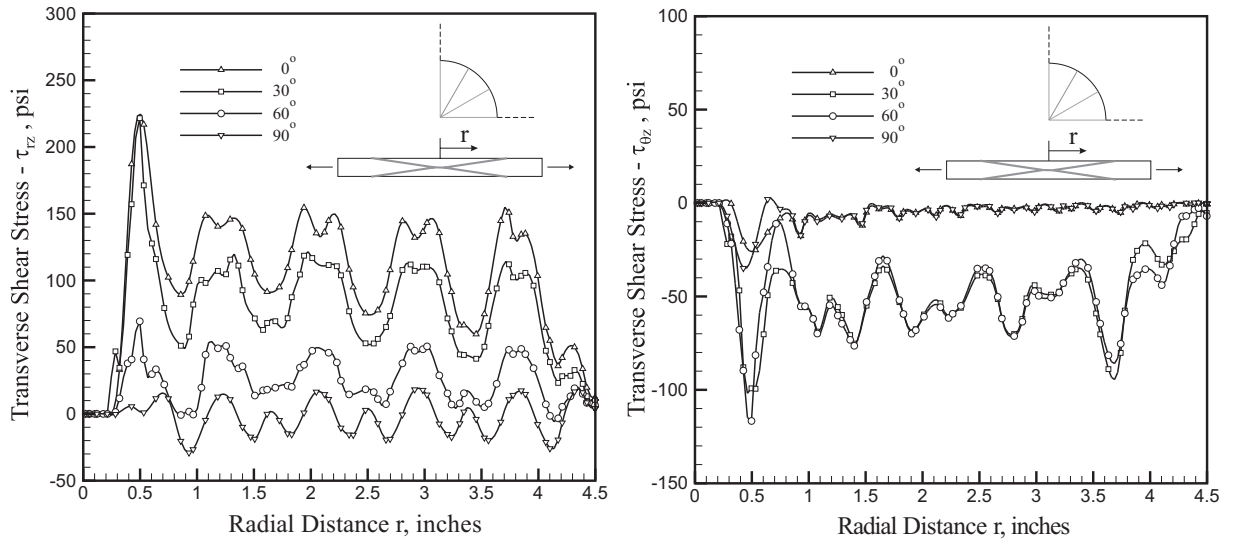
Figure 12. Shear stresses, (a) τ_{rz} and (b) $\tau_{\theta z}$, inside the adhesive between the top repair and base of a composite panel with a double-sided repair.
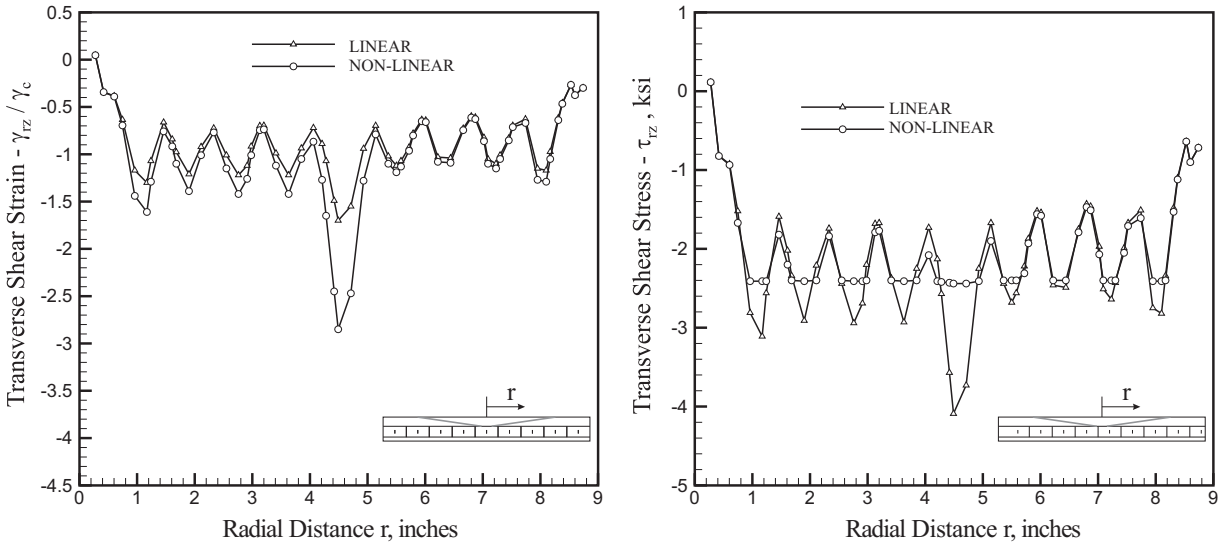
Figure 13. (a) Shear strain, γ_{rz}, and (b) shear stress, τ_{rz}, variations obtained from the current analysis for a sandwich under prescribed displacement.

is subjected to a displacement of $u_x = 0.2$ in. Under the influence of the prescribed displacement, the effective strain inside the adhesive exceeds the critical strain, thereby triggering the nonlinear material response. The transverse shear strain, γ_{rz}, and stress, σ_{rz}, inside the adhesive along the x-axis are shown in Figure 13. Since the effective strain in certain regions exceeds the critical value of $\gamma_c = 0.04$, the elastic modulus in those regions gets degraded. This leads to higher strain values in comparison to the
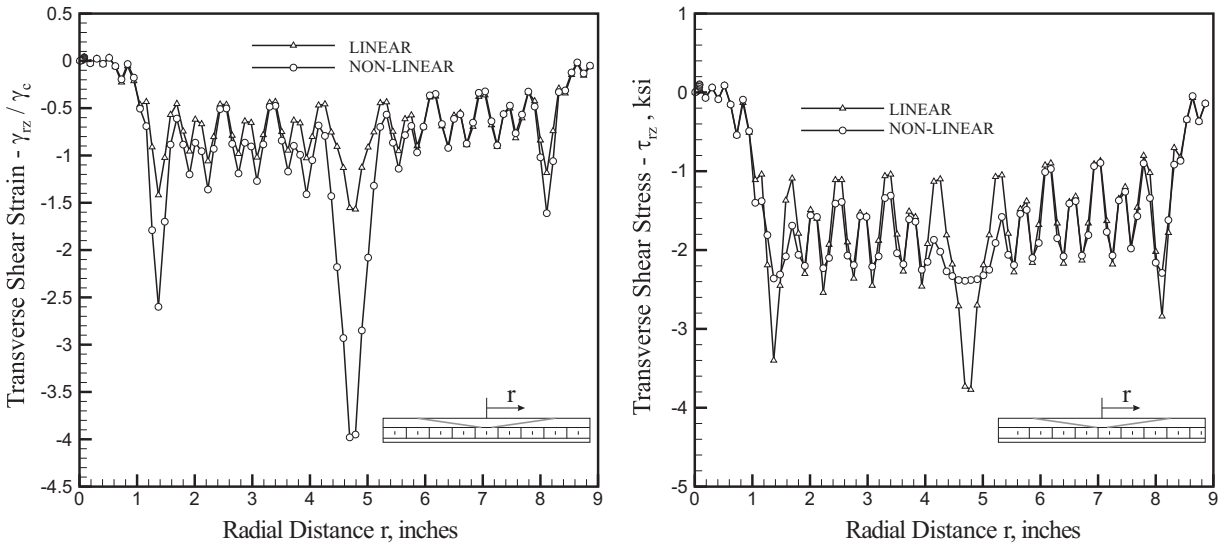
Figure 14. (a) Shear strain, γ_{rz}, and (b) shear stress, τ_{rz}, variations obtained from AN-SYS for a sandwich under prescribed displacement.

linear response, reduced stresses in these regions, and an additional load carried by the face sheet in the undamaged region. As shown in Figure 14, the results from ANSYS show a similar trend.

7. Conclusion

An analysis tool for scarf repair analysis of composite laminates and sandwich panels has been developed. Apart from analyzing two-dimensional scarf joints, the current tool can be used for three-dimensional analysis of scarf repair. Composite laminates with single-sided or double-sided repairs and sandwich panels with complete or partial repairs of the top face sheet can be analyzed. The analysis takes into account both geometric and material nonlinearity. The loading, material properties, and panel geometry can be arbitrary. Although computationally efficient, the stress and strain fields can be accurately predicted. Depending on the type and magnitude of loading, there can be a considerable difference between the linear and nonlinear solutions.

References

[Bair et al. 1991] D. L. Bair, P. O. Hudson, and G. R. Ghanimati, "Analysis and repair of damaged composite laminates", pp. 2264–2278 in *How concept becomes reality: 36th International SAMPE Symposium and Exhibition* (San Diego, CA, 1991), vol. 2, edited by J. Stinson et al., SAMPE, Covina, CA, 1991.

[Baker et al. 1999] A. A. Baker, R. J. Chester, G. R. Hugo, and T. C. Radtke, "Scarf repairs to highly strained graphite/epoxy structure", *Int. J. Adhes. Adhes.* **19**:2–3 (1999), 161–171.

[Barut et al. 2001] A. Barut, E. Madenci, J. Heinrich, and A. Tessler, "Analysis of thick sandwich construction by a {3, 2}-order theory", *Int. J. Solids Struct.* **38**:34–35 (2001), 6063–6077.

[Campilho et al. 2007] R. D. S. G. Campilho, M. F. S. F. de Moura, and J. J. M. S. Domingues, "Stress and failure analyses of scarf repaired CFRP laminates using a cohesive damage model", *J. Adhes. Sci. Technol.* **21**:9 (2007), 855–870.

[Carpenter 1973] W. Carpenter, "Finite element analysis of bonded connections", *Int. J. Numer. Methods Eng.* **6**:3 (1973), 450–451.

[Cook and Tessler 1998] G. M. Cook and A. Tessler, "A {3, 2}-order bending theory for laminated composite and sandwich beams", *Compos. B Eng.* **29**:5 (1998), 565–576.

[Das et al. 2005] M. Das, A. Barut, E. Madenci, and D. R. Ambur, "Complete stress field in sandwich panels with a new triangular finite element of single-layer theory", *Comput. Methods Appl. Mech. Eng.* **194**:27–29 (2005), 2969–3005.

[Das et al. 2006] M. Das, A. Barut, E. Madenci, and D. R. Ambur, "A triangular plate element for thermo-elastic analysis of sandwich panels with a functionally graded core", *Int. J. Numer. Methods Eng.* **68**:9 (2006), 940–966.

[Du et al. 2004] J. Du, F. T. Salmon, and A. V. Pocius, "Modeling of cohesive failure processes in structural adhesive bonded joints", *J. Adhes. Sci. Technol.* **18**:3 (2004), 287–299.

[Erdogan and Ratwani 1971] F. Erdogan and M. Ratwani, "Stress distribution in bonded joints", *J. Compos. Mater.* **5**:3 (1971), 378–393.

[Gunnion and Herszberg 2006] A. J. Gunnion and I. Herszberg, "Parametric study of scarf joints in composite structures", *Compos. Struct.* **75**:1–4 (2006), 364–376.

[Harman and Wang 2006] A. B. Harman and C. H. Wang, "Improved design methods for scarf repairs to highly strained composite aircraft structure", *Compos. Struct.* **75**:1–4 (2006), 132–144.

[Hart-Smith 1973] L. J. Hart-Smith, "Adhesive-bonded scarf and stepped-lap joints", report NASA-CR-112237, NASA, 1973, Available at http://tinyurl.com/59wc5s.

[Johnson 1989] C. L. Johnson, "Effect of ply stacking sequence on stress in a scarf joint", *AIAA J.* **27**:1 (1989), 79–86.

[Kumar et al. 2006] S. B. Kumar, I. Sridhar, S. Sivashanker, S. O. Osiyemi, and A. Bag, "Tensile failure of adhesively bonded CFRP composite scarf joints", *Mater. Sci. Eng. B* **132**:1–2 (2006), 113–120.

[Mortensen and Thomsen 1997] F. Mortensen and O. T. Thomsen, "Simplified linear and non-linear analysis of stepped and scarfed adhesive-bonded lap-joints between composite laminates", *Compos. Struct.* **38**:1–4 (1997), 281–294.

[Odi and Friend 2002] R. A. Odi and C. M. Friend, "A comparative study of finite element models for the bonded repair of composite structures", *J. Reinf. Plast. Compos.* **21**:4 (2002), 311–332.

[Soutis and Hu 1997] C. Soutis and F. Z. Hu, "Repair design of composites and efficiency of scarf patch repairs", pp. 395–404 in *Proceedings of the 11th International Conference on Composite Materials (ICCM-11)* (Gold Coast, Queensland), vol. VI, edited by M. L. Scott, Woodhead Publishing, Cambridge, 1997.

[Tomblin et al. 2004] J. S. Tomblin, L. Salah, J. M. Welch, and M. D. Borgman, "Bonded repair of aircraft composite sandwich structures", Report DOT/FAA/AR-03/74, US FAA, 2004, Available at http://www.tc.faa.gov/its/worldpac/techrpt/ar03-74.pdf.

[Wang and Gunnion 2008] C. H. Wang and A. J. Gunnion, "On the design methodology of scarf repairs to composite laminates", *Compos. Sci. Technol.* **68**:1 (2008), 35–46.

MANABENDRA DAS: mdas@email.arizona.edu
Department of Aerospace and Mechanical Engineering, The University of Arizona, 1130 N. Mountain Avenue, Tucson, AZ 85721, United States

ERDOGAN MADENCI: madenci@email.arizona.edu
Department of Aerospace and Mechanical Engineering, The University of Arizona, 1130 N. Mountain Avenue, Tucson, AZ 85721, United States

DAMODAR R. AMBUR: damodar.r.ambur@nasa.gov
Research and Technology Directorate, NASA Langley Research Center, Hampton, VA 23681-2199, United States

CRACK FRONT POSITION AND CRACK BACK POSITION TECHNIQUES FOR EVALUATING THE *T*-STRESS AT CRACK TIP USING FUNCTIONS OF A COMPLEX VARIABLE

Y. Z. CHEN, Z. X. WANG AND X. Y. LIN

In this paper, the crack front position and the crack back position techniques for evaluating the *T*-stress using complex variables are suggested. In the crack front technique, an expression for stress components in the crack front position is expressed through a complex variable. The limit value of the expression from the crack front position will give the *T*-stress. In the crack back technique, the other expression of stress components in the crack back position is expressed through the complex variable. The limit value of the expression from the crack back position will give the *T*-stress. The suggested techniques are used to evaluate *T*-stress in the arc crack and the curved crack problems. It is found from a detailed derivation that both techniques give the same result in the crack problem. Numerical examples are carried out for two problems: an elliptic crack with a central crack and a curved crack with parabolic configuration.

1. Introduction

The *T*-stress term at the vicinity of a crack tip was introduced in earlier years [Williams 1957; Rice 1974]. The *T*-stress term may affect the plastic zone ahead of crack tip [Larsson and Carlsson 1973; Betegon and Hancock 1991]. In addition, the *T*-stress has significant influence on the directional stability for the crack growth path [Rice 1974; Melin 2002]. A maximum tensile stress criterion for the onset of crack growth was suggested, which considers the role of the stress intensity factors and *T*-stress [Smith et al. 2006]. The *T*-stress before and after crack kinking in two-dimensional elastic solids was studied [Li and Xu 2007]. Contributions from the *T*-stress before crack kinking to the *T*-stress and stress intensity factors of the kinked crack are clearly described.

A variety of methods were used to evaluate the *T*-stress. The Eshelby technique was used [Kfouri 1998]. The *T*-stress evaluation is completed by using the weight function method [Sham 1989; 1991; Chen 1997]. The boundary collocation method and the weight function were developed to evaluate the *T*-stress [Fett 1997; 1998a; 1998b; 2001; Fett and Rizzi 2005].

The finite element method was used to evaluate the *T*-stress in crack problems [Ayatollahi et al. 1998; Chen et al. 2001]. A hybrid finite element at the vicinity of the crack tip was suggested [Tong et al. 1973; Cheung and Chen 1991; Karihaloo and Xiao 2001; Xiao and Karihaloo 2002; Xiao et al. 2004]. The formulation of a hybrid finite element depends on the Williams expansion. The element is embedded in the usual finite elements. Once the problem is solved, the higher-order terms as well as the *T*-stress in the expansion are obtainable. Using the HCE (hybrid crack element), the higher-order terms in the stress distribution of a three-point bend beam are evaluated [Karihaloo and Xiao 2001]. The problem for an edge crack in a finite plate with wedge force on the crack face was studied [Xiao and Karihaloo 2002].

The problem was reduced to a problem of a traction-free edge crack with loading on the outer boundary. The usage of the Williams expansion and the boundary collocation method gave the final solution.

A stress difference method was developed to evaluate the T-stress in the crack problem [Yang and Ravi-Chandar 1999]. It was proved that a limit of the difference between two normal stress components ahead of a crack tip would give the T-stress.

Using the dislocation distribution method and the singular integral equation, several T-stress problems were solved [Broberg 2005]. Those problems include the problems of: (i) two collinear cracks, (ii) an edge crack, and (iii) cracks emanating from a circular hole. A Fredholm integral equation was used to evaluate the T-stress in the multiple crack problems [Chen 1994]. The solved problems were limited to the line crack case. In addition, a compendium of the T-stress solutions in the crack problems was carried out [Sherry et al. 1995].

From the methodology for evaluating the T-stress, researchers suggested two techniques for obtaining the T-stress in the line crack case. In the stress difference method, the T-stress is obtained from the stress difference in crack front position [Yang and Ravi-Chandar 1999]. In the mode I fracture case, the T-stress evaluation was related to a stress evaluation in the crack back position [Ayatollahi et al. 1998]. The mentioned derivations were related to the real analysis only. It is seen that those methods are not easy to use in some complicated cases, for example, for evaluating the T-stress in the curved crack problem.

It is known that in most cases the complex potentials in the plane elasticity crack problem can be formulated successfully [Savruk 1981; Chen and Lin 2006]. In addition, the stress components can be expressed by the complex potentials explicitly. Therefore, it is a particular advantage to use a complex variable for evaluating the SIF (stress intensity factor) as well as the T-stress. In this paper, the crack front position and crack back position techniques for evaluating T-stress using the complex variable are suggested. In the crack front technique, an expression for stress components in the crack front position is expressed through the complex variable. The limit value of the expression from the crack front position will give the T-stress. In addition, in the crack back technique, the other expression for stress components in the crack back position is expressed through the complex variable. The limit value of the expression from the crack back position will give the T-stress. It is found from a detailed derivation that both techniques give the same result in the crack problem.

2. Basic equations in the crack front position and the crack back position techniques

In the crack front position technique, the T-stress is evaluated in the front position of the crack. In addition, in the crack back position technique, the T-stress is evaluated in the back position of the crack. The two techniques with usage of a complex variable are introduced below.

2.1. *The stress expansions in the vicinity of crack tip.* The stress distribution near a crack tip under the traction-free crack face was investigated early on by Williams [1957]. A little modification for the Williams expansion is suggested below. It is assumed that the crack face has the following loadings (Figure 1)

$$\sigma_y^+ = \sigma_y^- = p_c, \qquad \sigma_{xy}^+ = \sigma_{xy}^- = q_c. \tag{1}$$

From the Williams expansion, the stresses at the crack tip area can be expressed as

$$\begin{bmatrix} \sigma_x & \sigma_{xy} \\ \sigma_{xy} & \sigma_y \end{bmatrix} = \frac{K_I}{\sqrt{2\pi r}} \begin{bmatrix} f_{11}(\theta) & f_{12}(\theta) \\ f_{12}(\theta) & f_{22}(\theta) \end{bmatrix} + \frac{K_{II}}{\sqrt{2\pi r}} \begin{bmatrix} g_{11}(\theta) & g_{12}(\theta) \\ g_{12}(\theta) & g_{22}(\theta) \end{bmatrix} + \begin{bmatrix} T & q_c \\ q_c & p_c \end{bmatrix}, \tag{2}$$

where the first two terms in the expansion form are singular at the crack tip, K_I, K_{II} denote the mode I and mode II stress intensity factors respectively, and the functions $f_{ij}(\theta)$, $g_{ij}(\theta)$ represent the angular distributions of stresses at crack tip. In Equation (2), the third term is finite and bounded. The term T is denoted as the T-stress and can be regarded as the stress acting parallel to the crack flanks. In Equation (1) the term $O(r^{1/2})$ has been neglected for clarity. In addition, the angular distribution can be expressed as [Williams 1957]

$$\begin{bmatrix} f_{11} \\ f_{12} \\ f_{22} \end{bmatrix} = \cos(\theta/2) \begin{bmatrix} 1 - \sin(\theta/2)\sin(3\theta/2) \\ \sin(\theta/2)\cos(3\theta/2) \\ 1 + \sin(\theta/2)\sin(3\theta/2) \end{bmatrix}, \quad \begin{bmatrix} g_{11} \\ g_{12} \\ g_{22} \end{bmatrix} = \begin{bmatrix} -\sin(\theta/2)[2 + \cos(\theta/2)\cos(3\theta/2)] \\ \cos(\theta/2)[1 - \sin(\theta/2)\sin(3\theta/2)] \\ \sin(\theta/2)\cos(\theta/2)\cos(3\theta/2) \end{bmatrix}. \tag{3}$$

Clearly, substituting $\theta = \pm\pi$ into Equation (2) will yield the stresses $\sigma_y = p_c$ and $\sigma_{xy} = q_c$, which are applied on the crack face.

Note that Equation (2) represents a pattern of stress distribution at the vicinity of crack tip. It is easily seen that the stress field defined by Figure 1 was solely determined by two factors: (1) the tractions $\sigma_y^+ = \sigma_y^- = p_c$, $\sigma_{xy}^+ = \sigma_{xy}^- = q_c$ applied on the crack face, (2) the tractions applied along the outer boundary CDEFGH in Figure 1. Therefore, the tractions $\sigma_y^+ = \sigma_y^- = p_c$, $\sigma_{xy}^+ = \sigma_{xy}^- = q_c$ applied on the crack face cannot alone determine the K_I, K_{II} and T values. Alternatively, there is no definite relation between (i) the tractions $\sigma_y^+ = \sigma_y^- = p_c$, $\sigma_{xy}^+ = \sigma_{xy}^- = q_c$ applied on the crack face and (ii) the stress field and the T-stress at the crack tip. In this study, it is assumed that p_c and q_c are given beforehand. In this case, the K_I, K_{II} and T values will be determined by the tractions applied on the boundary CDEFGH.

Figure 1. A finite cracked plate with loadings on the crack face.

Let $\theta = 0$ and $r = s_1$ in Figure 1, from Equations (2), (3), we have

$$\sigma_x = \frac{K_I}{\sqrt{2\pi s_1}} + T + O(s_1^{1/2}), \qquad \sigma_y = \frac{K_I}{\sqrt{2\pi s_1}} + p_c + O(s_1^{1/2}). \tag{4}$$

Therefore, from Equation (4), the following equation is obtained

$$T = \lim_{s_1 \to 0} (\sigma_x - \sigma_y) + p_c \qquad \text{or} \qquad T = -\lim_{s_1 \to 0} (\sigma_y - \sigma_x) + p_c \tag{5}$$

This equation will be used for the crack front position technique. In fact, this equation was suggested in [Yang and Ravi-Chandar 1999].

The necessity for introducing Equations (1), (2), and (5) can be seen from an example described in Section 5. In the example, the T-stress in the curve crack problem is evaluated. In the problem, the stress field of the original problem must be decomposed into the uniform stress field and the perturbation stress field. In the perturbation stress field, the crack face is applied by the normal and shear tractions. Clearly, for investigating the T-stress in the perturbation field (in Figure 2b), the usage of Equations (1), (2), and (5) is necessary simply because the normal and shear tractions are applied on the crack face. When some solutions to the traction-free condition on the crack face are available, we simply let $p_c = 0$ and $q_c = 0$ in the relevant equations.

Alternatively, let $\theta = \pi$ and $r = s_2$ in Figure 1, and from Equations (2), (3) we have

$$\sigma_x^+ = -\frac{2K_{II}}{\sqrt{2\pi s_2}} + T + O(s_2^{1/2}), \qquad \sigma_y^+ = p_c + O(s_2^{1/2}). \tag{6}$$

In addition, let $\theta = -\pi$ and $r = s_2$, and we have

$$\sigma_x^- = \frac{2K_{II}}{\sqrt{2\pi s_2}} + T + O(s_2^{1/2}), \qquad \sigma_y^- = p_c + O(s_2^{1/2}). \tag{7}$$
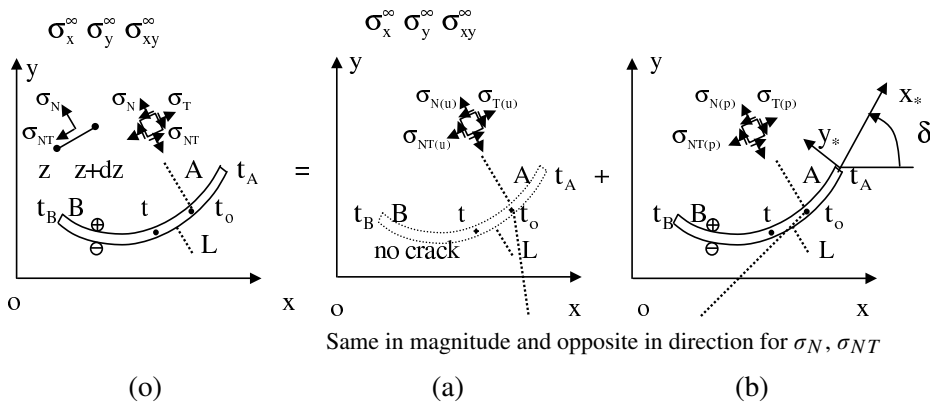
Figure 2. Superposition method: (o) the original field, a curved crack in an infinite plate with the remote loading $\sigma_y^\infty = p_2$, or $\sigma_x^\infty = p_1$, or $\sigma_{xy}^\infty = q$; (a) the uniform field, a perfect plate with remote loading $\sigma_y^\infty = p_2$, or $\sigma_x^\infty = p_1$, or $\sigma_{xy}^\infty = q$, the subscript u denoting the uniform field; (b) the perturbation field, a curved crack with loading on the crack face, the subscript p denoting the perturbation field.

In Equations (6) and (7), σ_x^+, $\sigma_y^+(\sigma_x^-, \sigma_y^-)$ denote the stress component along the upper (lower) side, respectively (Figure 1). Therefore, from Equations (6) and (7), the following equation is obtained:

$$T = \lim_{s_2 \to 0}\{[(\sigma_x^+ + \sigma_y^+) + (\sigma_x^- + \sigma_y^-)]/2\} - p_c \quad \text{or} \quad T = \lim_{s_2 \to 0}\{(\sigma_x^+ + \sigma_x^-)/2\}. \tag{8}$$

Equation (8) can be used for the general case, which is first suggested by us in this paper.

In the case of a mode I fracture, or $K_{II} = 0$, the above-mentioned equations can be reduced to

$$T = \lim_{s_2 \to 0}\{\sigma_x^+ + \sigma_y^+\} - p_c = \lim_{s_2 \to 0}\{\sigma_x^- + \sigma_y^-\} - p_c \quad \text{or} \quad T = \lim_{s_2 \to 0}\sigma_x^+ = \lim_{s_2 \to 0}\sigma_x^-. \tag{9}$$

This equation will be used in the crack back position technique. In fact, Equation (9) was suggested in [Ayatollahi et al. 1998].

2.2. T-stress expressions in crack front position and crack back position techniques using a complex variable.

The following analysis depends on the complex variable function method in plane elasticity [Muskhelishvili 1953]. In this method, the stresses $(\sigma_x, \sigma_y, \sigma_{xy})$, the resultant forces (X, Y), and the displacements (u, v) are expressed in terms of complex potentials $\phi(z)$, $\psi(z)$, $\Phi(z) = \phi'(z)$, and $\Psi(z) = \psi'(z)$ such that

$$\sigma_x + \sigma_y = 4\,\text{Re}\,\Phi(z), \tag{10}$$

$$\sigma_y - i\sigma_{xy} = 2\,\text{Re}\,\Phi(z) + z\overline{\Phi'(z)} + \overline{\Psi(z)}, \tag{11}$$

$$\sigma_y - \sigma_x + 2i\sigma_{xy} = 2(\bar{z}\Phi'(z) + \Psi(z)), \tag{12}$$

or

$$\sigma_y - \sigma_x - 2i\sigma_{xy} = 2(z\overline{\Phi'(z)} + \overline{\Psi(z)}), \tag{13}$$

$$f = -Y + iX = \phi(z) + z\overline{\phi'(z)} + \overline{\psi(z)}, \tag{14}$$

$$2G(u + iv) = \kappa\phi(z) - z\overline{\phi'(z)} - \overline{\psi(z)}, \tag{15}$$

where $z = x + iy$ denotes a complex variable, G is the shear modulus of elasticity, $\kappa = (3 - v)/(1 + v)$ is for the plane stress problems, $\kappa = 3 - 4v$ is for the plane strain problems, and v is the Poisson's ratio. In the present study, the plane strain condition is assumed thoroughly.

It is assumed that a concrete crack problem, for example, the problem shown by Figure 1 has been solved. Alternatively, the relevant complex potentials are obtained in advance. Therefore, from Equations (5) and (12), we have

$$T = -\,\text{Re}(\sigma_y - \sigma_x + 2i\sigma_{xy})|_{z=s_1, s_1 \to 0} + p_c$$
$$= -2\,\text{Re}(\bar{z}\Phi'(z) + \Psi(z))|_{z=s_1, s_1 \to 0} + p_c, \tag{16}$$

(see Figure 1). This is the formula for evaluating the T-stress in the crack front position technique.

In addition, from Equations (8) and (10) we have (Figure 1)

$$T = \lim_{s_2 \to 0}\{[(\sigma_x^+ + \sigma_y^+) + (\sigma_x^- + \sigma_y^-)]/2\} - p_c$$
$$= 2\,\text{Re}(\Phi^+(z) + \Phi^-(z))|_{z=-s_2, s_2 \to 0} - p_c. \tag{17}$$

This is the formula for evaluating the T-stress in the crack back position technique.

3. Closed form solution for the *T*-stress in an arc crack using the crack front position and crack back position techniques

A closed form solution for the *T*-stress in the arc crack by using the crack front position and crack back position techniques is introduced below. The configuration of the arc crack is shown in Figure 3. The arc crack has a spanning angle 2α with the remote loading σ_x^∞, σ_y^∞, σ_{xy}^∞. In addition to two complex potentials $\Phi(z)$ and $\Psi(z)$, the following complex potential $\Omega(z)$ is introduced:

$$\Omega(z) = \bar{\Phi}\left(\frac{1}{z}\right) - \frac{1}{z}\bar{\Phi}'\left(\frac{1}{z}\right) - \frac{1}{z^2}\bar{\Psi}\left(\frac{1}{z}\right). \tag{18}$$

Here and after, for example, the following definition is used [Muskhelishvili 1953]

$$\bar{\Phi}\left(\frac{1}{z}\right) = \overline{\Phi\left(\frac{1}{\bar{z}}\right)}. \tag{19}$$

After some manipulation, the stress components in (r, θ) coordinates can be expressed as [Muskhelishvili 1953]

$$\sigma_r + \sigma_\theta = 4\,\mathrm{Re}\,\Phi(z), \tag{20}$$

$$\sigma_r - \sigma_\theta - 2i\sigma_{r\theta} = -2\Phi(z) + 2\bar{\Omega}\left(\frac{1}{z}\right) + 2z\left(z - \frac{1}{\bar{z}}\right)\Psi(z). \tag{21}$$

For the arc crack problem under the remote loading σ_x^∞, σ_y^∞, σ_{xy}^∞, there is a solution as follows [Muskhelishvili 1953]:

$$\Phi(z) = F_1(z) + F_2(z), \qquad \Omega(z) = F_1(z) + F_2(z), \tag{22}$$
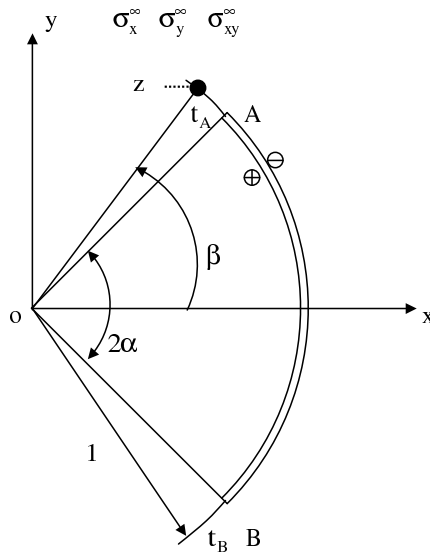
Figure 3. An arc crack.

where

$$F_1(z) = \frac{1}{2X(z)}\left(C_o z + C_1 + \frac{D_1}{z} + \frac{D_2}{z^2}\right), \qquad F_2(z) = \frac{D_o}{2} + \frac{\bar{\Gamma}_1}{2z^2}, \tag{23}$$

$$
\begin{aligned}
C_o &= \frac{1}{2}(\Gamma_1 - \bar{\Gamma}_1)\sin^2(\alpha/2) + \frac{4\Gamma + (\Gamma_1 + \bar{\Gamma}_1)\sin^2(\alpha/2)\cos^2(\alpha/2)}{2(1 + \sin^2(\alpha/2))}, \\
C_1 &= -C_o \cos\alpha, \\
D_o &= 2\Gamma - C_o, \\
D_1 &= -\bar{\Gamma}_1 \cos\alpha, \\
D_2 &= \bar{\Gamma}_1,
\end{aligned}
\tag{24}
$$

$$\Gamma = \frac{\sigma_x^\infty + \sigma_y^\infty}{4}, \qquad \Gamma_1 = \frac{\sigma_y^\infty - \sigma_x^\infty}{2} + i\sigma_{xy}^\infty, \tag{25}$$

$$X(z) = \sqrt{(z - \exp(-i\alpha))(z - \exp(i\alpha))} \quad \text{(taking the branch } \lim_{z \to \infty} X(z)/z = 1). \tag{26}$$

The *T*-stress at the crack tip *A* is evaluated by using the crack front position technique. Similar to Equation (16), the *T*-stress at the crack tip *A* can be evaluated by (Figure 3)

$$T_A = -\operatorname{Re}\{\sigma_r - \sigma_\theta - 2i\sigma_{r\theta}\}|_{z=\exp(i\beta),\beta>\alpha,\beta\to\alpha} + p_c, \tag{27}$$

where the point $z = \exp(i\beta)$ with $\beta > \alpha$ is actually located in front of the crack tip A (Figure 3).

Considering (i) the traction-free crack face, where $p_c = 0$, (ii) $z - 1/\bar{z} = 0$ for $z = \exp(i\beta)$, and (iii) substituting Equation (21) into (27), the above-mentioned equation can be reduced to

$$T_A = 2\operatorname{Re}\left(\Phi(z) - \bar{\Omega}\left(\frac{1}{z}\right)\right)_{z=\exp(i\beta),\beta>\alpha,\beta\to\alpha}. \tag{28}$$

Substituting Equations (22), (23), and (24) into (28) yields

$$
\begin{aligned}
T_A = 2\operatorname{Re}(D_o + \bar{\Gamma}_1 \exp(-2i\alpha)) = \sigma_x^\infty\left(-\cos 2\alpha + \frac{(1 - \cos\alpha)(3 + \cos\alpha)}{2(3 - \cos\alpha)}\right) \\
+ \sigma_y^\infty\left(\cos 2\alpha + \frac{(1 - \cos\alpha)^2}{2(3 - \cos\alpha)}\right) - 2\sigma_{xy}^\infty \sin 2\alpha, \quad (29)
\end{aligned}
$$

which was obtained previously by using a different method [Chen 2000].

Since $\sigma_x + \sigma_y (= \sigma_r + \sigma_\theta)$ is invariant, similar to Equation (17), the *T*-stress in the crack back position technique can be defined as

$$T_A = \{[(\sigma_r^+ + \sigma_\theta^+) + (\sigma_r^- + \sigma_\theta^-)]/2\}|_{t=\exp(i\beta),\beta<\alpha,\beta\to\alpha} - p_c. \tag{30}$$

Considering the traction-free crack face, where $p_c = 0$, and substituting Equations (20) and (22) into (30), the above-mentioned equation can be reduced to

$$T_A = 2\operatorname{Re}(\Phi^+(t) + \Phi^-(t))|_{t=\exp(i\beta),\beta<\alpha,\beta\to\alpha}. \tag{31}$$

In the crack back position, or for $t = \exp(i\beta)$, where $\beta < \alpha$, we have $X^+(t) = -X^-(t)$, where $X^+(t)$, $X^-(t)$ denotes the value of $X(z)$ at $z = t^+$, the positive side, and $z = t^-$, the negative side, respectively. Considering this point and substituting (22) into (31) yields the same result as shown by Equation (29):

$$T_A = 2\operatorname{Re}(D_o + \bar{\Gamma}_1 \exp(-2i\alpha)). \tag{29}$$

4. Evaluation of the *T*-stress for an elliptic plate with a central crack and normal loading on the contour

In the following analysis, we can let $\omega(z) = z\bar{\phi}'(z) + \bar{\psi}(z)$, $\Omega(z) = \omega'(z)$. From Equations (10)–(15), the stresses $(\sigma_x, \sigma_y, \sigma_{xy})$, the resultant forces (X, Y), and the displacements (u, v) are expressed in terms of the complex potentials $\phi(z)$ and $\omega(z)$ in the following form:

$$\sigma_x + \sigma_y = 4\operatorname{Re}\Phi(z),$$
$$\sigma_x - \sigma_y + 2i\sigma_{xy} = 2\overline{\Phi(z)} - 2(z - \bar{z})\overline{\Phi'(z)} - 2\Omega(\bar{z}), \tag{32}$$

$$f = -Y + iX = \phi(z) + (z - \bar{z})\overline{\phi'(z)} + \omega(\bar{z}), \tag{33}$$

$$2G(u + iv) = \kappa\phi(z) - (z - \bar{z})\overline{\phi'(z)} - \omega(\bar{z}). \tag{34}$$

For an elliptic plate with a crack under the condition of symmetric loading (Figure 4), the complex potentials can be expressed in the form [Chen 1983]:

$$\phi(z) = \phi_1(z) + \phi_2(z), \tag{35}$$
$$\omega(z) = \omega_1(z) + \omega_2(z), \tag{36}$$

where

$$\phi_1(z) = \omega_1(z) = \sum_{k=1}^{M} a_k X(z) z^{2k-2}, \tag{37}$$

$$\phi_2(z) = -\omega_2(z) = \sum_{k=1}^{M} b_k z^{2k-1}, \tag{38}$$

$$X(z) = \sqrt{z^2 - a^2} \quad \text{(taking the branch } \lim_{z \to \infty} X(z)/z = 1\text{)}. \tag{39}$$
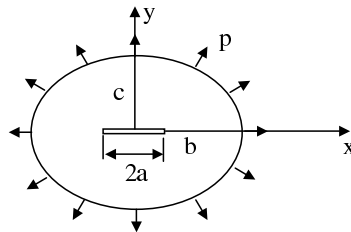
Figure 4. An elliptic plate with a central crack and normal loading p.

In Equations (37) and (38), a_k and b_k $(k = 1, 2, \ldots, M)$ are real undetermined coefficients. The complex potentials shown by Equations (37) and (38) satisfy the traction-free condition [Chen 1983]. Therefore, only the condition on the elliptic boundary needs to be satisfied for the complex potentials. The eigenexpansion variational method is used to evaluate the coefficients a_k and b_k $(k = 1, 2, \ldots, M)$ [Chen 1983]. In Equations (37) and (38), we can denote

$$\Phi_1(z) = \phi_1'(z) = \Omega_1(z) = \omega_1'(z), \tag{40}$$

$$\Phi_2(z) = \phi_2'(z) = -\Omega_2(z) = -\omega_2'(z). \tag{41}$$

Note that, for $z = s_1$, $s_1 > a$ and $s_1 \to a$, we have $\overline{\Phi_1(z)} - \Omega_1(\bar{z}) = 0$ and $\overline{\Phi_2(z)} - \Omega_2(\bar{z}) = 2\Phi_2(z)$. If the crack front position method is used, from Equations (5) and (32), and $p_c = 0$, we have

$$T = \lim_{z=s_1,\, s_1>a,\, s_1\to a} (\sigma_x - \sigma_y) = 4 \lim_{z=s_1,\, s_1>a,\, s_1\to a} \Phi_2(z) = 4\sum_{k=1}^{M} b_k(2k-1)a^{2k-2}. \tag{42}$$

If the crack back position method is used, from Equations (8) and (32), and $p_c = 0$, we have

$$T = \lim_{z=s_2,\, s_2<a,\, s_2\to a} \{[(\sigma_x^+ + \sigma_y^+) + (\sigma_x^- + \sigma_y^-)]/2\} = \lim_{z=s_2,\, s_2<a,\, s_2\to a} 2\,\mathrm{Re}\{\Phi^+(z) + \Phi^-(z)\}. \tag{43}$$

For $z = s_2$, $s_2 < a$ and $s_2 \to a$, both $\Phi_1^+(z)$ and $\Phi_1^-(z)$ take pure imaginary values and $\Phi_2^+(z) = \Phi_2^-(z)$ takes a real value. Therefore, from Equations (43), the same result is obtainable

$$T = 4\sum_{k=1}^{M} b_k(2k-1)a^{2k-2}. \tag{44}$$

For the normal loading p (Figure 4), we choose $M = 15$ in Equations (37) and (38) in the eigenexpansion variational method [Chen 1983]. Finally, the computed results for the T-stress is expressed as

$$T = H(c/b, a/b)p, \tag{45}$$

which are tabulated in Table 1. From Table 1 we see that, for a circular plate $(c/b = 1)$ with a central crack, we have $T = -0.0199P$ for $a/b = 0.1$, which is a rather small value. However, we have $T = -3.8334p$ for $a/b = 0.9$, which is a rather large value. It is also seen from tabulated results that the deviation of the computed results for the $c/b = 1$ case from previously obtained results [Fett 2001] is rather small.

5. Evaluation for the T-stress in a curved crack using the crack front position and crack back position techniques

The T-stress in the curved crack problem can also be evaluated with the usage of two techniques and the relevant complex potentials. In addition, one numerical example is presented below.

For evaluating the T-stress at the crack tip, it is suitable to use the superposition method. The original problem is shown in Figure 2o. Without losing generality, it is assumed that the remote loading is $\sigma_y^\infty = p_2$, or $\sigma_x^\infty = p_1$, or $\sigma_{xy}^\infty = q$. The original field can be considered as a superposition of a uniform field and a perturbation field, which are shown by Figure 2a–b, respectively. The T-stress at the crack

$a/b =$	0.1	0.2	0.3	0.4	0.5	0.6	0.7	0.8	0.9
$c/b =$									
0.5	-0.0529	-0.1701	-0.2713	-0.3012	-0.2418	-0.0982	0.0904	0.1489	-0.9572
1.0	-0.0199	-0.0778	-0.1705	-0.2960	-0.4603	-0.6870	-1.0447	-1.7523	-3.8334
$1.0^\dagger$	-0.0216	-0.0806	-0.1712	-0.2937	-0.4568	-0.6868	-1.0515	-1.7589	-3.8466
1.5	-0.0114	-0.0464	-0.1079	-0.2023	-0.3439	-0.5636	-0.9370	-1.6859	-3.5710
2.0	-0.0090	-0.0373	-0.0887	-0.1713	-0.3012	-0.5118	-0.8803	-1.6178	-3.2109

Table 1. Nondimensional T-stresses $H(c/b, a/b)$ for an elliptic plate with a central crack and the normal loading p on contour (see Figure 4 and Equation (45)). † From an equation in [Fett 2001].

tip A is denoted by T_A, which is composed of two portions and can be expressed as

$$T_A = T_{A(u)} + T_{A(p)}, \tag{46}$$

where $T_{A(u)}$ and $T_{A(p)}$ are derived from the uniform field and the perturbation field, respectively.

The uniform field is defined for an infinite perfect plate with the remote loading $\sigma_y^\infty = p_2$, $\sigma_x^\infty = p_1$, or $\sigma_{xy}^\infty = q$ (Figure 2a). This stress field is easy to evaluate. The stress components along the prospective site of the crack are denoted by $\sigma_{N(u)}$, $\sigma_{T(u)}$, $\sigma_{NT(u)}$, where the subscript (u) denotes the stress components defined in the uniform field. Clearly, for the right crack tip A, we have the following T-stress contribution (Figure 2a):

$$T_{A(u)} = \sigma_{T(u), \text{ at point } t_A} = \sigma_{T(u)}(t_A). \tag{47}$$

In the notation for $\sigma_{T(u)}(t_A)$, the subscript T denotes the stress in the T-direction, (u) represents the stress from the uniform field, and t_A denotes the location of a point for finding the T-stress.

In the following, the perturbation field for the curved crack is studied (Figure 2b). It was proved that the complex potentials for this field could be expressed as [Savruk 1981; Chen and Lin 2006]

$$\phi'(z) = \Phi(z) = \frac{1}{2\pi} \int_L \frac{g'(t)dt}{t - z}, \qquad \phi''(z) = \Phi'(z) = \frac{1}{2\pi} \int_L \frac{g'(t)dt}{(t - z)^2}, \tag{48}$$

$$\psi'(z) = \Psi(z) = \frac{1}{2\pi} \int_L \frac{\overline{g'(t)}d\bar{t}}{t - z} - \frac{1}{2\pi} \int_L \frac{\bar{t}g'(t)dt}{(t - z)^2}, \tag{49}$$

where $g'(t)$ denotes the dislocation distribution along the curved crack and is defined by

$$g'(t) = \frac{dg(t)}{dt}, \quad (t \in L, \ L - \text{the curved crack}). \tag{50}$$

In Equation (50), $g(t)$ is the COD (crack opening displacement) function defined by

$$g(t) = -\frac{2Gi}{\kappa + 1}\{(u(t) + iv(t))^+ - (u(t) + iv(t))^-\}, \quad (t \in L, \ L - \text{the curved crack}), \tag{51}$$

where $(u(t) + iv(t))^+ ((u(t) + iv(t))^-)$ denotes the displacement in the upper side (lower side) of the curved crack, respectively.

For the curved crack problem, a singular integral equation was suggested previously [Savruk 1981; Chen and Lin 2006]:

$$\frac{1}{\pi} \int_L \frac{g'(t)dt}{t - t_o} + M(t_o) = \sigma_{N(p)}(t_o) + i\sigma_{NT(p)}(t_o), \quad (t_o \in L), \tag{52}$$

where

$$M(t_o) = \frac{1}{2\pi} \int_L K_1(t, t_o)g'(t)dt + \frac{1}{2\pi} \int_L K_2(t, t_o)\overline{g'(t)}d\bar{t}, \tag{53}$$

L denotes the curved crack configuration, and

$$K_1(t, t_o) = \frac{d}{dt_o}\left\{\ln\frac{t - t_o}{\bar{t} - \bar{t}_o}\right\} = -\frac{1}{t - t_o} + \frac{1}{\bar{t} - \bar{t}_o}\frac{d\bar{t}_o}{dt_o}, \tag{54}$$

$$K_2(t, t_o) = -\frac{d}{dt_o}\left\{\frac{t - t_o}{\bar{t} - \bar{t}_o}\right\} = \frac{1}{\bar{t} - \bar{t}_o} - \frac{t - t_o}{(\bar{t} - \bar{t}_o)^2}\frac{d\bar{t}_o}{dt_o}. \tag{55}$$

For the perturbation field, the applied tractions on the crack face must be opposite to those from the uniform field (Figure 2a–b). Clearly, the right hand term in Equation (52) is defined by

$$\sigma_{N(p)}(t_o) + i\sigma_{NT(p)}(t_o) = -(\sigma_{N(u)}(t_o) + i\sigma_{NT(u)}(t_o)), (t_o \in L). \tag{56}$$

In addition, the dislocation distribution $g'(t)$ should satisfy the following single-valued condition of displacements [Savruk 1981; Chen and Lin 2006],

$$\int_L g'(t)dt = 0. \tag{57}$$

Substituting Equations (48) and (49) into (12) yields

$$\sigma_y - \sigma_x - 2i\sigma_{xy} = \frac{1}{\pi} \int_L \frac{g'(t)dt}{\bar{t} - \bar{z}} - \frac{1}{\pi} \int_L \frac{(t - z)\overline{g'(t)}d\bar{t}}{(\bar{t} - \bar{z})^2}. \tag{58}$$

In the vicinity of the right crack tip A, we can assume the coordinates Ax_*y_* (Figure 2b). In these coordinates, we have

$$(\sigma_y - \sigma_x - 2i\sigma_{xy})_* = (\sigma_y - \sigma_x - 2i\sigma_{xy})\exp(-2i\delta) = \left(\frac{1}{\pi} \int_L \frac{g'(t)dt}{\bar{t} - \bar{z}} - \frac{1}{\pi} \int_L \frac{(t - z)\overline{g'(t)}d\bar{t}}{(\bar{t} - \bar{z})^2}\right)\frac{d\bar{t}_A}{dt_A}, \tag{59}$$

with $d\bar{t}_A/dt_A = \exp(-2i\delta)$. It is convenient to introduce the following equality

$$\text{Re}\left(-\frac{1}{\pi} \int_L \frac{g'(t)dt}{t - z} + \frac{1}{\pi} \int_L \frac{\overline{g'(t)}\,d\bar{t}}{\bar{t} - \bar{z}}\right) = 0. \tag{60}$$

Therefore, from Equations (59) and (60) we have

$$(\sigma_y - \sigma_x)_* = \text{Re}\left\{\left(\frac{1}{\pi} \int_L \frac{g'(t)dt}{\bar{t} - \bar{z}} - \frac{1}{\pi} \int_L \frac{(t - z)\overline{g'(t)}d\bar{t}}{(\bar{t} - \bar{z})^2}\right)\frac{d\bar{t}_A}{dt_A}\right\}$$

$$+ \text{Re}\left(-\frac{1}{\pi} \int_L \frac{g'(t)dt}{t - z} + \frac{1}{\pi} \int_L \frac{\overline{g'(t)}d\bar{t}}{\bar{t} - \bar{z}}\right). \tag{61}$$

Similar to Equation (16), the T-stress in the perturbation field can be defined by

$$T_{A(p)} = -(\sigma_y - \sigma_x)_*|_{z \to t_A} + p_c, \tag{62}$$

where t_A denotes the complex value for the crack tip A, and $z \to t_A$ represents a limit from the crack front position. In this case, we have

$$p_c = \sigma_{N(p)}(t_A) = -\sigma_{N(u)}(t_A). \tag{63}$$

Substituting Equations (61) and (63) into (62) yields

$$T_{A(p)} = -\sigma_{N(u)}(t_A) - 2\operatorname{Re} M(t_A), \tag{64}$$

where the integral $M(t_A) = M(t_A)|_{t_o = t_A}$ has been defined by Equation (53). Finally, from Equations (46), (47), and (64), we have

$$T_A = T_{A(u)} + T_{A(p)} = \sigma_{T(u)}(t_A) - \sigma_{N(u)}(t_A) - 2\operatorname{Re} M(t_A). \tag{65}$$

A particular case is introduced below. It is assumed that there is a line crack in an infinite plate. In this case, from Equations (53), (54), and (55) we find $M(t_o) = 0$ and $M(t_A) = 0$, and Equation (65) can be reduced to

$$T_A = \sigma_{T(u)}(t_A) - \sigma_{N(u)}(t_A). \tag{66}$$

Therefore, the term $-2\operatorname{Re}(M(t_A))$ in Equation (65) represents the influence caused by curvature to the T-stress. For a straight-line crack, this term $-2\operatorname{Re}(M(t_A))$ is generally equal to zero.

On the other hand, the crack back technique is introduced below. From Equations (17) and (48), we have

$$T_{A(p)} = 2\operatorname{Re}\big(\Phi^+(t_o) + \Phi^-(t_o)\big)\big|_{t_o \to t_A} - \sigma_{N(p)}(t_A) = \operatorname{Re}\left(\frac{2}{\pi} \int_L \frac{g'(t)dt}{t - t_o}\right)_{t_o \to t_A} - \sigma_{N(p)}(t_A). \tag{67}$$

In Equation (67), the Plemelj formula is used for obtaining $\Phi^+(t_o)$ and $\Phi^-(t_o)$ [Muskhelishvili 1953].

Substituting Equation (52) into (67), the same result as shown by Equation (64) will be found. It is seen that the two techniques give the same result.

Similarly, at the left crack tip B we have

$$T_B = T_{B(u)} + T_{B(p)} = \sigma_{T(u)}(t_B) - \sigma_{N(u)}(t_B) - 2\operatorname{Re}\big(M(t_B)\big). \tag{68}$$

Once the solution for the function $g'(t)$ is obtained, the SIFs (stress intensity factors) at the right crack tip A and the left crack tip B can be evaluated by [Savruk 1981; Chen and Lin 2006]

$$\begin{aligned}
(K_1 - iK_2)_A &= -\sqrt{2\pi} \lim_{t \to t_A} \sqrt{|t - t_A|} g'(t), \\
(K_1 - iK_2)_B &= \sqrt{2\pi} \lim_{t \to t_B} \sqrt{|t - t_B|} g'(t).
\end{aligned} \tag{69}$$

To obtain the final solution, successive steps for evaluating the T-stresses and SIFs in the numerical solution are summarized as follows.

(i) The first step is to obtain the dislocation function $g'(t)$ from the integral equation pair composed of Equations (52) and (57).
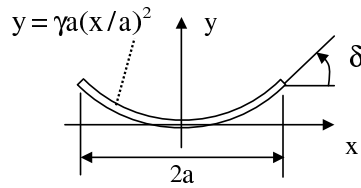
Figure 5. A parabolic crack.

(ii) The second step is to obtain two values $M(t_A) = M(t_o)|_{t_o=t_A}$ and $M(t_B) = M(t_o)|_{t_o=t_B}$, where $M(t_o)$ was defined by Equation (53).

(iii) The third step is to evaluate the T-stresses and SIFs at the crack tips by using Equations (65), (68), and (69).

One numerical example is carried out: a parabolic curved crack is defined by (see Figure 5)

$$y = \gamma\, a(x/a)^2. \tag{70}$$

In computation, the curve length coordinates method is used to solve the singular integral equation [Chen 2004]. The computed T-stresses is expressed as

$$T = G_1(\gamma)p \quad \text{(for } \sigma_y^\infty = p \text{ case)}, \tag{71}$$

$$T = G_2(\gamma)p \quad \text{(for case } \sigma_x^\infty = \sigma_y^\infty = p). \tag{72}$$

The computed results for $\gamma = 0.1, 0.2, \ldots, 1.0$ are listed in Table 2. It is known that for a line crack in horizontal position under loading $\sigma_y^\infty = p$ we have $T = -p$. In addition, for a line crack in vertical position under loading $\sigma_y^\infty = p$ we have $T = p$. The tabulated results for $G_1(\gamma)$ (for $\sigma_y^\infty = p$) reflect the following property. If the tangential angle δ at the crack tip is changed gradually, the relevant T-stress is also changed simultaneously, for example from $T = -0.9051p$ (for $\delta = \arctan 0.2$) to from $T = 0.6527p$ (for $\delta = \arctan 2.0$).

6. Conclusions

It is known that the T-stress is a particular term for a stress component parallel to the crack face in the vicinity of the crack tip. However, depending on the position where the stress component is evaluated, the situations for this particular term are quite different. We assume that the fracture is mode I and the crack face is traction-free. In this case, the T-stress is a term embedded in the singular value of

γ	0.1	0.2	0.3	0.4	0.5	0.6	0.7	0.8	0.9	1.0
$G_1(\gamma)$	−0.9051	−0.6674	−0.3793	−0.1062	0.1185	0.2813	0.4276	0.5183	0.5936	0.6527
$G_2(\gamma)$	0.0184	0.0603	0.1015	0.1299	0.1409	0.1326	0.1301	0.1107	0.0946	0.0791

Table 2. Nondimensional T-stresses $G_1(\gamma)$ (for $\sigma_y^\infty = p$ case) and $G_2(\gamma)$ (for $\sigma_x^\infty = \sigma_y^\infty = p$ case) for a parabolic crack (see Figure 5 and Equations (71), (72)).

the stress component if the stress distribution at the crack front position is considered. However, if the stress distribution at the crack back position is considered under the condition $K_{II} = 0$, the T-stress is a regular term in the stress component. All of those situations cause people to investigate the crack front position and crack back position techniques for evaluating the T-stress. It is known that in the crack front technique, one needs to evaluate a limit taking the form of $\lim_{r \to 0}(\sigma_x - \sigma_y)$. However, in this case, this limit generally takes the type $\infty - \infty$. This is an inconvenient point in computation.

In this study, all derivations including the T-stress are related to complex potentials. In this case, one can use the two techniques to evaluate T-stress in more complicated crack problems, for example, in the curved crack problem. In addition, the obtained T-stress expression, or the equation shown by Equation (65) for the curved crack, are a regular integral plus some terms.

References

[Ayatollahi et al. 1998] M. R. Ayatollahi, M. J. Pavier, and D. J. Smith, "Determination of T-stress from finite element analysis for mode I and mixed mode I/II loading", *Int. J. Fract.* **91**:3 (1998), 283–298.

[Betegon and Hancock 1991] C. Betegon and J. W. Hancock, "Two parameter characterization of elastic-plastic crack-tip fields", *J. Appl. Mech.* (*ASME*) **58**:1 (1991), 104–110.

[Broberg 2005] K. B. Broberg, "A note on T-stress determination using dislocation arrays", *Int. J. Fract.* **131**:1 (2005), 1–14.

[Chen 1983] Y. Z. Chen, "An investigation of the stress intensity factor for a finite internally cracked plate by using variational method", *Eng. Fract. Mech.* **17**:5 (1983), 387–394.

[Chen 1994] Y. Z. Chen, "T-stress in multiple crack problem for an infinite plate", *Eng. Fract. Mech.* **48**:5 (1994), 641–647.

[Chen 1997] Y. Z. Chen, "Novel weight function approach for evaluating T-stress in plane elasticity crack problem", *Int. J. Fract.* **85**:4 (1997), L35–L40.

[Chen 2000] Y. Z. Chen, "Closed form solutions of T-stress in plane elasticity crack problems", *Int. J. Solids Struct.* **37**:11 (2000), 1629–1637.

[Chen 2004] Y. Z. Chen, "Solution of integral equation in curve crack problem by using curve length coordinate", *Eng. Anal. Bound. Elem.* **28**:8 (2004), 989–994.

[Chen and Lin 2006] Y. Z. Chen and X. Y. Lin, "Complex potentials and integral equations for curved crack and curved rigid line problems in plane elasticity", *Acta Mech.* **182**:3–4 (2006), 211–230.

[Chen et al. 2001] C. S. Chen, R. Krause, R. G. Pettit, L. Banks-Sills, and A. R. Ingraffea, "Numerical assessment of T-stress computation using a p-version finite element method", *Int. J. Fract.* **107**:2 (2001), 177–199.

[Cheung and Chen 1991] Y. K. Cheung and Y. Z. Chen, "Hybrid finite element formulation in plane elasticity by using complex variable function", pp. 1149–1155 in *Computational mechanics: proceedings of the Asian Pacific Conference on Computational Mechanics* (Hong Kong, 1991), edited by Y. K. Cheung et al., Balkema, Brookfield, VT, 1991.

[Fett 1997] T. Fett, "A Green's function for T-stresses in an edge-cracked rectangular plate", *Eng. Fract. Mech.* **57**:4 (1997), 365–373.

[Fett 1998a] T. Fett, "Stress intensity factors and T-stress in edge-cracked rectangular plates under mixed boundary condition", *Eng. Fract. Mech.* **60**:5–6 (1998), 625–630.

[Fett 1998b] T. Fett, "T-stresses in rectangular plates and circular disks", *Eng. Fract. Mech.* **60**:5–6 (1998), 631–652.

[Fett 2001] T. Fett, "Stress intensity factors and T-stress for internally cracked circular disks under various boundary conditions", *Eng. Fract. Mech.* **68**:9 (2001), 1119–1136.

[Fett and Rizzi 2005] T. Fett and G. Rizzi, "Weight functions for stress intensity factors and T-stress for oblique cracks in a half-space", *Int. J. Fract.* **132**:1 (2005), L9–L16.

[Karihaloo and Xiao 2001] B. L. Karihaloo and Q. Z. Xiao, "Higher order terms of the crack tip asymptotic field for a notched three-point bend beam", *Int. J. Fract.* **112**:2 (2001), 111–128.

[Kfouri 1998] A. P. Kfouri, "Some evaluations of the elastic *T*-term using Eshelby's method", *Int. J. Fract.* **30**:4 (1998), 301–315.

[Larsson and Carlsson 1973] S. G. Larsson and A. J. Carlsson, "Influence of non-singular stress terms and specimen geometry on small-scale yielding at crack tips in elastic-plastic materials", *J. Mech. Phys. Solids* **21**:4 (1973), 263–277.

[Li and Xu 2007] X. F. Li and L. R. Xu, "*T*-stresses across static crack kinking", *J. Appl. Mech.* (*ASME*) **74**:2 (2007), 181–190.

[Melin 2002] S. Melin, "The influence of the *T*-stress on the directional stability of cracks", *Int. J. Fract.* **114**:3 (2002), 259–265.

[Muskhelishvili 1953] N. I. Muskhelishvili, *Some basic problems of the mathematical theory of elasticity: fundamental equations, plane theory of elasticity, torsion, and bending*, Noordhoff, Groningen, 1953.

[Rice 1974] J. R. Rice, "Limitations to the small scale yielding approximation of elastic-plastic crack-tip fields", *J. Mech. Phys. Solids* **22**:1 (1974), 17–26.

[Savruk 1981] M. P. Savruk, Двухмерные задачи упругости для тел с трещинами, Naukova Dumka, Kiev, 1981.

[Sham 1989] T. L. Sham, "The theory of higher order weight functions for linear elastic plane problems", *Int. J. Solids Struct.* **25**:4 (1989), 357–380.

[Sham 1991] T. L. Sham, "The determination of the elastic *T*-term using higher order weight functions", *Int. J. Fract.* **48**:2 (1991), 81–102.

[Sherry et al. 1995] A. H. Sherry, C. C. France, and M. R. Goldthorpe, "Compendium of *T*-stress solutions for two and three dimensional cracked geometries", *Fatigue Fract. Eng. Mater. Struct.* **18**:1 (1995), 141–155.

[Smith et al. 2006] D. J. Smith, M. R. Ayatollahi, and M. J. Pavier, "On the consequences of *T*-stress in elastic brittle fracture", *Proc. R. Soc. Lond. A* **462**:2072 (2006), 2415–2437.

[Tong et al. 1973] P. Tong, T. H. H. Pian, and S. J. Lasry, "A hybrid-element approach to crack problems in plane elasticity", *Int. J. Numer. Methods Eng.* **7**:3 (1973), 297–308.

[Williams 1957] M. L. Williams, "On the stress distribution at the base of a stationary crack", *J. Appl. Mech.* (*ASME*) **24** (1957), 109–114.

[Xiao and Karihaloo 2002] Q. Z. Xiao and B. L. Karihaloo, "Approximate Green's functions for singular and higher order terms of an edge crack in a finite plate", *Eng. Fract. Mech.* **69**:8 (2002), 959–981.

[Xiao et al. 2004] Q. Z. Xiao, B. L. Karihaloo, and X. Y. Liu, "Direct determination of SIF and higher order terms of mixed mode cracks by a hybrid crack element", *Int. J. Fract.* **125**:3–4 (2004), 207–225.

[Yang and Ravi-Chandar 1999] B. Yang and K. Ravi-Chandar, "Evaluation of elastic *T*-stress by the stress difference method", *Eng. Fract. Mech.* **64**:5 (1999), 589–605.

Y. Z. CHEN: chens@ujs.edu.cn
Division of Engineering Mechanics, Jiangsu University, Xue Fu Road 301, Zhenjiang, Jiangsu 212013, China

Z. X. WANG: wzx-5566@163.com
Division of Engineering Mechanics, Jiangsu University, Xue Fu Road 301, Zhenjiang, Jiangsu 212013, China

X. Y. LIN: xiaoyun39527@yahoo.com
Division of Engineering Mechanics, Jiangsu University, Xue Fu Road 301, Zhenjiang, Jiangsu 212013, China

SPATIAL EVOLUTION OF HARMONIC VIBRATIONS IN LINEAR ELASTICITY

STAN CHIRIŢĂ AND MICHELE CIARLETTA

In the present paper we consider a prismatic cylinder occupied by an anisotropic homogeneous compressible linear elastic material that is subject to zero body force and zero displacement on the lateral boundary. The elasticity tensor is strongly elliptic and the motion is induced by a harmonic time–dependent displacement specified pointwise over the base. We establish some spatial estimates for appropriate cross–sectional measures associated with the harmonic vibrations that describe how the corresponding amplitude evolves with respect to the axial distance at the excited base. The results are established for finite as well as for semi-infinite cylinders (where alternatives results of Phragmén-Lindelöf type are obtained) and the exciting frequencies can take appropriate low and high values. In fact, for the low frequency range the established spatial estimates are of exponential type, while for the high frequency range the spatial estimates are of a certain algebraic type.

1. Introduction

In the construction of buildings, bridges, aircraft, nuclear reactors and automobiles, the engineer must determine the depth to which local stresses, such as those produced by fasteners and at joints, or vibrations can penetrate girders, I-beams, braces and other similar structural elements. The determination of the extent of local or edge effects in structural systems allows the engineer to have a clear distinction between the global structure (where strength of materials approximations can be used) and the local excited portions which require a separate and more elaborate analysis based on some exact theories as that of linear elasticity. The standard procedure used in engineering practice to determine the extent of local stresses or edge effects is based on some form of the celebrated Saint Venant principle. A comprehensive surveys of contemporary research concerning Saint Venant principle can be found in [Horgan and Knowles 1983; Horgan 1989; 1996].

As regards elastic vibrations, it was observed in these papers that high frequency effects might be expected to propagate with little spatial attenuation (see also [Boley 1955; 1960]). It is outlined in [Horgan and Knowles 1983] that one would not expect to find unqualified decay estimates of the kind concerning Saint–Venant's principle in problems involving elastic wave propagation, even if the end loads are self-equilibrated at each instant. In this connection, Flavin and Knops [1987] have carried out an analysis of spatial decay for certain damped acoustic and elastodynamic problems in the low frequency range which substantiates the early work of Boley. These results are extended to linear anisotropic

materials in [Flavin et al. 1990]. It should be noted that all of the investigations mentioned in the foregoing were concerned with elastic materials having a positive definite elasticity tensor.

In the present paper we address the question of spatial behavior of the harmonic vibrations in an anisotropic elastic cylinder under the condition of strong ellipticity for the elasticity tensor. In this respect, for vibrations in the low frequency range, our expected results describe exponential spatial estimates similar with those previously established by Flavin et al. [1987; 1990]. Moreover, for harmonic vibrations with appropriate high frequencies, the present results predict some algebraic spatial estimates, confirming the foregoing observations made by Boley in related context.

We consider a prismatic cylinder occupied by an anisotropic linear elastic material and subjected to zero body force and zero lateral boundary data and zero initial conditions. The motion is induced by a harmonic time–dependent displacement specified pointwise over the base and the other end is subjected to zero displacement (when a cylinder of finite extent is considered, to say). The elasticity tensor is assumed to be strongly elliptic and so a very large class of anisotropic elastic materials is considered, including those new materials with extreme and unusual physical properties like negative Poisson's ratio (that is, so called auxetic materials).

The primary purpose of the present paper is to examine how the amplitude of the harmonic vibration evolves with respect to the axial variable. To this end we associate with the amplitude of the harmonic vibration in concern, an appropriate cross–sectional integral function and further we prove that the strong ellipticity conditions assure that it is an acceptable measure. This is possible thanks to some appropriate auxiliary identities relating the amplitude of the harmonic vibrations. For these measures we are able to establish some differential inequalities whose integration allows us to obtain spatial estimates describing the spatial behavior of the amplitude in concern. In fact, when an identity of conservation energy type is used then certain exponential spatial estimates are obtained for all frequencies lower than a critical value. When a Rellich identity is involved then certain type of algebraic spatial estimates are established for appropriate high frequencies. All results are illustrated for transversely isotropic materials as well as for the rhombic systems.

2. Formulation of the problem

Consider a prismatic cylinder $B \subset \mathbb{R}^3$ whose bounded uniform cross–section $D \subset \mathbb{R}^2$ has piecewise continuously differentiable boundary ∂D. The origin of a rectangular Cartesian coordinate system is located in the cylinder's base and the positive x_3-axis is directed along that of the cylinder. It is convenient to introduce the further abbreviation

$$B_z = \{x \in B : z > x_3\} \tag{2.1}$$

and, moreover, we employ $D(x_3)$ to indicate that relevant quantities are to be evaluated over the cross–section whose distance from the origin is x_3.

The cylinder is occupied by an anisotropic compressible elastic material and is subject to a deformation in which the displacement field $u(x, t)$ is a smooth function satisfying the requirements of the classical dynamical theory of elasticity [Gurtin 1972]. The corresponding stress tensor $\mathbf{S}(x, t)$ has Cartesian components given by

$$S_{rs} = C_{rsmn}\varepsilon_{mn}, \tag{2.2}$$

where

$$\varepsilon_{mn} = \tfrac{1}{2}\left(u_{m,n} + u_{n,m}\right) \tag{2.3}$$

are the components of the strain tensor. Moreover, the constant elasticities C_{rsmn} possess the symmetries

$$C_{rsmn} = C_{mnrs} = C_{srmn}, \tag{2.4}$$

and satisfy the strong ellipticity condition

$$C_{rskl} m_r m_k n_s n_l > 0 \quad \text{for all nonzero vectors } (m_1, m_2, m_3), \ (n_1, n_2, n_3). \tag{2.5}$$

The cylinder is set in motion subject to a pointwise prescribed base harmonic time–dependent displacement, zero body–force and zero displacement on the lateral surface and the other end (when a finite cylinder is considered). Furthermore, the prescribed displacement is such that a classical solution exists on the interval $[0, \infty)$. Consequently, the problem to be considered is specified by

$$(C_{rskl} u_{k,l})_{,r} = \rho \ddot{u}_s, \quad (x, t) \in B \times [0, \infty), \tag{2.6}$$

$$u_r(x, 0) = u_r^0(x), \quad \dot{u}_r(x, 0) = \dot{u}_r^0(x), \quad x \in B, \tag{2.7}$$

$$u_r(x, t) = 0, \quad (x, t) \in \partial D \times [0, L] \times [0, \infty), \tag{2.8}$$

$$u_r(x, t) = f_r(x_1, x_2)\, e^{i\omega t}, \quad (x, t) \in D(0) \times [0, \infty), \tag{2.9}$$

$$u_r(x, t) = 0, \quad (x, t) \in D(L) \times [0, \infty), \tag{2.10}$$

in the case where L is finite (say). In the limiting case $L \to \infty$ a condition of the type (2.10) is unnecessary. In the above relations we have used a superposed dot for denoting differentiation with respect to time and a subscript comma indicates partial differentiation. Moreover, ρ is the constant positive mass density, ω is a positive constant (frequency of vibration), $u_r^0(x)$, $\dot{u}_r^0(x)$ and $f_r(x_1, x_2)$ are prescribed differentiable functions compatible with the initial and lateral boundary conditions and $i = \sqrt{-1}$ is the complex unit. We are interested in the study of the spatial behavior of the solution u_r of the above initial boundary value problem (2.6)–(2.10).

To this end we use the decomposition

$$u_r = U_r(x, t) + v_r(x)\, e^{i\omega t}, \tag{2.11}$$

where U_r (transient solution) satisfies the above initial boundary value problem with null boundary conditions and appropriate initial conditions, while v_r satisfies the boundary value problem

$$\left(C_{rskl} v_{k,l}\right)_{,r} + \rho \omega^2 v_s = 0, \quad x \in B, \tag{2.12}$$

$$v_r(x) = 0, \quad x \in \partial D \times [0, L], \tag{2.13}$$

$$v_r(x) = f_r(x_1, x_2), \quad x \in D(0), \tag{2.14}$$

$$v_r(x) = 0, \quad x \in D(L), \tag{2.15}$$

in the case where L is finite.

We note that the spatial behavior of the transient solution U_r can be described by the methods developed in [Chiriţă and Ciarletta 1999; Tibullo and Vaccaro 2008]. The exponential spatial decay of

the amplitude v_r of the forced oscillation has been established in [Flavin and Knops 1987; Flavin et al. 1990; Knops 1991] for isotropic and anisotropic elastic materials with a positive definite elasticity tensor, provided the exciting frequency is less than a certain critical value. Considering an appropriate region filled with an isotropic elastic material an algebraical spatial decay of the amplitude of vibration has been established in [Chiriță and Quintanilla 1996] under the assumption that the elasticity tensor is positive definite and without any restriction upon the frequency of vibration.

The main purpose of this paper consists of studying how the amplitude of harmonic vibration evolves with respect to the axial distance at the excited base, provided the strong ellipticity condition is assumed for the elasticity tensor. Under such hypotheses we will establish some appropriate algebraic and exponential spatial estimates describing the spatial decay of the amplitude of harmonic vibration. In fact, for all frequencies lower than a certain critical value we are able to establish exponential estimates describing how the amplitude evolves with the distance to the excited end. While, for all frequencies greater than an appropriate critical value, we can establish spatial estimates describing a specific algebraical behavior of the amplitude. Moreover, some alternatives of Phragmén–Lindelöf type are established for the semi-infinite cylinder.

Since the coefficients in the differential system (2.12) are real numbers, we can assume that v_r are real functions. Otherwise, we can proceed with the same method for the real part as well as for the imaginary part of v_r. So in what follows we shall consider the solution v_r to be real functions.

3. Some auxiliary identities

Before proceeding to derive *a priori* estimates for a solution to equations (2.12)–(2.15), we need some auxiliary identities concerning the equations (2.12), with the lateral boundary condition (2.13). Some of these are achieved via some Rellich–like identities (used for example in [Chiriță et al. 2006; Chiriță and Ciarletta 2008]).

Theorem 1. *Let v_r be a solution of the boundary value problem defined by relations (2.12) and (2.13). Then*

$$\int_{D(x_3)} \left(C_{rsmn} v_{r,s} v_{m,n} - \rho \omega^2 v_s v_s \right) da = \frac{d}{dx_3} \int_{D(x_3)} C_{3smn} v_{m,n} v_s \, da. \tag{3.1}$$

Proof. We form the identity

$$\int_{D(x_3)} v_s \left(\left(C_{rsmn} v_{m,n} \right)_{,r} + \rho \omega^2 v_s \right) da = 0. \tag{3.2}$$

Now integrate by parts in succession and use the boundary condition (2.13) to find (3.1). □

Theorem 2. *Let v_r be a solution of the boundary value problem defined by (2.12) and (2.13). Then*

$$\frac{1}{2} \int_{D(x_3)} \left(C_{rsmn} v_{r,s} v_{m,n} - 3\rho \omega^2 v_s v_s \right) da$$

$$= -\frac{d}{dx_3} \int_{D(x_3)} \left(x_\rho C_{3smn} v_{s,\rho} v_{m,n} + \frac{1}{2} x_3 \left(C_{r3m3} v_{r,3} v_{m,3} - C_{ram\beta} v_{r,\alpha} v_{m,\beta} + \rho \omega^2 v_s v_s \right) \right) da$$

$$- \int_{\partial D(x_3)} \frac{1}{2} x_\rho n_\rho C_{ram\beta} n_\alpha n_\beta \frac{\partial v_r}{\partial n} \frac{\partial v_m}{\partial n} ds, \tag{3.3}$$

where n_α are the components of the outward unit normal vector to ∂D and $\partial/\partial n$ represents the normal derivative.

Proof. We start with the identity

$$\int_{D(x_3)} x_p v_{s,p} \left(\left(C_{rskl} v_{k,l} \right)_{,r} + \rho\omega^2 v_s \right) da = 0 \tag{3.4}$$

which can be written as

$$\int_{D(x_3)} \left(C_{rsmn} v_{r,s} v_{m,n} + x_p \left(\tfrac{1}{2} C_{rsmn} v_{r,s} v_{m,n} \right)_{,p} - x_p \left(\tfrac{1}{2} \rho\omega^2 v_s v_s \right)_{,p} \right) da$$
$$= \int_{D(x_3)} \left(x_p C_{rsmn} v_{m,n} v_{s,p} \right)_{,r} da; \tag{3.5}$$

moreover,

$$\frac{1}{2} \int_{D(x_3)} \left(C_{rsmn} v_{r,s} v_{m,n} - 3\rho\omega^2 v_s v_s \right) da = - \int_{D(x_3)} \left(x_p v_{r,p} C_{rsmn} v_{m,n} \right)_{,s} da$$
$$+ \int_{D(x_3)} \left(\tfrac{1}{2} x_p C_{rsmn} v_{r,s} v_{m,n} \right)_{,p} da - \int_{D(x_3)} \left(\tfrac{1}{2} x_p \rho\omega^2 v_r v_r \right)_{,p} da. \tag{3.6}$$

Using the divergence theorem and (2.13), we obtain from (3.6)

$$\frac{1}{2} \int_{D(x_3)} \left(C_{rsmn} v_{r,s} v_{m,n} - 3\rho\omega^2 v_s v_s \right) da$$
$$= -\frac{d}{dx_3} \int_{D(x_3)} \left(C_{3smn} v_{m,n} x_p v_{s,p} - \tfrac{1}{2} x_3 \left(C_{rsmn} v_{r,s} v_{m,n} - \rho\omega^2 v_s v_s \right) \right) da$$
$$+ \int_{\partial D(x_3)} \left(\tfrac{1}{2} x_\rho n_\rho C_{rsmn} v_{r,s} v_{m,n} - x_p v_{r,p} C_{r\rho mn} v_{m,n} n_\rho \right) ds. \tag{3.7}$$

At this point we note that the boundary condition (2.13) implies

$$v_{r,3} = 0, \quad x \in \partial D \times [0, L]. \tag{3.8}$$

Moreover, we write $v_{r,\alpha}$ on the curve $\partial D(x_3)$ as $v_{r,\alpha} = n_\alpha \left(\partial v_r/\partial n \right) + \tau_\alpha \left(\partial v_r/\partial \tau \right)$, where τ_α are the components of the tangential unit vector, $\partial/\partial n$ is the normal derivative and $\partial/\partial \tau$ is the tangential derivative. In view of the boundary condition (2.13) we have $\left(\partial v_r/\partial \tau \right) = 0$ on $\partial D(x_3)$ and hence we deduce that $v_{r,\alpha} = n_\alpha \left(\partial v_r/\partial n \right)$ on $\partial D(x_3)$. Thus, we obtain

$$\int_{\partial D(x_3)} \left(x_\rho n_\rho C_{r\alpha m\beta} v_{r,\alpha} v_{m,\beta} - 2 x_\alpha v_{r,\alpha} C_{r\rho m\beta} v_{m,\beta} n_\rho \right) ds = - \int_{\partial D(x_3)} x_\rho n_\rho C_{r\alpha m\beta} n_\alpha n_\beta \frac{\partial v_r}{\partial n} \frac{\partial v_m}{\partial n} ds. \tag{3.9}$$

Substituting (3.9) into (3.7) we obtain (3.3). $\qquad\square$

By combining these two theorems we obtain the following result.

Theorem 3. *Let v_r be a solution of the boundary value problem defined by (2.12) and (2.13). Then*

$$\frac{d}{dx_3} \int_{D(x_3)} \left(2 C_{3rmn} v_{m,n} v_r + 2 x_\rho C_{3smn} v_{s,\rho} v_{m,n} + x_3 \left(C_{r3m3} v_{r,3} v_{m,3} - C_{r\alpha m\beta} v_{r,\alpha} v_{m,\beta} + \rho\omega^2 v_s v_s \right) \right) da$$
$$= \int_{D(x_3)} \left(C_{rsmn} v_{r,s} v_{m,n} + \rho\omega^2 v_s v_s \right) da - \int_{\partial D(x_3)} x_\rho n_\rho C_{r\alpha m\beta} n_\alpha n_\beta \frac{\partial v_r}{\partial n} \frac{\partial v_m}{\partial n} ds. \tag{3.10}$$

Remarks. (1) By using the integration by parts and the lateral boundary condition (2.13) we can establish the identities

$$\int_{D(x_3)} v_{r,3} v_{m,\beta}\, da - \int_{D(x_3)} v_{r,\beta} v_{m,3}\, da = \frac{d}{dx_3} \int_{D(x_3)} v_r v_{m,\beta}\, da, \tag{3.11}$$

$$\int_{D(x_3)} v_{r,3} v_{m,\beta}\, da - \int_{D(x_3)} v_{r,\beta} v_{m,3}\, da = -\frac{d}{dx_3} \int_{D(x_3)} v_{r,\beta} v_m\, da. \tag{3.12}$$

(2) Theorem 1 can be viewed in connection with a (dynamic) virtual work expression, while Theorems 2 and 3 are closer to the mathematical Rellich identity often used in the study of structural stability. See [Chiriță et al. 2006; Chiriță and Ciarletta 2008], for example.

4. Some spatial estimates for appropriate low frequencies

Throughout this section we will study the spatial evolution of the amplitude v_r by starting with the identity established in Theorem 1. To this end we combine the identity (3.1) with (3.11) and (3.12) in the same manner like that used in [Chiriță and Ciarletta 2006]. Our objective consists of finding measures of the amplitude that are able to furnish information on the spatial evolution of the amplitude v_r for the entire class of anisotropic strongly elliptic elastic materials. Since such task can be too complex for general anisotropic elastic materials we will proceed to pursue our method for some particularly important classes of anisotropic materials, namely those of transversely isotropic and rhombic systems. We recall that for these systems we have established explicit necessary and sufficient conditions in [Chiriță et al. 2007] characterizing the strong ellipticity condition.

4.1. *Transversely isotropic materials.* Many natural and man–made materials are classified as *transversely isotropic* (or *hexagonal*). Such materials are characterized by the fact that one can find a line that allows a rotation of the material about it without changing its properties. The plane, which is perpendicular to this line (the axis of rotational symmetry) is called a *plane of elastic symmetry* or *plane of isotropy*. A modern example for such a material are laminates made of randomly oriented chopped fibers that are in general placed in a certain plane. The effective material properties for a bundled structure have no profound direction in that plane, which then becomes a plane of elastic symmetry. Hence, each plane that contains the axis of rotation is a plane of symmetry, and therefore, transversely isotropic material admits an infinite number of elastic symmetries.

Necessary and sufficient conditions for strong ellipticity to hold for a transversely isotropic linearly elastic solid are established in [Chiriță et al. 2007; Chiriță 2006]. In this connection we recall the standard notation

$$c_{ij} = C_{iijj}, \quad i, j \in \{1, 2, 3\} \ \ (\text{not summed}), \quad c_{22} = c_{11}, \quad c_{23} = c_{13},$$
$$c_{44} = c_{55} = C_{2323} = C_{1313}, \quad c_{66} = C_{1212} = \tfrac{1}{2}(c_{11} - c_{12}), \tag{4.1}$$

corresponding to the direction of transverse isotropy coinciding with the x_3 coordinate axis. Apart from terms obtained by use of the symmetries (2.4), these are the only nonzero components C_{ijkl}. Then the necessary and sufficient conditions for strong ellipticity to hold are (*loc. cit.*)

$$c_{11} > 0, \quad c_{33} > 0, \quad c_{55} > 0, \quad c_{11} > c_{12}, \quad |c_{13} + c_{55}| < c_{55} + \sqrt{c_{11} c_{33}}. \tag{4.2}$$

Combining relations (3.1), (3.11) and (3.12) and using (4.1), we obtain

$$\frac{d}{dx_3} \int_{D(x_3)} \left(v_\alpha((c_{55} - \varkappa)v_{3,\alpha} + c_{55}v_{\alpha,3}) + v_3(c_{33}v_{3,3} + (c_{13} + \varkappa)(v_{1,1} + v_{2,2})) \right) da$$

$$= \int_{D(x_3)} \left(c_{66}(v_{1,2} - v_{2,1})^2 - \rho\omega^2 v_\alpha v_\alpha \right) da + \int_{D(x_3)} \left(c_{11}(v_{1,1} + v_{2,2})^2 + c_{33}v_{3,3}^2 + 2(c_{13} + \varkappa)(v_{1,1} + v_{2,2})v_{3,3} \right) da$$

$$+ \int_{D(x_3)} \left((c_{55}(v_{3,1}^2 + v_{1,3}^2) + 2(c_{55} - \varkappa)v_{1,3}v_{3,1}) + (c_{55}(v_{3,2}^2 + v_{2,3}^2) + 2(c_{55} - \varkappa)v_{2,3}v_{3,2}) - \rho\omega^2 v_3^2 \right) da, \quad (4.3)$$

where $\varkappa \in (0, 2c_{55})$ is a positive parameter at our disposal.

Now we choose the parameter $\varkappa$ in such a way that

$$\max \left(-c_{13} - \sqrt{c_{11}c_{33}}, 0 \right) < \varkappa < \min \left(2c_{55}, -c_{13} + \sqrt{c_{11}c_{33}} \right), \quad (4.4)$$

so

$$|c_{13} + \varkappa| < \sqrt{c_{11}c_{33}}, \quad |c_{55} - \varkappa| < c_{55}. \quad (4.5)$$

We deduce that

$$c_{55} \left(v_{3,1}^2 + v_{1,3}^2 \right) + 2 \left(c_{55} - \varkappa \right) v_{1,3}v_{3,1} \geq \nu_1 \left(v_{3,1}^2 + v_{1,3}^2 \right),$$
$$c_{55} \left(v_{3,2}^2 + v_{2,3}^2 \right) + 2 \left(c_{55} - \varkappa \right) v_{2,3}v_{3,2} \geq \nu_1 \left(v_{3,2}^2 + v_{2,3}^2 \right), \quad (4.6)$$

where

$$\nu_1 = \min \left(\varkappa, \ 2c_{55} - \varkappa \right). \quad (4.7)$$

Moreover, we have

$$c_{11}(v_{1,1} + v_{2,2})^2 + c_{33}v_{3,3}^2 + 2(c_{13} + \varkappa)(v_{1,1} + v_{2,2})v_{3,3} \geq \nu_2 \left((v_{1,1} + v_{2,2})^2 + v_{3,3}^2 \right), \quad (4.8)$$

where

$$\nu_2 = \tfrac{1}{2} \left(c_{11} + c_{33} - \sqrt{(c_{11} - c_{33})^2 + 4(c_{13} + \varkappa)^2} \right). \quad (4.9)$$

On the other hand, in view of the boundary condition (2.13), we obtain

$$\int_{D(x_3)} v_{\alpha,\beta}v_{\alpha,\beta} \, da \geq \lambda \int_{D(x_3)} v_\alpha v_\alpha \, da, \quad \int_{D(x_3)} v_{3,\beta}v_{3,\beta} \, da \geq \lambda \int_{D(x_3)} v_3^2 \, da, \quad (4.10)$$

where $\lambda > 0$ is the first eigenvalue in the two-dimensional clamped membrane eigenvalue problem for the cross section $D(x_3)$.

At this instant we introduce the critical frequency

$$\omega_1 = \sqrt{\frac{\lambda}{\rho} \min \left(\nu_1, \min \left(c_{66}, \nu_2 \right) \right)} \quad (4.11)$$

and then assume that the frequency of vibration ω is lower than ω_1, that is

$$0 < \omega < \omega_1. \quad (4.12)$$

Throughout in the remainder of this subsection we will assume that relations (4.4) and (4.12) hold true. Then we introduce the function

$$I_\varkappa(x_3) = - \int_{D(x_3)} \left[v_\alpha \left((c_{55} - \varkappa)v_{3,\alpha} + c_{55}v_{\alpha,3} \right) + v_3 \left(c_{33}v_{3,3} + (c_{13} + \varkappa)v_{\alpha,\alpha} \right) \right] da \quad (4.13)$$

for all $x_3 \in [0, L]$ and note that relations (4.3)–(4.12) imply

$$-\frac{dI_\varkappa}{dx_3}(x_3) \geq \min(c_{66}, v_2)\left(1 - \frac{\omega^2}{\omega_1^2}\right) \int_{D(x_3)} v_{\alpha,\beta} v_{\alpha,\beta}\, da$$

$$+v_2 \int_{D(x_3)} v_{3,3}^2\, da + v_1 \int_{D(x_3)} v_{\alpha,3} v_{\alpha,3}\, da + v_1 \left(1 - \frac{\omega^2}{\omega_1^2}\right) \int_{D(x_3)} v_{3,\beta} v_{3,\beta}\, da \geq 0 \quad (4.14)$$

and hence $I_\varkappa(x_3)$ is a nonincreasing function with respect to x_3 on $[0, L]$.

We have now all preliminary material in order to state and proof the following result.

Theorem 4. *Let v_r be the amplitude of a harmonic vibration whose frequency is lower than the critical frequency ω_1 given by (4.11). Then, for every $\varkappa$ satisfying (4.4), the cross section integral $I_\varkappa(x_3)$ as defined by (4.13) is an acceptable measure of the amplitude v_r (that is, $I_\varkappa(x_3) \geq 0$ and $I_\varkappa(x_3) = 0$ implies that $v_r = 0$) and it satisfies the spatial decay estimate*

$$0 \leq I_\varkappa(x_3) \leq I_\varkappa(0)\, e^{-\sigma_1 x_3} \quad \text{for all}\ x_3 \in [0, L], \quad (4.15)$$

where σ_1 is given by

$$\frac{1}{\sigma_1} = \frac{1}{\sqrt{\lambda}} \max \left\{ \frac{c_{55} + \sqrt{c_{11}c_{33}}}{\min(c_{66}, v_2)\left(1 - \omega^2/\omega_1^2\right)}, \frac{c_{33}}{2v_2}, \frac{c_{55}}{2v_1}, \frac{c_{33} + c_{55} + \sqrt{c_{11}c_{33}}}{2v_1\left(1 - \omega^2/\omega_1^2\right)} \right\}. \quad (4.16)$$

Proof. On the basis of the end boundary condition (2.15) and relation (4.13) we deduce that $I_\varkappa(L) = 0$, so that we have

$$I_\varkappa(x_3) \geq 0 \quad \text{for all}\ x_3 \in [0, L]. \quad (4.17)$$

Thus, $I_\varkappa(x_3)$ represents an acceptable measure for the amplitude v_r of the harmonic vibration.

Now, by using the Schwarz and arithmetic-geometric mean inequalities, from (4.5) and (4.13) we obtain the estimate

$$|I_\varkappa(x_3)| \leq \frac{1}{\sqrt{\lambda}}\left(c_{55} + \sqrt{c_{11}c_{33}}\right) \int_{D(x_3)} v_{\alpha,\beta} v_{\alpha,\beta}\, da + \frac{1}{2\sqrt{\lambda}}c_{33} \int_{D(x_3)} v_{3,3}^2\, da$$

$$+ \frac{1}{2\sqrt{\lambda}}c_{55} \int_{D(x_3)} v_{\alpha,3} v_{\alpha,3}\, da + \frac{1}{2\sqrt{\lambda}}\left(c_{33} + c_{55} + \sqrt{c_{11}c_{33}}\right) \int_{D(x_3)} v_{3,\beta} v_{3,\beta}\, da. \quad (4.18)$$

By combining (4.14) and (4.18) we obtain the first order differential inequality

$$\frac{dI_\varkappa}{dx_3}(x_3) + \sigma_1 I_\varkappa(x_3) \leq 0 \quad \text{for all}\ x_3 \in [0, L], \quad (4.19)$$

which, when integrated, furnishes the exponential spatial decay estimate (4.15). □

4.2. *Rhombic materials.* Suppose the cylinder is filled with a rhombic elastic material with the group $\mathscr{C}_3$ generated by $\mathbf{R}_{e_3}^\pi$, $\mathbf{R}_{e_2}^\pi$ (here $\mathbf{R}_e^\theta$ is the orthogonal tensor corresponding to a right–handed rotation through the angle $\theta \in (0, 2\pi)$, about an axis in the direction of the unit vector $\mathbf{e}$). According to Gurtin

[1972], this class of materials is characterized by

$$C_{1123} = C_{1131} = C_{1112} = C_{2223} = C_{2231} = C_{2212} = 0,$$
$$C_{3323} = C_{3331} = C_{3312} = C_{2331} = C_{2312} = C_{3112} = 0,$$
$$c_{11} = C_{1111}, \quad c_{22} = C_{2222}, \quad c_{33} = C_{3333}, \quad c_{12} = C_{1122}, \quad c_{23} = C_{2233},$$
$$c_{31} = C_{3311}, \quad c_{44} = C_{2323}, \quad c_{55} = C_{1313}, \quad c_{66} = C_{1212}. \tag{4.20}$$

The strong ellipticity condition (2.5) becomes

$$c_{11}n_1^2m_1^2 + c_{22}n_2^2m_2^2 + c_{33}n_3^2m_3^2 + c_{66}(n_1m_2 + n_2m_1)^2 + c_{44}(n_3m_2 + n_2m_3)^2$$
$$+ c_{55}(n_1m_3 + n_3m_1)^2 + 2c_{12}n_1m_1n_2m_2 + 2c_{23}n_2m_2n_3m_3 + 2c_{31}n_3m_3n_1m_1 > 0, \tag{4.21}$$

for all nonzero vectors (m_1, m_2, m_3) and (n_1, n_2, n_3). It is equivalent to the conditions [Chiriță et al. 2007]

$$c_{11} > 0, \quad c_{22} > 0, \quad c_{33} > 0, \quad c_{44} > 0, \quad c_{55} > 0, \quad c_{66} > 0, \tag{4.22}$$

$$-2c_{66} + \varkappa_3^i \sqrt{c_{11}c_{22}} < c_{12} < \varkappa_3^s \sqrt{c_{11}c_{22}}, \qquad -2c_{44} + \varkappa_1^i \sqrt{c_{22}c_{33}} < c_{23} < \varkappa_1^s \sqrt{c_{22}c_{33}},$$

$$-2c_{55} + \varkappa_2^i \sqrt{c_{11}c_{33}} < c_{13} < \varkappa_2^s \sqrt{c_{11}c_{33}}, \tag{4.23}$$

where $(\varkappa_1^i, \varkappa_1^s)$, $(\varkappa_2^i, \varkappa_2^s)$ and $(\varkappa_3^i, \varkappa_3^s)$ are solutions with respect to x, y and z of the equation $x^2 + y^2 + z^2 - 2xyz - 1 = 0$, satisfying $|x| < 1$, $|y| < 1, |z| < 1$ and

$$x \in \left\{ \frac{c_{23}}{\sqrt{c_{22}c_{33}}}, \frac{c_{23} + 2c_{44}}{\sqrt{c_{22}c_{33}}} \right\}, \quad y \in \left\{ \frac{c_{13}}{\sqrt{c_{11}c_{33}}}, \frac{c_{13} + 2c_{55}}{\sqrt{c_{11}c_{33}}} \right\}, \quad z \in \left\{ \frac{c_{12}}{\sqrt{c_{11}c_{22}}}, \frac{c_{12} + 2c_{66}}{\sqrt{c_{11}c_{22}}} \right\}. \tag{4.24}$$

This statement is equivalent with the relation (4.22) and all points $P(x, y, z)$, with coordinates satisfying (4.24) lie inside the region limited by the surface $S(x, y, z) \equiv x^2 + y^2 + z^2 - 2xyz - 1 = 0$, with $|x| < 1$, $|y| < 1, |z| < 1$.

In the case of a rhombic material the relation (4.3) is replaced by

$$\frac{d}{dx_3} \int_{D(x_3)} \left[v_1 \left(c_{55}v_{1,3} + (c_{55} - \varkappa_2)v_{3,1} \right) + v_2 \left(c_{44}v_{2,3} + (c_{44} - \varkappa_1)v_{3,2} \right) \right.$$
$$\left. + v_3 \left((c_{13} + \varkappa_2)v_{1,1} + (c_{23} + \varkappa_1)v_{2,2} + c_{33}v_{3,3} \right) \right] da$$

$$= \int_{D(x_3)} \left[c_{11}v_{1,1}^2 + c_{22}v_{2,2}^2 + c_{33}v_{3,3}^2 + 2(c_{12} + \varkappa_3)v_{1,1}v_{2,2} + 2(c_{13} + \varkappa_2)v_{1,1}v_{3,3} + 2(c_{23} + \varkappa_1)v_{2,2}v_{3,3} \right] da$$

$$+ \int_{D(x_3)} \left[c_{66}(v_{1,2}^2 + v_{2,1}^2) + 2(c_{66} - \varkappa_3)v_{1,2}v_{2,1} \right] da + \int_{D(x_3)} \left[c_{55}(v_{3,1}^2 + v_{1,3}^2) + 2(c_{55} - \varkappa_2)v_{1,3}v_{3,1} \right] da$$

$$+ \int_{D(x_3)} \left[c_{44}(v_{3,2}^2 + v_{2,3}^2) + 2(c_{44} - \varkappa_1)v_{2,3}v_{3,2} \right] da - \int_{D(x_3)} \rho\omega^2 v_s v_s \, da, \tag{4.25}$$

where $\varkappa_1 \in [0, 2c_{44}]$, $\varkappa_2 \in [0, 2c_{55}]$ and $\varkappa_3 \in [0, 2c_{66}]$ are positive parameters at our disposal. In view of the assumptions (4.22) and (4.23) we can choose $\varkappa_1 \in [0, 2c_{44}]$, $\varkappa_2 \in [0, 2c_{55}]$, $\varkappa_3 \in [0, 2c_{66}]$ so that $P(x, y, z)$, with coordinates

$$x = \frac{c_{23} + \varkappa_1}{\sqrt{c_{22}c_{33}}}, \qquad y = \frac{c_{13} + \varkappa_2}{\sqrt{c_{11}c_{33}}}, \qquad z = \frac{c_{12} + \varkappa_3}{\sqrt{c_{11}c_{22}}},$$

lies inside the region limited by the surface $S(x, y, z)$. With these choices we have

$$c_{44} \left(v_{3,2}^2 + v_{2,3}^2 \right) + 2 \left(c_{44} - \varkappa_1 \right) v_{2,3} v_{3,2} \geq \xi_1 \left(v_{3,2}^2 + v_{2,3}^2 \right), \tag{4.26}$$

$$c_{55} \left(v_{3,1}^2 + v_{1,3}^2 \right) + 2 \left(c_{55} - \varkappa_2 \right) v_{1,3} v_{3,1} \geq \xi_2 \left(v_{3,1}^2 + v_{1,3}^2 \right), \tag{4.27}$$

$$c_{66} \left(v_{1,2}^2 + v_{2,1}^2 \right) + 2 \left(c_{66} - \varkappa_3 \right) v_{1,2} v_{2,1} \geq \xi_3 \left(v_{1,2}^2 + v_{2,1}^2 \right), \tag{4.28}$$

$$c_{11} v_{1,1}^2 + c_{22} v_{2,2}^2 + c_{33} v_{3,3}^2 + 2 \left(c_{12} + \varkappa_3 \right) v_{1,1} v_{2,2}$$
$$+ 2 \left(c_{13} + \varkappa_2 \right) v_{1,1} v_{3,3} + 2 \left(c_{23} + \varkappa_1 \right) v_{2,2} v_{3,3} \geq \xi_4 \left(v_{1,1}^2 + v_{2,2}^2 + v_{3,3}^2 \right), \tag{4.29}$$

where

$$\xi_1 = \min \left(2c_{44} - \varkappa_1, \varkappa_1 \right), \quad \xi_2 = \min \left(2c_{55} - \varkappa_2, \varkappa_2 \right), \quad \xi_3 = \min \left(2c_{66} - \varkappa_3, \varkappa_3 \right) \tag{4.30}$$

and ξ_4 is the lowest positive eigenvalue of the 3×3 matrix

$$\begin{pmatrix} c_{11} & c_{12} + \varkappa_3 & c_{13} + \varkappa_2 \\ c_{12} + \varkappa_3 & c_{22} & c_{23} + \varkappa_1 \\ c_{13} + \varkappa_2 & c_{23} + \varkappa_1 & c_{33} \end{pmatrix}. \tag{4.31}$$

So we have to introduce the function

$$J_\varkappa(x_3) = - \int_{D(x_3)} \left[v_1 \left((c_{55} - \varkappa_2) v_{3,1} + c_{55} v_{1,3} \right) + v_2 \left((c_{44} - \varkappa_1) v_{3,2} + c_{44} v_{2,3} \right) \right.$$
$$\left. + v_3 \left((c_{13} + \varkappa_2) v_{1,1} + (c_{23} + \varkappa_1) v_{2,2} + c_{33} v_{3,3} \right) \right] da \tag{4.32}$$

and note that identity (4.25) and relations (4.10) and (4.26)–(4.29) imply

$$-\frac{dJ_\varkappa}{dx_3}(x_3) \geq \int_{D(x_3)} \left(\xi_4 \left(v_{1,1}^2 + v_{2,2}^2 \right) + \xi_3 \left(v_{1,2}^2 + v_{2,1}^2 \right) - \frac{\rho \omega^2}{\lambda} v_{\alpha,\beta} v_{\alpha,\beta} \right) da$$
$$+ \int_{D(x_3)} \left(\xi_1 v_{3,2}^2 + \xi_2 v_{3,1}^2 - \frac{\rho \omega^2}{\lambda} v_{3,\alpha} v_{3,\alpha} \right) da + \int_{D(x_3)} \left(\xi_1 v_{2,3}^2 + \xi_2 v_{1,3}^2 + \xi_4 v_{3,3}^2 \right) da. \tag{4.33}$$

At this point we introduce the critical frequency

$$\omega_2 = \sqrt{\frac{\lambda}{\rho} \min \left(\min \left(\xi_1, \xi_2 \right), \min \left(\xi_3, \xi_4 \right) \right)} \tag{4.34}$$

and assume that the vibration frequency ω is lower than ω_2:

$$0 < \omega < \omega_2. \tag{4.35}$$

Thus, we have

$$-\frac{dJ_\varkappa}{dx_3}(x_3) \geq \min \left(\xi_3, \xi_4 \right) \left(1 - \frac{\omega^2}{\omega_2^2} \right) \int_{D(x_3)} v_{\alpha,\beta} v_{\alpha,\beta} \, da + \min \left(\xi_1, \xi_2 \right) \left(1 - \frac{\omega^2}{\omega_2^2} \right) \int_{D(x_3)} v_{3,\alpha} v_{3,\alpha} \, da$$
$$+ \int_{D(x_3)} \left(\xi_1 v_{2,3}^2 + \xi_2 v_{1,3}^2 + \xi_4 v_{3,3}^2 \right) da \geq 0. \tag{4.36}$$

Consequently, $J_\varkappa(x_3)$ is a nonincreasing function with respect to x_3 on $[0, L]$.

Theorem 5. *Let v_r be the amplitude of a harmonic vibration whose frequency is lower than the critical frequency ω_2 of (4.34). Then the cross section integral $J_\varkappa(x_3)$ as defined by (4.32) is an acceptable measure of the amplitude v_r (that is, $J_\varkappa(x_3) \geq 0$ and $J_\varkappa(x_3) = 0$ implies that $v_r = 0$) and it satisfies the spatial decay estimate*

$$0 \leq J_\varkappa(x_3) \leq J_\varkappa(0)\, e^{-\sigma_2 x_3} \quad \text{for all} \ \ x_3 \in [0, L], \tag{4.37}$$

where σ_2 is given by

$$\frac{1}{\sigma_2} = \frac{1}{2\sqrt{\lambda}} \max \left\{ \frac{\max \left(2c_{55} + \sqrt{c_{11}c_{33}},\, 2c_{44} + \sqrt{c_{22}c_{33}}\right)}{\min\left(\xi_3, \xi_4\right)\left(1 - \omega^2/\omega_2^2\right)}, \right.$$
$$\left. \frac{c_{44}}{\xi_1},\, \frac{c_{55}}{\xi_2},\, \frac{c_{33}}{\xi_4},\, \frac{\max\left(c_{44}, c_{55}\right) + \sqrt{c_{33}}\left(\sqrt{c_{11}} + \sqrt{c_{22}} + \sqrt{c_{33}}\right)}{\min\left(\xi_1, \xi_2\right)\left(1 - \omega^2/\omega_2^2\right)} \right\}. \tag{4.38}$$

Proof. On the basis of the end boundary condition (2.15) and relation (4.32) we deduce that $J_\varkappa(L) = 0$, so that we have

$$J_\varkappa(x_3) \geq 0 \quad \text{for all} \ \ x_3 \in [0, L]. \tag{4.39}$$

Thus, $J_\varkappa(x_3)$ represents an acceptable measure for the amplitude v_r of the harmonic vibration.

We further note that

$$|c_{44} - \varkappa_1| < c_{44}, \quad |c_{55} - \varkappa_2| < c_{55}, \quad |c_{13} + \varkappa_2| < \sqrt{c_{11}c_{33}}, \quad |c_{23} + \varkappa_1| < \sqrt{c_{22}c_{33}}. \tag{4.40}$$

On this basis and by using the Schwarz and arithmetic-geometric mean inequalities and (4.10), we obtain from (4.32) the estimate

$$|J_\varkappa(x_3)| \leq \frac{1}{2\sqrt{\lambda}} \max\left(2c_{55} + \sqrt{c_{11}c_{33}},\, 2c_{44} + \sqrt{c_{22}c_{33}}\right) \int_{D(x_3)} v_{\alpha,\beta} v_{\alpha,\beta}\, da$$
$$+ \frac{1}{2\sqrt{\lambda}} \left[\max\left(c_{44}, c_{55}\right) + \sqrt{c_{33}}\left(\sqrt{c_{11}} + \sqrt{c_{22}} + \sqrt{c_{33}}\right)\right] \int_{D(x_3)} v_{3,\alpha} v_{3,\alpha}\, da$$
$$+ \frac{1}{2\sqrt{\lambda}} \int_{D(x_3)} \left(c_{33} v_{3,3}^2 + c_{44} v_{2,3}^2 + c_{55} v_{1,3}^2\right) da. \tag{4.41}$$

By combining (4.36), (4.38) and (4.41) we obtain the first order differential inequality

$$\frac{dJ_\varkappa}{dx_3}(x_3) + \sigma_2 J_\varkappa(x_3) \leq 0 \quad \text{for all} \ \ x_3 \in [0, L], \tag{4.42}$$

whose integration furnishes the spatial decay expressed by (4.37). $\qquad \square$

The analysis of this section can be extended to the case of a semi-infinite cylinder, that is the case when $L \to \infty$. We shall exemplify this for the case of measure $J_\varkappa(x_3)$. In view of (4.25) and (4.32), by an integration $[x_3, L]$, we obtain

$$J_\varkappa(x_3) - J_\varkappa(L) = E(x_3, L), \tag{4.43}$$

where

$$
\begin{aligned}
E(x_3, L) = \int_{B(x_3,L)} \Big(& c_{11}v_{1,1}^2 + c_{22}v_{2,2}^2 + c_{33}v_{3,3}^2 + 2(c_{12}+\varkappa_3)v_{1,1}v_{2,2} + 2(c_{13}+\varkappa_2)v_{1,1}v_{3,3} \\
& + 2(c_{23}+\varkappa_1)v_{2,2}v_{3,3} + c_{66}(v_{1,2}^2+v_{2,1}^2) + 2(c_{66}-\varkappa_3)v_{1,2}v_{2,1} + c_{55}(v_{3,1}^2+v_{1,3}^2) \\
& + 2(c_{55}-\varkappa_2)v_{1,3}v_{3,1} + c_{44}(v_{3,2}^2+v_{2,3}^2) + 2(c_{44}-\varkappa_1)v_{2,3}v_{3,2} - \rho\omega^2 v_s v_s \Big) dv \geq 0, \quad (4.44)
\end{aligned}
$$

with $B(x_3, L) = B_{x_3} \backslash B_L$ and B_{x_3} is defined by relation (2.1). We conclude that $J_\varkappa(\infty) = \lim_{L\to\infty} J_\varkappa(L)$ exists and is finite if and only if there is finite the energetic measure $E(x_3) = \lim_{L\to\infty} E(x_3, L)$ associated with the amplitude v_r in the cylinder B_{x_3}. Since $J_\varkappa(x_3)$ is a nonincreasing function with respect to x_3, there are the only two possibilities: (a) $J_\varkappa(x_3) \geq 0$ for all $x_3 \in [0, \infty)$ or (b) there exists $x_3^* \in [0, \infty)$ so that $J_\varkappa(x_3^*) < 0$.

In the case (a) we can apply the same procedure as in the above to obtain the spatial decay estimate (4.37). So in what follows we shall consider the case (b), that is we will suppose that $J_\varkappa(x_3^*) < 0$. Then we have

$$
J_\varkappa(x_3) < 0 \quad \text{for all} \;\; x_3 \in [x_3^*, \infty), \tag{4.45}
$$

so that (4.36), (4.38), (4.41) and (4.45) now give

$$
\frac{dJ_\varkappa}{dx_3}(x_3) - \sigma_2 J_\varkappa(x_3) \leq 0 \quad \text{for all} \;\; x_3 \in [0, L], \tag{4.46}
$$

which implies

$$
-J_\varkappa(x_3) \geq -J_\varkappa(x_3^*) e^{\sigma_2(x_3-x_3^*)} \quad \text{for all} \;\; x_3 \in [x_3^*, \infty) \tag{4.47}
$$

and hence $J_\varkappa(\infty) = -\infty$ and the energetic measure $E(x_3)$ is infinite.

We may summarize this analysis in the following alternative of Phragmén–Lindelöf type result.

Theorem 6. *In the context of a semi-infinite cylinder made of a rhombic elastic material, for all harmonic vibrations with frequency lower than the critical value ω_2, the amplitude v_r either has a finite energetic measure $E(x_3)$ and then we have*

$$
E(x_3) \leq E(0) e^{-\sigma_2 x_3} \quad \text{for all} \;\; x_3 \in [0, \infty), \tag{4.48}
$$

or it has an infinite energetic measure and then $-J_\varkappa(x_3)$ goes to infinity faster than the exponential $e^{\sigma_2(x_3-x_3^*)}$.

5. Spatial estimates for appropriate high frequencies

Throughout this section we will study the spatial evolution of the amplitude v_r by starting with the identity established in Theorem 3. To this end we note that the strong ellipticity condition (2.5) implies that

$$
C_{k3l3}\zeta_k\zeta_l > 0 \quad \text{for all nonzero vectors} \;\; \zeta_r, \tag{5.1}
$$

and

$$
C_{ras\beta}m_r m_s n_\alpha n_\beta > 0 \quad \text{for all nonzero vectors} \;\; (m_1, m_2, m_3), \;\; (n_1, n_2). \tag{5.2}
$$

We further assume that ∂D is star shaped with respect to the origin so that $x_\rho n_\rho \geq h_0 > 0$, with h_0 constant.

On this basis we observe that

$$0 \leq \int_{\partial D(x_3)} x_\rho n_\rho C_{ram\beta} n_\alpha n_\beta \frac{\partial v_r}{\partial n} \frac{\partial v_m}{\partial n} ds \leq dC \int_{\partial D(x_3)} \frac{\partial v_r}{\partial n} \frac{\partial v_r}{\partial n} ds, \tag{5.3}$$

where $C = \sqrt{C_{ram\beta} C_{ram\beta}}$ and

$$d = \sup_{(x_1,x_2) \in \partial D} \sqrt{x_\alpha x_\alpha}. \tag{5.4}$$

Further, we introduce

$$m_0 = \max_{x_3 \in [0,L]} \frac{\int_{\partial D} \frac{\partial v_r}{\partial n} \frac{\partial v_r}{\partial n} ds}{\int_D v_r v_r \, da}, \qquad \omega^* = \frac{1}{\rho} dC m_0, \tag{5.5}$$

and assume that

$$\omega \geq \omega^*. \tag{5.6}$$

Whereas one cannot, in general, obtain m_0 explicitly, we have the crude bound

$$m_0 \leq m_1, \quad \text{with} \quad m_1 = \sup_{v_i \in H_0^1(D)} \frac{\int_{\partial D} \frac{\partial v_r}{\partial n} \frac{\partial v_r}{\partial n} ds}{\int_D v_r v_r \, da}. \tag{5.7}$$

So, when m_1 is finite, we can take $\omega^* = \frac{1}{\rho} dC m_1$ and obtain an explicit critical value for the frequency of vibration.

Then the identity (3.10), relations (5.3) and (5.6), and the definition of m_0 in (5.5) give

$$\frac{d}{dx_3} \int_{D(x_3)} \left[2C_{3rmn} v_{m,n} v_r + 2x_\rho C_{3smn} v_{s,\rho} v_{m,n} + x_3 \left(C_{r3m3} v_{r,3} v_{m,3} - C_{ram\beta} v_{r,\alpha} v_{m,\beta} + \rho\omega^2 v_s v_s \right) \right] da$$
$$\geq \int_{D(x_3)} C_{rsmn} v_{r,s} v_{m,n} \, da. \tag{5.8}$$

Our objective now is to find measures of the amplitude that are able to furnish information on the spatial evolution of the amplitude v_r for the entire class of anisotropic strongly elliptic elastic materials. We now pursue our method for transversely isotropic and rhombic systems.

5.1. *Transversely isotropic materials.*
We first consider the class of transversely isotropic materials as defined in Section 4.1. Relations (5.8), (3.11) and (3.12) give

$$\frac{d}{dx_3} \int_{D(x_3)} \left(v_\alpha \left((2c_{55} - \varkappa) v_{3,\alpha} + 2c_{55} v_{\alpha,3} \right) + v_3 \left(2c_{33} v_{3,3} + (2c_{13} + \varkappa) v_{\alpha,\alpha} \right) \right.$$
$$+ 2c_{55} x_\rho v_{\alpha,\rho} (v_{3,\alpha} + v_{\alpha,3}) + 2x_\rho v_{3,\rho} (c_{13} v_{\alpha,\alpha} + c_{33} v_{3,3})$$
$$+ x_3 \left[c_{55} (v_{1,3}^2 + v_{2,3}^2) + c_{33} v_{3,3}^2 - c_{66} (v_{1,2} - v_{2,1})^2 - c_{11} (v_{1,1} + v_{2,2})^2 \right.$$
$$\left. \left. - 2c_{13} v_{\alpha,\alpha} v_{3,3} - c_{55} v_{3,\alpha} v_{3,\alpha} - 2c_{55} v_{\alpha,3} v_{3,\alpha} + \rho\omega^2 v_s v_s \right] \right) da$$
$$\geq \int_{D(x_3)} c_{66} (v_{1,2} - v_{2,1})^2 \, da + \int_{D(x_3)} \left[c_{11} (v_{1,1} + v_{2,2})^2 + c_{33} v_{3,3}^2 + 2(c_{13} + \varkappa)(v_{1,1} + v_{2,2}) v_{3,3} \right] da$$
$$+ \int_{D(x_3)} \left[c_{55} (v_{3,1}^2 + v_{1,3}^2) + 2(c_{55} - \varkappa) v_{1,3} v_{3,1} + c_{55} (v_{3,2}^2 + v_{2,3}^2) + 2(c_{55} - \varkappa) v_{2,3} v_{3,2} \right] da, \tag{5.9}$$

where $\varkappa \in (0, 2c_{55})$ is a positive parameter chosen in such way to satisfy relation (4.4). Therefore, we can introduce the function

$$
\begin{aligned}
\mathcal{I}_\varkappa(x_3) = -\int_{D(x_3)} \Big(& v_\alpha\big((2c_{55} - \varkappa)v_{3,\alpha} + 2c_{55}v_{\alpha,3}\big) + v_3\big(2c_{33}v_{3,3} + (2c_{13} + \varkappa)v_{\alpha,\alpha}\big) \\
& + 2c_{55}x_\rho v_{\alpha,\rho}(v_{3,\alpha} + v_{\alpha,3}) + 2x_\rho v_{3,\rho}(c_{13}v_{\alpha,\alpha} + c_{33}v_{3,3}) \\
& + x_3\big[c_{55}(v_{1,3}^2 + v_{2,3}^2) + c_{33}v_{3,3}^2 - c_{66}(v_{1,2} - v_{2,1})^2 - c_{11}(v_{1,1} + v_{2,2})^2 \\
& - 2c_{13}v_{\alpha,\alpha}v_{3,3} - c_{55}v_{3,\alpha}v_{3,\alpha} - 2c_{55}v_{\alpha,3}v_{3,\alpha} + \rho\omega^2 v_s v_s\big] \Big) \, da \quad (5.10)
\end{aligned}
$$

and note that relations (4.4), (4.6), (4.8) and (5.9) imply

$$
-\frac{d\mathcal{I}_\varkappa}{dx_3}(x_3) \geq \min(c_{66}, \nu_2) \int_{D(x_3)} v_{\alpha,\beta}v_{\alpha,\beta} \, da + \nu_2 \int_{D(x_3)} v_{3,3}^2 \, da + \nu_1 \int_{D(x_3)} v_{\alpha,3}v_{\alpha,3} \, da + \nu_1 \int_{D(x_3)} v_{3,\beta}v_{3,\beta} \, da
$$
$$
\geq 0. \tag{5.11}
$$

Thus, $\mathcal{I}_\varkappa(x_3)$ is a nonincreasing function with respect to x_3 on $[0, L]$.

Theorem 7. *Let v_r be the amplitude of a harmonic vibration whose frequency is greater than the critical frequency*

$$
\omega_1^* = \frac{dm_0}{\rho}\sqrt{2c_{11}^2 + 2c_{12}^2 + (c_{11} - c_{12})^2 + 2c_{55}^2}.
$$

Then the cross section integral $\mathcal{I}_\varkappa(x_3)$ as defined by (5.10) is an acceptable measure of the amplitude v_r (that is, $\mathcal{I}_\varkappa(x_3) \geq 0$ and $\mathcal{I}_\varkappa(x_3) = 0$ implies that $v_r = 0$) and it satisfies the spatial decay estimate

$$
0 \leq \mathcal{I}_\varkappa(x_3) \leq \mathcal{I}_\varkappa(0)\left(1 + \frac{\beta}{\alpha}x_3\right)^{-1/\beta} \quad \text{for all } x_3 \in [0, L], \tag{5.12}
$$

where α and β are positive constants computable in terms of the elastic coefficients, λ, d, ω and ρ.

Proof. On the basis of the end boundary condition (2.15) and relation (5.10) we deduce that $\mathcal{I}_\varkappa(L) = 0$, so that we have

$$
\mathcal{I}_\varkappa(x_3) \geq 0 \quad \text{for all } x_3 \in [0, L]. \tag{5.13}
$$

Thus, $\mathcal{I}_\varkappa(x_3)$ represents an acceptable measure for the amplitude v_r of the harmonic vibration.

On the other hand, by using the Schwarz and arithmetic-geometric mean inequalities, from (4.10), (5.4) and (5.10) we obtain the estimates

$$
\left| \int_{D(x_3)} \big[v_\alpha\big((2c_{55} - \varkappa)v_{3,\alpha} + 2c_{55}v_{\alpha,3}\big) + v_3\big(2c_{33}v_{3,3} + (2c_{13} + \varkappa)v_{\alpha,\alpha}\big)\big] \, da \right|
$$
$$
\leq \frac{2}{\sqrt{\lambda}}(2c_{55} + \sqrt{c_{11}c_{33}}) \int_{D(x_3)} v_{\alpha,\beta}v_{\alpha,\beta} \, da + \frac{c_{55}}{\sqrt{\lambda}} \int_{D(x_3)} v_{\alpha,3}v_{\alpha,3} \, da
$$
$$
+ \frac{1}{\sqrt{\lambda}}(2c_{55} + c_{33} + \sqrt{c_{11}c_{33}}) \int_{D(x_3)} v_{3,\alpha}v_{3,\alpha} \, da + \frac{c_{33}}{\sqrt{\lambda}} \int_{D(x_3)} v_{3,3}^2 \, da, \tag{5.14}
$$

$$\left| \int_{D(x_3)} \left[2c_{55}x_\rho v_{\alpha,\rho}(v_{3,\alpha}+v_{\alpha,3}) + 2x_\rho v_{3,\rho}(c_{13}v_{\alpha,\alpha}+c_{33}v_{3,3}) \right] da \right|$$

$$\leq d(c_{55}+2\,|c_{13}|) \int_{D(x_3)} v_{\alpha,\beta}v_{\alpha,\beta}\,da + 2dc_{55} \int_{D(x_3)} v_{\alpha,3}v_{\alpha,3}\,da$$

$$+ d(2c_{55}+2c_{33}+|c_{13}|) \int_{D(x_3)} v_{3,\alpha}v_{3,\alpha}\,da + 2dc_{33} \int_{D(x_3)} v_{3,3}^2\,da, \quad (5.15)$$

$$\left| \int_{D(x_3)} \left[c_{55}(v_{1,3}^2+v_{2,3}^2) + c_{33}v_{3,3}^2 - c_{66}(v_{1,2}-v_{2,1})^2 - c_{11}(v_{1,1}+v_{2,2})^2 \right.\right.$$

$$\left.\left. - 2c_{13}v_{\alpha,\alpha}v_{3,3} - c_{55}v_{3,\alpha}v_{3,\alpha} - 2c_{55}v_{\alpha,3}v_{3,\alpha} + \rho\omega^2 v_s v_s \right] da \right|$$

$$\leq \left(\max(c_{11},c_{66}) + 2\,|c_{13}| + \frac{\rho\omega^2}{\lambda} \right) \int_{D(x_3)} v_{\alpha,\beta}v_{\alpha,\beta}\,da + 2c_{55} \int_{D(x_3)} v_{\alpha,3}v_{\alpha,3}\,da$$

$$+ \left(2c_{55} + \frac{\rho\omega^2}{\lambda} \right) \int_{D(x_3)} v_{3,\alpha}v_{3,\alpha}\,da + (c_{33}+|c_{13}|) \int_{D(x_3)} v_{3,3}^2\,da. \quad (5.16)$$

Therefore, if we use the estimates (5.14)–(5.16) in (5.10) and then use (5.11), we obtain the differential inequality

$$|\mathcal{I}_\varkappa(x_3)| \leq -(\alpha+\beta x_3)\frac{d\mathcal{I}_\varkappa}{dx_3}(x_3) \quad \text{for all } x_3 \in [0, L], \quad (5.17)$$

where

$$\alpha = \max \left\{ \frac{1}{\min(c_{66}, v_2)} \left[\left(\frac{4}{\sqrt{\lambda}} + d \right)c_{55} + \frac{2}{\sqrt{\lambda}}\sqrt{c_{11}c_{33}} + 2d\,|c_{13}| \right], \right.$$

$$\frac{1}{v_1} \left[2\left(\frac{1}{\sqrt{\lambda}} + d \right)c_{55} + \left(\frac{1}{\sqrt{\lambda}} + 2d \right)c_{33} + \frac{1}{\sqrt{\lambda}}\sqrt{c_{11}c_{33}} + d\,|c_{13}| \right],$$

$$\left. \frac{1}{v_1}\left(\frac{1}{\sqrt{\lambda}} + 2d \right)c_{55}, \frac{1}{v_2}\left(\frac{1}{\sqrt{\lambda}} + 2d \right)c_{33} \right\}, \quad (5.18)$$

$$\beta = \max \left\{ \frac{1}{\min(c_{66}, v_2)}\left(\max(c_{11}, c_{66}) + 2\,|c_{13}| + \frac{\rho\omega^2}{\lambda} \right), \frac{1}{v_1}\left(2c_{55} + \frac{\rho\omega^2}{\lambda} \right), \frac{2c_{55}}{v_1}, \frac{c_{33}+|c_{13}|}{v_2} \right\}. \quad (5.19)$$

To integrate the differential inequality (5.17) we write it in the form

$$\frac{d\mathcal{I}_\varkappa}{dx_3}(x_3) + \frac{d}{dx_3}\left(\int_0^{x_3} \frac{1}{\alpha+\beta t}dt \right)\mathcal{I}_\varkappa(x_3) \leq 0 \quad \text{for all } x_3 \in [0, L], \quad (5.20)$$

which, multiplied by $\exp\left(\int_0^{x_3} dt/(\alpha+\beta t) \right)$ and then integrated with respect to x_3, gives the estimate (5.12). □

5.2. Rhombic materials. For a rhombic material, we proceed similarly. Relation (5.8) combined with (3.11) and (3.12) gives

$$-\frac{d}{dx_3}\mathcal{J}_\varkappa(x_3)$$

$$\geq \int_{D(x_3)} \left(c_{11}v_{1,1}^2 + c_{22}v_{2,2}^2 + c_{33}v_{3,3}^2 + 2(c_{12}+\varkappa_3)v_{1,1}v_{2,2} + 2(c_{13}+\varkappa_2)v_{1,1}v_{3,3} + 2(c_{23}+\varkappa_1)v_{2,2}v_{3,3} \right) da$$

$$+ \int_{D(x_3)} \left(c_{66}v_{1,2}^2 + c_{66}v_{2,1}^2 + 2(c_{66}-\varkappa_3)v_{1,2}v_{2,1} \right) da + \int_{D(x_3)} \left(c_{55}v_{3,1}^2 + c_{55}v_{1,3}^2 + 2(c_{55}-\varkappa_2)v_{1,3}v_{3,1} \right) da$$

$$+ \int_{D(x_3)} \left(c_{44}v_{3,2}^2 + c_{44}v_{2,3}^2 + 2(c_{44}-\varkappa_1)v_{2,3}v_{3,2} \right) da, \quad (5.21)$$

where $\varkappa_1$, $\varkappa_2$, $\varkappa_3$ satisfy the conditions requested in Section 4.2 and we have introduced the function

$$\mathcal{J}_\varkappa(x_3) = -\int_{D(x_3)} \Big(v_1\big((2c_{55}-\varkappa_2)v_{3,1} + 2c_{55}v_{1,3}\big) + v_2\big((2c_{44}-\varkappa_1)v_{3,2} + 2c_{44}v_{2,3}\big)$$

$$+ v_3\big((2c_{13}+\varkappa_2)v_{1,1} + (2c_{23}+\varkappa_1)v_{2,2} + 2c_{33}v_{3,3}\big) + 2c_{55}x_\rho v_{1,\rho}(v_{3,1}+v_{1,3})$$

$$+ 2c_{44}x_\rho v_{2,\rho}(v_{3,2}+v_{2,3}) + 2x_\rho v_{3,\rho}(c_{13}v_{1,1}+c_{23}v_{2,2}+c_{33}v_{3,3})$$

$$+ x_3\big[c_{55}v_{1,3}^2 + c_{44}v_{2,3}^2 + c_{33}v_{3,3}^2 - c_{66}(v_{1,2}+v_{2,1})^2$$

$$- (c_{11}v_{1,1}^2 + c_{22}v_{2,2}^2 + 2c_{12}v_{1,1}v_{2,2} + c_{55}v_{3,1}^2 + c_{44}v_{3,2}^2) + \rho\omega^2 v_s v_s\big] \Big) da. \quad (5.22)$$

Now (4.26)–(4.29) and (5.21) give

$$-\frac{d\mathcal{J}_\varkappa}{dx_3}(x_3) \geq \int_{D(x_3)} \left(\xi_4(v_{1,1}^2+v_{2,2}^2) + \xi_3(v_{1,2}^2+v_{2,1}^2) + \xi_1 v_{3,2}^2 + \xi_2 v_{3,1}^2 \right) da + \int_{D(x_3)} \left(\xi_1 v_{2,3}^2 + \xi_2 v_{1,3}^2 + \xi_4 v_{3,3}^2 \right) da$$

$$\geq 0; \quad (5.23)$$

hence $\mathcal{J}_\varkappa(x_3)$ is a nonincreasing function with respect to x_3 on $[0, L]$. Moreover, by means of the end condition (2.15) and relation (5.22) we obtain $\mathcal{J}_\varkappa(L) = 0$ and hence $\mathcal{J}_\varkappa(x_3) \geq 0$ for all $x_3 \in [0, L]$, that is $\mathcal{J}_\varkappa(x_3)$ is a measure of the amplitude of the harmonic vibration.

By using the Schwarz and arithmetic-geometric mean inequalities and with the aid of (4.10), (4.40) and (5.4), we obtain

$$\left| \int_{D(x_3)} \Big(v_1\big((2c_{55}-\varkappa_2)v_{3,1} + 2c_{55}v_{1,3}\big) + v_2\big((2c_{44}-\varkappa_1)v_{3,2} + 2c_{44}v_{2,3}\big) \right.$$

$$\left. + v_3\big((2c_{13}+\varkappa_2)v_{1,1} + (2c_{23}+\varkappa_1)v_{2,2} + 2c_{33}v_{3,3}\big) \Big) da \right|$$

$$\leq \frac{1}{\sqrt{\lambda}} \int_{D(x_3)} \Big[\big(3c_{55} + \sqrt{c_{11}c_{33}}\big)v_{1,1}^2 + \big(3c_{44} + \sqrt{c_{22}c_{33}}\big)v_{2,2}^2 + 2c_{55}v_{1,2}^2 + 2c_{44}v_{2,1}^2$$

$$+ \big(c_{33}+c_{44}+2c_{55}+\sqrt{c_{11}c_{33}}+\sqrt{c_{22}c_{33}}\big)v_{3,1}^2$$

$$+ \big(c_{33}+2c_{44}+c_{55}+\sqrt{c_{11}c_{33}}+\sqrt{c_{22}c_{33}}\big)v_{3,2}^2 + c_{55}v_{1,3}^2 + c_{44}v_{2,3}^2 + c_{33}v_{3,3}^2 \Big] da, \quad (5.24)$$

$$\left| \int_{D(x_3)} \big(2c_{55}x_\rho v_{1,\rho}(v_{3,1}+v_{1,3}) + 2c_{44}x_\rho v_{2,\rho}(v_{3,2}+v_{2,3}) + 2x_\rho v_{3,\rho}(c_{13}v_{1,1}+c_{23}v_{2,2}+c_{33}v_{3,3})\big) da \right|$$

$$\leq d \int_{D(x_3)} \Big[(c_{55}+|c_{13}|)v_{1,1}^2 + (c_{44}+|c_{23}|)v_{2,2}^2 + c_{55}v_{1,2}^2 + c_{44}v_{2,1}^2 + (c_{33}+2c_{55}+|c_{13}|+|c_{23}|)v_{3,1}^2$$

$$+ (c_{33}+2c_{44}+|c_{13}|+|c_{23}|)v_{3,2}^2 + 2c_{55}v_{1,3}^2 + 2c_{44}v_{2,3}^2 + c_{33}v_{3,3}^2 \Big] da, \quad (5.25)$$

$$\left| \int_{D(x_3)} \left[c_{55}v_{1,3}^2 + c_{44}v_{2,3}^2 + c_{33}v_{3,3}^2 - c_{66}(v_{1,2} + v_{2,1})^2 \right. \right.$$
$$- (c_{11}v_{1,1}^2 + c_{22}v_{2,2}^2 + 2c_{12}v_{1,1}v_{2,2} + c_{55}v_{3,1}^2 + c_{44}v_{3,2}^2) + \rho\omega^2 v_s v_s \big] da \bigg|$$

$$\leq \int_{D(x_3)} \left[\left(c_{11} + |c_{12}| + \frac{\rho\omega^2}{\lambda} \right) v_{1,1}^2 + \left(c_{22} + |c_{12}| + \frac{\rho\omega^2}{\lambda} \right) v_{2,2}^2 + \left(2c_{66} + \frac{\rho\omega^2}{\lambda} \right) (v_{1,2}^2 + v_{2,1}^2) \right.$$
$$\left. + \left(c_{55} + \frac{\rho\omega^2}{\lambda} \right) v_{3,1}^2 + \left(c_{44} + \frac{\rho\omega^2}{\lambda} \right) v_{3,2}^2 + c_{55}v_{1,3}^2 + c_{44}v_{2,3}^2 + c_{33}v_{3,3}^2 \right] da. \quad (5.26)$$

To conclude, we obtain from (5.22)–(5.26) a first order differential inequality of type (5.17), where now we have

$$\alpha = \max \left\{ \frac{1}{\xi_4} \left(\frac{1}{\sqrt{\lambda}} (3c_{55} + \sqrt{c_{11}c_{33}}) + d(c_{55} + |c_{13}|) \right), \ \frac{1}{\xi_3} c_{55} \left(\frac{2}{\sqrt{\lambda}} + d \right), \ \frac{1}{\xi_3} c_{44} \left(\frac{2}{\sqrt{\lambda}} + d \right), \right.$$
$$\frac{1}{\xi_4} \left(\frac{1}{\sqrt{\lambda}} (3c_{44} + \sqrt{c_{22}c_{33}}) + d(c_{44} + |c_{23}|) \right), \ \frac{1}{\xi_2} c_{55} \left(\frac{1}{\sqrt{\lambda}} + 2d \right), \ \frac{1}{\xi_1} c_{44} \left(\frac{1}{\sqrt{\lambda}} + 2d \right),$$
$$\frac{1}{\xi_2} \left(\frac{1}{\sqrt{\lambda}} (c_{44} + 2c_{55} + c_{33} + \sqrt{c_{11}c_{33}} + \sqrt{c_{22}c_{33}}) + d(c_{33} + 2c_{55} + |c_{13}| + |c_{23}|) \right),$$
$$\frac{1}{\xi_1} \left(\frac{1}{\sqrt{\lambda}} (2c_{44} + c_{55} + c_{33} + \sqrt{c_{11}c_{33}} + \sqrt{c_{22}c_{33}}) + d(c_{33} + 2c_{44} + |c_{13}| + |c_{23}|) \right),$$
$$\left. \frac{1}{\xi_4} c_{33} \left(\frac{1}{\sqrt{\lambda}} + d \right) \right\}, \quad (5.27)$$

$$\beta = \max \left\{ \frac{1}{\xi_4} \left(c_{11} + |c_{12}| + \frac{\rho\omega^2}{\lambda} \right), \ \frac{1}{\xi_4} \left(c_{22} + |c_{12}| + \frac{\rho\omega^2}{\lambda} \right), \ \frac{1}{\xi_3} \left(2c_{66} + \frac{\rho\omega^2}{\lambda} \right), \right.$$
$$\left. \frac{1}{\xi_2} \left(c_{55} + \frac{\rho\omega^2}{\lambda} \right), \ \frac{1}{\xi_1} \left(c_{44} + \frac{\rho\omega^2}{\lambda} \right), \ \frac{1}{\xi_4} c_{33} \right\}. \quad (5.28)$$

Therefore, the spatial evolution of the amplitude is described by the estimate (5.12), where α and β are given now by relations (5.27) and (5.28) and ω_1^* is replaced by

$$\omega_2^* = \frac{dm_0}{\rho} \sqrt{c_{11}^2 + c_{22}^2 + c_{44}^2 + c_{55}^2 + 2c_{12}^2 + 4c_{66}^2}. \quad (5.29)$$

The analysis of this section can be extended to a semi-infinite cylinder using the procedure developed at the end of the above section.

6. Concluding remarks

We have addressed some exponential and algebraic spatial estimates for describing how the amplitude of a harmonic vibration evolves in an anisotropic elastic cylinder. The discussion is based on the assumption regarding the strong ellipticity of the elasticity tensor. This hypothesis allows us to obtain results valid for a very large class of anisotropic elastic materials, including auxetic materials (which, having a negative Poisson's ratio or negative stiffness, expand laterally when stretched in contrast to ordinary materials; see [Park and Lakes 2007], for example).

Exponential spatial decay estimates are predicted for harmonic vibrations whose frequency is lower than a certain critical value, as defined by relations (4.11) and (4.34), for example. However, as we can see from relations (4.15), (4.16), (4.37) and (4.38), these estimates fall to give information regarding the spatial evolution for harmonic vibrations with frequency close to the critical value.

On the other hand, the algebraic spatial estimate (5.12) proves how the spatial behavior evolves in the case of harmonic vibrations with frequency greater than the critical value ω^* as defined in (5.5).

The extent to which our present results cover the entire range of frequencies remains open question.

Acknowledgement

References

[Boley 1955] B. A. Boley, "Application of Saint-Venant's principle in dynamical problems", *J. Appl. Mech.* (*ASME*) **22** (1955), 204–206.

[Boley 1960] B. A. Boley, "On a dynamical Saint Venant principle", *J. Appl. Mech.* (*ASME*) **27** (1960), 74–78.

[Chiriţă 2006] S. Chiriţă, "On the strong ellipticity condition for transversely isotropic linearly elastic solids", *An. Ştiinţ. Univ. Al. I. Cuza Iaşi. Mat.* (*N.S.*) **52**:2 (2006), 245–250.

[Chiriţă and Ciarletta 1999] S. Chiriţă and M. Ciarletta, "Time-weighted surface power function method for the study of spatial behaviour in dynamics of continua", *Eur. J. Mech. A Solids* **18**:5 (1999), 915–933.

[Chiriţă and Ciarletta 2006] S. Chiriţă and M. Ciarletta, "Spatial estimates for the constrained anisotropic elastic cylinder", *J. Elasticity* **85**:3 (2006), 189–213.

[Chiriţă and Ciarletta 2008] S. Chiriţă and M. Ciarletta, "On the structural stability of thermoelastic model of porous media", *Math. Methods Appl. Sci.* **31**:1 (2008), 19–34.

[Chiriţă and Quintanilla 1996] S. Chiriţă and R. Quintanilla, "On Saint-Venant's principle in linear elastodynamics", *J. Elasticity* **42**:3 (1996), 201–215.

[Chiriţă et al. 2006] S. Chiriţă, M. Ciarletta, and B. Straughan, "Structural stability in porous elasticity", *Proc. R. Soc. Lond. A* **462**:2073 (2006), 2593–2605.

[Chiriţă et al. 2007] S. Chiriţă, A. Danescu, and M. Ciarletta, "On the strong ellipticity of the anisotropic linearly elastic materials", *J. Elasticity* **87**:1 (2007), 1–27.

[Flavin and Knops 1987] J. N. Flavin and R. J. Knops, "Some spatial decay estimates in continuum dynamics", *J. Elasticity* **17**:3 (1987), 249–264.

[Flavin et al. 1990] J. N. Flavin, R. J. Knops, and L. E. Payne, "Energy bounds in dynamical problems for a semi-infinite elastic beam", pp. 101–111 in *Elasticity: mathematical methods and applications*, edited by G. Eason and R. W. Ogden, Horwood, Chichester, 1990.

[Gurtin 1972] M. E. Gurtin, "The linear theory of elasticity", pp. 1–295 in *Mechanics of solids*, edited by C. Truesdell, Handbuch der Physik **VIa/2**, Springer, Berlin, 1972.

[Horgan 1989] C. O. Horgan, "Recent developments concerning Saint-Venant's principle: an update", *Appl. Mech. Rev.* **42**:11-1 (1989), 295–303.

[Horgan 1996] C. O. Horgan, "Recent developments concerning Saint-Venant's principle: a second update", *Appl. Mech. Rev.* **49** (1996), S101–S111.

[Horgan and Knowles 1983] C. O. Horgan and J. K. Knowles, "Recent developments concerning Saint-Venant's principle", *Adv. Appl. Mech.* **23** (1983), 179–269.

[Knops 1991] R. J. Knops, "Spatial decay estimates in the vibrating anisotropic elastic beam", pp. 192–203 in *Waves and stability in continuous media* (Sorrento, 1989), edited by S. Rionero, Series on Advances in Mathematics for Applied Science **4**, World Scientific, River Edge, NJ, 1991.

[Park and Lakes 2007] J. B. Park and R. S. Lakes, *Biomaterials: an introduction*, 3rd ed., Springer, Berlin, 2007.

[Tibullo and Vaccaro 2008] V. Tibullo and M. Vaccaro, "Spatial behaviour for constrained motion of a cylinder made of a strongly elliptic anisotropic material", *J. Mech. Mater. Struct.* **3**:5 (2008), 983–993.

STAN CHIRIȚĂ: schirita@uaic.ro
Faculty of Mathematics, Al.I. Cuza University of Iași, Blvd. Carol I, nr. 11, 700506 - Iași, Romania

MICHELE CIARLETTA: ciarlett@diima.unisa.it
Dipartimento di Ingegneria dell'Informazione e Matematica Applicata (DIIMA), Università di Salerno, Via Ponte Don Melillo, 84084 Fisciano (SA), Italy

SOFTENING HYPERVISCOELASTICITY FOR MODELING RATE-DEPENDENT MATERIAL FAILURE

KONSTANTIN VOLOKH AND PAVEL TRAPPER

New models of viscoelastic solids at small and finite deformations are proposed that describe material failure by enforcing the energy limiter — the average bond energy. Basically, the bond energy defines the energy that is necessary to separate two attracting particles. In the case of a solid composed of many particles there exists a magnitude of the average bond energy that is necessary to separate particles in a small material volume. The average bond energy can be calculated if a statistical distribution of the bond density is known for a particular material. Alternatively, the average bond energy can be determined in macroscopic experiments if the energy limiter is introduced in a material constitutive model. Traditional viscoelastic models of materials do not have energy limiters and, consequently, they allow for unlimited energy accumulation under the strain increase. The latter is unphysical, of course, because no material can sustain large enough deformations without failure. The average bond energy is the energy limiter that controls material softening, which indicates failure. Thus, by limiting the stored energy we include a description of material failure in the constitutive model. Viscoelasticity including energy limiters can be called softening hyperviscoelasticity. We present two softening hyperviscoelasticity models for small and finite deformations. In all cases the elastic and viscoelastic responses are described by potentials with limiters, which control material softening. The models are studied in the case of simple shear and uniaxial tension. The results of the calculations show that softening hyperviscoelasticity can be used for analysis of rate-dependent failure of materials.

1. Introduction

Existing continuum mechanics approaches for modeling material failure can be divided in two groups: surface and bulk models. The surface models, pioneered by Barenblatt [1959], are called cohesive zone models (CZMs) in the modern literature. They present material surfaces — cohesive zones — where displacement discontinuities occur. The discontinuities are enhanced with constitutive laws relating normal and tangential displacement jumps with the corresponding tractions. There are plenty of proposals of constitutive equations for cohesive zones [Dugdale 1960; Rice and Wang 1989; Tvergaard and Hutchinson 1992; Xu and Needleman 1994; Camacho and Ortiz 1996]. All CZMs are constructed qualitatively as follows: tractions increase, reach a maximum, and then approach zero with increasing separation. Such a scenario is in harmony with our intuitive understanding of the rupture process. Since the work by Needleman [1987] CZMs are used increasingly in finite element simulations of many phenomena, such as crack tip plasticity and creep, crazing in polymers, adhesively bonded joints, interface cracks in bimaterials, delamination in composites and multilayers, and fast crack propagation in polymers. Cohesive zones can be inside finite elements or along their boundaries [Xu and Needleman 1994; Belytschko

---

et al. 2001; De Borst 2001]. Crack nucleation, propagation, branching, kinking, and arrest are natural outcomes of the computations where the discontinuity surfaces are spread over the bulk material. This is in contrast to the traditional approach of fracture mechanics where stress analysis is separated from a description of the actual process of material failure. The CZM approach is natural for simulation of fracture at the *internal material interfaces* in polycrystals, composites, and multilayers. It is less natural for modeling bulk fracture because it leads to the simultaneous use of two material models for the same real material: one model describes the bulk while the other model describes a CZM imbedded in the bulk. Such a two-model approach is rather artificial physically. It seems preferable to incorporate a material failure law directly in the constitutive description of the bulk.

Remarkably, the first models of bulk failure — damage mechanics — proposed by Kachanov [1958] and Rabotnov [1963] for analysis of the gradual failure accumulation and propagation in *creep* and *fatigue* appeared almost simultaneously with the cohesive zone approach. The need to describe the failure *accumulation*, that is, evolution of the material microstructure, explains why damage mechanics is very similar to plasticity theories including the internal damage variable (inelastic strain), the critical threshold condition (yield surface), and the damage evolution equation (flow rule). The subsequent development of the formalism of damage mechanics [Kachanov 1986; Krajcinovic 1996; Skrzypek and Ganczarski 1999; Lemaitre and Desmorat 2005] left its physical origin well behind the mathematical and computational techniques and, eventually, led to the use of damage mechanics for the description of *any* bulk failure. Theoretically, the approach of damage mechanics is very flexible and allows reflecting physical processes triggering macroscopic damage at small length scales. Practically, the experimental calibration of damage theories is not trivial because it is difficult to measure the damage parameter directly. The experimental calibration should be implicit and include both the damage evolution equation and criticality condition.

A physically motivated alternative to damage mechanics in the cases of failure related with the bond rupture has been considered recently by Gao and Klein [1998] and Klein and Gao [1998] who showed how to mix the atomic/molecular and continuum descriptions in order to simulate material failure. They applied the Cauchy–Born rule linking micro and macro scales to empirical potentials, which include a possibility of the full atomic separation. The continuum-atomistic link led to the formulation of the macroscopic strain energy potentials allowing for the stress/strain softening and strain localization. The continuum-atomistic method is very effective at small length scales where purely atomistic analysis becomes computationally intensive. Unfortunately, a direct use of the continuum-atomistic method in macroscopic failure problems is not very feasible because its computer implementation includes a numerically involved procedure of the averaging of the interatomic potentials over a representative volume.

In order to bypass the computational intensity of the continuum-atomistic method while preserving its sound physical basis the *softening hyperelasticity* approach was proposed by Volokh [2004; 2007a; 2007b]. The basic idea of the approach was to formulate an expression of the stored macroscopic energy, which would include the energy limiter — the average bond energy. Such a limiter automatically induces strain softening, that is, a material failure description, in the constitutive law. The softening hyperelasticity approach is computationally simple yet physically appealing. The approach proved itself in a number of problems varying from failure of brittle materials to rubbers and soft biological tissues [Volokh 2007a; 2007b; 2008a; 2008b; Trapper and Volokh 2008; Volokh and Trapper 2008; Volokh and Vorp 2008]. Besides Gei et al. [2004] used a variant of softening hyperelasticity for modeling plastic softening. One should be careful, however, with doing that because material failure during plastic

deformation is essentially due to microstructural changes rather than the bond rupture and the approach of energy limiters may not be applicable in this case on physical grounds.

It should be noted that softening hyperelasticity has been used for the prediction of the global material/structural instability in all mentioned works. To extend the approach to problems of dynamic failure propagation it is necessary to include rate-dependence in the constitutive description. In other words, the softening hyperelasticity should be extended to the softening hyperviscoelasticity, which is the main goal of the present work. Including viscosity in the constitutive framework is important physically. It is also important computationally because viscosity naturally regularizes the potentially ill conditioned problems related to tracking the propagation of dynamic failure.

The outline of the paper is as follows. Section 2 introduces the idea of the energy limiters providing a physical multiscale link for the phenomenological quantity of the average bond energy. Sections 3 and 4 present the softening hyperviscoelasticity theories for small and finite deformations respectively. A general discussion of the new theories is present in Section 5.

2. Energy limiters

To motivate the introduction of energy limiters and softening hyperelasticity we briefly describe the continuum-atomistic link. A more detailed exposition of the issue can be found in [Volokh and Trapper 2008; Trapper and Volokh 2008], for example.

Interaction of two particles (atoms, molecules, et cetera) can be described as

$$\psi(F) = \varphi(F) - \varphi_0, \qquad \varphi_0 = \min_L \varphi(F = 1). \tag{2-1}$$

Here ψ is the particle interaction potential; F is the one-dimensional deformation gradient mapping the distance between particles from the reference, L, to the current, l, state: $l = FL$. To be specific we choose the Lennard-Jones potential, for example, $\varphi(l) = 4\varepsilon((\sigma/l)^{12} - (\sigma/l)^6)$, where ε and σ are the bond energy and length constants accordingly. By direct computation we can find the energy limiter or the failure energy, Φ. Indeed, increasing deformation we cannot increase the energy unlimitedly:

$$\psi(F \to \infty) = -\varphi_0 = \Phi = \text{constant}. \tag{2-2}$$

Analogously to the case of the pair interaction it is possible to consider particle assemblies. Applying the assumption of applicability of continuum mechanics to the description of such assemblies, meaning using the Cauchy–Born rule, it is possible to derive a stored energy function analogously to (2-1),

$$\psi(\boldsymbol{C}) = \langle \varphi(\boldsymbol{C}) \rangle - \langle \varphi \rangle_0, \qquad \langle \varphi \rangle_0 = \min_L \langle \varphi(\boldsymbol{C} = \boldsymbol{1}) \rangle.$$

Here $\boldsymbol{C} = \boldsymbol{F}^T \boldsymbol{F}$ is the right Cauchy–Green deformation tensor and $\boldsymbol{F} = \partial \boldsymbol{x}/\partial \boldsymbol{X}$ is the deformation gradient of a generic material macroparticle of body Ω occupying position $\boldsymbol{X}$ at the reference state and position $\boldsymbol{x}(\boldsymbol{X})$ at the current state of deformation. The average means

$$\langle \varphi(\boldsymbol{C}) \rangle = V_0^{-1} \int_{V_0^*} 4\varepsilon\left(\left(\frac{\sigma}{L\|\boldsymbol{C}\|}\right)^{12} - \left(\frac{\sigma}{L\|\boldsymbol{C}\|}\right)^6\right) D_V \, dV,$$

in the case of the Lennard-Jones potential, where the tensorial norm designates stretch in a bond direction, D_V is the volumetric bond density function, V_0^* is the integration volume defined by the range of influence of φ, and V_0 is the reference representative volume.

Analogously to (2-2), we can find the energy limiter, Φ, increasing the deformation unlimitedly as

$$\Phi = \psi\big(\|\boldsymbol{C}\| \to \infty\big) = -\langle \varphi \rangle_0 = \text{constant}.$$

Thus, *the average bond energy sets a limit for the energy accumulation.* This conclusion generally does not depend on the choice of the particle potential and is valid for any interaction that includes a possible particle separation.

Contrary to the conclusion above traditional hyperelastic models of materials do not include the energy limiter. The stored energy of hyperelastic materials is defined as $\psi = W$. Here W is used for the strain energy of the *intact* material, which can be characterized as $\|\boldsymbol{C}\| \to \infty \Rightarrow \psi = W \to \infty$, where $\|\cdots\|$ is a tensorial norm.

In other words, the increasing strain increases the accumulated energy unlimitedly. Evidently, the consideration of only intact materials is restrictive and unphysical. The energy increase of a real material should be limited, as shown above:

$$\|\boldsymbol{C}\| \to \infty \Rightarrow \psi \to \Phi = \text{constant}, \tag{2-3}$$

where the average bond energy, $\Phi = \text{constant}$, can be called the *material failure energy*.

Equation (2-3) presents the fundamental idea of introducing a limiter of the stored energy in the elasticity theory. Such a limiter induces material softening, indicating material failure, automatically. *The choice of the limited stored energy expression should generally be material-specific.* Nonetheless, a somewhat universal formula [Volokh 2007b] can be introduced to enrich the already existing models of intact materials with the failure description

$$\psi(W) = \Phi - \Phi \exp\Big(\frac{-W}{\Phi}\Big), \tag{2-4}$$

where $\psi(W = 0) = 0$ and $\psi(W = \infty) = \Phi$.

Formula (2-4) obeys the condition $\|\boldsymbol{C}\| \to \infty \Rightarrow \psi(W(\boldsymbol{C})) \to \Phi$ and, in the case of the intact material behavior, $W \ll \Phi$, we have $\psi(W) \approx W$ preserving the features of the intact material.

Taking (2-4) into account, the constitutive equation can be written in the general form

$$\boldsymbol{\sigma} = 2J^{-1}\boldsymbol{F}\frac{\partial \psi}{\partial \boldsymbol{C}}\boldsymbol{F}^T = 2J^{-1}\boldsymbol{F}\frac{\partial W}{\partial \boldsymbol{C}}\boldsymbol{F}^T \exp\Big(\frac{-W}{\Phi}\Big), \tag{2-5}$$

where $\boldsymbol{\sigma}$ is the Cauchy stress tensor, $J = \det \boldsymbol{F}$, and the exponential multiplier enforces material softening. Constitutive equation (2-5) is especially effective for *incompressible soft materials undergoing finite deformations.* We strongly emphasize again, however, that *the best form of the energy function is not universal and should be material/problem-specific.*

In what follows we will extend the idea of the energy limiter to viscous deformations and examine the role of the rate-dependence in the description of material failure.

3. Softening hyperviscoelasticity at small deformations

We use a rheological model of the standard solid shown in Figure 1 as a prototype for the integral formulation of the constitutive law.
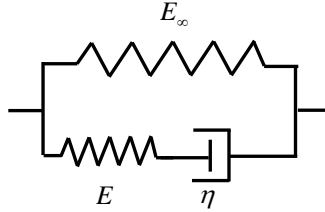
Figure 1. Rheological model of the standard solid.

3.1. *Constitutive law.* Following Simo and Hughes [1998] we define the hyperviscoelastic constitutive law in the form

$$\boldsymbol{\sigma}(t) = \frac{\partial \hat{\psi}(\varepsilon)}{\partial \varepsilon}\mathbf{1} + \int_{-\infty}^{t} m(t-\tau)\frac{\partial}{\partial \tau}\left(\mathrm{dev}\,\frac{\partial \overline{\psi}(e(\tau))}{\partial e}\right)d\tau, \tag{3-1}$$

where

$$\varepsilon = \mathrm{tr}\,\boldsymbol{\varepsilon}, \qquad \boldsymbol{e} = \mathrm{dev}\,\boldsymbol{\varepsilon} \equiv \boldsymbol{\varepsilon} - \tfrac{1}{3}\varepsilon\mathbf{1},$$

and $\boldsymbol{\varepsilon}$ is a linearized strain, that is, the symmetric part of the displacement gradient.

The relaxation function is defined in the form

$$m(t-\tau) = \beta_{\infty} + \beta \exp\left(-\frac{t-\tau}{\theta}\right), \qquad \beta_{\infty} = \frac{E_{\infty}}{E_{\infty}+E}, \quad \beta = \frac{E}{E_{\infty}+E}, \quad \theta = \frac{\eta}{E},$$

where β_{∞} and β are dimensionless relative moduli and θ is the relaxation time (see Figure 1).

The elastic potential is decomposed into the volumetric and distortional parts accordingly as

$$\psi(\boldsymbol{\varepsilon}) = \hat{\psi}(\varepsilon) + \overline{\psi}(\boldsymbol{e}), \tag{3-2}$$

and the hyperelastic constitutive law is derived as

$$\boldsymbol{\sigma} = \frac{\partial \psi}{\partial \boldsymbol{\varepsilon}} = \frac{\partial \hat{\psi}}{\partial \varepsilon}\mathbf{1} + \mathrm{dev}\,\frac{\partial \overline{\psi}}{\partial \boldsymbol{e}}. \tag{3-3}$$

We define the separate potentials with softening that have not been considered in the literature yet,

$$\hat{\psi}(\varepsilon) = \Phi_1 - \Phi_1\left(1 + \sqrt{\frac{K}{\Phi_1}}\varepsilon\right)\exp\left(-\sqrt{\frac{K}{\Phi_1}}\varepsilon\right), \qquad \overline{\psi}(\boldsymbol{e}) = \Phi_2 - \Phi_2\exp\left(-\frac{\mu}{\Phi_2}\boldsymbol{e}:\boldsymbol{e}\right), \tag{3-4}$$

where K and μ are the bulk and shear moduli of the isotropic Hookean solid and Φ_1 and Φ_2 are the failure energies for volumetric and distortional deformations. By introducing different failure constants we increase the flexibility of the phenomenological description of material failure.

Substituting (3-4) in (3-3) we have

$$\boldsymbol{\sigma} = \tilde{K}\varepsilon\mathbf{1} + 2\tilde{\mu}\boldsymbol{e}, \qquad \tilde{K} = K\exp\left(-\sqrt{\frac{K}{\Phi_1}}\varepsilon\right), \qquad \tilde{\mu} = \mu\exp\left(-\frac{\mu}{\Phi_2}\boldsymbol{e}:\boldsymbol{e}\right). \tag{3-5}$$

Linearization of these equations leads to the classical linear elasticity with $\tilde{K} = K$ and $\tilde{\mu} = \mu$.

The motivation for the specific forms of the softening hyperelastic potentials (3-4) comes from the consideration of two simple deformations.

Firstly, in the case of hydrostatic tension $(3\text{-}5)_1$ takes the form

$$\sigma = \sigma_{11} = \sigma_{22} = \sigma_{33} = K\varepsilon \exp\left(-\sqrt{\frac{K}{\Phi_1}}\varepsilon\right),$$

and its graph is shown in Figure 2, left.

Evidently, the hydrostatic compression does not lead to material failure while the hydrostatic tension does. The maximum point on the tension branch of the curve corresponds to the onset of static instability when the material failure starts propagating.

Secondly, in the case of pure shear, e_{12}, $(3\text{-}5)_1$ takes the form

$$\sigma_{12} = 2\mu e_{12} \exp\left(-\frac{\mu}{\Phi_2} e_{12}^2\right),$$

and its graph is shown in Figure 2, right.

Evidently, the skew-symmetry of the failure response is desirable and expected.

3.2. Simple shear. In this subsection we examine rate-dependent response of the model described above in the case of simple shear

$$\sigma_{12}(t) = 2\mu \int_0^t \left[\beta_\infty + \beta \exp\left(-\frac{t-\tau}{\theta}\right)\right] \frac{\partial}{\partial\tau}\left[e_{12} \exp\left(-\frac{\mu}{\Phi_2}e_{12}^2\right)\right] d\tau, \qquad (3\text{-}6)$$

where there is no stressing until $t = 0$.

Further simplifications are due to the assumption of the constant stretch/strain rate as $\dot{\gamma} = \text{constant}$. The latter assumption leads to the simple formulae for time

$$t = \frac{e_{12}}{\dot{\gamma}}, \qquad \tau = \frac{\xi_{12}}{\dot{\gamma}},$$
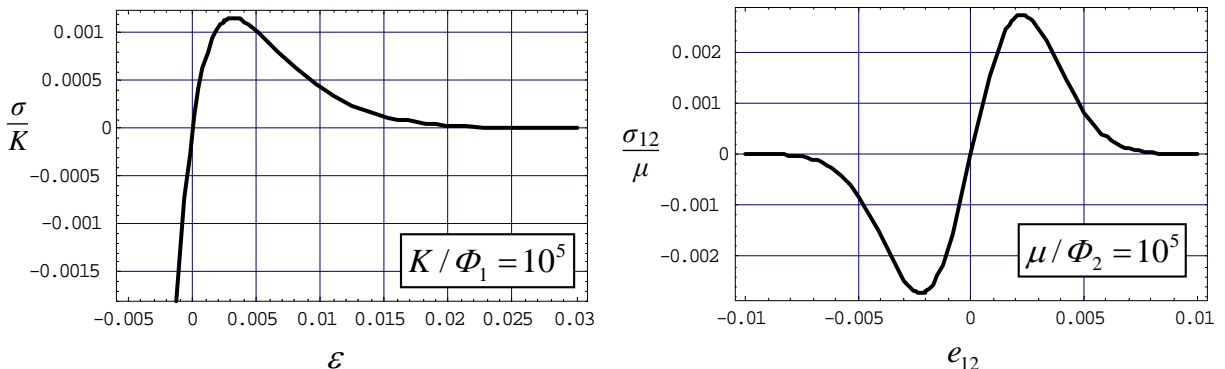
Figure 2. Left: Hydrostatic tension σ/K. Right: Simple shear σ_{12}/μ.
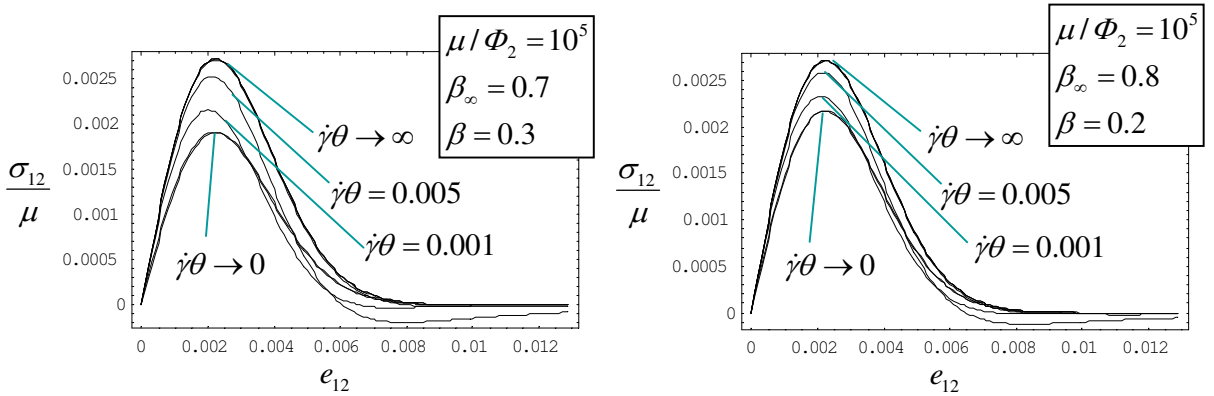
Figure 3. Simple shear for various strain rates.

where $\xi_{12} = e_{12}(\tau)$ and, consequently, (3-6) takes the form

$$\sigma_{12}(t) = 2\mu \int_0^{e_{12}} \left[\beta_\infty + \beta \exp\left(-\frac{e_{12} - \xi_{12}}{\theta\dot\gamma}\right) \right] \frac{\partial}{\partial\xi_{12}} \left[\xi_{12} \exp\left(-\frac{\mu}{\Phi_2}\xi_{12}^2\right) \right] d\xi_{12}. \tag{3-7}$$

Stress-strain curves defined by (3-7) are present in Figure 3 for different strain rates.

Evidently, material stiffness and strength — the curve maximum — increase with the increasing deformation rate for a given relaxation time. This conclusion is expected intuitively. Moreover, the stable (prior to failure) branches of the response curves are limited by the curve corresponding to $\dot\gamma\theta \to 0$ from the bottom and $\dot\gamma\theta \to \infty$ from the top. Physically the limit cases correspond to the very slow quasistatic response and the fastest instantaneous response of the material accordingly. Interestingly, the range of the strength variation depends on the relative contribution of the elastic springs in the rheological model shown in Figure 1. The greater the contribution of the spring corresponding to the dashpot, E, the larger the strength range.

4. Softening hyperviscoelasticity at finite deformations

The integral hyperviscoelasticity formulation for small deformations considered in the previous section can be equivalently reformulated in the differential form [Simo and Hughes 1998]. Unfortunately, in the case of finite deformation the integral and differential formulations are not necessarily equivalent in general. There are plenty of integral formulations of nonlinear viscoelasticity. We should mention, however, that the foundations of the theory have been set by Green and Rivlin [1957; 1959] and Green et al. [1959]. Further developments are reviewed in [Lockett 1972; Carreau et al. 1997; Hoo Fatt and Ouyang 2007], for example. There are also numerous differential formulations of nonlinear viscoelasticity based on the introduction of internal variables and their evolution equations. The most popular scheme includes the multiplicative decomposition of the deformation gradient into elastic and inelastic parts [Lubliner 1985; Lion 1996; Govindjee and Reese 1997; 1998; Bergström and Boyce 1998; Huber and Tsakmakis 2000; Amin et al. 2006; Hoo Fatt and Ouyang 2008]. Despite its popularity the scheme including the multiplicative decomposition of the deformation gradient is not entirely perfect: the intermediate elastically-relaxed configuration cannot be determined uniquely. Indeed, it is always possible to superimpose a local rotation on such a configuration without violating the multiplicative decomposition.

The nonuniqueness of the multiplicative decomposition is often eliminated by a specific and explicit choice of the deformation or by the use of certain computational schemes, which regularize the problem implicitly. Unfortunately, the artificial regularizations cannot improve the general formulation. Since the elastically-relaxed configuration is not unique one may question the necessity to define it. Instead of looking for a specific elastically-relaxed *configuration* it is possible to look only for a family of such configurations enjoying the same *metric*. In the latter case there is no need in the use of the nonunique multiplicative decomposition of the deformation gradient and it is enough to track the evolution of the metric tensor of possible elastically-relaxed configurations. Such a line of thought was pioneered by Eckart [1948] and further developed in [Leonov 1976; Rubin 1994; Rubin and Bodner 2002]. It is worth mentioning that the refusal to look for a unique elastically-relaxed configuration is justified by the fact that such a configuration is incompatible and, consequently, unobservable physically.

4.1. *Constitutive law.* We will use the rheological model shown in Figure 1 as a prototype for the nonlinear model too. The springs should be thought of as nonlinear in this case. We extend (3-1) to finite deformations directly following Simo and Hughes [1998]:

$$\boldsymbol{\tau}(t) = J\frac{\partial\hat{\psi}(\varepsilon)}{\partial\varepsilon}\mathbf{1} + \int_{-\infty}^{t} m(t-\tau)\frac{\partial}{\partial\tau}\left(\text{dev}\left[2\overline{\boldsymbol{F}}(\tau)\frac{\partial\overline{\psi}(\overline{\boldsymbol{C}}(\tau))}{\partial\overline{\boldsymbol{C}}}\overline{\boldsymbol{F}}^T(\tau)\right]\right)d\tau,$$

where $\boldsymbol{\tau} = J\boldsymbol{\sigma}$ is the so-called Kirchhoff stress tensor and

$$\varepsilon = J = \det\boldsymbol{F}, \qquad \overline{\boldsymbol{F}} = J^{-1/3}\boldsymbol{F}(\det\overline{\boldsymbol{F}} = 1), \qquad \overline{\boldsymbol{C}} = \overline{\boldsymbol{F}}^T\overline{\boldsymbol{F}}. \qquad (4\text{-}1)$$

The stored energy is also decomposed analogously to (3-2) as $\psi(\boldsymbol{C}) = \hat{\psi}(\varepsilon) + \overline{\psi}(\overline{\boldsymbol{C}})$, and the hyperelastic constitutive law is derived as

$$\boldsymbol{\tau} = J\frac{\partial\hat{\psi}}{\partial\varepsilon}\mathbf{1} + \text{dev}\left[2\overline{\boldsymbol{F}}\frac{\partial\overline{\psi}}{\partial\overline{\boldsymbol{C}}}\overline{\boldsymbol{F}}^T\right].$$

We mention that the idea to extend the volumetric-distortional decomposition of small strains to the case of large strains based on the volume-preserving deformation gradient, (4-1)$_2$, is due to Flory [1961].

Though the formulation above is the most general the majority of soft materials undergoing finite deformations are incompressible. The latter means that the analytical formulation can be simplified as

$$\varepsilon = J = \det\boldsymbol{F} = 1, \qquad (4\text{-}2)$$

$$\overline{\boldsymbol{F}} = \boldsymbol{F}, \qquad \overline{\boldsymbol{C}} = \boldsymbol{C}, \qquad \psi(\boldsymbol{C}) = \overline{\psi}(\overline{\boldsymbol{C}}), \qquad \boldsymbol{\sigma} = \boldsymbol{\tau} = -p\mathbf{1} + \text{dev}\left[2\boldsymbol{F}\frac{\partial\psi}{\partial\boldsymbol{C}}\boldsymbol{F}^T\right], \qquad (4\text{-}3)$$

and

$$\boldsymbol{\sigma}(t) = \boldsymbol{\tau}(t) = -p\mathbf{1} + \int_{-\infty}^{t} m(t-\tau)\frac{\partial}{\partial\tau}\left(\text{dev}\left[2\boldsymbol{F}(\tau)\frac{\partial\psi(\boldsymbol{C}(\tau))}{\partial\boldsymbol{C}}\boldsymbol{F}^T(\tau)\right]\right)d\tau, \qquad (4\text{-}4)$$

where the indefinite Lagrange multiplier, p, is used to enforce the incompressibility condition (4-2).

We further use a stored energy with softening that was calibrated for analysis of the material of the abdominal aortic aneurysm [Volokh and Vorp 2008]

$$\psi(I_1) = \Phi - \Phi\exp\left[-\frac{\alpha_1}{\Phi}(I_1 - 3) - \frac{\alpha_2}{\Phi}(I_1 - 3)^2\right], \qquad (4\text{-}5)$$
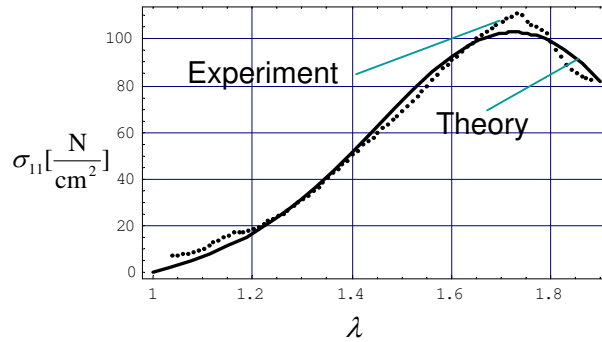
Figure 4. Theory versus experiment for the uniaxial tension test [Volokh and Vorp 2008].

where $I_1 = \text{tr}\, \boldsymbol{C}$, α_1 and α_2 are the elasticity constants of the material, and Φ is the failure energy, which is another material constant controlling its softening.

The uniaxial tension test results are shown in Figure 4, where model (4-5) was fitted with the following constants: $\alpha_1 = 10.3\,\text{N/cm}^2$, $\alpha_2 = 18.0\,\text{N/cm}^2$, and $\Phi = 40.2\,\text{N/cm}^2$.

Substituting (4-5) in (4-4) we have

$$\boldsymbol{\sigma}(t) = -p\mathbf{1} + \int_{-\infty}^{t} m(t-\tau)\frac{\partial}{\partial \tau}\Big(\text{dev}\big[2\psi_1(\tau)\boldsymbol{B}(\tau)\big]\Big)\,d\tau,$$

where $\boldsymbol{B} = \boldsymbol{F}\boldsymbol{F}^T$ and

$$\psi_1 \equiv \frac{\partial \psi}{\partial I_1} = \big[\alpha_1 + 2\alpha_2(I_1 - 3)\big]\exp\Big[-\frac{\alpha_1}{\Phi}(I_1 - 3) - \frac{\alpha_2}{\Phi}(I_1 - 3)^2\Big].$$

4.2. *Uniaxial tension.* In the case of the uniaxial tension we have the following simplifications within the Cartesian coordinate framework $\{\boldsymbol{k}_1, \boldsymbol{k}_2, \boldsymbol{k}_3\}$:

$$\boldsymbol{F} = \lambda\boldsymbol{k}_1 \otimes \boldsymbol{k}_1 + \lambda^{-1/2}(\boldsymbol{k}_2 \otimes \boldsymbol{k}_2 + \boldsymbol{k}_3 \otimes \boldsymbol{k}_3), \qquad \boldsymbol{B} = \lambda^2\boldsymbol{k}_1 \otimes \boldsymbol{k}_1 + \lambda^{-1}(\boldsymbol{k}_2 \otimes \boldsymbol{k}_2 + \boldsymbol{k}_3 \otimes \boldsymbol{k}_3),$$

where λ is the axial stretch.

The nontrivial stress components accordingly take the forms

$$\sigma_{11}(t) = -p + \frac{4}{3}\int_{-\infty}^{t} m(t-\tau)\frac{\partial}{\partial \tau}\Big(\psi_1(\tau)\big[\lambda^2(\tau) - \lambda^{-1}(\tau)\big]\Big)\,d\tau, \tag{4-6}$$

$$\sigma_{22}(t) = \sigma_{33}(t) = -p - \frac{2}{3}\int_{-\infty}^{t} m(t-\tau)\frac{\partial}{\partial \tau}\Big(2\psi_1(\tau)\big[\lambda^2(\tau) - \lambda^{-1}(\tau)\big]\Big)\,d\tau. \tag{4-7}$$

Since $\sigma_{22}(t) = \sigma_{33}(t) = 0$ we can find the Lagrange multiplier from (4-7) and substitute it in (4-6) getting the final formula

$$\sigma_{11}(t) = 2\int_{0}^{t} m(t-\tau)\frac{\partial}{\partial \tau}\Big(\psi_1(\tau)\big[\lambda^2(\tau) - \lambda^{-1}(\tau)\big]\Big)\,d\tau, \tag{4-8}$$

where $\xi = \lambda(\tau)$ and the lower integration boundary has been shifted assuming no stressing before time $t = 0$.

Further simplifications are due to the assumption of the constant stretch/strain rate

$$\dot{\xi} = \dot{\lambda} = \dot{\gamma} = \text{constant}.$$
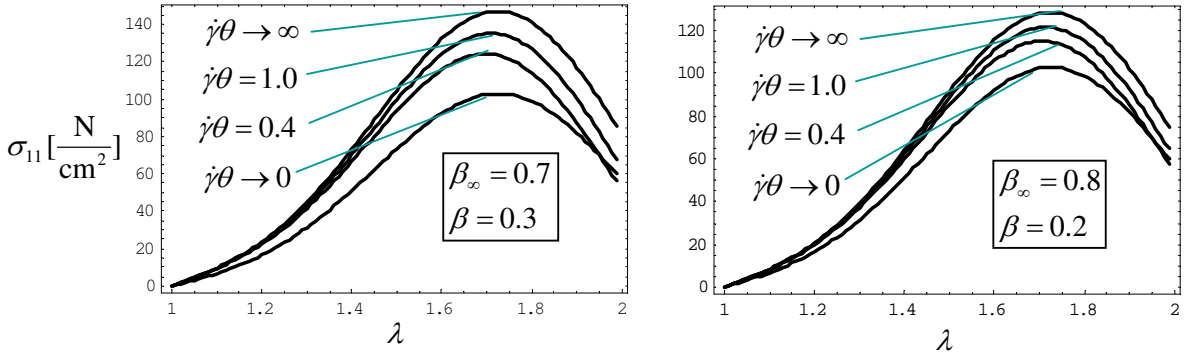
Figure 5. Uniaxial tension for various strain rates.

The latter assumption leads to the simple formulae

$$t = \frac{\lambda - 1}{\dot{\gamma}}, \qquad \tau = \frac{\xi - 1}{\dot{\gamma}},$$

for the times; consequently, (4-8) takes the form

$$\sigma_{11}(t) = 2 \int_1^\lambda \left[\beta_\infty + \beta \exp\left(-\frac{\lambda - \xi}{\dot{\gamma}\,\theta}\right) \right] \frac{\partial}{\partial \xi} \left[\psi_1(\xi)(\xi^2 - \xi^{-1}) \right] d\xi. \tag{4-9}$$

Computations based on (4-9) are shown in Figure 5 for various stretch rates. We also scaled the material constants $\alpha_1 \rightarrow \alpha_1/\beta_\infty$, $\alpha_2 \rightarrow \alpha_2/\beta_\infty$, and $\Phi \rightarrow \Phi/\beta_\infty$ in order to preserve the form of the quasistatic curve, $\dot{\gamma}\,\theta \rightarrow 0$, shown in Figure 5.

As in the case of small deformations, material stiffness and strength increase with the increasing deformation rate for a given relaxation time. The stable (prior to failure) branches of the response curves are limited by the curve corresponding to $\dot{\gamma}\,\theta \rightarrow 0$ from the bottom and $\dot{\gamma}\,\theta \rightarrow \infty$ from the top. The range of the strength variation depends on the relative contribution of the elastic springs in the rheological model shown in Figure 1. The greater the contribution of the spring corresponding to the dashpot the larger the strength range. There is a complete analogy between the cases of small and finite deformations as expected.

5. Discussion

A new approach for modeling rate-dependent failure of materials has been proposed. Its basic idea is the introduction of energy limiters in the constitutive description of materials. Such limiters control softening providing a failure account. The energy limiters were introduced in the models of isotropic Hookean solids, which are suitable for a description of quasibrittle failure in ceramics, concrete, glass, or even metals at high-velocity dynamic processes where the plastic deformation can be ignored. Besides, the energy limiters were considered for soft materials at finite deformations. It should be clearly realized that the proposed approach is suitable for materials whose failure is due to the bond rupture and cannot be used for materials that fail due to large plastic deformations. If failure is accompanied by a gradual accumulation of inelastic deformations then the approach of damage mechanics is probably more relevant and should be used.

Though we used essentially different material models in the considered examples of small and finite deformations the qualitative results are very similar. Particularly, we observed that the increasing rate of deformations leads to the increase of both stiffness and strength of the material. Such a conclusion corresponds well to the experimental observations. Moreover, while the existing viscoelasticity theories can describe the phenomenon of material stiffening under increasing deformation rate it is for the first time that the presented approach clearly predicts the increase of the material strength (and not only stiffening) with the increase of the deformation rate.

Concerning the limitations of the presented computations it should be emphasized that the considered examples include only proportional loading and there are no returning deformation waves. Such waves may lead to the material healing within the hyperelastic framework, which should be suppressed. To avoid the material healing in the finite element computations it is possible, for example, to reduce the values of the material parameters by orders of magnitude in the elements, which reached the critical failure energy or arrived at zero stresses. This circle of questions is beyond the scope of the present note where only a principal possibility of inducing a failure description in nonlinear viscoelasticity has been considered. Nonetheless, the finite element implementation of the proposed method is important and will be considered in a separate work.

Acknowledgements

References

[Amin et al. 2006] A. F. M. S. Amin, A. Lion, S. Sekita, and Y. Okui, "Nonlinear dependence of viscosity in modeling the rate-dependent response of natural and high damping rubbers in compression and shear: experimental identification and numerical verification", *Int. J. Plast.* **22**:9 (2006), 1610–1657.

[Barenblatt 1959] G. I. Barenblatt, "The formation of equilibrium cracks during brittle fracture. General ideas and hypotheses. Axially-symmetric cracks", *J. Appl. Math. Mech.* **23**:3 (1959), 622–636.

[Belytschko et al. 2001] T. Belytschko, N. Moës, S. Usiu, and C. Parimi, "Arbitrary discontinuities in finite elements", *Int. J. Numer. Methods Eng.* **50**:4 (2001), 993–1013.

[Bergström and Boyce 1998] J. S. Bergström and M. C. Boyce, "Constitutive modeling of the large strain time-dependent behavior of elastomers", *J. Mech. Phys. Solids* **46**:5 (1998), 931–954.

[Camacho and Ortiz 1996] G. T. Camacho and M. Ortiz, "Computational modelling of impact damage in brittle materials", *Int. J. Solids Struct.* **33**:20-22 (1996), 2899–2938.

[Carreau et al. 1997] P. J. Carreau, D. C. R. De Kee, and R. P. Chhabra, *Rheology of polymeric systems*, Hanser, Munich, 1997.

[De Borst 2001] R. De Borst, "Some recent issues in computational failure mechanics", *Int. J. Numer. Methods Eng.* **52**:1-2 (2001), 63–95.

[Dugdale 1960] D. S. Dugdale, "Yielding of steel sheets containing slits", *J. Mech. Phys. Solids* **8**:2 (1960), 100–104.

[Eckart 1948] C. Eckart, "The thermodynamics of irreversible processes, IV: The theory of elasticity and anelasticity", *Phys. Rev.* **73**:4 (1948), 373–382.

[Flory 1961] P. J. Flory, "Thermodynamic relations for high elastic materials", *Trans. Faraday Soc.* **57** (1961), 829–838.

[Gao and Klein 1998] H. Gao and P. Klein, "Numerical simulation of crack growth in an isotropic solid with randomized internal cohesive bonds", *J. Mech. Phys. Solids* **46**:2 (1998), 187–218.

[Gei et al. 2004] M. Gei, D. Bigoni, and S. Guicciardi, "Failure of silicon nitride under uniaxial compression at high temperature", *Mech. Mater.* **36**:4 (2004), 335–345.

[Govindjee and Reese 1997] S. Govindjee and S. Reese, "A presentation and comparison of two large deformation viscoelasticity models", *J. Eng. Mater. Technol.* (*ASME*) **119**:3 (1997), 251–255.

[Green and Rivlin 1957] A. E. Green and R. S. Rivlin, "The mechanics of non-linear materials with memory, I", *Arch. Ration. Mech. An.* **1** (1957), 1–21.

[Green and Rivlin 1959] A. E. Green and R. S. Rivlin, "The mechanics of non-linear materials with memory, III", *Arch. Ration. Mech. An.* **4** (1959), 387–404.

[Green et al. 1959] A. E. Green, R. S. Rivlin, and A. J. M. Spencer, "The mechanics of non-linear materials with memory, II", *Arch. Ration. Mech. An.* **3** (1959), 82–90.

[Hoo Fatt and Ouyang 2007] M. S. Hoo Fatt and X. Ouyang, "Integral-based constitutive equation for rubber at high strain rates", *Int. J. Solids Struct.* **44**:20 (2007), 6491–6506.

[Hoo Fatt and Ouyang 2008] M. S. Hoo Fatt and X. Ouyang, "Three-dimensional constitutive equations for Styrene Butadiene Rubber at high strain rates", *Mech. Mater.* **40**:1-2 (2008), 1–16.

[Huber and Tsakmakis 2000] N. Huber and C. Tsakmakis, "Finite deformation viscoelasticity laws", *Mech. Mater.* **32**:1 (2000), 1–18.

[Kachanov 1958] L. M. Kachanov, "Time of the rupture process under creep conditions", *Izv. Akad. Nauk SSSR, Otd. Tekh. Nauk* **8** (1958), 26–31.

[Kachanov 1986] L. M. Kachanov, *Introduction to continuum damage mechanics*, Mechanics of Elastic Stability **10**, Martinus Nijhoff, Dordrecht, 1986.

[Klein and Gao 1998] P. Klein and H. Gao, "Crack nucleation and growth as strain localization in a virtual-bond continuum", *Eng. Fract. Mech.* **61**:1 (1998), 21–48.

[Krajcinovic 1996] D. Krajcinovic, *Damage mechanics*, North-Holland Series in Applied Mathematics and Mechanics **41**, Elsevier, Amsterdam, 1996.

[Lemaitre and Desmorat 2005] J. Lemaitre and R. Desmorat, *Engineering damage mechanics: ductile, creep, fatigue and brittle failures*, Springer, Berlin, 2005.

[Leonov 1976] A. I. Leonov, "Nonequilibrium thermodynamics and rheology of viscoelastic polymer media", *Rheol. Acta* **15**:2 (1976), 85–98.

[Lion 1996] A. Lion, "A constitutive model for carbon black filled rubber: experimental investigations and mathematical representation", *Continuum Mech. Therm.* **8**:3 (1996), 153–169.

[Lockett 1972] F. J. Lockett, *Nonlinear viscoelastic solids*, Academic Press, London, 1972.

[Lubliner 1985] J. Lubliner, "A model of rubber viscoelasticity", *Mech. Res. Commun.* **12**:2 (1985), 93–99.

[Needleman 1987] A. Needleman, "A continuum model for void nucleation by inclusion debonding", *J. Appl. Mech.* (*ASME*) **54** (1987), 525–531.

[Rabotnov 1963] Y. N. Rabotnov, "On the equations of state for creep", pp. 307–315 in *Progress in applied mechanics: the Prager anniversary volume*, MacMillan, New York, 1963.

[Reese and Govindjee 1998] S. Reese and S. Govindjee, "A theory of finite viscoelasticity and numerical aspects", *Int. J. Solids Struct.* **35**:26-27 (1998), 3455–3482.

[Rice and Wang 1989] J. R. Rice and J.-S. Wang, "Embrittlement of interfaces by solute segregation", *Mater. Sci. Eng. A* **107** (1989), 23–40.

[Rubin 1994] M. B. Rubin, "Plasticity theory formulated in terms of physically based microstructural variables, I: Theory", *Int. J. Solids Struct.* **31**:19 (1994), 2615–2634.

[Rubin and Bodner 2002] M. B. Rubin and S. R. Bodner, "A three-dimensional nonlinear model for dissipative response of soft tissue", *Int. J. Solids Struct.* **39**:19 (2002), 5081–5099.

[Simo and Hughes 1998] J. C. Simo and T. J. R. Hughes, *Computational inelasticity*, Springer, New York, 1998.

[Skrzypek and Ganczarski 1999] J. Skrzypek and A. Ganczarski, *Modeling of material damage and failure of structures*, Springer, Berlin, 1999.

[Trapper and Volokh 2008] P. Trapper and K. Y. Volokh, "Cracks in rubber", *Int. J. Solids Struct.* **45**:24 (2008), 6034–6044.

[Tvergaard and Hutchinson 1992] V. Tvergaard and J. W. Hutchinson, "The relation between crack growth resistance and fracture process parameters in elastic-plastic solids", *J. Mech. Phys. Solids* **40**:6 (1992), 1377–1397.

[Volokh 2004] K. Y. Volokh, "Nonlinear elasticity for modeling fracture of isotropic brittle solids", *J. Appl. Mech.* (*ASME*) **71**:1 (2004), 141–143.

[Volokh 2007a] K. Y. Volokh, "Softening hyperelasticity for modeling material failure: analysis of cavitation in hydrostatic tension", *Int. J. Solids Struct.* **44**:14-15 (2007), 5043–5055.

[Volokh 2007b] K. Y. Volokh, "Hyperelasticity with softening for modeling materials failure", *J. Mech. Phys. Solids* **55**:10 (2007), 2237–2264.

[Volokh 2008a] K. Y. Volokh, "Fung's arterial model enhanced with a failure description", *Mol. Cell. Biomech.* **5**:3 (2008), 207–216.

[Volokh 2008b] K. Y. Volokh, "Prediction of arterial failure based on a microstructural bi-layer fiber-matrix model with softening", *J. Biomech.* **41**:2 (2008), 447–453.

[Volokh and Trapper 2008] K. Y. Volokh and P. Trapper, "Fracture toughness from the standpoint of softening hyperelasticity", *J. Mech. Phys. Solids* **56**:7 (2008), 2459–2472.

[Volokh and Vorp 2008] K. Y. Volokh and D. A. Vorp, "A model of growth and rupture of abdominal aortic aneurysm", *J. Biomech.* **41**:5 (2008), 1015–1021.

[Xu and Needleman 1994] X.-P. Xu and A. Needleman, "Numerical simulations of fast crack growth in brittle solids", *J. Mech. Phys. Solids* **42**:9 (1994), 1397–1434.

KONSTANTIN VOLOKH: cvolokh@technion.ac.il
Faculty of Civil and Environmental Engineering, Technion - Israel Institute of Technology, Haifa 32000, Israel

PAVEL TRAPPER: p.trapper@gmail.com
Faculty of Civil and Environmental Engineering, Technion - Israel Institute of Technology, Haifa 32000, Israel

DYNAMICS OF DISCRETE FRAMED STRUCTURES:
A UNIFIED HOMOGENIZED DESCRIPTION

STEPHANE HANS AND CLAUDE BOUTIN

The dynamic behavior of discrete periodic one-dimensional structures is approached by considering transverse vibrations of structures made of repeated unbraced frames. Assuming the frame size is small compared to the modal wavelength, equivalent macroscopic beam descriptions are obtained by the homogenization method of periodic discrete media. The macroscopic parameters are expressed as functions of the mechanical and geometrical properties of the frame elements.

Depending on the order of magnitude (relative to the scale ratio) of the shear force, the global bending and the inner bending, four families of beams are shown to be possible. A generic beam governed by a differential equation of the sixth degree is shown to encompass all the other types.

Simple criteria are established to identify the relevant model for real structures. A comparison of these theoretical results with numerical modeling is satisfactory even in the case of weak scale separation. In fact, an investigation of the higher orders terms shows that zero order descriptions are valid up to the second order. Lastly, analogies with micromorphic media are discussed.

1. Introduction

Understanding the behavior of reticulated materials and structures is of interest in aeronautics (lattice beams), in civil engineering (buildings), in materials science (mechanics of foam or glass wool), in biomechanics (vegetable tissue or bones), and so on. When the dimensions of the representative cell are smaller than the overall size, such three-, two-, or one-dimensional systems may be described respectively by effective continuum media, plate or beam models. Numerous studies have been aimed at relating the local structure to the global behavior. Particularly, periodic lattices have been studied through various approaches such as transfer matrices, variational calculus [Kerr and Accorsi 1985], and finite difference operators [Renton 1984]; see also the reviews [Noor 1988; Mead 1996]. Asymptotic homogenization methods [Sánchez-Palencia 1980] have been developed for homogeneous and periodic beams [Trabucho and Viaño 1996; Buannic and Cartraud 2001a; 2001b], for periodic discrete structures [Bakhvalov and Panasenko 1989; Caillerie et al. 1989], and in parallel with the homogenization of periodic media with multiple parameters and scale changes [Cioranescu and Saint Jean Paulin 1999]. Amongst the applications of homogenization of periodic discrete media (HPDM) we mention the papers [Tollenaere 1994; Moreau and Caillerie 1998; Boutin and Hans 2003], dealing respectively with the statics, buckling and dynamics of trusses; [Pradel and Sab 1998], on the constitutive laws of foams; and [Le Corre et al. 2004], involving fluid mechanics.

The present study, initially motivated by earthquake engineering, is concerned with the dynamics of framed beams, which may be seen as "idealized buildings". Among the numerous possible basic

Keywords: discrete structure, modal analysis, beam theory, homogenization, micromorphic media.

cell architectures of one-dimensional repetitive structures, HPDM investigation of an orthogonal grid geometry is of interest for the following reasons:

– The lack of bracing means that cells have a much lower shear stiffness than compression stiffness. In this case, which is not uncommon in structural engineering, the method of multiple parameters and scale changes [Cioranescu and Saint Jean Paulin 1999] captures the leading order (compression) but misses the shear properties, which are found to vanish (with a loss of convexity of the elastic potential), whereas in fact they are of lower order. HPDM overcomes this bias and predicts behaviors that are not derivable by more classical upscaling methods. See [Buannic and Cartraud 2001a; 2001b], for example.

– It will be shown that the diversity of beam-like behaviors of repetitive structures [Stephen 1999] is recovered by varying the mechanical properties of the basic frame elements. The high contrast of shear and compression deformability enriches the local kinematics, inducing new beam-like models. The macro behaviors can be classified according to three intrinsic mechanical parameters characterizing the cell. Since these global parameters can be derived for any cell (braced or not), framed beams can be considered as an archetypical case and the results extended to other kind of reticulated beams.

– The strength of HPDM is to derive, without any prerequisite other than scale separation, a rigorous and analytical continuous beam-like description in direct relation with the characteristics of the cell elements. The formulation enables a parametric study and provides a clear understanding of the several mechanisms governing the global behavior. The continuous description also highlights and simplifies the modal analysis of the structure. This global vision is not accessible through finite element modeling, which gives accurate numerical descriptions attached to a particular structure.

A first investigation on this topic was initiated in [Boutin and Hans 2003]. The wider objectives of the present work are:

– To work out all possible transverse dynamic behaviors of these structures and to define in each case the equivalent beam modeling. Depending on the mechanical properties of the cell, four families of beams are identified. A *generic beam*, governed by a differential equation of sixth degree, is proved to include all other mechanisms. This macro beam modeling involves three kinematic variables, namely section translation, rotation and inner deformation dual to shear force, bending and inner moments.

– To provide criteria to identify which model is relevant to a given real structure and to analyze the range of validity and the accuracy of the continuum modeling. It is demonstrated that *the maximum number of homogenizable modes is of the order of a third of the number of cells*. By investigating correctors of higher orders, the zero order description is shown to be correct up to second order. This may explain the fairly good accuracy of the continuum beam method that is observed numerically.

– To point out the analogy between these descriptions and those of micromorphic materials such as Cosserat media or inner deformation media. Using a dimensional analysis based on the intrinsic parameters of the cell, the conditions under which a reticulated medium may behave as a generalized medium at the zero order are presented and discussed.

The principles of the method will be given in Section 2 and applied to framed structures in Section 3. The beam models are presented in Section 4. Their applications and numerical validation are discussed in Section 5. Analogies with micromorphic media are developed in Section 6. The detailed implementation of HPDM for framed structures is reported in Section 7.

2. The method of homogenization of discrete periodic media (HDPM)

The modal analysis of periodic lattices of interconnected beams is performed by HDPM in two steps [Tollenaere and Caillerie 1998]: discretization of the balance of the structure under harmonic vibrations, followed by the homogenization, leading to a continuous model obtained from the discrete description. An outline of this method is given now; a detailed exposition including an example is given in Section 7.

Discretization of the dynamic balance. The structures we consider (see Figure 1 on page 1713) are made of plate behaving as pure Euler-Bernoulli beam in out-of-plane motion. They are assembled with perfectly stiff connections. Thus, the motions of each endpoint connected to the same node are identical and define the discrete nodal kinematic variables of the system. The discretization consists in integrating the dynamic balance (in harmonic regime) of the beams, the unknown displacements and rotations at their endpoints being taken as boundary conditions. Forces applied by an element on its endpoints are then expressed explicitly as functions of the nodal kinematic variables; see (7-7). The dynamic balance of each element being satisfied, it remains to express the balance of forces applied by the elements connected to a same node. Thus, the balance of the whole structure is rigorously reduced to the balance of the set of nodes; that is, the discrete description using only the nodal variables is fully equivalent to the complete description.

Asymptotic expansions. The key assumption of HPDM is scale separation. This means that the cell size ℓ (in the direction of the periodicity) is small compared to the unknown characteristic size L of the deformation of the structure under vibrations. Thus the scale ratio $\varepsilon = \ell/L$ is such that $\varepsilon \ll 1$. The existence of a macroscale implies that HDPM is limited to low frequency modes whose wavelength is large compared to the cell size. In this case, the forces and displacements vary slowly from one node to the next and can be considered as the discrete values of continuous functions to be determined. For this purpose, a macroscopic space variable x is introduced along the periodicity axis and variables are expressed as continuous functions of x coinciding with the discrete variable at any node n ($x = x_n$). For instance, a continuous displacement $U_\varepsilon(x)$ is defined in such a way that

$$U_\varepsilon(x = x_n) = U(\text{node } n).$$

These quantities, assumed to converge when ε tends to zero, are expanded in powers of ε. This introduces the continuous functions U^i of order i:

$$U_\varepsilon(x) = U^0(x) + \varepsilon\, U^1(x) + \varepsilon^2\, U^2(x) + \cdots. \tag{2-1}$$

Later on, the physically observable variables of a given order in ε will be denoted by a tilde; for example,

$$\tilde{U}^i(x) = \varepsilon^i U^i(x).$$

All unknowns, including the modal frequency, will be expanded in powers of ε.

Since $\ell = \varepsilon L$ is small with respect to x, the variation in variables between neighboring nodes $n-1$ and $n+1$ is expressible using Taylor series; this in turn leads to the macroscopic derivatives. For instance,

$$U(n \pm 1) = U^0(x_n) + \varepsilon \left(U^1(x_n) \pm L \, U^{0\prime}(x_n) \right) + \varepsilon^2 \left(U^2(x_n) \pm L \, U^{1\prime}(x_n) + \tfrac{1}{2} L^2 \, U^{0\prime\prime}(x_n) \right) + \cdots$$

Here, the periodicity is explicitly used and the constant internodal distance enables one to express these Taylor expansions with a single parameter ε. Finally, scale separation requires that, at the modal frequency of the global system, the wavelength generated in each local element be much longer than the element's length. Consequently, nodal forces can be developed in Taylor series with respect to ε (expressions are given in Section 7D).

Normalization. To account properly for the local physics, it is necessary to integrate correctly the properties of the cell through a normalization. Indeed, the method of asymptotic expansions is based on the identification of terms of the same power of ε in the expansions of the balance equations. The identification makes sense under the condition that ε tends to 0.

The normalization consists in scaling the geometric and mechanical characteristics of the element according to the powers of ε. As for the modal frequency, scaling is imposed by the balance of elastic and inertia forces at the macro level. Such a normalization insures that each mechanical effect appears at the same order whatever the value of ε. Therefore, the same physics is kept at the limit $\varepsilon \to 0$, which represents the homogenized model.

Macroscopic description. Expansions in powers of ε are introduced in the nodal balances. The relations obtained being valid for any small enough ε, the orders can be separated. This leads to balance equations for each order, whose resolution defines the macroscopic governing equations. The descriptions presented in Section 4 are limited to the leading order. Correctors of interest in the case of poor scale separation are examined in Section 5.

3. Class of structures

Our study focuses on the harmonic transverse vibrations in the plane (e_1, e_2) of structures constituted by a pile of a large number N of identical unbraced frames called cells (Figure 1). Cell elements, of length h in the direction e_3, are linked by stiff massless connections and behave as Euler-Bernoulli beams. The following notation will be used:

- Level n contains two nodes, n_1 on the left and n_2 on the right. Cell n is made of one horizontal element fn (the floor) of level n, supported by two vertical elements wn_1 and wn_2 (walls) linking level $n-1$ and level n.

- The parameters of walls $(i = w)$ and floors $(i = f)$ are: length ℓ_i; thickness a_i; section area A_i; inertia in direction e_3 $I_i = a_i^3 h/12$; density ρ_i; elastic modulus E_i (Young's modulus E_Y in the case of beam or $E_Y/(1-\nu)$ in the case of plates as considered here). The height of the structure is $H = N\ell_w$.

Local variables. At level n, the motion of node n_i $(i = 1, 2)$ in the plane (e_1, e_2) is described by the displacements $u_1(n_i), u_2(n_i)$ in the two directions and by the rotation $\theta(n_i)$. Because of longitudinal symmetry, these six variables can be replaced by the three variables $(U(n), \alpha(n), V(n))$ associated to the
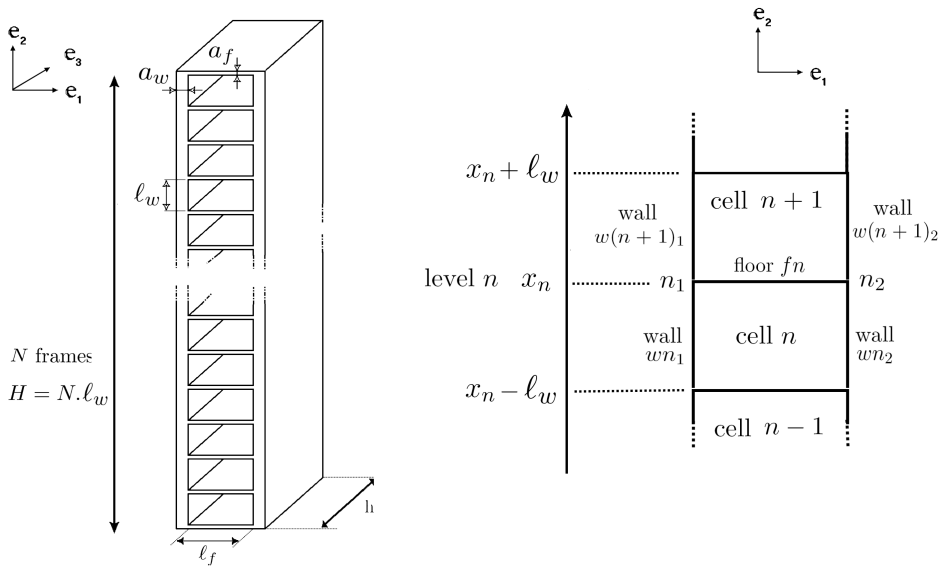
Figure 1. The class of unbraced framed structures studied in this paper (left) and the basic frame and notations (right).

rigid body motion of the pair of nodes (n_1, n_2) and the three variables $(\theta(n), \Delta(n), \Phi(n))$ corresponding to the deformation of (n_1, n_2); see Figure 2. The expressions of the variables are

$$
\left\{
\begin{array}{rcll}
U(n) & = & (u_1(n_1) + u_1(n_2))/2 & \text{Mean transverse displacement (along } e_1) \\
\alpha(n) & = & (u_2(n_1) - u_2(n_2))/\ell_f & \text{Rotation of level } n \\
\theta(n) & = & (\theta(n_1) + \theta(n_2))/2 & \text{Mean rotation of nodes}
\end{array}
\right.
$$

$$
\left\{
\begin{array}{rcll}
V(n) & = & (u_2(n_1) + u_2(n_2))/2 & \text{Mean axial displacement (along } e_2) \\
\Delta(n) & = & u_1(n_2) - u_1(n_1) & \text{Transverse dilatation} \\
\Phi(n) & = & \theta(n_2) - \theta(n_1) & \text{Differential rotation of nodes}
\end{array}
\right.
$$

At level n, the action of cell n on cell $n + 1$ consists in the transverse and longitudinal forces $\mathrm{T}(n_i)$ and $\mathrm{N}(n_i)$, and the moments $\mathrm{M}(n_i)$, $i = 1, 2$. These forces are exactly the opposite of those in the two walls of cell $n + 1$ at the connections with cell n. It is convenient to introduce the total and differential
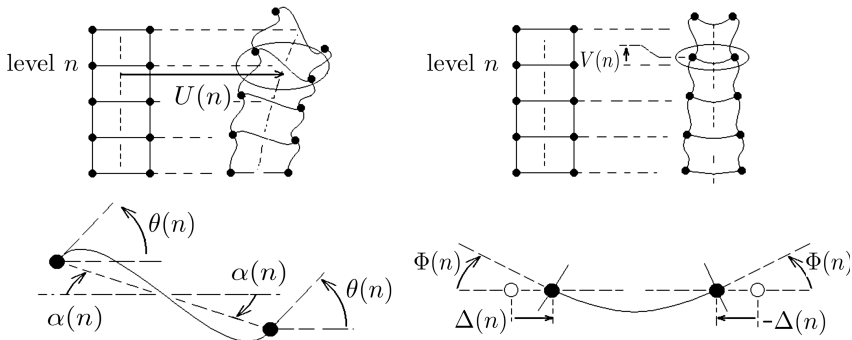
Figure 2. Decoupling of transverse (left) and longitudinal (right) kinematics.

forces defined by

$$
\begin{cases}
\mathrm{T}_t(n) & = & \mathrm{T}(n_1) + \mathrm{T}(n_2) & \text{Total transverse force} \\
\mathrm{M}(n) & = & \ell_f(\mathrm{N}(n_2) - \mathrm{N}(n_1)) & \text{Moment of the differential longitudinal force} \\
\mathrm{M}_t(n) & = & \mathrm{M}(n_1) + \mathrm{M}(n_2) & \text{Total inner moment}
\end{cases}
$$

$$
\begin{cases}
\mathrm{N}_t(n) & = & \mathrm{N}(n_1) + \mathrm{N}(n_2) & \text{Total longitudinal force} \\
\mathrm{T}_d(n) & = & \mathrm{T}(n_2) - \mathrm{T}(n_1) & \text{Differential transverse force} \\
\mathrm{M}_d(n) & = & \mathrm{M}(n_2) - \mathrm{M}(n_1) & \text{Differential inner moment}
\end{cases}
$$

There are six nodal balance equations, derived in Section 7 as (7-8), (7-9):

Node n_1: $\mathrm{T}^E_{wn_1} - \mathrm{T}^B_{w(n+1)_1} - \mathrm{N}^B_{fn} = 0$, $\mathrm{N}^E_{wn_1} - \mathrm{N}^B_{w(n+1)_1} - \mathrm{T}^B_{fn} = 0$, $\mathrm{M}^E_{wn_1} - \mathrm{M}^B_{w(n+1)_1} - \mathrm{M}^B_{fn} = 0$, (3-1)

Node n_2: $\mathrm{T}^E_{wn_2} - \mathrm{T}^B_{w(n+1)_2} + \mathrm{N}^E_{fn} = 0$, $\mathrm{N}^E_{wn_2} - \mathrm{N}^B_{w(n+1)_2} + \mathrm{T}^E_{fn} = 0$, $\mathrm{M}^E_{wn_2} - \mathrm{M}^B_{w(n+1)_2} + \mathrm{M}^E_{fn} = 0$, (3-2)

Longitudinal symmetry enables to split them into two uncoupled sets of three equations, governing independently the transverse and longitudinal vibrations. Transverse vibrations are described by $U(n)$, $\theta(n)$ and $\alpha(n)$ involved in the following balance equations associated with the forces $\mathrm{T}_t(n)$, $\mathrm{M}_t(n)$ and $\mathrm{M}(n)$:

$$
\text{Balance of} \begin{cases}
\mathrm{T}_t(n) & \text{given by } (3\text{-}1)_1 + (3\text{-}2)_1 \\
\mathrm{M}(n) & \text{given by } (3\text{-}2)_2 - (3\text{-}1)_2 \\
\mathrm{M}_t(n) & \text{given by } (3\text{-}2)_3 + (3\text{-}1)_3
\end{cases}
\tag{3-3}
$$

We will focus on transverse vibrations, but longitudinal vibrations, described by the complementary set (namely $(3\text{-}1)_1 + (3\text{-}2)_1$, $(3\text{-}2)_2 - (3\text{-}1)_2$, $(3\text{-}2)_3 - (3\text{-}1)_3$) and involving $V(n)$, $\Delta(n)$ and $\Phi(n)$ and the forces $\mathrm{N}_t(n)$, $\mathrm{T}_d(n)$ and $\mathrm{M}_d(n)$, can be analyzed in the same manner [Boutin and Hans 2003].

Scaling. We consider structures whose walls and floors have similar lengths and are made of elastic linear materials with moduli and densities of the same order of magnitude:

$$
E_f/E_w = O(1), \qquad \rho_f/\rho_w = O(1), \qquad \ell_f/\ell_w = O(1).
$$

The various physics of the basic frame are introduced through the walls and floors thicknesses that may be different, hence inducing a large range of contrast of stiffness between elements, in compression and bending. Those properties are specified by scaling the wall and floor thicknesses:

$$
a_w/\ell_w = O(\varepsilon^{k_w}) \text{ and } a_f/\ell_w = O(\varepsilon^{k_f}),
$$

where k_w and k_f are fixed for each investigated structure. The reference frequency used for scaling the modal frequencies is taken by convention as

$$
\omega_r = \frac{1}{L}\sqrt{\frac{2\,E_w A_w}{\Lambda}},
\tag{3-4}
$$

where Λ is the global linear mass of the structure. The modal frequency is scaled through the ratio of the length of elements to their wavelength at this frequency. Because of linearity, the modes can be normalized and the mean transverse displacement order is chosen at zero. The effective orders of magnitude with respect to U^0/L of the rotation of the section α and of the mean nodal rotation θ, are deduced through the homogenization process.

Macroscopic parameters. In the expansions there appear naturally

(a) the linear masses of
$$\begin{cases} \text{the two walls,} & \Lambda_w = 2\rho_w A_w, \\ \text{the floor,} & \Lambda_f = \rho_f A_f \ell_f/\ell_w, \\ \text{the cell,} & \Lambda = \Lambda_f + \Lambda_w; \end{cases}$$

(b) the bending stiffnesses of the two walls,
$$\begin{cases} \text{(inner bending)} & 2E_w I_w, \quad \text{where } I_w = a_w^3 h/12, \\ \text{(global bending)} & E_w I = E_w A_w \ell_f^2/2; \end{cases}$$

(c) the macroscopic shear stiffnesses of
$$\begin{cases} \text{the two walls,} & K_w = 2\kappa_w \ell_w, \quad \text{where } \kappa_w = 12E_w I_w/\ell_w^3, \\ \text{the floor,} & K_f = \kappa_f \ell_f^2/\ell_w, \text{ where } \kappa_f = 12E_f I_f/\ell_f^3, \\ \text{the cell,} & K^{-1} = K_w^{-1} + K_f^{-1}. \end{cases}$$

The macroscopic area moment of inertia I is that of a beam made of the two walls distant of ℓ_f, and $\kappa_i = 12E_i I_i/\ell_i^3$ is the static bending stiffness of a bi-embedded beam.

4. Transverse dynamics of multi-framed structures

This section shows that the structures considered can exhibit four main kinds of behavior, according to the frame characteristics. Starting from the three discrete kinematic variables $U(n)$, $\alpha(n)$ and $\theta(n)$, the beam-like model can be governed either

- by the single continuous variable U, corresponding to a *shear beam*,
- or by the two independent continuous variables U and α, corresponding to a *slender-Timoshenko beam*,
- or by U and θ, corresponding to an *inner bending / shear beam*,
- or by the three independent continuous variables U, α and θ when transferred to a macroscopic scale, in which case a *double bending shear beam* is obtained.

These models can be considered as particular cases of a *generic beam*.

Shear beam. The simplest macroscopic description is obtained (for instance) when walls and floors have thicknesses of order ε^2: in symbols, $a_w/\ell_w = O(\varepsilon^2)$ and $a_f/\ell_w = O(\varepsilon^2)$.

Leading macroscopic balance equations. In this case, the macroscopic transverse dynamics occurs at frequency ω of order $O(\omega_r(a_w/\ell_w)) = O(\omega_r\varepsilon^2)$, denoted for this reason $\tilde{\omega}_2$. The variables $\tilde{U}^0$ and $\tilde{\theta}^0$ are of the zero order, while the section rotation $\tilde{\alpha}^2$ is of the second order. Considered to leading order, Equations (3-3) give

$$\begin{cases} K_w(\tilde{U}^{0''} + \tilde{\theta}^{0'}) + \Lambda\tilde{\omega}_2^2 \tilde{U}^0 = 0 & (\text{T}_t) \\ K_w(\tilde{U}^{0'} + \tilde{\theta}^0) + K_f \tilde{\theta}^0 = 0 & (\text{M}_t) \\ K_f\tilde{\theta}^0 + E_w I\tilde{\alpha}^{2''} = 0 & (\text{M}) \end{cases} \tag{4-1}$$

These equations represent the balance of, respectively, transverse forces, inner moments and differential axial forces (inducing a macroscopic moment). The relation (4-1)M_t defines the inner kinematic of the section. Using this relation for eliminating $\tilde{\theta}^0$ in (4-1)T_t, we obtain a differential equation of second degree in $\tilde{U}^0$:

$$K\tilde{U}^{0''} + \Lambda\tilde{\omega}_2^2 \tilde{U}^0 = 0. \tag{4-2}$$

Thus, $\tilde{U}^0$ appears as the single driving macroscopic variable. The inner deformation of the section measured by $\tilde{\theta}^0$ and the rotation $\tilde{\alpha}^2$ can be derived from the knowledge of $\tilde{U}^0$ by means of the equations

$$\tilde{\theta}^0 = -\frac{K}{K_f}\tilde{U}^{0\prime}, \qquad \tilde{\alpha}^{2\prime\prime} = \frac{K}{E_w I}\tilde{U}^{0\prime}. \tag{4-3}$$

Equivalent beam. These results allow one to construct an equivalent beam by defining the appropriate behavior law. Equation (4-2) suggests that we define a macroscopic shear force $\tilde{T}^0$ dual to the section translation $\tilde{U}^0$ whose variations balance the inertia:

$$\tilde{U}^{0\prime} = \Lambda\tilde{\omega}_2^2\,\tilde{U}^0. \tag{4-4}$$

This gives

$$\tilde{T}^0 = -K\,\tilde{U}^{0\prime}. \tag{4-5}$$

The force $\tilde{T}^0$ results from the balance of transverse force T_t, but they are not identical; the former is built from the elastic deformation (of the first order) exclusively, whereas T_t contains all the effects, including the inertia. Equations (4-4) and (4-5) correspond to the macroscopic shear beam equivalent to (4-2) and governed by the two dual variables, $\tilde{U}^0$ and $\tilde{T}^0$ that are sufficient to define the proper boundary conditions for transverse vibrations. The macroscopic shear force is generated by the shear mechanism of the frame. This latter results from the bending of frames beams bi-embedded at their endpoints, as suggested by physical intuition and confirmed by the expression of K (item (c) on page 1715). The shear beam reduces the three degrees of freedom at the local scale to one - the section translation - at the macro scale. Although $\tilde{\theta}^0$ is of the zero order, it disappears, as $\tilde{\alpha}^2$, in the macro description. These last variables have the status of "hidden" internal variables driven by the macro variable, as indicated in (4-3). This shear beam is the continuous version of the shear model widely used in earthquake engineering.

Slender-Timoshenko beam. Consider now structures whose wall and floor thicknesses are of the same order as the scale ratio, so $a_w/\ell_w = O(\varepsilon)$ and $a_f/\ell_w = O(\varepsilon)$.

Leading macroscopic balance equations. In this case, detailed in Section 7F, transverse vibrations occur at frequency $\tilde{\omega}_1$ of order $O(\omega_r(a_w/\ell_w)) = O(\omega_r\varepsilon)$ and variables $\tilde{U}^0$, $\tilde{\theta}^0$, $\tilde{\alpha}^0$ are of the zero order. Considered to leading order, Equations (3-3) yield

$$\begin{cases} K_w\big(\tilde{U}^{0\prime\prime} + \tilde{\theta}^{0\prime}\big) + \Lambda\tilde{\omega}_1^2\,\tilde{U}^0 = 0 & (\text{T}_t) \\ K_w\big(\tilde{U}^{0\prime} + \tilde{\theta}^0\big) + K_f\big(\tilde{\theta}^0 - \tilde{\alpha}^0\big) = 0 & (\text{M}_t) \\ K_f\big(\tilde{\theta}^0 - \tilde{\alpha}^0\big) + E_w I\tilde{\alpha}^{0\prime\prime} = 0 & (\text{M}) \end{cases} \tag{4-6}$$

As above, the balance of inner moments (4-6)M_t provides the inner kinematic of the section,

$$\tilde{\theta}^0 = K\left(\frac{\tilde{\alpha}^0}{K_w} - \frac{\tilde{U}^{0\prime}}{K_f}\right). \tag{4-7}$$

The use of this relation to eliminate $\tilde{\theta}^0$ in (4-6)T_t and (4-6)M gives

$$\begin{cases} K\big(\tilde{U}^{0\prime\prime} + \tilde{\alpha}^{0\prime}\big) + \Lambda\tilde{\omega}_1^2\tilde{U}^0 = 0, \\ K\big(\tilde{U}^{0\prime} + \tilde{\alpha}^0\big) - E_w I\tilde{\alpha}^{0\prime\prime} = 0. \end{cases} \tag{4-8}$$

This shows that the translation $\tilde{U}^0$ and the rotation $\tilde{\alpha}^0$ of the section are the two independent governing variables, while $\tilde{\theta}^0$ is linked to them by (4-7). Combining the two parts of (4-8) we obtain

$$E_w I \left(\tilde{U}^{0''''} + \frac{\Lambda \tilde{\omega}_1^2}{K} \tilde{U}^{0''} \right) - \Lambda \tilde{\omega}_1^2 \tilde{U}^0 = 0 \tag{4-9}$$

Equivalent beam. The preceding description is close to that of a Timoshenko beam. The presence of two kinematic variables leads us to introduce a shear force $\tilde{T}^0$ dual to the translation and a bending moment $\tilde{M}^0$ dual to the section rotation. From (4-8), they are defined by

$$\tilde{T}^0 = -K \left(\tilde{U}^{0'} + \tilde{\alpha}^0 \right), \qquad \tilde{M}^0 = E_w I \, \tilde{\alpha}^{0'}, \tag{4-10}$$

so that the macro description (4-8) is now

$$\tilde{T}^{0'} = \Lambda \tilde{\omega}_1^2 \, \tilde{U}^0, \qquad \tilde{M}^{0'} = -\tilde{T}^0 \tag{4-11}$$

meaning that the variations of shear force balance the inertial effect, and those of bending moment balance the shear force (as in classical beam theory). The macroscopic shear force (4-10)$_1$ is generated by the shear deformation of the cell already described for the shear beam. The shear distortion of the cell now combines the gradient of the translation and the section rotation. The macroscopic bending moment of the whole structure comes from simultaneous traction-compression of walls, as indicated by the expression of the macro area moment of inertia I (item (b) on page 1715). The behavior laws (4-10) are those of a beam described by

 – the translation $\tilde{U}^0$ and rotation $\tilde{\alpha}^0$ of the section, and
 – the shear force $\tilde{T}^0$ and bending moment $\tilde{M}^0$.

which suffice to express the correct macroscopic boundary conditions. The number of degrees of freedom is once again reduced since $\tilde{\theta}^0$ disappears from the macro description to become a "hidden" internal variable defined from the driving variables by (4-7).

Despite similarities, this model does not exactly fit the usual Timoshenko beam for two reasons. First, for massive beams, the Timoshenko correction due to shear only arises in case of small slenderness. Here the shear effect is present even for large slenderness. Secondly, for a Timoshenko massive beam, no effect of rotation inertia appears (although the discrete moment balances include all the contributions). These differences come from the framed cell whose shear deformability is much larger than in a massive beam and whose rotation inertia is much smaller (so its effect appears only at higher orders).

Note on the scaling. We will prove for the case at hand that transverse modes only occur for frequencies $\omega = O(\omega_r (a_w/\ell_w))$ (the arguments apply to other cases as well). At a frequency $\omega \ll \omega_r (a_w/\ell_w)$, the inertia $\Lambda_w \omega^2 \tilde{U}^0$ disappears from (4-6)$_{\mathrm{T}_t}$, so a quasistatic solution would be obtained. Conversely, at a frequency $\omega \gg \omega_r (a_w/\ell_w)$, (4-6)$_{\mathrm{T}_t}$ reduces to $\Lambda_w \omega^2 \tilde{U}^0 = 0$, so $\tilde{U}^0 = 0$. Thus, we are left with equations involving $\tilde{\alpha}^0$ and $\tilde{\theta}^0$. Such *gyration* deformations without translation at the leading order do not correspond to a transverse mode.

Inner bending / shear beam. A less usual behavior arises when $a_w = O(\varepsilon \ell_w)$ and, say $a_f = O(\varepsilon^{5/3} \ell_w)$: in other words, when the floors are significantly more flexible than the walls, since $K_f = O(\varepsilon^2 K_w)$.

Leading macroscopic balance equations. In this case, transverse vibrations occur for frequencies $\tilde{\omega}_2$ of order $O(\omega_r(a_w/\ell_w)^2)$; $\tilde{U}^0$ and $\tilde{\theta}^0$ are of zero order, and $\tilde{\alpha}^2$ is of second order. The derivation of the behavior requires considering the first two orders of the transverse force and inner moment balances, (3-3)$_1$ and (3-3)$_3$, together with the leading order of the bending moment balance (3-3)$_2$. We obtain

$$
\begin{aligned}
K_w\big(\tilde{U}^{0''} + \tilde{\theta}^{0'}\big) &= 0 \quad &\text{(T}_t) \\
K_w\big(\tilde{U}^{2''} + \tilde{\theta}^{2'}\big) + \Lambda_w\tilde{\omega}_2^2\tilde{U}^0 + 2E_wI_w\big(\tilde{U}^{0''''} + 2\tilde{\theta}^{0'''}\big) &= 0 \quad &\text{(T}_{t1}) \\
K_w\big(\tilde{U}^{0'} + \tilde{\theta}^0\big) &= 0 \quad &\text{(M}_t) \\
K_w\big(\tilde{U}^{2'} + \tilde{\theta}^2\big) + K_f\tilde{\theta}^0 + 2E_wI_w\big(2\tilde{U}^{0'''} + 2\tilde{\theta}^{0''}\big) &= 0 \quad &\text{(M}_{t1}) \\
K_f\tilde{\theta}^0 + E_wI\tilde{\alpha}^{2''} &= 0 \quad &\text{(M)}
\end{aligned}
$$

$$(4\text{-}12)$$

As before, the zero order nodal moment balance supplies the inner kinematic of the section:

$$
\tilde{U}^{0'} + \tilde{\theta}^0 = 0 \tag{4-13}
$$

The elimination of the second order terms between (4-12)$_{\text{T}t1}$ and (4-12)$_{\text{M}t1}$ leads to

$$
2E_wI_w\,\tilde{U}^{0''''} = K_f\,\tilde{U}^{0''} + \Lambda_w\tilde{\omega}_2^2\,\tilde{U}^0. \tag{4-14}
$$

The behavior (4-14) differs fundamentally from that of the slender-Timoshenko beam. Here, the fourth degree term results from inner bending of walls. The quantity $2E_wI_w$ indicates the coupling between walls, due to the nonlengthening of floors, very stiff in their axis. This coupling enforces the bi-embedded bending of the floors (of very low transverse stiffness K_f), which in turn induces a transverse force. Equations (4-14) and (4-13) imply that the driving variables are the translation $\tilde{U}^0$ and the inner deformation of the section expressed by $\tilde{\theta}^0$. The section rotation, of order two, is a *hidden* internal variable defined by

$$
\tilde{\alpha}^{2''} = \frac{K_f}{E_wI}\,\tilde{U}^{0'}. \tag{4-15}
$$

Equivalent beam. According to these results, two macroscopic forces are defined, a shear force $\tilde{T}^0$ dual to the translation and an inner bending moment $\tilde{\mathcal{M}}^0$ dual to the inner deformation:

$$
\tilde{T}^0 = -K_f\,\tilde{U}^{0'}, \qquad \tilde{\mathcal{M}}^0 = -2E_wI_w\,\tilde{\theta}^{0'}. \tag{4-16}
$$

$\tilde{T}^0$ takes a form similar to that of the previous beams, except that shear stiffness is induced by the floors alone and the section rotation disappears. The inner moment $\tilde{\mathcal{M}}^0$ due to the simultaneous bending of the walls is new. Using these variables, (4-13) and (4-14) become

$$
\big(\tilde{T}^0 + \tilde{\mathcal{M}}^{0'}\big)' = \Lambda\tilde{\omega}_2^2\,\tilde{U}^0, \qquad \tilde{\theta}^0 = -\tilde{U}^{0'}. \tag{4-17}
$$

The first of these equations means that the inertia is balanced by the variation of the total shear force, which includes $\tilde{T}^0$, induced by the shear of the cell, and the shear force $\tilde{\mathcal{M}}^{0'}$, due to the inner bending of the walls. The inner moment balance (4-17)$_2$ defines the inner kinematic of the section. In accordance with (4-12)$_\text{M}$, a global bending moment $\tilde{M}^0 = E_wI\tilde{\alpha}^{2'}$ such that $\tilde{M}^{0'} = -\tilde{T}^0$ could also be defined, but its effect (traction-compression of walls) is insignificant.

We conclude that the inner bending / shear beam is described by the following macroscopic variables, sufficient to express the macroscopic boundary conditions:

– the section translation $\tilde{U}^0$ and inner deformation associated to the rotation $\tilde{\theta}^0$;

– the shear force $\tilde{T}^0$ and inner bending moment $\tilde{\mathcal{M}}^0$.

This beam model, where the cell inner deformation subsists as a macroscopic variable, is of the same kind as the one proposed by [Kerr and Accorsi 1985].

Double bending shear beam. Here is now investigated the particular situation allowing the global bending, the inner bending of walls and the shear of the cell to have similar intensity. This specific case occurs when $a_w/\ell_w = O(1)$ and $a_f/\ell_w = O(\varepsilon^{2/3})$ so that $K_f = O(\varepsilon^2 K_w)$.

Leading macroscopic balance equations. In this case, the transverse vibrations occur at frequency $\tilde{\omega}_1$ of order $O(\omega_r(a_w/\ell_w))$ and $\tilde{U}^0$, $\tilde{\theta}^0$, $\tilde{\alpha}^0$ are of zero order. As in the previous case, the determination of the behavior requires the first two orders of the mean transverse force and inner moment balances, (3-3)$_1$ and (3-3)$_3$, and the leading order of global moment balance (3-3)$_2$. We obtain

$$
\begin{aligned}
K_w\big(\tilde{U}^{0''} + \tilde{\theta}^{0'}\big) &= 0 \quad (\text{T}_t)\\
K_w\big(\tilde{U}^{2''} + \tilde{\theta}^{2'}\big) \;+\; \Lambda_w\tilde{\omega}_1^2\tilde{U}^0 + 2E_w I_w\big(\tilde{U}^{0''''} + 2\tilde{\theta}^{0'''}\big) &= 0 \quad (\text{T}_{t1})\\
K_w\big(\tilde{U}^{0'} + \tilde{\theta}^0\big) &= 0 \quad (\text{M}_t)\\
K_w\big(\tilde{U}^{2'} + \tilde{\theta}^2\big) + K_f\big(\tilde{\theta}^0 - \tilde{\alpha}^0\big) + 2E_w I_w\big(2\tilde{U}^{0'''} + 2\tilde{\theta}^{0''}\big) &= 0 \quad (\text{M}_{t1})\\
K_f\big(\tilde{\theta}^0 - \tilde{\alpha}^0\big) + E_w I\tilde{\alpha}^{0''} &= 0 \quad (\text{M})
\end{aligned}
\tag{4-18}
$$

This system is similar to that of the inner bending / shear beam, but $\tilde{\alpha}^0$ appears in (4-18)M$_{t1}$ and (4-18)M. Elimination of the second order terms between (4-18)T$_{t1}$ and (4-18)M$_{t1}$ leads to

$$
\tilde{U}^{0'} + \tilde{\theta}^0 = 0, \qquad K_f\big(\tilde{\theta}^0 - \tilde{\alpha}^0\big) - \Lambda_w\tilde{\omega}_1^2\tilde{U}^0 + 2E_w I_w\tilde{U}^{0''''} = 0, \qquad K_f\big(\tilde{\theta}^0 - \tilde{\alpha}^0\big) + E_w I\tilde{\alpha}^{0''} = 0. \tag{4-19}
$$

Combining these three equations gives the sixth-degree differential equation

$$
\frac{2E_w I_w E_w I}{K_f}\tilde{U}^{0''''''} - \big(2E_w I_w + E_w I\big)\tilde{U}^{0''''} - \frac{E_w I\,\Lambda_w\tilde{\omega}_1^2}{K_f}\tilde{U}^{0''} + \Lambda_w\tilde{\omega}_1^2\,\tilde{U}^0 = 0. \tag{4-20}
$$

Equation (4-20) shows that this nonclassical beam integrates the three previously identified mechanisms and requires three kinematic variables. Remarkably, the degrees of freedom at the macro scale are identical to those at the micro scale. Consequently, this is the richest continuous modeling that can be extracted from the class of discrete structures under study.

Equivalent beam. The beam-like description involves three forces dual to the section translation $\tilde{U}^0$ and rotation $\tilde{\alpha}^0$, the inner deformation $\tilde{\theta}^0$. They are defined by

$$
\begin{cases}
\text{shear force} & \tilde{T}^0 = -K_f\big(\tilde{U}^{0'} + \tilde{\alpha}^0\big)\\
\text{bending moment} & \tilde{M}^0 = E_w I\tilde{\alpha}^{0'}\\
\text{inner moment} & \tilde{\mathcal{M}}^0 = -2E_w I_w\tilde{\theta}^{0'}
\end{cases}
\tag{4-21}
$$

and Equations (4-19) now read

$$\left(\tilde{T}^0 + \tilde{M}^{0'}\right)' = \Lambda_w \tilde{\omega}_1^2 \tilde{U}^0, \qquad \tilde{M}^{0'} = -\tilde{T}^0, \qquad \tilde{U}^{0'} + \tilde{\theta}^0 = 0 \tag{4-22}$$

The beam model (4-21), (4-22) combines features of the inner bending shear beam and of the slender-Timoshenko beam (for which $K_f/K_w = O(1)$ so that the shear force and the inner kinematic differ from the present case). We conclude that the double bending shear beam requires six macroscopic boundary conditions to be expressed with the above defined macroscopic variables.

Continuous family of macro behaviors. A systematic study demonstrates that the behaviors evolve gradually according to the properties of the frame elements. To illustrate this, let us fix the thickness of walls at $a_w/\ell_w = O(\varepsilon)$ and decrease the thickness of the floors. The following descriptions are obtained (for briefness, only the equations expressed with $\tilde{U}^0$ are given):

$$\frac{a_f}{\ell_w} = O(\varepsilon^{1/2}) \; : \quad E_w I\left(\tilde{U}^{0''''} + \frac{\Lambda_f \tilde{\omega}_{5/4}^2}{K_w}\tilde{U}^{0''}\right) = \Lambda_f \tilde{\omega}_{5/4}^2 \tilde{U}^0$$

$$\frac{a_f}{\ell_w} = O(\varepsilon) \qquad : \qquad E_w I\left(\tilde{U}^{0''''} + \frac{\Lambda \tilde{\omega}_1^2}{K}\tilde{U}^{0''}\right) = \Lambda \tilde{\omega}_1^2 \tilde{U}^0$$

$$\frac{a_f}{\ell_w} = O(\varepsilon^{3/2}) \; : \qquad\qquad K_f \tilde{U}^{0''} + \Lambda_w \tilde{\omega}_{7/4}^2 \tilde{U}^0 = 0$$

$$\frac{a_f}{\ell_w} = O(\varepsilon^{5/3}) \; : \qquad\qquad K_f \tilde{U}^{0''} + \Lambda_w \tilde{\omega}_2^2 \, \tilde{U}^0 = 2 E_w I_w \tilde{U}^{0''''}$$

$$\frac{a_f}{\ell_w} = O(\varepsilon^2) \quad : \qquad\qquad\qquad \Lambda_w \tilde{\omega}_2^2 \tilde{U}^0 = 2 E_w I_w \tilde{U}^{0''''}$$

For floors thickness such that $a_f/\ell_w = O(\varepsilon^{1/2})$ or $O(\varepsilon)$, the global bending and shear of the cell (governed by the wall or the frame flexibility) are of the same magnitude and lead to slender Timoshenko models. The decrease of the floor thickness increases their flexibility and in turn prevents the global bending. Thus, in a first step, where $a_f/\ell_w = O(\varepsilon^{3/2})$, a shear beam governed by the floor flexibility is recorded; in a second step, where $a_f/\ell_w = O(\varepsilon^{5/3})$, the inner bending of walls appears leading to an inner bending / shear beam; and lastly, with $a_f/\ell_w = O(\varepsilon^2)$, the floor's participation (which only synchronize the wall motions) vanishes and an inner bending beam is obtained.

The second example concerns beams of identical walls and floors thickness. A continuous passage from the global bending beam (as a perforated beam) through a Timoshenko beam and finally a shear beam is observed when reducing the thicknesses:

$$\begin{cases} \dfrac{a_w}{\ell_w} = O\left(\dfrac{a_f}{\ell_f}\right) = O(\varepsilon^{1/2}) : & E_w I \tilde{U}^{0''''} = \Lambda \tilde{\omega}_1^2 \tilde{U}^0, \\[2mm] \dfrac{a_w}{\ell_w} = O\left(\dfrac{a_f}{\ell_f}\right) = O(\varepsilon) \quad : & E_w I\left(\tilde{U}^{0''''} + \dfrac{\Lambda \tilde{\omega}_1^2}{K}\,\tilde{U}^{0''}\right) = \Lambda \tilde{\omega}_1^2 \tilde{U}^0, \\[2mm] \dfrac{a_w}{\ell_w} = O\left(\dfrac{a_f}{\ell_f}\right) = O(\varepsilon^{3/2}) : & K \tilde{U}^{0''} + \Lambda \tilde{\omega}_{3/2}^2 \tilde{U}^0 = 0. \end{cases} \tag{4-23}$$

To summarize, three elastic parameters determine the different macroscopic behaviors:

– the cell shear stiffness K, which may be reduced to the wall or floor stiffness (K_w or K_f);

- the global bending stiffness $E_w I$;

- the inner bending stiffness $2E_w I_w$.

Owing to scale separation, these parameters are given by the static properties of the elements (see (b) and (c) on page 1715). The scaling of the thicknesses (then stiffnesses) is essential to capture the physics and to identify all possible models. Without scaling, meaning in fact $a_w/\ell_w = O(a_f/\ell_f) = O(1)$, the only model that could be obtained would be a global bending model, irrelevant for most cases.

Despite a common architecture, the various structures exhibit very different dynamic behaviors: for instance, the eigenfrequencies f_k follow the series of odd integers, $f_k/f_1 = (2k-1)$ for cantilever shear beam and are approximately proportional to the series of square odd integers, $f_k/f_1 \approx (2k-1)^2/1.44$ ($k > 1$), for the bending beam.

Generic beam model. The aim is to build a model that may degenerate to any of the previous model. To include all the mechanisms, such a model must involve the three kinematic variables U, α, θ. This generalization sacrifices the uniformity in order of magnitude of the several terms (i.e., according to the value of the parameters, some terms could be negligible in this generalized model). For this reason, the tilde and exponent order are removed from the variables. The natural way to associate in a generic beam the slender-Timoshenko and inner bending shear beam properties is to define the following behavior laws:

$$
\begin{cases}
\text{shear force} & T = -K(U' + \alpha) \\
\text{bending moment} & M = E_w I \alpha' \\
\text{inner moment} & \mathcal{M} = 2E_w I_w U''
\end{cases}
\tag{4-24}
$$

and the force and moment balance equations, associated with the inner kinematic of the section:

$$
(T + \mathcal{M}')' = \Lambda \omega^2 U, \qquad M' = -T, \qquad K_w(U' + \theta) + K_f(\theta - \alpha) = 0.
\tag{4-25}
$$

Thus, the sixth order equation governing the generic beam takes the generalized form

$$
\frac{2E_w I_w E_w I}{K} U'''''' - (2E_w I_w + E_w I) U'''' - \frac{E_w I}{K} \Lambda \omega^2 U'' + \Lambda \omega^2 U = 0.
\tag{4-26}
$$

Energy balance and boundary conditions. The consistency of those definitions can be checked by establishing the energy balance of this generic beam. For this purpose, multiply (4-25)a by U and integrate by part over the beam length H:

$$
\int_0^H \Lambda \omega^2 U^2 dx = \int_0^H (T' + \mathcal{M}'') U dx = \left[(T + \mathcal{M}') U \right]_0^H - \int_0^H (T + \mathcal{M}') U' \, dx.
$$

Taking into account (4-25)$_2$ and then integrating again by parts, the last integral becomes

$$
\int_0^H T(U' + \alpha) \, dx + \int_0^H M' \alpha \, dx + \int_0^H \mathcal{M}' U' \, dx
$$
$$
= \int_0^H \left(T(U' + \alpha) - M\alpha' - \mathcal{M}U'' \right) dx + [M\alpha]_0^H + [\mathcal{M}U']_0^H.
$$

Finally, using the behavior laws (4-24), we get

$$\int_0^H \Lambda \omega^2 U^2 \, dx = \underbrace{\int_0^H \left(\frac{T^2}{K} + \frac{M^2}{E_w I} + \frac{\mathcal{M}^2}{2E_w I_w} \right) dx}_{\text{Elastic energy}} + \underbrace{\left[(T + \mathcal{M}')U \right]_0^H - \left[M\alpha \right]_0^H - \left[\mathcal{M}U' \right]_0^H}_{\text{Work of boundary conditions}} \quad (4\text{-}27)$$

This energy balance equation states the equality of the kinetic energy with the elastic energy associated to the three mechanisms and the energy provided at the boundaries (which defines explicitly the appropriate boundary conditions). This suggests that, to define the macroscopic constitutive laws of the equivalent continuous beam, it is more general to use the three global cell parameters involved in the shear, global and inner bending rather than the precise frame cell geometry. When expressed with these global cell parameters, the beam-like descriptions established above may be employed for other symmetric cells, as explained in the next section.

5. Behavior of real structures

This section deals with practical applications of the preceding results. Real structures, made up of a finite (even if large) number of cells, themselves of finite size, match only imperfectly the homogenization conditions stipulating that the scale ratio should tend to zero.

As a first consequence, the homogenized descriptions only provide reasonable approximations to the behavior. What is meant by reasonable will be clarified in Section 5B, devoted to numerical modeling, and in Section 5C, where the effective order of the corrector is analyzed. A second consequence is of first importance for problems involving, in addition to the scale ratio, other small physical parameters (here the thickness to length ratios). For a given structure, what is the proper choice amongst the possible behaviors, or, in other words, what is the appropriate scaling?

5A. *Identification of the relevant modeling.* To establish the modeling, hence the proper scaling for a real structure, let's proceed as follows. Consider a given periodic structure of cell size ℓ, vibrating at macro scale and admit for the moment that the physical macro length L associated to these oscillations can be correctly assessed. Since ℓ is known, the *finite physical scale ratio*

$$\tilde{\varepsilon} = \frac{\ell}{L}$$

of this structure under these vibrations is therefore defined. The numerical finite value of each small parameter (here geometrical) characterizing the real cell can also be quantified and equalized to the physical scale ratio $\tilde{\varepsilon}$ at a particular power. This power, then replaced by a close integer or rational number, supply unambiguously the physical scaling consistent with the real problem in consideration.

Performing homogenization with this scaling consists in replacing the physical value $\tilde{\varepsilon}$ by a mathematical ε tending to zero. By doing so, the relative orders of magnitude of the physical terms are kept identical from the real cell to the continuous model obtained at the limit. Finally, the real structure can be seen as an imperfect realization (for the small but finite mathematical value $\varepsilon = \tilde{\varepsilon}$) of the homogenized continuous model built with the proper scaling. The smaller $\tilde{\varepsilon}$ is, the better would be the continuous approximation. Thus, in real cases it is possible to identify the right continuous description, provided that the macro length L is reliably estimated.

Macroscopic length of modal vibrations. Length L is evaluated by a dimensional analysis realized at the macroscopic scale, which gives classically [Boutin and Auriault 1990]

$$L = \frac{O(U)}{O(\partial_x U)} \tag{5-1}$$

This estimation is consistent with the asymptotic expansion since the increment of the macroscopic variable on one cell, $\ell\, \partial_x U$, has to be of order ε compared to its current value, U. This implies: $\ell\, \partial_x U = O(\varepsilon\, U) = O(\ell\, U/L)$, leading to (5-1). Apply this result to the k-th eigenmode of cantilever beams (embedded at base and free at the top) of length H (the cantilever conditions are taken for concreteness):

- For shear beams, the modal analysis shows that modal shape are expressed on the basis of two exponentials $\{e^{(\pm ix/L_k)}\}$, L_k being solutions of $\cos(H/L_k) = 0$ so that $L_k = 2H/(\pi(2k-1))$. From the estimation (5-1), L_k is the researched characteristic length of the k-th mode of shear beams.

- For bending beams, the decomposition basis is $\{e^{(\pm ix/L_k)}, e^{(\pm x/L_k)}\}$, where L_k is a solution of $\cos(H/L_k) = 1/\cosh(H/L_k)$, whose zeros are close to $L_k \simeq 2H/(\pi(2k-1))$. Here again from (5-1), L_k is the characteristic length of the k-th mode of bending beams.

- For other beams combining shear and one (or two) bending effects, two (or three) spatial constants appear in the basis of exponentials. It can be proved algebraically that the smaller value (which must be considered for defining the characteristic length) is always close to $L_k \simeq 2H/(\pi(2k-1))$.

Thus, for an N-level structure ($H = N\,\ell_w$) and *independently of the model*, the macroscopic length L_k of the k-th embedded-free mode is known and the physical scale parameter is related to the mode number and to the number of cells:

$$\tilde{\varepsilon}_k = \frac{\ell}{L_k} \simeq \frac{\pi(2k-1)}{2N}, \qquad L_k \simeq \frac{2H}{\pi(2k-1)} \tag{5-2}$$

To illustrate (5-2), consider the first mode of a ten-level building as in Figure 1. From (5-2) $\tilde{\varepsilon}_1 = 0.15$ and if $\ell_w = \ell_f = 3$ m and $a_w = a_f = 50$ cm $= O(\tilde{\varepsilon}_1 \ell_w)$, a slender-Timoshenko beam is expected. If $a_w = a_f = 20$ cm $= O(\tilde{\varepsilon}_1^{1.5} \ell_w)$, the behavior would be that of a shear beam, and so on.

Interestingly, (5-2) indicates that the maximum number of modes respecting the scale separation is limited to $N/3$ (a third of the number of cells), beyond which HPDM is irrelevant.

Identification criterion based on dimensionless parameters. To identify the global behavior of a given structure, more physical insight, as well as generality, would be obtained by working in terms of macroscopic elastic coefficients of the cell rather than in terms of its elements thicknesses. In this aim, since the macro lengths are quite similar whatever the modeling, a dimensional analysis is realized on the generic beam. The change of variables $\boldsymbol{x} = x/L$ (with the mode to be specified later) transforms the governing equation (4-26) into

$$C\,\gamma\,U^{*''''''} - (1+\gamma)\,U^{*''''} - \Omega^2\,U^{*''} + \frac{\Omega^2}{C}\,U^* = 0, \tag{5-3}$$

where, by construction, the dimensionless terms marked with $*$ are $O(1)$ and

$$C = \frac{E_w I}{K L^2}, \qquad \gamma = \frac{2 E_w I_w}{E_w I} = \frac{2 I_w}{I}, \qquad \Omega^2 = \frac{\Lambda \omega^2 L^2}{K}. \tag{5-4}$$

C evaluates the global bending effect compared to shear effect and γ the inner bending compared to global bending. C and γ supply efficient identification criteria of behavior: according to their order of magnitude with respect to $\tilde{\varepsilon}$, Equation (5-3) degenerates into simplified forms in such a way that all the models are recovered. For instance, if $C = O(1)$ and $\gamma = O(\tilde{\varepsilon})$, the terms related to $C\gamma$ and γ disappear and the resulting model is

$$U^{*''''} + \Omega^2 U^{*''} - \frac{\Omega^2}{C} U^* = 0,$$

which corresponds to a slender Timoshenko beam, and similarly for the other cases. By doing so, seven behaviors are obtained depending on the value of C, $C\gamma$ and γ compared to $\tilde{\varepsilon}$ and $\tilde{\varepsilon}^{-1}$. A synthetic representation (Figure 3) is deduced by mapping the domain of validity of each behavior according to the two parameters p and q defined by

$$C = \tilde{\varepsilon}^p \quad \text{and} \quad \gamma = \tilde{\varepsilon}^q. \tag{5-5}$$

We remark that γ and the constant β defined by

$$\beta = \frac{E_w I}{K \ell_w^2} = \frac{E_w I}{K L^2} \left(\frac{L}{\ell_w}\right)^2 = C \tilde{\varepsilon}^{-2} = \tilde{\varepsilon}^{p-2} \tag{5-6}$$
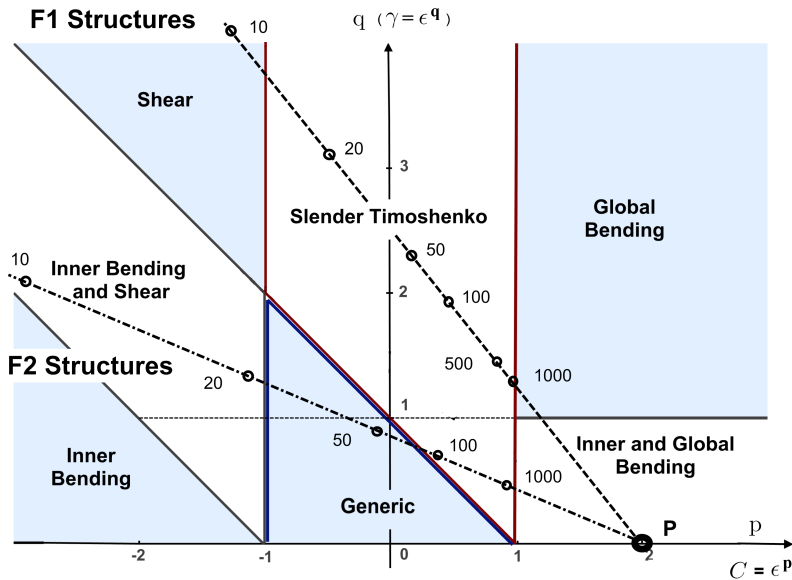
Figure 3. Domains of validity of the equivalent beams according to values of p and q defined by $C = \tilde{\varepsilon}^p$ and $\gamma = \tilde{\varepsilon}^q$. Beams made of a given cell are located on a straight line issued from point P ($p = 2$, $q = 0$). On this line, the representative point moves away from P when increasing the order k of the mode and closer to P when increasing the number N of cells. For example, the two dotted straight lines correspond to the behavior of the first mode in function of the number of levels (numbered points) for the F_1 and F_2 structures studied in Section 5B.

provide two intrinsic parameters of the cell (for the structures being studied, $a_w < \ell_w = O(\ell_f)$ implies $\gamma < 1$). Therefore, values of p and q enabling one to define the behavior of beams made of a *given cell* (β and γ fixed) are determined in the following manner: in terms of $\tilde{\varepsilon}$ — which depends on the number of cells and on the mode number; see (5-2) — p and q are given by

$$(p-2) \log \tilde{\varepsilon} = \log \beta \quad \text{and} \quad q \log \tilde{\varepsilon} = \log \gamma;$$

then, eliminating $\tilde{\varepsilon}$, we get

$$(p-2) \log \gamma - q \log \beta = 0. \tag{5-7}$$

Thus, in the (p, q) plane, the possible behaviors of beams made of a *given cell* necessarily lie on the straight line issuing from point P $(p = 2, q = 0)$ of (5-7). For beams made of a given number of cells, the position on the line moves away from P as the mode number is increased ($\tilde{\varepsilon}$ increases). Conversely, for a given mode number, the position on the line approaches P as the number of cells increases (and $\tilde{\varepsilon}$ decreases). Consequently, the modes of a given structure are not necessarily described by a unique macroscopic model. For instance, the description could be a bending beam for the first few modes, then a slender-Timoshenko beam and finally a shear beam for the higher modes: see Figure 3. Conversely, at a given mode order, if the number of cells is increased, the opposite evolution from shear to bending beam arises. This corresponds to the well known effect of slenderness in beam theory.

5B. *Numerical validation.* To investigate the relevance of the homogenized descriptions for structures of finite number of cells, we made comparisons with numerical simulations. We modeled a large number of fictitious structures, each made of basic frames having walls and floor of length 3 m and modulus $E = 200$ GPa. The diversity that allows most of the cases to be covered was introduced in two ways. First, the number N of cells varies from 5 to 1000; secondly, two basic frame have been used:

- F_1, whose walls and floor thicknesses are identical (0.1 m), and

- F_2, whose walls are thicker (1 m) than the floor (0.15 m).

For each of these structures, considering clamped-free boundary conditions, the four first eigenmodes were calculated using three independent methods:

- First, a direct numerical treatment of the structure was carried out with the finite element code RDM6, using a beam element for meshing each beam of the structure. The convergence criterion was based on the relative eigenfrequency error being less than 10^{-4}.

- Next, the eigenmodes were determined using generic beam modeling, with appropriate intrinsic parameters for the basic frames ($\beta = 675$ and $\gamma = 1/2700$ for F_1, and $\beta = 1336$ and $\gamma = 1/27$ for F_2) and appropriate boundary conditions ($U = 0$, $\alpha = 0$, $\theta = 0$ on the clamped base, and $T = 0$, $M = 0$, $\mathcal{M} = 0$ on the top). The resolution (not presented here) followed the modal method; the eigenfrequencies are the zeros of the 6×6 determinant of equations describing the boundary conditions.

- Finally, the proper modeling of each structure is identified from the calculated values of C and γ, compared to $\tilde{\varepsilon} = \pi/2N$ power. The proper boundary conditions are expressed with the macro variables of the identified model, and the eigenmodes are determined; following this approach, F_1-structures are always well modeled by a slender-Timoshenko beam, but simpler models are efficient: shear beam when $N < 30$; global bending beam when $N > 300$ (Figure 6, top). The F_2-structures vary from an
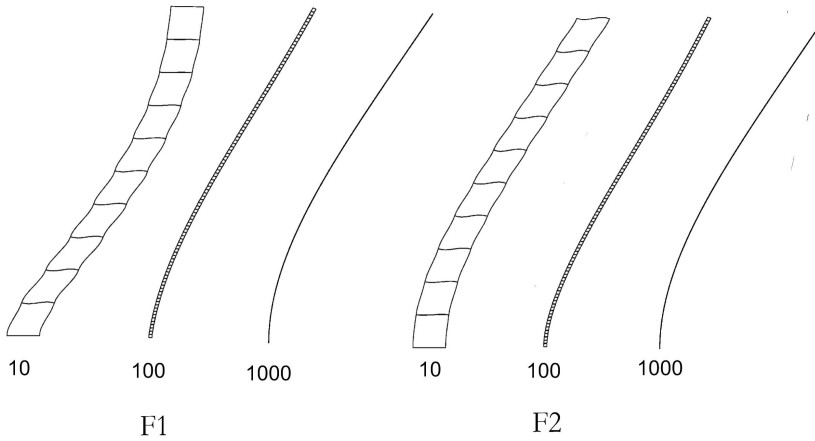
Figure 4. Fundamental mode shape of F_1-structures (left) and F_2-structures (right) made of 10, 100 or 1000 identical frames. For comparison, all the structures are drawn at the same size.

inner bending beam ($N < 20$) to a generic beam close to a shear beam ($N \approx 60$) and tend to a global bending beam for $N > 200$ (Figure 3 and 6, bottom).

The analysis of the results focuses on three points:

(1) the diversity of behaviors, illustrated by the variety of the mode shapes (Figure 4),

(2) a comparison of the eigenfrequencies derived by the three methods (Figures 5 and 6), and

(3) the series of eigenfrequency ratios f_i/f_1 for $i = 2, 3, 4$ (Figure 6). This series of ratios characterizes very efficiently the nature of the behavior, and so constitutes a stringent criterion for the reliability of equivalent beams. Shear and bending beams correspond respectively to the series $(1, 3, 5, 7)$ and $(1, 6.25, 17.36, 34.03)$.

Figure 5 shows excellent agreement of the generic beam modeling with the numerical calculations. This highlights the relevance of the analytical generic beam for the wide range of cases we tested. Even with poor scale separation (and even very poor, e.g., the fourth mode of the five-frame structure), the generic beam provides surprisingly good results. An attempt to explain this observation is made in Section 5C.

The comparison in Figure 6 between the results derived from the proper specific beam and the generic beam (and numerical modeling) shows that both coincide only in the validity range established theoretically. As expected, outside this range, both significantly diverge, meaning that the specific model loses its relevancy, and has to be replaced by the actual proper beam in this other range. The continuous evolution from one model to another is consistent with that predicted above (Figure 3). To summarize:

– In the scale separation frequency range, the tested structures reach most of the possible cases (shear, slender-Timoshenko, double bending, generic beam); it appears that every case can be described accurately by one of these modeling, meaning that all the physical mechanisms are properly described by the homogenized behavior.
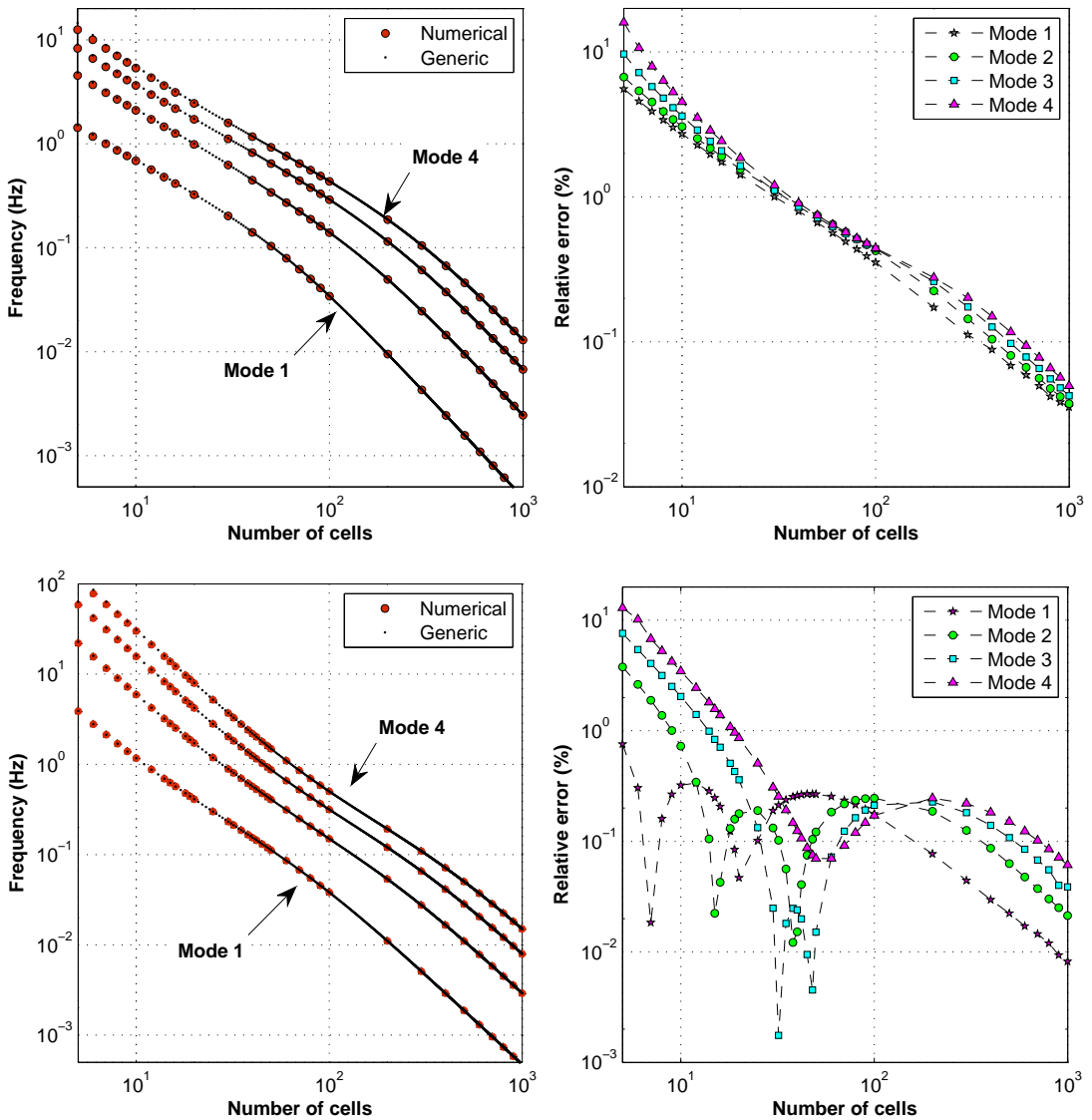
Figure 5. Eigenfrequencies of the four first modes of F_1 structures (top) and F_2 structures (bottom), versus the number of frames. Comparison between generic beam modeling and numerical calculations (left) and errors evaluation in percent (right).

– The interest and the accuracy of the generic beam clearly appears, specially in intermediate cases where none of the simplified beams provides sufficiently accurate results.

– The proposed procedure of determining the proper macro beam for a specific case is confirmed numerically.

– Complementary to the generic beam, the interest and the accuracy of the relevant homogenized beam model, of easier use than the generic beam model, are confirmed in their own validity range.
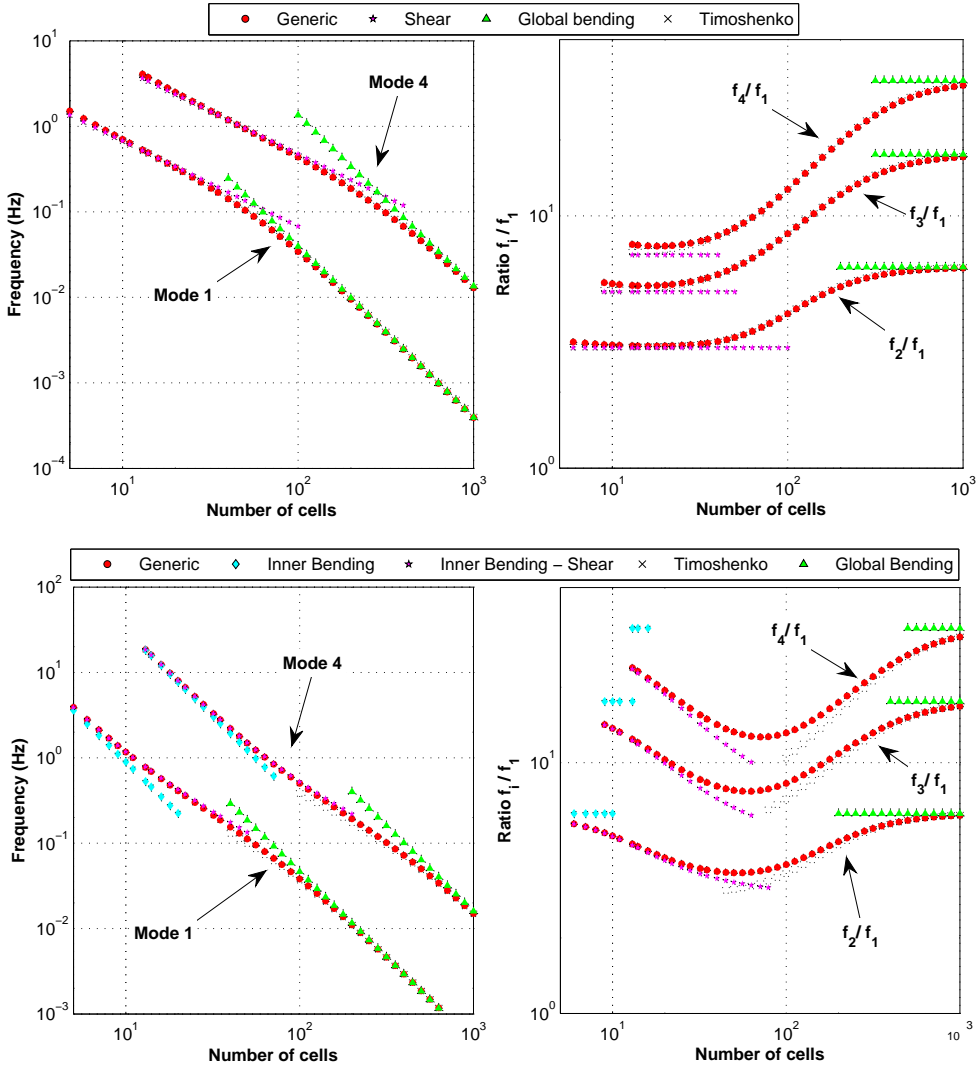
Figure 6. Comparison between generic beam modeling and identified proper beam model (top: shear and slender-Timoshenko, F_1-structures; bottom: inner bending beam and global bending, F_2-structures). On the left are shown the eigenfrequencies of the first and fourth modes; other modes are not drawn for the clarity. On the right, ratios f_i/f_1 versus the number of frames.

5C. *Effective corrector order: the slender-Timoshenko case.* The numerical examples have shown that HPDM provides accurate results even though the scale separation is poor. A possible explanation may be found in the effective order of magnitude of the terms neglected by the zero order description. In fact, despite the form of the expansion (2-1), it will be shown that the corrector is of order ε^2 (at least for slender-Timoshenko beams). This argument is in favor of a largest extent of validity and reliability of the homogenized description.

Investigate high order terms for improving the description in the presence of poor scale separation have already been proposed for continuous media [Bensoussan et al. 1978; Bakhvalov and Panasenko 1989; Gambin and Kröner 1989; Boutin and Auriault 1993], for discrete media [Verna 1991; Tollenaere 1994; Pradel and Sab 1998] and for beams [Buannic and Cartraud 2001a; 2001b]. A detailed analysis of higher order correctors is beyond the scope of this paper; the single case of the slender-Timoshenko beam is studied hereafter to identify its effective order.

Macroscopic balance equations at the first order. To pursue at the next order the resolution begun in Section 4 and Section 7, the balance equations concerning $\tilde{U}^1$, $\tilde{\theta}^1$, $\tilde{\alpha}^1$ are established, whose beam theory interpretation is similar to that of the zero order. The behavior laws remain identical:

$$\tilde{T}^1 = -K\left(\tilde{\alpha}^1 + \tilde{U}^{1'}\right), \qquad \tilde{M}^1 = E_w I\,\tilde{\alpha}^{1'}, \tag{5-8}$$

whereas the balance equations read ($\tilde{\omega}_2$ is the second term of the modal frequency expansion):

$$\tilde{T}^{1'} - \Lambda\tilde{\omega}_1^2\,\tilde{U}^1 = 2\Lambda\tilde{\omega}_1\tilde{\omega}_2\,\tilde{U}^0, \qquad \tilde{M}^{1'} = -\tilde{T}^1. \tag{5-9}$$

The difference with (4-11) comes from the term induced by the zero order solution $\tilde{U}^0$, playing the role of an inner body force. Combining (5-8) and (5-9), we see that the first order is governed by

$$\Gamma[\tilde{U}^1] = E_w I\left(\tilde{U}^{1''''} + \frac{\Lambda\tilde{\omega}_1^2}{K}\,\tilde{U}^{1''}\right) - \Lambda\tilde{\omega}_1^2\,\tilde{U}^1 = \frac{2\tilde{\omega}_2}{\tilde{\omega}_1}E_w I\,\tilde{U}^{0''''}, \tag{5-10}$$

where the differential operator Γ is the same as at the zero order; see (4-9).

Cancellation of the first order. The first corrective term generally presents a particular energetic property. In composite media, the work of the first corrector under the zero order solution is null at the period scale; see for example [Boutin and Auriault 1993; 1995]. For discrete media, a similar result was obtained for braced framed structures in [Tollenaere 1994].

This property is related to the Fredholm alternative [Bensoussan et al. 1978]. In fact, the order zero solution is the eigenfunction associated to the null eigenvalue of the differential operator. This latter being unmodified at the next order, a solution exists if and only if the source term is orthogonal to the eigenfunction with eigenvalue zero, which is the order zero solution.

We apply this idea here by calculating the virtual work of $\tilde{U}^0$ under $\tilde{U}^1$ and reciprocally, these motions being governed by

$$\Gamma[\tilde{U}^0] = 0, \qquad \Gamma[\tilde{U}^1] = \frac{2\tilde{\omega}_2}{\tilde{\omega}_1}E_w I\,\tilde{U}^{0''''}. \tag{5-11}$$

For simplicity we consider cantilever beams, so the energy at the boundary conditions cancels out. Algebra similar to that presented in Section 4 gives

$$\int_0^H \Gamma[\tilde{U}^0]\,\tilde{U}^1 dx = W(\tilde{U}^0, \tilde{U}^1) + E_c(\tilde{U}^0, \tilde{U}^1) = 0 \tag{5-12}$$

and

$$\int_0^H \left(\Gamma[\tilde{U}^1] - \frac{2\tilde{\omega}_2}{\tilde{\omega}_1}E_w I\,\tilde{U}^{0''''}\right)\tilde{U}^0 dx = W(\tilde{U}^0, \tilde{U}^1) + E_c(\tilde{U}^0, \tilde{U}^1) + \int_0^H 2\Lambda\tilde{\omega}_1\tilde{\omega}_2\left(\tilde{U}^0\right)^2 dx = 0, \tag{5-13}$$

where the elastic energy W and the virtual kinetic energy E_c take on the form

$$W(\tilde{U}^0, \tilde{U}^1) = \int_0^H \left(\frac{\tilde{T}^0 \tilde{T}^1}{K} + \frac{\tilde{M}^0 \tilde{M}^1}{E_w I} \right) dx, \qquad E_c(\tilde{U}^0, \tilde{U}^1) = \int_0^H \Lambda \tilde{\omega}_1^2 \, \tilde{U}^0 \tilde{U}^1 dx.$$

Comparison of (5-12) and (5-13) leads directly to $\tilde{\omega}_2 = 0$, and then the source term induced by $\tilde{U}^0$ cancels out in the first order balance (5-11)$_2$. Therefore the equations describing the zero and first order are identical, and the first order can be set to zero without restriction. Consequently, the first corrector of the continuous description is only $O(\varepsilon^2)$. It can be inferred from the general argument of the demonstration that this still holds in the other cases.

6. Analogy with micromorphic media

This section points out an analogy between the derived beam behavior and the behavior of micromorphic materials [Eringen 1968]. Toward this aim, we use the physical insight gathered from the dimensional analysis of one-dimensional periodic structures to investigate the features of bi-dimensional periodic structures. For convenience this section focuses on the first mode of transverse vibration polarized in the direction e_2, propagating in the direction e_1. Similar arguments apply for higher modes.

From one- to two-dimensional structures. Consider a cell F_{frame} of shear stiffness K, inner bending stiffness $E I_w$ and global bending stiffness $E I$ corresponding to the intrinsic coefficients $\beta = E I / K \ell_w^2$ and $\gamma = I_w / I$. From this frame, build a periodic $B_{eam} = N_{e_1} \times F_{rame}$, made of N_{e_1} frame cells repeated in the direction e_1, as in Figure 1. The first transverse mode behavior of the B_{eam} is driven by

$$C_B = \beta \left(\frac{\pi}{2 N_{e_1}} \right)^2, \qquad \gamma_B = \gamma.$$

Now build the two-dimensional periodic $S_{tructure}$ by repeating N_{e_2} times in the transverse direction e_2 the same primitive B_{eam}:

$$S_{tructure} = N_{e_2} \times B_{eam} = N_{e_1} \times (N_{e_2} \times F_{rame}).$$

(See figure on the right.) Taking advantage of the periodicity in the e_1 direction, apply to this $S_{tructure}$ the one-dimensional homogenization process.

The properties of the cell made of N_{e_2} copies of F_{rame} (with $N_{e_2} + 1$ walls) can be estimated from those of the basic frame F_{rame}: the shear stiffness is $O(N_{e_2} K)$, the inner bending stiffness is $O(N_{e_2} E I_w)$, and the global bending stiffness is $O(N_{e_2}^3 E I)$. Thus the behavior of $S_{tructure}$ under the first
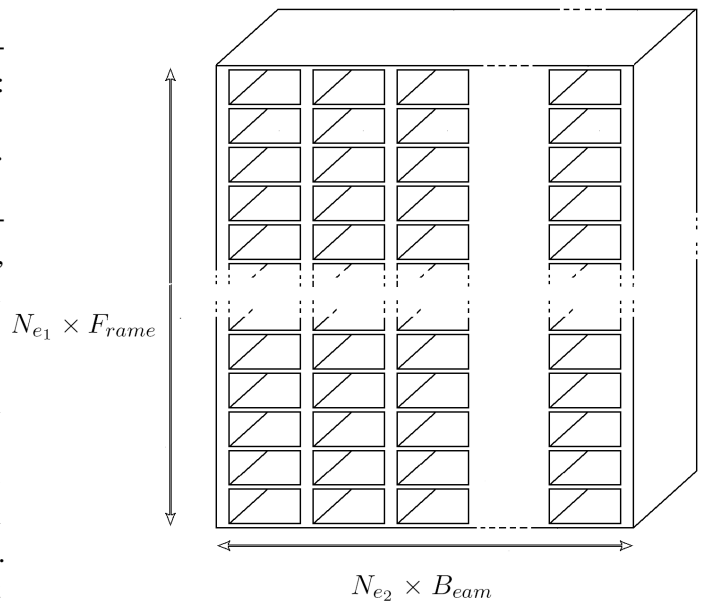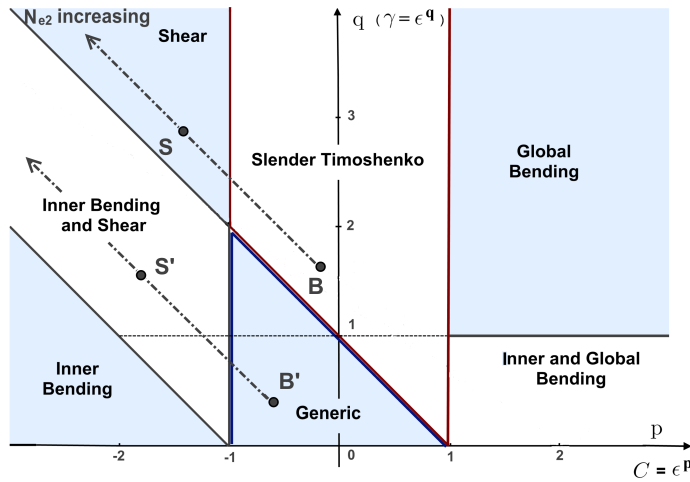
Figure 7. Behavior of the $S_{tructure} = N_{e_2} \times B_{eam}$ in relation to that of the primitive $B_{eam} = N_{e_1} \times F_{rame}$.

transverse mode is driven by the two dimensionless parameters related to those of the primitive frame F_{rame}:

$$C_S = \left(\frac{\pi N_{e_2}}{2N_{e_1}}\right)^2 \beta > C_B, \qquad \gamma_S = \left(\frac{1}{N_{e_2}}\right)^2 \gamma < \gamma_B, \qquad C_S \gamma_S = C_B \gamma_B = \left(\frac{\pi}{2N_{e_1}}\right)^2 \beta \gamma. \tag{6-1}$$

The scale ratio is the same for both B_{eam} and $S_{tructure}$, since they have the same number N_{e_1} of cells in the direction e_1:

$$\tilde{\varepsilon}_S = \tilde{\varepsilon}_B = \tilde{\varepsilon} = \pi/(2N_{e_1}).$$

Therefore, introducing (p_S, q_S) and (p_B, q_B) such that

$$C_S = \tilde{\varepsilon}^{\ p_S}, \quad \gamma_S = \tilde{\varepsilon}^{\ q_S}, \quad C_B = \tilde{\varepsilon}^{p_B}, \quad \gamma_B = \tilde{\varepsilon}^{q_B},$$

the relations (6-1) lead to $p_S + q_S = p_B + q_B$, $p_S < p_B$, and $q_S > q_B$, meaning that in the plane (p, q) of Figure 7, the points S (p_S, q_S) and B (p_B, q_B) representing $S_{tructure}$ and B_{eam} lie on the diagonal of slope -1 going through B. According to the results of Section 5A, the behaviors of the B_{eam} and $S_{tructure}$ are of the same nature if $p_B \leq -1$, but may differ if $p_B > -1$.

Micromorphic media. Consider a L_{ayer} of a "cellular material" of finite thickness $N_{e_1} \ell_w$ and infinite length by making N_{e_2} tend to ∞. From the same reasoning, the point L (p_L, q_L) representative for the L_{ayer} submitted to transverse motion of infinite lateral extent is such that

$$p_L + q_L = p_B + q_B, \qquad |p_L|, q_L \to +\infty.$$

Two possibilities appear (see Figure 7):

– $C_B \gamma_B \leq \tilde{\varepsilon} = \pi/(2N_{e_1})$. The behavior of the L_{ayer} is necessarily that of a shear beam. The single remaining macroscopic kinematic variable is the translation, which satisfies periodicity in the two directions. Thus, at the leading order the layer behaves as a classical Cauchy medium, as could be derived via two-dimensional periodic homogenization. (For the cell under study, this case occurs when
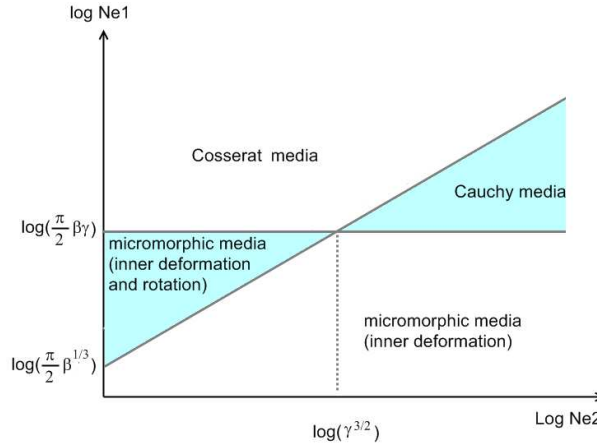
Figure 8. Macroscopic behaviors of a medium whose basic frame is characterized by the intrinsic parameters β and γ, when submitted to a shear in the direction e_1 polarized in the direction e_2 acting on the $D_{omain} = N_{e_2} \times N_{e_1} \times F_{rame}$.

the properties of the elements of the frame are of the same order: an isotropic or weakly anisotropic cellular material.)

– $C_B \gamma_B \geq \tilde{\varepsilon} = \pi/(2N_{e_1})$. In this case, the L_{ayer} tends to behave as an inner bending beam (with or without shear). The description requires that the translation and the inner deformation both satisfy periodicity in the two directions. The inner deformation introduces local rotation (θ) *inside* the cell, but no rigid body rotation of the cell itself ($\alpha = 0$). Thus, this micromorphic behavior is neither that of a Cauchy medium nor that of a Cosserat material. (For the cell under study, this case requires walls significantly stiffer than the floor: a strongly anisotropic cellular material.)

Finally, consider an infinite media made of the frame F_{rame} and assume that, in a D_{omain} restricted to $N_{e_2} \times N_{e_1} \times F_{rame}$, appropriate boundary conditions impose normally to the direction e_1 a shear polarized in the direction e_2. The equivalent behavior of the medium in the D_{omain} is given by comparing the two parameters

$$C_D = \left(\frac{\pi N_{e_2}}{2N_{e_1}}\right)^2 \beta, \qquad \gamma_D = \left(\frac{1}{N_{e_2}}\right)^2 \gamma$$

with the power of $\tilde{\varepsilon}$. Four behaviors (see Figure 8) can occur, according to the independent kinematic variable(s):

(1) The sole kinematic variable is the translation U. This situation (shear beams) is observed when $C_D \gamma_D \leq \tilde{\varepsilon}$ and $C_D \geq \tilde{\varepsilon}^{-1}$. In terms of domain geometry, these conditions require, in the direction normal to the shear motion, that

$$N_{e_1} \geq \beta \gamma \pi /2$$

(i.e., a number of cells higher than the intrinsic critical number $\frac{1}{2}\pi\beta\gamma = EI_w/K\ell_w^2$) and, in the direction of the shear motion, that

$$N_{e_2} \geq \left(\frac{\pi}{2}N_{e_1}\right)^{3/2} \frac{1}{\sqrt{\beta}},$$

(i.e., a weak slenderness whose aspect ratio is governed by N_{e_1} and $\beta = EI/K\ell_w^2$). The equivalent continuum behavior within the domain is that of a Cauchy medium.

(2) The kinematic variables are the translation U and the inner rotation θ. This occurs when $C_D\gamma_D \geq \tilde{\varepsilon}$ and $C_D \geq \tilde{\varepsilon}^{-1}$ (inner bending beam with or without shear), which means

$$N_{e_1} \leq \frac{\pi}{2}\beta\gamma, \qquad N_{e_2} \geq \left(\frac{2}{\pi}N_{e_1}\right)^{3/2}\frac{1}{\sqrt{\beta}}.$$

The equivalent continuum behavior within the domain is that of a micromorphic medium with inner deformation.

(3) The kinematic variables are the translation U and the rotation α. This happens when $C_D\gamma_D \leq \tilde{\varepsilon}$ and $C_D \leq \tilde{\varepsilon}^{-1}$ (slender-Timoshenko and bending beams), i.e.,

$$N_{e_1} \geq \frac{\pi}{2}\beta\gamma, \qquad N_{e_2} \leq \left(\frac{2}{\pi}N_{e_1}\right)^{3/2}\frac{1}{\sqrt{\beta}}.$$

In this case the cell rotation breaks the lateral periodicity, whereas the periodicity in the perpendicular direction is kept. For this reason, such a phenomenon is not be described by the usual two-dimensional homogenization (which would impose the periodicity in both directions). Nevertheless, the deformation presents a scale separation in a single direction that enables the treatment by a one-dimensional homogenization. In such a domain, the effects of global bending and shear are of same order and the medium behaves as a Cosserat medium.

(4) Finally, all three variables U, α and θ can be kinematic variables; this situation obtains when $C_D\gamma_D \geq \tilde{\varepsilon}$ and $C_D \leq \tilde{\varepsilon}^{-1}$ (generic beam). This is possible only for a restricted domain geometry defined by

$$N_{e_1} \leq \frac{\pi}{2}\beta\gamma, \qquad N_{e_2} \leq \left(\frac{2}{\pi}N_{e_1}\right)^{3/2}\frac{1}{\sqrt{\beta}}.$$

The behavior is that of a complex micromorphic medium with inner deformation and rotation. Such behavior cannot be derived if the periodicity is assumed in both directions.

Note that to respect the scale separation, the micromorphic behavior with inner deformation can only be observed if the critical number $\frac{1}{2}\pi\beta\gamma$ is significantly larger than 1 (referring to the frames studied in Section 5B, this is the case for F_2 but not for F_1). Cells such that $\frac{1}{2}\pi\beta\gamma \gg 1$ require a lack of diagonal bracing, since a diagonal element, which works in extension and prevents the cell flexibility, increases considerably the shear stiffness up to $K = O(E\ell^2)$ and the global and inner bending become of the same order, so that $\beta = O(1)$, $\gamma = O(1)$ and $\frac{1}{2}\pi\beta\gamma = O(1)$.

7. Implementing HMPD for framed structures

This section revisits in some detail the homogenization of the class of structures considered. Sections 7A–7D are an exposition of the discrete formulation of the global dynamic balance equations, following [Tollenaere 1994]. This material is then developed for square lattice beams in 7E and applied to the case of a slender-Timoshenko beam in 7F.
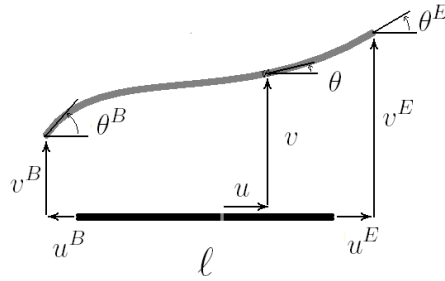
Figure 9. Notation for the deformation of a beam element in the plane (e_1, e_2).

7A. *Local balance of the elements.* Consider a beam element from point B to point E, of length ℓ, section A, and inertia I_b (Figure 9). In the local beam frame, s stands for the coordinate along the axis, and u, v, θ for the axial and transverse displacements and the rotation respectively. No external force is applied along the beam and the axial force N, the shear force T and the bending moment M act by convention from the left part to the right part. To describe global vibrations at the (unknown) modal frequencies $f = \omega/2\pi$ of the whole structure, any variable reads $Q(s, t) = Q(s)\, e^{i\omega t}$. By linearity, the time dependence is systematically simplified.

For longitudinal vibrations, the balance on the beam axis e_1, together with the compression behavior, can be written as

$$N'(s) = \rho\, A\, \omega^2 u(s), \qquad N(s) = -E\, A\, u'(s) \tag{7-1}$$

(primes stands for differentiation with respect to s). This leads to the governing equation

$$\ell_L^2\, u''(s) = -u(s), \quad \text{where } \ell_L = \sqrt{E/\rho\omega^2}. \tag{7-2}$$

The compression wavelength of the element is $2\pi\,\ell_L$.

For transverse (bending) vibrations, we have the balance of shear force of axis e_2 and moment of axis e_3, plus the bending behavior law:

$$T'(s) = \rho\, A\, \omega^2\, v(s), \qquad M'(s) = -T(s), \qquad M(s) = -E\, I_b\, v''(s). \tag{7-3}$$

Together these yield

$$\ell_T^4\, v''''(s) = v(s), \quad \text{where } \ell_T = \sqrt[4]{E\, I_b/\rho\, A\, \omega^2}. \tag{7-4}$$

The transverse bending wavelength of the element is $2\pi\,\ell_T$. The longitudinal and transverse wavelengths are linked by the purely geometric relationship

$$\frac{\ell_T^4}{\ell_L^2} = \frac{I_b}{A}. \tag{7-5}$$

7B. *Nodal forces and moment.* Now integrate equations (7-2) and (7-4) between the origin B and the end E using the unknown displacements u^B, u^E, v^B, v^E and rotations θ^B and θ^E of the endpoints as boundary conditions (Figure 9). The forces at the endpoints, expressed in the local frame of the element

and deduced from the beam behavior laws, take on the form

$$
\begin{aligned}
\text{N}^B &= \text{N}(u^B, u^E), & \text{N}^E &= -\text{N}(u^E, u^B), \\
\text{T}^B &= \text{T}(v^B, v^E, \theta^B, \theta^E), & \text{T}^E &= -\text{T}(v^E, v^B, -\theta^E, -\theta^B), \\
\text{M}^B &= \text{M}(v^B, v^E, \theta^B, \theta^E), & \text{M}^E &= \text{M}(v^E, v^B, -\theta^E, -\theta^B),
\end{aligned}
\tag{7-6}
$$

where we have set, with $\ell_i^* = \ell/\ell_i$, $c_i^* = \cos \ell_i^*$, $s_i^* = \sin \ell_i^*$, $ch_i^* = \cosh \ell_i^*$, $sh_i^* = \sinh \ell_i^*$ $(i = T, L)$,

$$
\text{N}(u_1, u_2) = \frac{EA}{\ell_L} \frac{u_1\cos(\ell_L^*) - u_2}{\sin \ell_L^*},
$$

$$
\text{T}(v_1, v_2, \theta_1, \theta_2) = \frac{EI_b}{\ell_T^3} \frac{v_1(ch_T^* s_T^* + sh_T^* c_T^*) - v_2(s_T^* + sh_T^*) + (\theta_1 s_T^* sh_T^* - \theta_2(c_T^* - ch_T^*))\ell_T}{c_T^* ch_T^* - 1},
\tag{7-7}
$$

$$
\text{M}(v_1, v_2, \theta_1, \theta_2) = \frac{EI_b}{\ell_T^2} \frac{v_1 s_T^* sh_T^* + v_2(c_T^* - ch_T^*) + (\theta_1(ch_T^* s_T^* - sh_T^* c_T^*) - \theta_2(s_T^* - sh_T^*))\ell_T}{1 - c_T^* ch_T^*}.
$$

7C. *Discrete dynamic balance.* To express the node balance of the whole structure, the geometry of the frame is explicitly used. Level n contains two nodes (Figure 1): node n_1 on the left (end of wall wn_1, origin of wall $w(n+1)_1$ and of floor fn) and node n_2 on the right (end of wall wn_2 and floor n, origin of wall $w(n+1)_2$). The equilibrium of the forces (in directions e_1 and e_2) and the moment (e_3) read at any level n:

Node n_1: $\quad \text{T}_{wn_1}^E - \text{T}_{w(n+1)_1}^B - \text{N}_{fn}^B = 0, \quad \text{N}_{wn_1}^E - \text{N}_{w(n+1)_1}^B - \text{T}_{fn}^B = 0, \quad \text{M}_{wn_1}^E - \text{M}_{w(n+1)_1}^B - \text{M}_{fn}^B = 0,$ (7-8)

Node n_2: $\quad \text{T}_{wn_2}^E - \text{T}_{w(n+1)_2}^B + \text{N}_{fn}^E = 0, \quad \text{N}_{wn_2}^E - \text{N}_{w(n+1)_2}^B + \text{T}_{fn}^E = 0, \quad \text{M}_{wn_2}^E - \text{M}_{w(n+1)_2}^B + \text{M}_{fn}^E = 0,$ (7-9)

where, in view of (7-6) and (7-7), the forces subscripted with wn_i ($i = 1$ or 2), at the endpoints of the wall wn_i, are functions of the motions of nodes $(n-1)_i$ and n_i, and the forces subscripted fn at the floor are functions of the motions of nodes n_1 and n_2 (Figure 2). Equations (7-8) and (7-9) encode the exact discrete expression of the balance of the structure.

7D. *Expansions of the nodal forces.* The scale separation implies that at the frequency of an homogenizable mode, the own wavelength of each beam is much larger than its length, and therefore $\ell/\ell_T \ll 1$ and $\ell/\ell_L \ll 1$. It follows that the forces can then be developed according to the powers of $\ell_T^* = \ell/\ell_T$ and $\ell_L^* = \ell/\ell_L$, giving

$$
\text{N}(u_1, u_2) = \frac{EA}{\ell}\left(u_1 - u_2 - \frac{2u_1 + u_2}{6}\ell_L^{*2} - \frac{8u_1 + 7u_2}{360}\ell_L^{*4} + O(\ell_L^{*6})\right),
$$

$$
\text{T}(v_1, v_2, \theta_1, \theta_2) = \frac{6EI_b}{\ell^3}\left(2(v_1 - v_2) + \ell(\theta_1 + \theta_2) - \frac{156v_1 + 54v_2 + \ell(22\theta_1 - 13\theta_2)}{2520}\ell_T^{*4} + O(\ell_T^{*8})\right),
$$

$$
\text{M}(v_1, v_2, \theta_1, \theta_2) = \frac{2EI_b}{\ell^2}\left(3(v_1 - v_2) + \ell(2\theta_1 + \theta_2) - \frac{22v_1 + 13v_2 + \ell(4\theta_1 - 3\theta_2)}{840}\ell_T^{*4} + O(\ell_T^{*8})\right).
$$

7E. *Balance equations for transverse vibrations.* In this case, the discrete variables $U(n)$, $\alpha(n)$, $\theta(n)$ are governed by the discrete balance equations (3-3):

$$\mathrm{T}^E_{wn_1} + \mathrm{T}^E_{wn_2} - \left(\mathrm{T}^B_{w(n+1)_1} + \mathrm{T}^B_{w(n+1)_2}\right) - (\mathrm{N}^B_{fn} - \mathrm{N}^E_{fn}) = 0,$$

$$\mathrm{N}^E_{wn_2} - \mathrm{N}^E_{wn_1} - \left(\mathrm{N}^B_{w(n+1)_2} - \mathrm{N}^B_{w(n+1)_1}\right) - (\mathrm{T}^E_{fn} - \mathrm{T}^B_{fn}) = 0, \qquad (7\text{-}10)$$

$$\mathrm{M}^E_{wn_1} + \mathrm{M}^E_{wn_2} - \left(\mathrm{M}^B_{w(n+1)_1} + \mathrm{M}^B_{w(n+1)_2}\right) - (\mathrm{M}^B_{fn} - \mathrm{M}^E_{fn}) = 0.$$

We now substitute the expansions for these quantities. For the case treated in the next section, it is sufficient to take terms up to order $(\ell/\ell_T)^8 \sim \omega^4$ and $(\ell/\ell_L)^4 \sim \omega^4$. We obtain for the balance in the transverse direction

$$\frac{24 E_w I_w}{\ell_w^2}\left(\frac{U_{(n+1)} - 2\,U_n + U_{(n-1)}}{\ell_w^2}\left[1 + \frac{3}{280}\left(\frac{\ell_w}{\ell_{Tw}}\right)^4\right] + \frac{\theta_{(n+1)} - \theta_{(n-1)}}{4\,\ell_w}\left[1 + \frac{13}{2520}\left(\frac{\ell_w}{\ell_{Tw}}\right)^4\right]\right.$$

$$\left. + \frac{U_n}{12}\left[\left(\frac{\ell_w}{\ell_{Tw}}\right)^4 + \frac{\ell_w}{\ell_f}\frac{E_f}{E_w}\frac{A_f \ell_w^2}{2\,I_w}\left(\frac{\ell_f}{\ell_{Lf}}\right)^2\right]\right) = O\left(\frac{\ell_w}{\ell_{Tw}}\right)^8 + O\left(\frac{\ell_f}{\ell_{Lf}}\right)^4. \quad (7\text{-}11)$$

Similarly, the other two balance equations become

$$\frac{E_w A_w \ell_f^2}{2}\left(\frac{\alpha_{(n+1)} - 2\,\alpha_n + \alpha_{(n-1)}}{\ell_w^2}\left[1 + \frac{1}{6}\left(\frac{\ell_w}{\ell_{Lw}}\right)^2\right] + \frac{\alpha_n}{\ell_w^2}\left(\frac{\ell_w}{\ell_{Lw}}\right)^2\right)$$

$$+ \frac{12\,E_f I_f}{\ell_w \ell_f}\left(\theta_n - \alpha_n - \frac{3\,\theta_n - 17\,\alpha_n}{1680}\left(\frac{\ell_f}{\ell_{Tf}}\right)^4\right) = O\left(\frac{\ell_f}{\ell_{Tf}}\right)^8 + O\left(\frac{\ell_w}{\ell_{Lw}}\right)^4,$$

$$\frac{24\,E_w I_w}{\ell_w^2}\left(\frac{U_{(n+1)} - U_{(n-1)}}{2\,\ell_w}\left[1 + \frac{13}{2520}\left(\frac{\ell_w}{\ell_{Tw}}\right)^4\right] + \frac{\theta_{(n+1)} - 2\,\theta_n + \theta_{(n-1)}}{6}\left[1 + \frac{1}{280}\left(\frac{\ell_w}{\ell_{Tw}}\right)^4\right]\right.$$

$$\left. + \theta_n\left[1 - \frac{1}{2520}\left(\frac{\ell_w}{\ell_{Tw}}\right)^4\right]\right) + \frac{12\,E_f I_f}{\ell_w \ell_f}\left[\theta_n - \alpha_n + \frac{2\,\theta_n - 9\,\alpha_n}{2520}\left(\frac{\ell_f}{\ell_{Tf}}\right)^4\right] = O\left(\frac{\ell_f}{\ell_{Tf}}\right)^8 + O\left(\frac{\ell_w}{\ell_{Tw}}\right)^8.$$

These equations may be modified in two steps. First we use the angular frequency ω_r of (3-4), to obtain (with $i = f, w$)

$$\left(\frac{\ell_i}{\ell_{Ti}}\right)^4 = \left(\frac{\ell_i}{L}\right)^2 \frac{2\,E_w A_w \ell_i^2}{E_i I_i}\frac{\lambda_i}{\Lambda}\left(\frac{\omega}{\omega_r}\right)^2, \qquad \left(\frac{\ell_i}{\ell_{Li}}\right)^2 = \left(\frac{\ell_i}{L}\right)^2 \frac{2\,E_w A_w}{E_i A_i}\frac{\lambda_i}{\Lambda}\left(\frac{\omega}{\omega_r}\right)^2. \qquad (7\text{-}12)$$

We then introduce the continuous variables and their Taylor expansions. For instance,

$$\frac{U_{(n+1)} - 2\,U_n + U_{(n-1)}}{\ell_w^2} = U''(x) + O(\varepsilon^2 U''''(x)).$$

7F. *Slender-Timoshenko beam.* We now narrow the analysis to the case

$$E_f/E_w = O(1), \quad \rho_f/\rho_w = O(1), \quad \ell_f/\ell_w = O(1), \quad a_w/\ell_w = O(\varepsilon), \quad a_f/\ell_w = O(\varepsilon),$$

so

$$O\left(\frac{\ell_w}{\ell_{Tw}}\right)^4 = O\left(\frac{\ell_f}{\ell_{Tf}}\right)^4 = O\left(\frac{\omega}{\omega_r}\right)^2, \qquad O\left(\frac{\ell_w}{\ell_{Lw}}\right)^2 = O\left(\frac{\ell_f}{\ell_{Lf}}\right)^2 = \varepsilon^2 O\left(\frac{\omega}{\omega_r}\right)^2. \qquad (7\text{-}13)$$

The transverse modes are attained when the inertia induced by the transverse motions is balanced by the transverse elastic forces. Therefore, focusing on the balance in the transverse direction (7-11), and

retaining the leading terms in the continuous representation, we get

$$\frac{2E_w I_w}{\ell_w^2}\left(12(U''+\theta')+\frac{A_w\ell_w^2}{I_w}\frac{U}{L^2}\left(\frac{\omega}{\omega_r}\right)^2\right)=O\left(\frac{E_w I_w}{\ell_w^2}\left(\frac{\omega}{\omega_r}\right)^4 U''\right). \tag{7-14}$$

Since $U''=O(U/L^2)$ and, in the slender-Timoshenko case under consideration, $A_w\ell_w^2/I_w=O(\varepsilon^{-2})$, the term $12(U''+\theta')$ on the left-hand side of (7-14) (the elastic force) will be of the same order as the term following it (the inertia force) provided that

$$\omega/\omega_r=O(\varepsilon), \qquad \text{that is,} \qquad \omega=\tilde{\omega}_1.$$

This estimate enables us to write the expansions in powers of ε only. In the case under consideration, the leading orders of the three balance equations become

$$\frac{24E_w I_w}{\ell_w^2}(\tilde{U}^{0''}+\tilde{\theta}^{0'})+\Lambda\tilde{\omega}_1^2\,\tilde{U}^0=0,$$
$$\frac{E_w A_w\ell_f^2}{2}\tilde{\alpha}^{0''}+\frac{12\,E_f I_f}{\ell_w\ell_f}(\tilde{\theta}^0-\tilde{\alpha}^0)=0, \tag{7-15}$$
$$\frac{24\,E_w I_w}{\ell_w^2}(\tilde{U}^{0'}+\tilde{\theta}^0)+\frac{12\,E_f I_f}{\ell_w\ell_f}(\tilde{\theta}^0-\tilde{\alpha}^0)=0.$$

This achieves zero order homogenization and leads to (4-6).

8. Conclusion

An application of HPDM is presented for dynamics of one-dimensional structures. Associated with a systematic use of scaling, the method provides four types of equivalent beam depending on the order of magnitude of the geometrical (then mechanical) characteristics of the cell. A generic beam of the sixth degree is shown to include all the mechanisms under transverse motions.

It is shown that, more than by the actual frame cell geometry, the macro behavior is governed by the three global cell parameters involved in the shear, global and inner bending constitutive beam laws. Then, expressed with those parameters, the beam-like descriptions may apply to other symmetric cells. The same principle could also be used for compression modes [Boutin and Hans 2003] and for twisting modes, not developed here.

Based on modal dimensional analysis, simple criteria of practical interest enable to identify the proper model for real structures, and to realize an easy, computer time efficient, analysis of the behavior. This approach provides large simplification for determining low frequency modes of discrete structures made of N cells. Provided that the dynamic excitation of the basis respects the scale separation, more precisely when its spectrum content does not exceed the frequency of the $(N/3)$-th mode, the complete dynamic calculation may be replaced by

(1) the calculation of the macroscopic parameters of a single cell submitted to a static strain, and

(2) the solving of the one-dimensional problem with the identified parameters, using either the generic beam model or the adequate specific beam.

The fact that in the specific case 5C the zero order description is valid up to the second order may explain the satisfactory accuracy of the beam modeling despite the weak scale separation.

Lastly, analogy with micromorphic media provides criteria to identify the nature of the effective behavior of discrete media. This latter may vary from Cauchy to complex micromorphic behavior according to the intrinsic parameters of the cell and the dimensions of the shearing zone.

The adaptability of the method enables extensions of this work from the field of structural dynamics to that of mechanics of heterogeneous materials. Recent experiments on regular buildings have demonstrated the reliability of this approach to describe the dynamics under shock, forced and ambient vibrations in term of a few first eigenmodes [Boutin et al. 2005]. Applications in biomechanics may also be envisaged.

Acknowledgements

References

[Bakhvalov and Panasenko 1989] N. Bakhvalov and G. Panasenko, *Homogenisation: averaging processes in periodic media: mathematical problems in the mechanics of composite materials*, Mathematics and its Applications (Soviet Series) **36**, Kluwer, Dordrecht, 1989.

[Bensoussan et al. 1978] A. Bensoussan, J.-L. Lions, and G. Papanicolaou, *Asymptotic analysis for periodic structures*, Studies in Mathematics and its Applications **5**, North-Holland, Amsterdam, 1978.

[Boutin 1995] C. Boutin, "Microstructural influence on heat conduction", *Int. J. Heat Mass Transf.* **38**:17 (1995), 3181–3195.

[Boutin and Auriault 1990] C. Boutin and J. L. Auriault, "Dynamic behaviour of porous media saturated by a viscoelastic fluid: application to bituminous concretes", *Int. J. Eng. Sci.* **28**:11 (1990), 1157–1181.

[Boutin and Auriault 1993] C. Boutin and J. L. Auriault, "Rayleigh scattering in elastic composite materials", *Int. J. Eng. Sci.* **31**:12 (1993), 1669–1689.

[Boutin and Hans 2003] C. Boutin and S. Hans, "Homogenisation of periodic discrete medium: application to dynamics of framed structures", *Comput. Geotech.* **30**:4 (2003), 303–320.

[Boutin et al. 2005] C. Boutin, S. Hans, E. Ibraim, and P. Roussillon, "*In situ* experiments and seismic analysis of existing buildings, II: Seismic integrity threshold", *Earthquake Eng. Struct. Dyn.* **34**:12 (2005), 1531–1546.

[Buannic and Cartraud 2001a] N. Buannic and P. Cartraud, "Higher-order effective modeling of periodic heterogeneous beams, I: Asymptotic expansion method", *Int. J. Solids Struct.* **38**:40-41 (2001), 7139–7161.

[Buannic and Cartraud 2001b] N. Buannic and P. Cartraud, "Higher-order effective modeling of periodic heterogeneous beams, II: Derivation of the proper boundary conditions for the interior asymptotic solution", *Int. J. Solids Struct.* **38**:40-41 (2001), 7163–7180.

[Caillerie et al. 1989] D. Caillerie, P. Trompette, and P. Verna, "Homogenisation of periodic trusses", pp. 7139–7180 in *10 years of progress in shell and spatial structures* (Madrid, 1989), CEDEX-Laboratorio Central de Estructuras y Materiales, Madrid, 1989.

[Cioranescu and Saint Jean Paulin 1999] D. Cioranescu and J. Saint Jean Paulin, *Homogenization of reticulated structures*, Applied Mathematical Sciences **136**, Springer, New York, 1999.

[Eringen 1968] A. C. Eringen, "Mechanics of micromorphic continua", pp. 18–35 in *IUTAM symposium on the generalized Cosserat continuum and the continuum theory of dislocations with applications*, Springer, Berlin, 1968.

[Gambin and Kröner 1989] B. Gambin and E. Kröner, "Higher-order terms in the homogenized stress-strain relation of periodic elastic media", *Phys. Status Solidi B* **151**:2 (1989), 513–519.

[Kerr and Accorsi 1985] A. D. Kerr and M. L. Accorsi, "Generalization of the equations for frame-type structures: a variational approach", *Acta Mech.* **56**:1-2 (1985), 55–73.

[Le Corre et al. 2004] S. Le Corre, D. Caillerie, L. Orgéas, and D. Favier, "Behavior of a net of fibers linked by viscous interactions: theory and mechanical properties", *J. Mech. Phys. Solids* **52**:2 (2004), 395–421.

[Mead 1996] D. M. Mead, "Wave propagation in continuous periodic structures: research contributions from Southampton 1964–1995", *J. Sound Vib.* **190**:3 (1996), 495–524.

[Moreau and Caillerie 1998] G. Moreau and D. Caillerie, "Continuum modeling of lattice structures in large displacement applications to buckling analysis", *Comput. Struct.* **68**:1-3 (1998), 181–189.

[Noor 1988] A. K. Noor, "Continuum modeling for repetitive lattice structures", *Appl. Mech. Rev.* (*ASME*) **41**:7 (1988), 285–296.

[Pradel and Sab 1998] F. Pradel and K. Sab, "Cosserat modelling of elastic periodic lattice structures", *C. R. Acad. Sci. II B Mec.* **326**:11 (1998), 699–704.

[Renton 1984] J. D. Renton, "The beam-like behavior of space trusses", *AIAA J.* **22**:2 (1984), 273–280.

[Sánchez-Palencia 1980] E. Sánchez-Palencia, *Non-homogeneous media and vibration theory*, Lecture Notes in Physics **127**, Springer, Berlin, 1980.

[Stephen 1999] N. G. Stephen, "On the vibration of one-dimensional periodic structures", *J. Sound Vib.* **227**:5 (1999), 1133–1142.

[Tollenaere 1994] H. Tollenaere, *Modèles bidimensionnels de tissés: homogénéisation des treillis en vibrations libres*, thèse de doctorat, Institut National Polytechnique de Grenoble, Grenoble, 1994.

[Tollenaere and Caillerie 1998] H. Tollenaere and D. Caillerie, "Continuum modeling of lattice structures by homogenization", *Adv. Eng. Software* **29**:7-9 (1998), 699–705.

[Trabucho and Viaño 1996] L. Trabucho and J. M. Viaño, "Mathematical modelling of rods", pp. 487–974 in *Handbook of numerical analysis*, vol. IV, edited by P. G. Ciarlet and J. L. Lions, North-Holland, Amsterdam, 1996.

[Verna 1991] P. Verna, *Modélisation continue des structures discrètes par homogénéisation: cas des treillis*, thèse de doctorat, Institut National Polytechnique de Grenoble, Grenoble, 1991.

STEPHANE HANS: stephane.hans@entpe.fr
École Nationale des Travaux Publics de l'État - Université de Lyon, Département Génie Civil et Bâtiment - URA CNRS 1652, rue Maurice Audin, 69518 Vaulx-en-Velin, France

CLAUDE BOUTIN: claude.boutin@entpe.fr
École Nationale des Travaux Publics de l'État - Université de Lyon, Département Génie Civil et Bâtiment - URA CNRS 1652, rue Maurice Audin, 69518 Vaulx-en-Velin, France

ANALYSIS OF IMPACT RESPONSE AND DAMAGE IN LAMINATED COMPOSITE SHELL INVOLVING LARGE DEFORMATION AND MATERIAL DEGRADATION

SURENDRA KUMAR

A nonlinear finite element analysis of impact response and impact-induced damage in curved composite laminates subjected to transverse impact by a foreign object is carried out. An eight-noded isoparametric quadrilateral shell element incorporating a nonlinear strain displacement relation due to large deflection is developed based on the total Lagrangian approach. The nonlinear system of equations is solved using a Newton–Raphson incremental-iterative method. Example problems of graphite/epoxy cylindrically curved laminates with different curvature are considered and the influence of geometrical nonlinearity on the impact response and the resulting damage is demonstrated. The concurrent effect of material degradation due to impact damage is also investigated.

1. Introduction

The impact damage tolerance of aircraft structural composite materials is one of the most important design considerations in designing aircraft structures. Accordingly, the understanding of impact response and impact damage mechanisms has drawn the attention of many investigators. A summary of most of the earlier work is reported in [Cantwell and Morton 1991; Abrate 1991; 1994].

In spite of the extensive literature available on the subject, issues associated with complex impact damage phenomena and the effects of several parameters still require further investigation. Most impact problems for laminated plates have been formulated using small deflection theory [Aggour and Sun 1988; Wu and Springer 1988; Choi and Chang 1992; Nosier et al. 1994; Pradhan and Kumar 2000], which is adequate if the impact load is small. However, it is necessary to include the effect of geometric nonlinearity if the laminate undergoes a large deflection. Ambur et al. [1995] have shown that nonlinear effects can be significant for thin plates subjected to low-velocity impact. The inclusion of geometrical nonlinearity in prediction of impact response and damage in thin and moderately thick laminated composites helps in improving the accuracy of the analysis. Chandrashekhara and Schroeder [1995] have studied the impact response of laminated curved shells using a finite element formulation based on Sander's shell theory considering geometric nonlinearity in the sense of the von Karman strains. However, impact damage was not investigated in their study. Kim et al. [1997] and Her and Liang [2004] have studied the effect of curvature on dynamic response and impact damage in cylindrical shells using a 3-D finite element formulation. However, the analyses of both these papers were linear and were based on small deflection theory. The effect of failed laminas on the stiffness of the laminate was also not accounted for in determining the impact response. Ganapathy and Rao [1998] used a 4-noded 48 degree of freedom shell element based

on the Kirchhoff-Love thin shell theory in the finite element analysis of cylindrical/spherical shell panels. The authors used a form of classical Hertzian contact law and predicted matrix cracking failure by applying the general Tsai-Wu failure criterion for composite materials. Although geometrical nonlinearity was included, the study assumes that low velocity impact force and deformation can be simulated by a static model and hence does not compute impact response as a function of time. Krishnamurthy et al. [2001] used a shell element based on the Mindlin-Reissener assumptions for transverse shear deformation in their parametric study of laminated cylindrical composite shells. In another paper [Krishnamurthy et al. 2003], the authors extended their work on the impact response of a laminated composite cylindrical shell as well as a full cylinder by incorporating the classical Fourier series method into the finite element formulation and also predicted impact-induced damage deploying the semiempirical damage prediction model of [Choi and Chang 1992]. According to the authors, the Fourier series method, which gives information regarding the natural frequencies of vibration of the impacted structure, provided a proper basis for adopting the appropriate size of the analysis time step. However, the paper doesn't address nonlinear effects. Zhu et al. [2006] incorporated the effects of strain rate dependency and inelastic behavior of matrix material for analyzing the mechanical response of laminated shell. It was shown by the authors that when the rate dependent modulus and inelastic effects are considered, the shell panels have a considerable damping effect. The study was, however, concentrated on the transient response of a laminated shell subjected to a suddenly applied static loading uniformly distributed over the bottom surface of the panel and did not address damage phenomena. More recently, Kumar et al. [2007] have carried out parametric studies on impact response and damage in curved composite laminates using a 3D eight-noded layered brick element with incompatible modes and have investigated the effect of material degradation on both impact response and damage. However, their finite element formulations were based on linear deformation theory.

In the present paper, a nonlinear finite element transient dynamic analysis is carried out to predict the impact response and the impact-induced damage in a laminated composite cylindrical shell subjected to transverse impact by a metallic impactor. An eight-noded isoparametric quadrilateral shell element incorporating geometrical nonlinearity due to a large deflection is implemented based on the total Lagrangian approach. The nonlinear system of equations resulting from the large displacement formulation and nonlinear contact law are simultaneously solved iteratively using a Newton–Raphson method. Example problems of graphite/epoxy cylindrically curved shells with different curvature are considered and the influence of geometrical nonlinearity on the impact response and impact-induced damage is demonstrated. The study also comprises the simultaneous effect of stiffness reduction of the damaged region in the laminate on impact response and the resulting damage as the solution progresses with time.

2. Mathematical formulation

Basic equations. Consider the laminated doubly curved shell shown in Figure 1. The displacement field at any point within the shell, according to a first order shear deformation theory is given by

$$
\begin{aligned}
u(x, y, z) &= u_0(x, y) + z\varphi_x(x, y), \\
v(x, y, z) &= v_0(x, y) + z\varphi_y(x, y), \\
w(x, y, z) &= w_0(x, y),
\end{aligned}
\tag{1}
$$
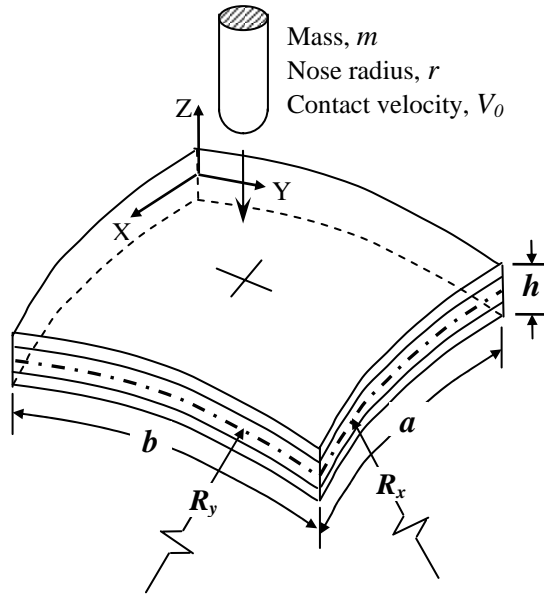
Figure 1. Problem description of impact on a general doubly curved shell.

where u is the membrane displacement in the x-direction, v is the membrane displacement in the y-direction and w is the out-of-plane transverse displacement in the z-direction. u_0, v_0 and w_0 are the midplane displacements. The positive φ_x and φ_y are the cross-sectional clockwise rotations around the y- and x-axes, respectively.

The strain-displacement relations based on Sander's shell theory [1959] and incorporating the geometrical nonlinearity given by [Stein 1986] can be written as

$$\varepsilon_x = \varepsilon_x^0 + z\kappa_x, \quad \varepsilon_y = \varepsilon_y^0 + z\kappa_y, \quad \gamma_{xy} = \gamma_{xy}^0 + z\kappa_{xy}, \quad \gamma_{yz} = \gamma_{yz}^0, \quad \gamma_{xz} = \gamma_{xz}^0, \tag{2}$$

where

$$\varepsilon_x^0 = \frac{\partial u_0}{\partial x} + \frac{w_0}{R_x} + \frac{1}{2}\left[\left(\frac{\partial u_0}{\partial x}\right)^2 + \left(\frac{\partial v_0}{\partial x}\right)^2 + \left(\frac{\partial w_0}{\partial x} - \frac{u_0}{R_x}\right)^2\right],$$

$$\varepsilon_y^0 = \frac{\partial v_0}{\partial y} + \frac{w_0}{R_y} + \frac{1}{2}\left[\left(\frac{\partial u_0}{\partial y}\right)^2 + \left(\frac{\partial v_0}{\partial y}\right)^2 + \left(\frac{\partial w_0}{\partial y} - \frac{v_0}{R_y}\right)^2\right], \tag{3a}$$

$$\gamma_{xy}^0 = \frac{\partial u_0}{\partial y} + \frac{\partial v_0}{\partial x} + \frac{\partial u_0}{\partial x}\frac{\partial u_0}{\partial y} + \frac{\partial v_0}{\partial x}\frac{\partial v_0}{\partial y} + \left(\frac{\partial w_0}{\partial x} - \frac{u_0}{R_x}\right)\left(\frac{\partial w_0}{\partial y} - \frac{v_0}{R_y}\right)$$

are the nonlinear mid-plane strains,

$$\kappa_x = \frac{\partial \varphi_x}{\partial x}, \quad \kappa_y = \frac{\partial \varphi_y}{\partial y}, \quad \kappa_{xy} = \frac{\partial \varphi_x}{\partial y} + \frac{\partial \varphi_y}{\partial x} + \frac{1}{2}\left(\frac{1}{R_y} - \frac{1}{R_x}\right)\left(\frac{\partial v_0}{\partial x} - \frac{\partial u_0}{\partial y}\right) \tag{3b}$$

are the changes in curvature, and

$$\gamma_{yz}^0 = \varphi_y + \frac{\partial w_0}{\partial y} - \frac{v_0}{R_y}, \quad \gamma_{xz}^0 = \varphi_x + \frac{\partial w_0}{\partial x} - \frac{u_0}{R_x} \tag{3c}$$

are the transverse shear strains. In these equations, R_x and R_y are the radii of curvature in x and y directions. In this equation, higher order terms for the derivatives of cross-sectional rotations and the nonlinear terms in transverse shear strains have been neglected.

If we set

$$\{\bar{\varepsilon}\} = \begin{bmatrix} \varepsilon_x^0 & \varepsilon_y^0 & \gamma_{xy}^0 & \kappa_x & \kappa_y & \kappa_{xy} & \gamma_{yz}^0 & \gamma_{xz}^0 \end{bmatrix}^T,$$

the laminate constitutive equation can be written as

$$\{F\} = [\bar{D}]\{\bar{\varepsilon}\}, \tag{4}$$

where

$$\{F\} = \begin{bmatrix} N_x & N_y & N_{xy} & M_x & M_y & M_{xy} & Q_{yz} & Q_{xz} \end{bmatrix}^T = \left[\int_{-h/2}^{h/2} \left(\sigma_x \ \sigma_y \ \tau_{xy} \ \sigma_x z \ \sigma_y z \ \tau_{xy} z \ \tau_{yz} \ \tau_{xz} \right) dz \right]^T \tag{5}$$

is the generalized stress resultant vector[1] and

$$[\bar{D}] = \begin{bmatrix} A_{ij} & B_{ij} & 0 \\ B_{ij} & D_{ij} & 0 \\ 0 & 0 & S_{pq} \end{bmatrix}$$

is the laminate stiffness matrix, with components

$$(A_{ij}, B_{ij}, D_{ij}) = \sum_{k=1}^{N} \int_{z_{k-1}}^{z_k} \bar{C}_{ij}^k (1, z, z^2) \, dz \quad (i, j = 1, 2, 4). \tag{6a}$$

(extensional, bending-stretching coupling and bending stiffness coefficients) and

$$S_{pq} = \sum_{k=1}^{N} \int_{z_{k-1}}^{z_k} \alpha \bar{C}_{pq}^k dz \quad (p, q = 5, 6). \tag{6b}$$

(transverse shear stiffness coefficients). In the last two equations, N is the number of layers, α is the shear correction factor, and $\bar{C}_{ij}^k$ ($i, j = 1, 2, 4, 5, 6$) represent the transformed elastic constants for the k-th layer, satisfying the relation

$$[\bar{C}] = [T]^T [C][T], \tag{7}$$

where $[T]$ is the transformation matrix relating the strains in the ply principal directions to those in the shell reference axis and $[C]$ is elasticity matrix relating the strains within the ply to the stresses in the ply coordinate system.

Finite element model. Using the principle of virtual work, the equation of equilibrium after including the inertia forces at time t_{n+1} can be given as

$$\{\Psi_{n+1}\} = \iint [B]^T \{F_{n+1}\} \, dx \, dy + \iint [N]^T [P]\{\ddot{u}_{n+1}\} \, dx \, dy - \{R_{n+1}\}, \tag{8}$$

---

[1]Here N_x, N_y, N_{xy} are the internal in-plane force resultants per unit length, M_x, M_y, M_{xy} are the internal moment resultants and Q_{yz}, Q_{xz} are the transverse shear resultants per unit length.

where $\{\Psi_{n+1}\}$ is residual vector, $[B]$ strain-displacement matrix corresponding to (3a)–(3c), $\{F_{n+1}\}$ is the stress resultant vector at any point, $[N]$ is the shape function matrix, $\{\ddot{u}_{n+1}\}$ is the acceleration vector at any point and $\{R_{n+1}\}$ is the applied load vector. The inertia matrix of the laminate $[P]$ is defined as

$$[P] = \begin{bmatrix} p & 0 & 0 & 0 & 0 \\ 0 & p & 0 & 0 & 0 \\ 0 & 0 & p & 0 & 0 \\ 0 & 0 & 0 & I & 0 \\ 0 & 0 & 0 & 0 & I \end{bmatrix}, \tag{9}$$

with

$$p = \sum_{k=1}^{N} \int_{z_{k-1}}^{z_k} \rho_k dz \quad \text{and} \quad I = \sum_{k=1}^{N} \int_{z_{k-1}}^{z_k} z^2 \rho_k dz, \tag{10}$$

where ρ_k is the mass density of the k-th layer.

In the large displacement problem,

$$[B] = [B_L] + [B_{NL}]$$

and

$$\{F_{n+1}\} = [\bar{D}]\big[[B_L] + \tfrac{1}{2}[B_{NL}]\big]\{U_{n+1}\} = [\bar{D}][\bar{B}]\{U_{n+1}\}, \tag{11}$$

where $[B_L]$ is the contribution from the linear part of the strain and $\frac{1}{2}[B_{NL}]$ is the contribution from the quadratic part of the strain and involves linear functions of the translational components of the element nodal degree of freedom vector $\{U_{n+1}\}$.

In (8),

$$\{\ddot{u}_{n+1}\} = [N]\{\ddot{U}_{n+1}\}. \tag{12}$$

Using the Newmark time integration method with a constant average acceleration ($\alpha = 0.5$ and $\beta = 0.25$), the nodal acceleration vectors $\{\ddot{U}_{n+1}\}$ can be expressed in terms of nodal displacements $\{U_{n+1}\}$ as

$$\{\ddot{U}_{n+1}\} = \frac{1}{\beta(\Delta t)^2}\{U_{n+1}\} - \left(\frac{1}{\beta(\Delta t)^2}\{U_n\} + \frac{1}{\beta(\Delta t)}\{\dot{U}_n\} + \frac{1-2\beta}{2\beta}\{\ddot{U}_n\}\right). \tag{13}$$

Equations (12) and (13) can be put into (8), yielding

$$\{\Psi_{n+1}\} = \iint [B]^T \{F_{n+1}\}\, dx\, dy + \frac{1}{\beta(\Delta t)^2}\left(\iint [N]^T [P][N]\, dx\, dy\right)\{U_{n+1}\} - \{R^M_{n+1}\} - \{R_{n+1}\}. \tag{14}$$

$\{R^M_{n+1}\}$ can be thought of as the load vector due to inertia term at time t_{n+1} and is given by

$$\{R^M_{n+1}\} = [M]\left(\frac{1}{\beta(\Delta t)^2}\{U_n\} + \frac{1}{\beta(\Delta t)}\{\dot{U}_n\} + \frac{1-2\beta}{2\beta}\{\ddot{U}_n\}\right), \tag{15}$$

with $[M] = \iint [N]^T [P][N]\, dx\, dy$ the mass matrix.

In the present analysis, the nonlinear equation (14) is solved iteratively using a Newton–Raphson scheme. It is, therefore, necessary to find the relation between $\{d\Psi_{n+1}\}$ and $\{dU_{n+1}\}$ by taking the variation of the residual force, (14), with respect to $\{U_{n+1}\}$. This relation is

$$[K^T_{n+1}]\delta\{U_{n+1}\} = \delta\{\Psi_{n+1}\}, \tag{16}$$

where

$$[K_{n+1}^T] = \iint [B]^T[\bar{D}][B]\,dx\,dy + \iint [G]^T[S_{n+1}][G]\,dx\,dy$$
$$+ \frac{1}{\beta(\Delta t)^2}\left(\iint [N]^T[P][N]\,dx\,dy\right) - \frac{\delta\{R_{n+1}\}}{\delta\{U_{n+1}\}} \quad (17)$$

is the tangent stiffness matrix, in whose expression we have used the following notations:

$$[S] = \begin{bmatrix} N_x[I] & N_{xy}[I] \\ sym & N_y[I] \end{bmatrix}$$

is the matrix of the stress resultant array (with $[I]$ the 3×3 identity matrix), and $[G]$ is matrix of shape function derivatives, defined by

$$\{g_{n+1}\} = [G]\{U_{n+1}\},$$

where

$$\{g\} = \left[\frac{\partial u_0}{\partial x}\ \ \frac{\partial v_0}{\partial x}\ \ \left(\frac{\partial w_0}{\partial x} - \frac{u_0}{R_x}\right)\ \ \frac{\partial u_0}{\partial y}\ \ \frac{\partial v_0}{\partial y}\ \ \left(\frac{\partial w_0}{\partial y} - \frac{v_0}{R_y}\right)\right]^T.$$

Calculation of contact force. In order to model contact conditions between the impactor and the laminate, the modified version of the Hertzian contact law proposed by [Yang and Sun 1982] based on static indentation tests for cylindrical shell is used in this study. This approach determines the relationship between the contact force, F^c with the indentation depth, α. Since the contact region is generally small in comparison with the dimensions of the shell, the resultant contact force is represented as a point load.

The contact laws as proposed in [Yang and Sun 1982] during loading, unloading and reloading phases are not reproduced here for the sake of brevity; they can be written in a general form as

$$F_{n+1}^c = \phi(\alpha_{n+1}) = \phi(d_{n+1} - w_{n+1}) = \phi\left(d_n + \dot{d}_n\Delta t - \frac{1}{4}\frac{F_n^c + F_{n+1}^c}{m}(\Delta t)^2 - w_{n+1}\right), \quad (18)$$

where φ represents a nonlinear relation, d_{n+1} is the displacement of the centre point of the impactor at the $(n+1)$-th time-step and is calculated by applying Newmark's method to the equation of motion of the impactor as in (18). w_{n+1} is the displacement of the mid-surface of the laminate at the impact point in the direction of impact. The last term in (17) consists of dF_{n+1}^c/dw_{n+1}, which can be found by differentiating (18).

Impact damage analysis. It is well known that damage in composite materials is generally complicated consisting of multiple failure modes such as fibre breakage, fibre pullout, matrix cracking, fibre-matrix debonding, delamination between plies, etc. Several investigators have demonstrated that upon impact by a low-velocity projectile, the major part of the damage in the composite laminate is caused by matrix cracking and delamination. Because the tensile failure stress for the fibre is high, damage caused by fibre breakage is generally very limited and confined to the region under and near the contact area between the impactor and the laminate. Based on the experimental observations on low-velocity impact, Choi et al. [1991] reported that intraply matrix cracking is the initial damage mode. Delamination initiates once the matrix crack reaches the interface between the ply groups having different fibre orientations after propagating throughout the thickness of the ply group consisting of the cracked ply. This type of matrix

crack can be referred to as the "critical matrix crack". Several further investigations have indicated that there exists a strong interaction between matrix cracking and delamination and the extent of delamination propagation effectively depends upon the location of matrix cracks.

In the present study, a three-dimensional matrix failure criterion originally proposed in [Hashin 1980] and modified in [Choi et al. 1991] is used. In the latter reference it was shown that there are only three major stresses contributing to transverse matrix cracking in the principal material coordinate system. These are the in-plane transverse normal stress σ_y, the interlaminar transverse shear stress τ_{yz} and the out-of-plane normal stress σ_z. However, the out-of-plane normal stress σ_z is found to be negligibly small compared to the others and decreases rapidly at locations away from the impacted area. Thus, the criterion for the n-th plygroup is simplified as

$$\left(\frac{n_{\bar{\sigma}_y}}{n_Y}\right)^2 + \left(\frac{n_{\bar{\tau}_{yz}}}{n_{S_i}}\right)^2 = e_m^2, \tag{19}$$

where

$$Y = \begin{cases} Y_t & \text{if } \bar{\sigma}_y \geq 0, \\ Y_c & \text{if } \bar{\sigma}_y < 0. \end{cases}$$

In (19), x-y-z is the right-handed ply coordinate system with x-axis representing the fibre direction. $Y_t Y_c$ and S_i are the *in situ* ply transverse tensile strength, *in situ* ply transverse compressive strength and *in situ* interlaminar shear strength respectively within the laminate and e_m is the strength ratio which indicates failure if its value exceeds unity. The bar over the stress components indicates that stresses are averaged within the n-th ply in the thickness direction for predicting the critical matrix cracking.

Although the above equation was proposed in [Choi et al. 1991] for the case of line-loading impact, several further investigators [Choi and Chang 1992; Pradhan and Kumar 2000; Her and Liang 2004; Krishnamurthy et al. 2001; Krishnamurthy et al. 2003; Kumar et al. 2007] assumed this equation to be equally applicable to point-nose impact. However, the present author is of the view that for point-nose impact on curved laminates, the in-plane shear stress τ_{xy} as found in Hashin's matrix failure criterion [1980] must be incorporated in (19) for more accurate estimation.

In (19), *in situ* ply strength refers to the strength of a single ply within a laminate which is considerably different from that measured directly from a unidirectional composite. This difference is generally attributed to the thickness effect of the laminate, adjacent ply constraints and thermal residual stresses [Flaggs and Kural 1982; Peters 1984; Chang and Lessard 1991]. Here empirical relations proposed by [Chang and Lessard 1991] are adopted for calculating *in situ* ply strengths as a function of the laminate thickness and stacking sequence. These relations are given as

$$Y_t = Y_t^0 \left(1 + A\frac{\sin(\Delta\theta)}{N^B}\right), \quad S_i = S_{xy}^0 \left(1 + C\frac{\sin(\Delta\theta)}{N^D}\right). \tag{20}$$

In (20), Y_t^0 is the transverse tensile strength of a $[90_n]_s$ laminate ($n \geq 6$), S_{xy}^0 is the ply shear strength measured from a unidirectional composite with more than eight layers, $\Delta\theta$ is the minimum ply angle difference between the ply under consideration and its neighbouring plies and N is the number of consecutive plies of the same ply angle. A, B, C and D are material parameters determined from experiment [Chang and Lessard 1991].

A semiempirical criterion to estimate the extent of delamination in composite was proposed in [Choi and Chang 1992], which is based on major stresses attributed to delamination formation. However, the present paper is focussed only on the prediction of critical matrix cracking, since geometrical nonlinearity and the material degradation concept used here will have similar effects on both critical matrix cracking and delamination.

Material degradation concept. Once the critical matrix cracking is predicted at any point within a particular ply group of the shell using the criterion (19), the load carrying capability of the shell decreases. This stiffness loss must be taken into account before the solution proceeds further. Two strategies can be applied to describe the postfailure behaviour of the material. One option is to assume that material fails instantaneously and stiffness values in the corresponding directions are immediately set to zero. Another approach is to use a postfailure model such as those reported in [Ladevèze and LeDantec 1992; Matzenmiller et al. 1995; Johnson et al. 2001; Iannucci and Willows 2006] based on continuum damage mechanics approach. This postfailure model characterizes the growth of damage by a gradual decrease in the corresponding stiffness values using some damage evolution parameter until they reach a final value of zero. It is obvious that, this damage model will provide considerable improvement in the prediction of damage as compared to the instantaneous failure model particularly for the impact of high velocity ranges. This approach may also reduce or eliminate nodal oscillations which may occur in the case of instantaneous failure because of the sudden release of finite amounts of energy. However, this modelling strategy has an inherent complexity in implementation and requires knowledge of the energy dissipation process as a function of the damage mode and its propagation, which must be determined experimentally for a specific damage mode.

For the sake of simplicity, the instantaneous failure model is adopted in the present analysis and the constitutive relation for the damaged element is modified by the use of the reduced material properties such as the one reported in [Choi et al. 1991]. This reduced elastic property matrix can be modified for the present shell element as given below:

$$[C_{\text{red}}] = \begin{bmatrix} E_x & 0 & 0 & 0 & 0 \\ 0 & 0 & 0 & 0 & 0 \\ 0 & 0 & G_{xy} & 0 & 0 \\ 0 & 0 & 0 & 0 & 0 \\ 0 & 0 & 0 & 0 & G_{zx} \end{bmatrix}. \tag{21}$$

Equation (21) is derived based on the reasoning that the damaged region within the element cannot endure any additional in-plane transverse tensile stress and interlaminar transverse shear stress due to the presence of the matrix crack. In order to take into account the partial failure of the element within a ply group, the [C] matrix is replaced by the [C_{red}] matrix in (7) during Gaussian integration only for those gauss points of the ply group in the element where the failure criterion is satisfied.

This simplified instantaneous stiffness reduction method is reasonable for low-velocity impact in the sense that a general tool is always sought for to predict the combined effect of various damage modes on the performance of the composite structure with complex geometry and loading conditions. Further, this approach will generally not lead to a singularity of the global finite element stiffness matrix, since in the 2D shell element formulation, the whole thickness of the laminate is analysed as an aggregate. For

the same reason, the nodal oscillations will be much less prominent as compared to three-dimensional finite element solutions. Further, stiffness modifications on a gauss point basis will partly ensure gradual stiffness reduction of failed elements.

3. Numerical results and discussions

The above nonlinear finite element formulation was implemented in a specially developed computer code and successfully validated with existing numerical solutions available in literature.

Having validated the present approach, some example problems of T300/976 graphite/epoxy laminated cylindrical shells with different curvatures have been considered to study the impact behaviour of curved composite laminate. Effects of geometrical nonlinearity and material degradation on impact response and resulting damage are also investigated. The problem description of impact on a general doubly curved shell is also depicted in Figure 1. The impacted side is the first layer in the stacking sequence.

Validation problem: Impact response of a rectangular glass/epoxy laminated plate. A square E-glass epoxy cross-ply [0/90/0] laminated plate with a side length of 140 mm and thickness 4.29 mm clamped around the four edges is analyzed. The impactor is a blunt-ended steel circular cylinder having diameter 9.525 mm, length 25.4 mm and mass 0.01417 kg and traveling at an initial velocity of 22.6 ms^{-1}. The material properties of the 1002E-glass epoxy are taken as follows:

$$E_x = 40.0 \, \text{GPa}, \quad E_y = E_z = 8.27 \, \text{GPa}, \quad G_{xy} = G_{xz} = 4.13 \, \text{GPa}, \quad G_{yz} = 0.03 \, \text{GPa},$$
$$\nu_{xy} = \nu_{yz} = \nu_{xz} = 0.25, \quad \rho = 1901.5 \, \text{kg m}^{-3}.$$

The linear and nonlinear solutions of the plate central transverse deflection as a function of time have been compared in Figure 2 with experimental results from [Takeda et al. 1981] and finite element results from [Aggour and Sun 1988]. Good agreement is observed between the present result and the numerical
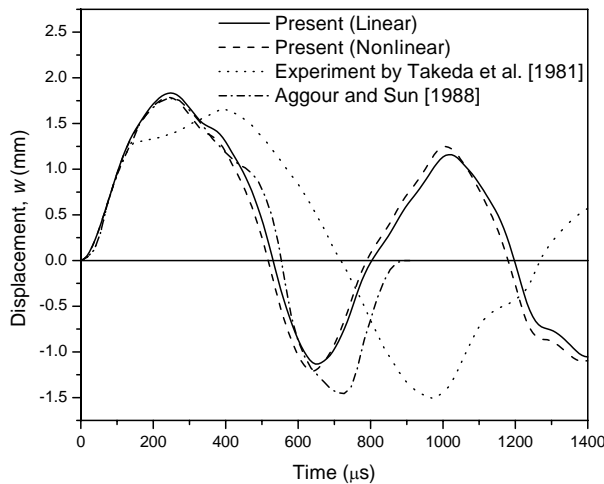
Figure 2. Comparison of plate central transverse deflection in a 140 mm × 140 mm × 4.29 mm E-glass epoxy cross-ply laminate with clamped edges and impacted by 14.175 gm steel projectile at a velocity of 22.6 ms^{-1}.

result. The reasons of discrepancy between numerical and experimental results were well explained in
[Aggour and Sun 1988]. It is also apparent from the figure that nonlinear effect is not significant in this
case mainly because the plate central deflection is considerably less than the plate thickness.

***Validation problem: Clamped [0/90] asymmetric cross-ply cylindrical shell panel subjected to uniform
load.*** As an example of large deflection of composite shell, the asymmetric cross-ply cylindrical shell
panel investigated in [Reddy and Chandrashekhara 1985] is considered. The radius and length of the
cylindrical shell panel are 64.5 m and 12.9 m respectively. The angle subtended by the arc is 0.2 radian.
The thickness of the shell is 64.5 mm. The material properties used are:

$$E_x = 172\,\text{GPa}, \quad E_y = E_z = 7\,\text{GPa}, \quad G_{xy} = G_{yz} = G_{xz} = 3.5\,\text{GPa}, \quad \nu_{xy} = \nu_{yz} = \nu_{xz} = 0.25.$$

The load-deflection curve of the nonlinear solution is given in Figure 3 along with the results of the
[Reddy and Chandrashekhara 1985]. Fairly good agreement is seen.

Impact response. T300/976 Graphite/epoxy cylindrical shells of different dimensions and curvatures
with $[90_4/0_8/90_4]$ lay-up are considered. At first, $[90_4/0_8/90_4]$ cylindrical shell is taken with $a = b =$
300 mm, $R_x = R = 10a$, and $R_y = \infty$ in Figure 1. The shell is clamped on its edges and is subjected
to impact by a steel mass of 300 gm having a half sphere head of 10 mm diameter and initial velocity
$7\,\text{ms}^{-1}$. The material property data of fiberite T300/976 graphite/epoxy composite are considered as
follows [Choi and Chang 1992]:

- Material constants: ply thickness = 0.14224 mm, $\rho = 1540\,\text{kg m}^{-3}$, $E_x = 156\,\text{GPa}$,
  $E_y = E_z = 9.09\,\text{GPa}$, $G_{xy} = G_{xz} = 6.96\,\text{GPa}$, $G_{yz} = 3.24\,\text{GPa}$, $\nu_{xy} = \nu_{xz} = 0.228$, $\nu_{yz} = 0.4$.

- Lamina strengths: $Y_t^0 = 45\,\text{MPa}$, $Y_c = 252\,\text{MPa}$, $S_{xy}^0 = 105\,\text{MPa}$.

- Empirical parameters: $A = 1.3$, $B = 0.7$, $C = 2.0$, $D = 1.0$.
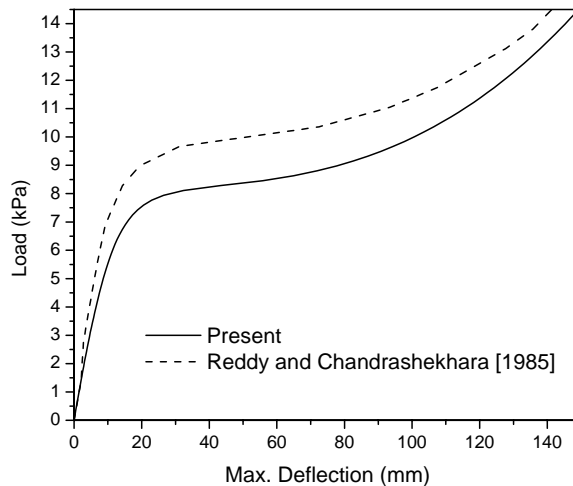
Figure 3. Load-deflection curve for clamped [0/90] asymmetric cross-ply cylindrical
shell panel subjected to uniform load.

The results of contact force, impactor displacement and shell centre displacement are presented in Figure 4 for both linear and nonlinear analyses. A reduction in maximum contact force and increase in contact duration and maximum central deflection is observed in the nonlinear solution of the shell with curvature $R = a$ when compared with linear results. Although the peak contact force also increased in the nonlinear solution of shell with curvature $R = 10a$, the contact duration and the maximum shell deflection decreased significantly. The effect of shell curvature is also shown in the Figure. Both the contact duration and the amplitude of shell response decrease with decrease in the shell radius indicating that increasing the curvature has a stiffening effect on the cylindrical shell. However, the results signify that a nonlinear approach has caused a reduction in flexural rigidity of the shell having higher stiffness due to curvature while this has resulted in an increase in flexural rigidity of the shell having lower curvature-induced stiffness.
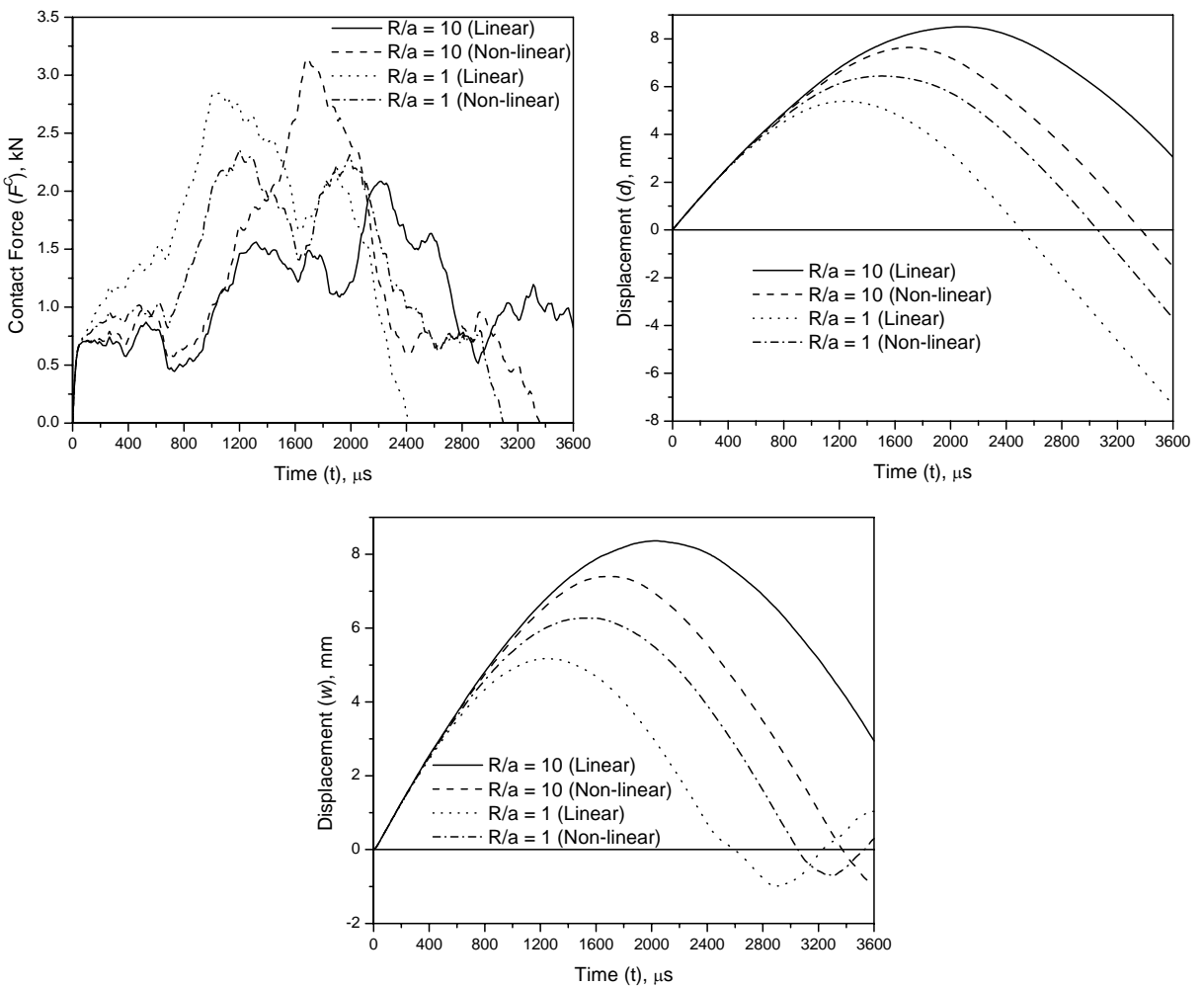
Figure 4. Contact force, impactor displacement and centre displacement in graphite/epoxy cylindrical shells ($[90_4/0_8/90_4]$) ($a = b = 300\,\text{mm}$; $R = 10a$ and $R = a$), with clamped edges and impacted by blunt-ended steel cylinder of nose radius 5 mm and mass 300 gm having initial velocity of $7\,\text{ms}^{-1}$.

Impact-induced damage. The impact-induced damage in the form of critical matrix cracking is studied for the above cylindrical shell. The shell with $[90_4/0_8/90_4]$ lay-up with dimensions $a = b = 300$ mm and curvature $R = a$ is subjected to an impact by a steel mass of 300 gm and nose radius 5 mm traveling at a velocity of $7\,\text{ms}^{-1}$. Critical matrix cracking takes place in the bottom $[90_4]$ ply group as shown in Figure 5. The value of strength ratio, e_m (critical matrix cracking failure criterion) at any point in the shell is found to be maximum in the bottom $[90_4]$ ply group at time approximately $1056\,\mu$s in case of linear analysis and $1212\,\mu$s in case of nonlinear analysis. The region where e_m is greater than or equal to unity represents the location of the critical matrix cracking. The failure contour is extended much wider along the fibre direction of the cracked $[90_4]$ ply group than in the direction normal to the fibre direction. Considerable changes in failure profile and a small increase in the damage region are observed in the case of the nonlinear solution even if the maximum contact force was lower as compared to the linear result (Figure 4). This occurs mainly because in the nonlinear case both the bending deformation and hence the bending stress are higher which significantly contributes to matrix cracking. Though the damage primarily occurs near the impact site, the figure indicates that for clamped shell panels damage can also evolve near the boundaries.

Material degradation effects. The effect of reducing the stiffness of damaged elements within the laminas concurrently while computing the impact response and damage is also studied. For this case, a $[90_4/0_8/90_4]$ layup cylindrical shell of dimensions $a = b = 100$ mm and curvature $R = a$ is taken. The impactor is a steel mass of 200 gm having a half sphere head of 10 mm diameter and initial velocity $5\,\text{ms}^{-1}$. The nonlinear results of contact force, impactor displacement and shell center deflection are plotted in Figure 6 for both the cases in which the reduction of stiffness was considered and was not considered. There is a sizeable reduction in peak contact force and increase in both contact duration and maximum shell deflection indicating that overall stiffness of the laminate has reduced considerably when material degradation is incorporated in the solution. The value of the strength ratio, e_m at any
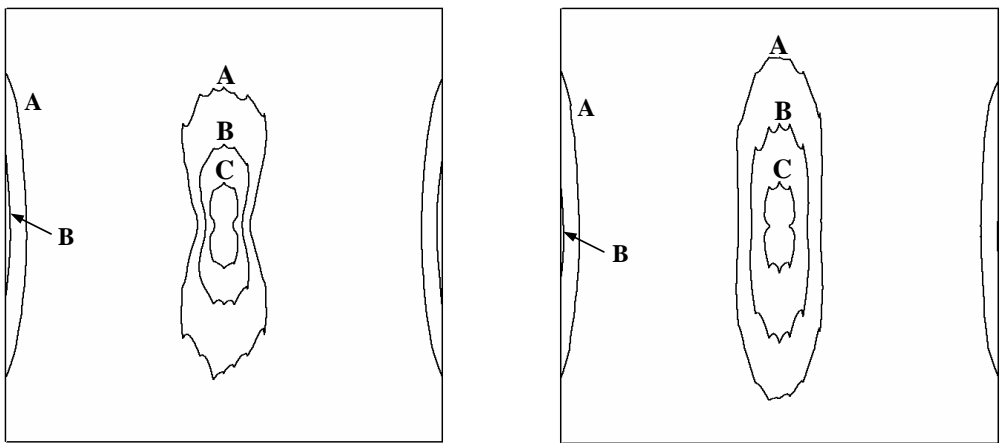
Figure 5. Contours of maximum strength ratio e_m ($A = 0.2$, $B = 0.5$, $C = 1.0$) in bottom $[90_4]$ ply of $[90_4/0_8/90_4]$ lay-up cylindrical shell (dimensions: $a = b = 300$ mm; $R = a$) with clamped edges and impacted by a 300 gm mass at a velocity of $7\,\text{ms}^{-1}$. Left: linear analysis; right: nonlinear analysis.

point in the shell is found to be a maximum at approximately $472 \, \mu$s in case of unmodified stiffness and at approximately $608 \, \mu$s in case of modified stiffness. The critical matrix cracking profile is plotted in Figure 7 for both the cases. A comparison of the two halves of the figure indicates that the critical matrix cracking has further extended in the direction of the fibre and has reduced in the direction normal to the fibre direction due to material degradation. This is mainly because loads that were sustained by the elements prior to damage are consequently transferred to adjacent elements. It is obvious that this stiffness modification concept will give better results and smooth failure contours with increasing mesh density and decreasing analysis time-step as appropriate.

Although it would be more appropriate to present some sample results depicting improvements brought by incorporating material degradation effects in the finite element solution, an indirect estimation can
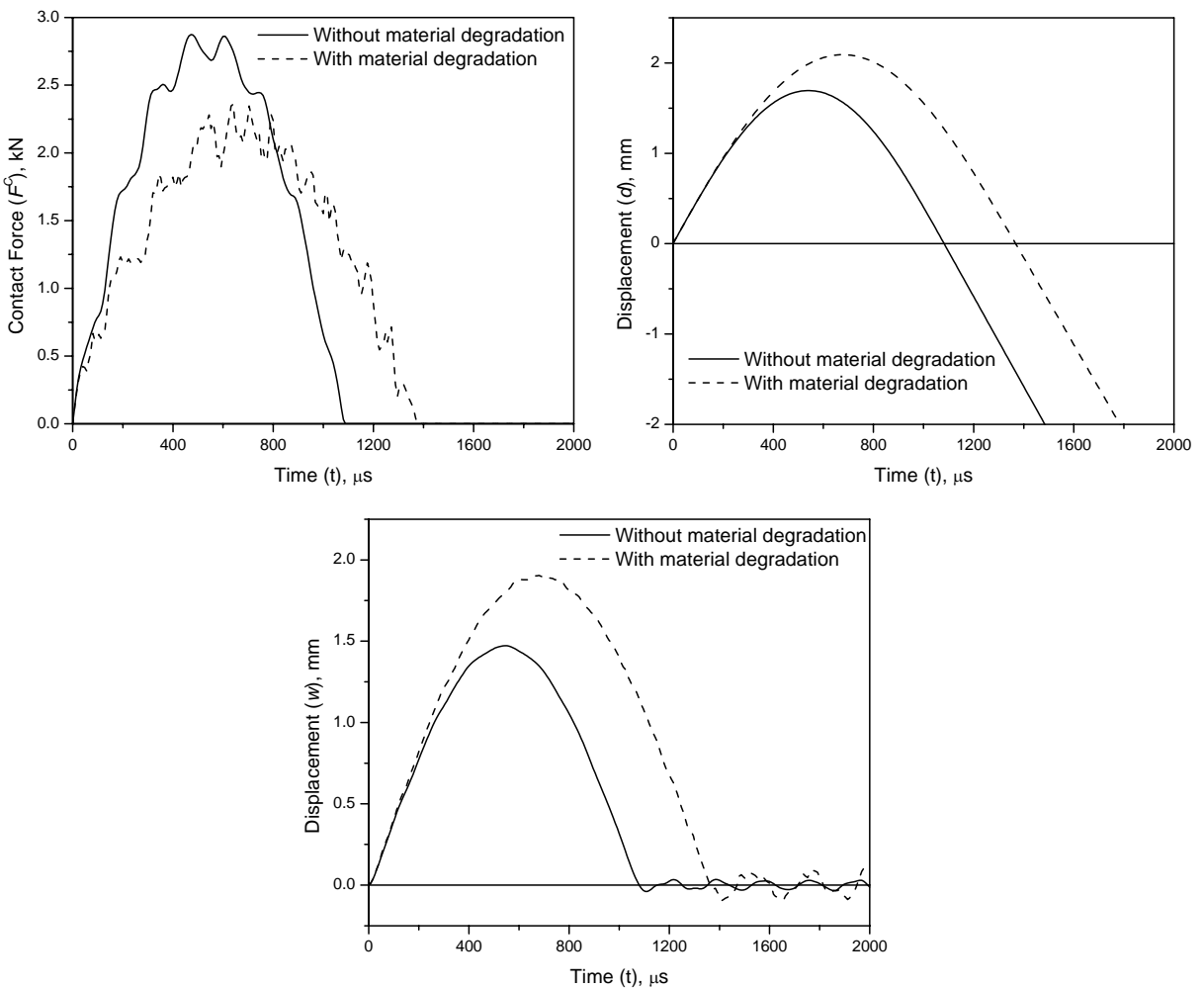
Figure 6. Effect of material degradation on contact force, impactor displacement and centre deflection in graphite/epoxy cylindrical shell ($[90_4/0_8/90_4]$ lay-up) ($a = b = 100$ mm; $R = a$; nonlinear analysis), with clamped edges and impacted by blunt-ended steel cylinder of nose radius 5 mm and mass 200 gm having initial velocity of $5 \, \text{ms}^{-1}$.
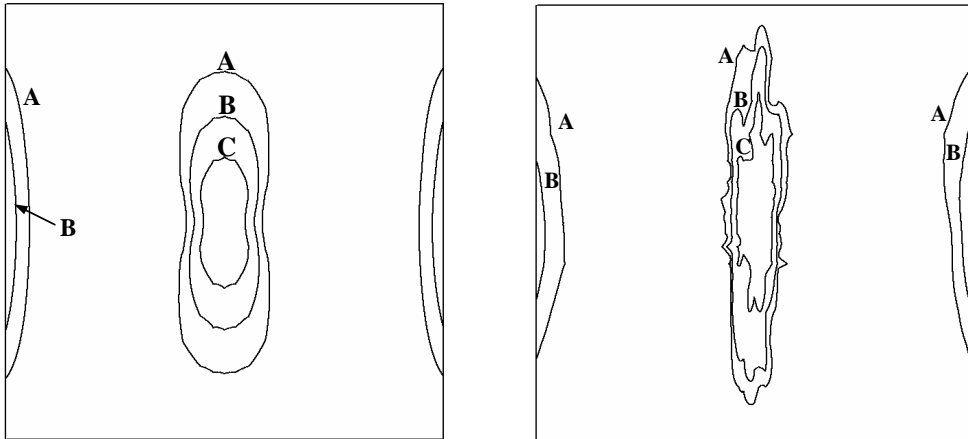
Figure 7. Effect of material degradation on maximum strength ratio e_m ($A = 0.2$, $B = 0.5$, $C = 1.0$) in bottom [90_4] ply of [$90_4/0_8/90_4$] lay-up cylindrical shell (dimensions: $a = b = 300$ mm; $R = a$) with clamped edges and impacted by a 200 gm mass at a velocity of 5 ms^{-1}. Left: without material degradation; right: with material degradation.

be made with regard to the verification problem of Figure 2. One of the reasons cited in [Aggour and Sun 1988] for the inconsistency between numerical and experimental results in Figure 2 was that as the contact time between impactor and plate increases, the failure in the form of matrix cracking and delamination may have started in the laminate reducing its overall stiffness and natural frequency. As in Figure 6, it is expected that if the material degradation concept is integrated in the solution of problem of Figure 2, the contact duration will increase and the mismatch between finite element result and experimental observation will reduce considerably.

4. Conclusion

A finite element and transient dynamic analysis of laminated composite cylindrical shells subjected to transverse impact has been performed using a nonlinear finite element shell formulation and implemented by a specially developed computer code. The tangent stiffness matrix accounting for the geometric nonlinearity is formulated using a generalized Green's strain tensor. The nonlinear system of equations was solved using a Newton–Raphson incremental-iterative method by considering suitable displacement and force convergence norms. Some numerical examples of graphite/epoxy laminated cylindrical shells have been considered with different curvature and nonlinear geometrical effects on impact response and the resulting damage has been studied. Some example problems are also considered in which the stiffness of the failed elements within the laminate is concurrently reduced to account for their loss of load-carrying capability due to matrix cracking. The following are some important observations made from the present study:

1. When the geometrical nonlinearity was included, considerable changes in the time-variation of contact force, impactor displacement and shell deflection occurred for the problems considered. This difference in impact response is found to be significantly dependent on the shell curvature considered.

2. Although damage primarily occurs near the impact site, damage can also evolve near the boundaries for clamped shell panels. A considerable change in the critical matrix cracking profile is noticed when a nonlinear approach is used in the solution.

3. The material property degradation approach used here is found to provide reasonable results and can be easily implemented in cases when a general tool is required to predict the combined effect of various damage modes on the performance of the composite structure with complex geometry and loading conditions.

4. When the stiffness of the failed region is reduced, there is a sizeable reduction in peak contact force in combination with increase in both contact duration and maximum shell deflection. Owing to material property degradation, the shape and extent of critical matrix cracking is noticeably changed extending largely in fibre direction while shrinking in the direction normal to the fibre direction of the cracked ply-group.

Acknowledgement

References

[Abrate 1991] S. Abrate, "Impact on laminated composite materials", *Appl. Mech. Rev.* (*ASME*) **44** (1991), 155–190.

[Abrate 1994] S. Abrate, "Impact on laminated composites recent advances", *Appl. Mech. Rev.* (*ASME*) **47** (1994), 517–544.

[Aggour and Sun 1988] H. Aggour and C. T. Sun, "Finite element analysis of a laminated composite plate subjected to circularly distributed central impact loading", *Comput. Struct.* **28**:6 (1988), 729–736.

[Ambur et al. 1995] D. R. Ambur, J. H. Starnes, Jr., and C. B. Prasad, "Low-speed impact damage-initiation characteristics of selected laminated composite plates", *AIAA J.* **33**:10 (1995), 1919–1925.

[Cantwell and Morton 1991] W. J. Cantwell and J. Morton, "The impact resistance of composite materials: a review", *Composites* **22**:5 (1991), 347–362.

[Chandrashekhara and Schroeder 1995] K. Chandrashekhara and T. Schroeder, "Nonlinear impact analysis of laminated cylindrical and doubly curved shells", *J. Compos. Mater.* **29**:16 (1995), 2160–2179.

[Chang and Lessard 1991] F. K. Chang and L. B. Lessard, "Damage tolerance of laminated composites containing an open hole and subjected to compressive loading, I: Analysis", *J. Compos. Mater.* **25** (1991), 2–43.

[Choi and Chang 1992] H. Y. Choi and F.-K. Chang, "A model for predicting damage in graphite/epoxy laminated composites resulting from low-velocity point impact", *J. Compos. Mater.* **26**:14 (1992), 2134–2169.

[Choi et al. 1991] H. Y. Choi, H. Y. T. Wu, and F. K. Chang, "A new approach towards understanding damage mechanisms and mechanics of laminated composites due to low-velocity impact, II: Analysis", *J. Compos. Mater.* **25** (1991), 1012–1038.

[Flaggs and Kural 1982] D. L. Flaggs and M. H. Kural, "Experimental determination of the in situ transverse lamina strength in graphite/epoxy laminates", *J. Compos. Mater.* **16**:2 (1982), 103–116.

[Ganapathy and Rao 1998] S. Ganapathy and K. P. Rao, "Failure analysis of laminated composite cylindrical/spherical shell panels subjected to low-velocity impact", *Comput. Struct.* **68**:6 (1998), 627–641.

[Hashin 1980] Z. Hashin, "Failure criteria for unidirectional fibre composites", *J. Appl. Mech.* (*ASME*) **47** (1980), 329–334.

[Her and Liang 2004] S.-C. Her and Y.-C. Liang, "The finite element analysis of composite laminates and shell structures subjected to low velocity impact", *Compos. Struct.* **66**:1-4 (2004), 277–285.

[Iannucci and Willows 2006] L. Iannucci and M. L. Willows, "An energy based damage mechanics approach to modelling impact onto woven composite materials, I: Numerical models", *Compos. A Appl. Sci. Manuf.* **37**:11 (2006), 2041–2056.

[Johnson et al. 2001] A. F. Johnson, A. K. Pickett, and P. Rozycki, "Computational methods for predicting impact damage in composites structures", *Compos. Sci. Technol.* **61**:15 (2001), 2183–2192.

[Kim et al. 1997] S. J. Kim, N. S. Goo, and T. W. Kim, "The effect of curvature on the dynamic response and impact-induced damage in composite laminates", *Compos. Sci. Technol.* **57**:7 (1997), 763–773.

[Krishnamurthy et al. 2001] K. S. Krishnamurthy, P. Mahajan, and R. K. Mittal, "A parametric study of the impact response and damage of laminated cylindrical composite shells", *Compos. Sci. Technol.* **61**:12 (2001), 1655–1669.

[Krishnamurthy et al. 2003] K. S. Krishnamurthy, P. Mahajan, and R. K. Mittal, "Impact response and damage in laminated composite cylindrical shells", *Compos. Struct.* **59**:1 (2003), 15–36.

[Kumar et al. 2007] S. Kumar, B. N. Rao, and B. Pradhan, "Effect of impactor parameters and laminate characteristics on impact response and damage in curved composite laminates", *J. Reinf. Plast. Compos.* **26**:13 (2007), 1273–1290.

[Ladevèze and LeDantec 1992] P. Ladevèze and E. LeDantec, "Damage modelling of the elementary ply for laminated composites", *Compos. Sci. Technol.* **43**:3 (1992), 257–267.

[Matzenmiller et al. 1995] A. Matzenmiller, J. Lubliner, and R. L. Taylor, "A constitutive model for anisotropic damage in fibre-composites", *Mech. Mater.* **20**:2 (1995), 125–152.

[Nosier et al. 1994] A. Nosier, R. K. Kapania, and J. N. Reddy, "Low-velocity impact of laminated composites using a layerwise theory", *Comput. Mech.* **13**:5 (1994), 360–379.

[Peters 1984] P. W. M. Peters, "The strength distribution of 90° plies in 0/90/0 graphite-epoxy laminates", *J. Compos. Mater.* **18**:6 (1984), 545–556.

[Pradhan and Kumar 2000] B. Pradhan and S. Kumar, "Finite element analysis of low-velocity impact damage in composite laminates", *J. Reinf. Plast. Compos.* **19**:4 (2000), 322–339.

[Reddy and Chandrashekhara 1985] J. N. Reddy and K. Chandrashekhara, "Nonlinear analysis of laminated shells including transverse shear strains", *AIAA J.* **23**:3 (1985), 440–441.

[Sanders 1959] J. L. Sanders, Jr., "An improved first-approximation theory for thin shells", Technical report R–24, NASA, 1959, Available at http://www.ntis.gov/search/product.aspx?ABBR=PB175839.

[Stein 1986] M. Stein, "Nonlinear theory for plates and shells including the effects of transverse shearing", *AIAA J.* **24**:9 (1986), 1537–1544.

[Takeda et al. 1981] N. Takeda, R. L. Sierakowski, and L. E. Malvern, "Wave propagation experiments on ballistically impacted composite laminates", *J. Compos. Mater.* **15**:2 (1981), 157–174.

[Wu and Springer 1988] H.-S. T. Wu and G. S. Springer, "Impact induced stresses, strains, and delaminations in composite plates", *J. Compos. Mater.* **22**:6 (1988), 533–560.

[Yang and Sun 1982] S. H. Yang and C. T. Sun, "Indentation law for composite laminates", pp. 425–449 in *Composite materials: testing and design* (*6th conference*) (Phoenix, AZ, 1991), edited by I. M. Daniel, ASTM Special Technical Publication **787**, American Society for Testing and Materials, Philadelphia, 1982. Paper ID: STP28494S.

[Zhu et al. 2006] L. Zhu, A. Chattopadhyay, and R. K. Goldberg, "Multiscale analysis including strain rate dependency for transient response of composite laminated shells", *J. Reinf. Plast. Compos.* **25**:17 (2006), 1795–1831.

SURENDRA KUMAR: surendra@cmmacs.ernet.in
Council of Scientific and Industrial Research, Centre for Mathematical Modelling and Computer Simulation,
NAL Belur Campus, Bangalore, Karnataka 560037, India

DETERMINATION OF STRAIN GAGE LOCATIONS FOR THE ACCURATE MEASUREMENT OF OPENING MODE STRESS INTENSITY FACTORS

B. Kaushik, K. S. R. K. Murthy and P. S. Robi

The accuracy of measurement of opening mode stress intensity factors using the strain gage techniques largely depends on location of the gages. The radial position of the strain gages is a major issue in measurement of the stress intensity factors. This paper describes an approach to resolve this problem. The present work proposes a method for practically accurate determination of a vital parameter designated as (r_{max}) which in turn is extremely useful in judging the valid positions of the strain gages. The results of the present investigation clearly show that the proposed method is simple and accurate values of r_{max} can be determined.

1. Introduction

The stress intensity factor (SIF) is extensively employed when applying the principles of linear elastic fracture mechanics (LEFM) to the analysis of the safety of engineering components containing cracks. It is used to understand the severity of the cracks while calculating the static strength, fatigue crack growth and life predictions. The SIF is of considerable importance in many engineering situations, since the critical value of this parameter determines whether or not the existing crack will propagate.

The use of LEFM principles in preventing the fracture of engineering components depends largely on the availability of accurate SIFs. As a result, analytical, numerical and experimental methods for SIF determination in cracked bodies have been developed over the years.

Experimental methods, in particular, play an important role in complex situations [Sanford 2003] and are essential to the validation and correct application of theoretical and numerical results. They include the compliance method [Bonesteel et al. 1978; Newman 1981], photoelasticity [Gdoutos and Theocaris 1978; Hyde and Warrior 1990], caustics [Theocaris 1970; Konsta-Gdoutos 1996] and strain gage methods [Dally and Berger 1993; Swamy et al. 2008]. Among these, the strain gage technique is relatively simple and straightforward [Sanford 2003].

Four strain gage techniques [Dally and Sanford 1987; Wei and Zhao 1997; Kuang and Chen 1995; Berger and Dally 1988] are currently available for experimental determination of mode I stress intensity factors under static loading. Factors such as the local yielding effect at the crack tip, high strain gradients, the three-dimensional state of stress at the crack tips and the finite size of the strain gages strongly affect the performance of strain gage techniques.

Dally and Sanford [1987] were the first to develop a strain gage technique for measuring the static opening mode stress intensity factor (K_I) in two dimensional isotropic bodies which overcomes these difficulties. This was achieved by identifying the valid region around the crack tip for accurate measurement of the strains. These authors proposed to determine the mode I SIF using a truncated strain

Keywords: stress intensity factors, cracks, fracture, strain gage, finite element analysis.

series containing only three parameters. The chief advantage of their approach is that only one strain gage is sufficient to determine the mode I SIF, by locating it at distances far away from the crack tip. However, the radial location of the strain gage should be within the realm of applicability of the of three-parameter representation. Thus this technique requires knowing beforehand the extent of validity of the three-parameter representation. In general, this extent depends on configuration and boundary conditions; no suggestions were made in [Dally and Sanford 1987] toward this end.

[Wei and Zhao 1997] and [Kuang and Chen 1995] devised different strain gage methods for measuring the static mode I SIF. Two strain gages are needed for measuring the opening mode SIF in the approach in the first of these papers. However, locations (radial distances) of the strain gages are suggested empirically and necessitate a priori knowledge about the plastic zone size, which depends on the unknown stress intensity factor of the configuration.

In contrast, Kuang and Chen [1995] used asymptotic strain expressions for the measurement of the mode I SIF. They suggested that strain gages can be placed at distances greater than half the thickness of the specimen from the crack tip despite the fact that at large distances from the crack tip the measured strains cannot be accurately represented by asymptotic terms alone. Their results show that the measured normalized SIF is a function of the applied loads, the thickness of the specimen and the angular position θ from the crack axis.

A very large number of strain gages is needed to measure the opening mode SIFs in an overdeterministic method proposed in [Berger and Dally 1988]. Among these techniques, the single strain gage method [Dally and Sanford 1987] is most popular.

Apart from development of various techniques, another important direction in experimental determination of static stress intensity factors is the application of the existing techniques to corroborate the analytical/numerical solutions of the SIFs. For example, application of photoelastic methods is dealt in [Marloff et al. 1971; Chan and Chow 1979; Kazemi et al. 1989; Nurse et al. 1994] and caustics techniques in [Baik et al. 1995; Lee and Hong 1993]. Such investigations establish the existing techniques as useful tools in real design situations of great complexity. In spite of these potential applications of the strain gage methods, very limited work has been reported to date [Swamy et al. 2008], particularly on applications of Dally and Sanford's single strain gage procedure in order to validate/suggest accurate mode I, static SIFs of the complex configurations. This is true even in case of the other strain gage methods.

One important reason which hampered the potential application of Dally and Sanford's method is the uncertainty over the radial location (r) of the strain gage, where (r) is the radial distance from the crack tip. Improper locations may lead to highly erroneous measurement of the surface strains. Theoretically, the three-parameter strain series of Dally and Sanford accurately estimates the strain field up to a certain radial distance, say $r_{\max}$ (depending on the angular position θ) from the crack tip. This distance depends on the given configuration and boundary conditions. As a result this quantity is not known a prior. From the strain gradient analysis in [Dally and Sanford 1987] and the behavior of a crack with a plastic zone ahead of it [Sanford 2003], it is preferable to paste the gages far way from the crack tip but not beyond $r_{\max}$. Therefore, it is evident that the knowledge of $r_{\max}$ is essential before conducting the experiments so as to access whether the selected radial distance of the strain gage is meeting the above requirement or not. If the chosen or guessed value of r is small then the measured strains may be severely affected due to plasticity and strain gradient effects. On the other hand if it is greater than the unknown $r_{\max}$, though the above errors decrease rapidly but the measured strains may not be as per the theoretical predictions.
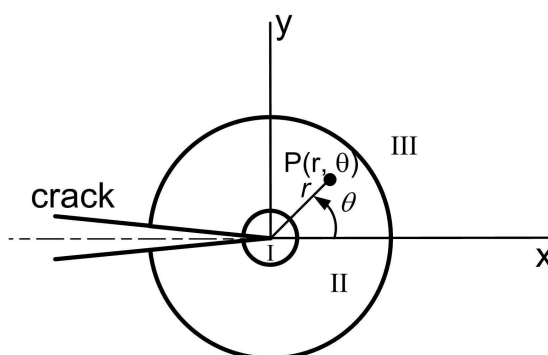
Figure 1. Various regions at the crack tip [Dally and Sanford 1987].

It is worth noting that, at least a reasonably approximate value of the extent of validity of three-parameter strain series or r_{max} is therefore needed for properly locating the gages. To the best of authors' knowledge no means are currently available to estimate the value of r_{max} in order to measure accurate opening mode SIFs using the approach of [Dally and Sanford 1987].

The present work attempts to suggest a computational approach to determine reasonably accurate values of r_{max} of a given configuration in line with the method of Dally and Sanford. The solution is presented using the finite element analysis of cracked specimens. Single edge cracked plate problems are considered with finite width and height to demonstrate the present approach. The outline of the paper is as follows. First, theoretical background for numerical determination of r_{max} is presented in Section 2. Section 3 presents numerical examples to demonstrate the proposed approach for determination of r_{max}. Finally some concluding remarks are summarized in Section 3.

2. Theoretical background

The main underlying idea behind single strain gage technique of [Dally and Sanford 1987] is identification of a suitable region around the crack tip within which accurate measurement of surface strains can be made. Therefore, the region around a crack tip (traction free crack faces) is divided into three zones viz. very near field, near field and far field zones as shown in Figure 1.

The very near field zone is close to the crack tip and first term of the strain series (singular strain term) is sufficient to represent the strains. However, it is not a valid zone for accurate strain measurements as the stress state in this region is three-dimensional (neither plane stress nor plane strain) [Rosakis and Ravi-Chandar 1986] and the measured strains will be severely affected by plasticity effects. Also errors in measuring the position of the strain gage are excessive if they are located very close to the crack tip.

The far field zone is again not suitable for collection of strain data because very large number of terms in the strain series is required to yield accurate results. Therefore, Dally and Sanford identified that the intermediate or near field zone is favorable and optimum zone for accurate measurement of the surface strains. In this zone, a singular term and a small number of higher order terms accurately describe the strain field.

The near field strain equations are obtained using the generalized Westergaard approach proposed by [Sanford 1979]. The modified Airy stress function in this approach is given by

$$\phi = \operatorname{Re} \bar{\bar{Z}}(z) + y \operatorname{Im} \bar{Z}(z) + \operatorname{Im} \bar{Y}(z),$$ (1)

where

$$\frac{d\bar{\bar{Z}}}{dz} = \bar{Z}, \qquad \frac{d\bar{Z}}{dz} = Z, \qquad \frac{d\bar{Y}}{dz} = Y$$ (2)

and the complex analytic functions $Z(z)$ and $Y(z)$ are defined as

$$Z(z) = \sum_{n=0}^{\infty} A_n z^{(n-1)/2} = \frac{K}{\sqrt{2\pi z}} + \sum_{n=1}^{\infty} A_n z^{(n-1)/2}, \qquad Y(z) = \sum_{m=0}^{\infty} B_m z^m = \frac{\sigma_{0x}}{2} + \sum_{m=1}^{\infty} B_m z^m,$$ (3)

which are series type functions (in terms of the complex variable $z = x + iy$) containing an infinite number of coefficients $A_1, A_2, \ldots, B_1, B_2, \ldots$ that can be determined using the boundary conditions of a given problem. The stress components for the entire domain are represented by Dally and Sanford as

$$\begin{aligned}
\sigma_{xx} &= \operatorname{Re} Z - y \operatorname{Im} Z' - y \operatorname{Im} Y' + 2 \operatorname{Re} Y, \\
\sigma_{yy} &= \operatorname{Re} Z + y \operatorname{Im} Z' + y \operatorname{Im} Y', \\
\tau_{xy} &= -y \operatorname{Re} Z' - y \operatorname{Re} Y' - \operatorname{Im} Y.
\end{aligned}$$ (4)

Assuming plane stress conditions, the stress-strain relations are given by

$$\varepsilon_{xx} = \frac{1}{E}(\sigma_{xx} - \nu\sigma_{yy}), \qquad \varepsilon_{yy} = \frac{1}{E}(\sigma_{yy} - \nu\sigma_{xx}), \qquad \gamma_{xy} = \frac{\tau_{xy}}{G}.$$ (5)

Equations for the strain field can be obtained upon substituting (4) in (5)

$$E\varepsilon_{xx} = (1-\nu)\operatorname{Re} Z - (1+\nu)y \operatorname{Im} Z' - (1+\nu)y \operatorname{Im} Y' + 2\operatorname{Re} Y$$ (6a)

$$E\varepsilon_{yy} = (1-\nu)\operatorname{Re} Z + (1+\nu)y \operatorname{Im} Z' + (1+\nu)y \operatorname{Im} Y' - 2\nu \operatorname{Re} Y$$ (6b)

$$G\gamma_{xy} = -y \operatorname{Re} Y' - \operatorname{Im} Y - y \operatorname{Re} Z'$$ (6c)

Substitution of series form of complex functions $Z(z)$ and $Y(z)$ from (3) gives exact representation of strain field in the domain with infinite number of unknown coefficients A_n and B_m. It is assumed that the strain field in the near field zone can be sufficiently represented by the three-parameter series with unknown coefficients A_0, A_1 and B_0. The three-term representation of strain field in this region is therefore

$$E\varepsilon_{xx} = A_0 r^{-1/2} \cos\frac{\theta}{2}\left((1-\nu)-(1+\nu)\sin\frac{\theta}{2}\sin\frac{3\theta}{2}\right) + 2B_0 + A_1 r^{1/2}\cos\frac{\theta}{2}\left((1-\nu)+(1+\nu)\sin^2\frac{\theta}{2}\right),$$

$$E\varepsilon_{yy} = A_0 r^{-1/2} \cos\frac{\theta}{2}\left((1-\nu)+(1+\nu)\sin\frac{\theta}{2}\sin\frac{3\theta}{2}\right) - 2\nu B_0 + A_1 r^{1/2}\cos\frac{\theta}{2}\left((1-\nu)-(1+\nu)\sin^2\frac{\theta}{2}\right),$$

$$2G\gamma_{xy} = A_0 r^{-1/2}\left(\sin\theta\cos\frac{3\theta}{2}\right) - A_1 r^{1/2}\left(\sin\theta\cos\frac{\theta}{2}\right),$$

where A_0, A_1 and B_0 are unknown coefficients that can be determined using the geometry of the specimen and the boundary conditions. Using the definition of K_I one can easily show that it is related to A_0 by

$$K_I = \sqrt{2\pi}\, A_0.$$ (7)
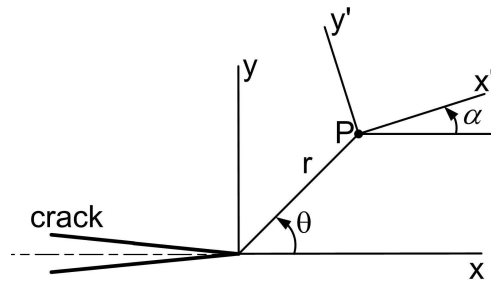
Figure 2. Strain gage location and orientation [Dally and Sanford 1987].

A single strain gage is sufficient to measure the constant A_0 (hence K_I) by placing and orienting the strain gage as given below.

Using the strain transformation equations, the strain component $\varepsilon_{x'x'}$ at the point P located by r and θ (Figure 2) is given by

$$2G\varepsilon_{x'x'} = A_0 r^{-1/2}\left(\kappa\cos\frac{\theta}{2} - \frac{1}{2}\sin\theta\sin\frac{3\theta}{2}\cos 2\alpha + \frac{1}{2}\sin\theta\cos\frac{3\theta}{2}\sin 2\alpha\right)$$
$$+ B_0(\kappa + \cos 2\alpha) + A_1 r^{1/2}\cos\frac{\theta}{2}\left(\kappa + \sin^2\frac{\theta}{2}\cos 2\alpha - \frac{1}{2}\sin\theta\sin 2\alpha\right), \quad (8)$$

where $\kappa = \dfrac{1-\nu}{1+\nu}$. The B_0 term in this equation can be eliminated by selecting the angle α so that

$$\cos 2\alpha = -\kappa = -\frac{1-\nu}{1+\nu}. \quad (9)$$

Similarly the coefficient A_1 vanishes if the angle θ is chosen so that

$$\tan\frac{\theta}{2} = -\cot 2\alpha. \quad (10)$$

Thus by placing a single strain gage (Figure 2) with α and θ as defined by (9) and (10) one can measure the strain $\varepsilon_{x'x'}$, which in turn is related to K_I by

$$\varepsilon_{x'x'} = \frac{1}{\sqrt{r}}\left[\frac{K_I}{G\sqrt{8\pi}}\left(\kappa\cos\frac{\theta}{2} - \frac{1}{2}\sin\theta\sin\frac{3\theta}{2}\cos 2\alpha + \frac{1}{2}\sin\theta\cos\frac{3\theta}{2}\sin 2\alpha\right)\right]. \quad (11)$$

This equation accurately determines $\varepsilon_{x'x'}$ up to a radial distance of $r_{\max}$. For a given configuration, applied load, Young's modulus E and Poisson's ratio ν, the bracketed part on right-hand side of (11) is a constant. Therefore

$$\varepsilon_{x'x'} = \frac{C}{\sqrt{r}}, \quad (12)$$

where C is a constant. Taking the logarithm on both sides of (12) we get

$$\ln\varepsilon_{x'x'} = -\tfrac{1}{2}\ln r + \ln C. \quad (13)$$

Equations (12) and (13) are valid along the line given by (10) until a radial distance of $r_{\max}$. Thus a log-log plot of (12) is a straight line of slope -0.5, with an intercept of $\ln C$. The straight line property generally breaks for $r > r_{\max}$, because then more than three parameters are needed in (8) to estimate $\varepsilon_{x'x'}$. Using (13), the value of $r_{\max}$ can be accurately estimated.
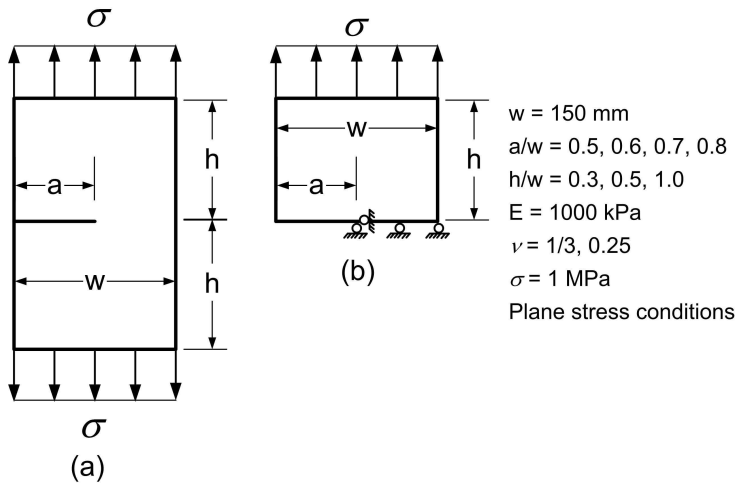
Figure 3. (a) Problem domain: Finite edge cracked plate subjected to uniform tension; (b) half-model along with the symmetry boundary conditions used for the finite element analysis.

3. Numerical examples

This section describes the proposed approach based on the finite element analysis of a given cracked configuration for reasonably accurate estimation of the corresponding $r_{\max}$. The method is presented with the aid of numerical examples. For this purpose finite width and finite height edge cracked plates subjected to uniform tensile stress are considered; see Figure 3(a). Due to symmetry only half the plate is modeled, as shown in Figure 3(b). We generate different configurations, with $a/w = 0.5, 0.6, 0.7, 0.8$ and $h/w = 0.3, 0.5, 1.0$. The width $w = 150\,mm$ of the plate is fixed in all cases, as is the value of $1000\,\text{kPa}$ for Young's modulus. Plane stress conditions are assumed. ANSYS 9 and 11 was used for the finite element analysis, with eight noded isoparametric quadrilateral elements (Q8). The crack tip is modelled by collapsed Q8 quarter-point elements [Barsoum 1976].

Example 1: Determination of $r_{\max}$ using finite element analysis. The primary purpose of this example is to demonstrate the basic procedure for determination reasonably accurate values of $r_{\max}$ of a configuration. The procedure is described using the edge cracked plates subjected to uniform tensile stress as shown in Figure 3(a) with $a/w = 0.5$ and $h/w = 0.3, 0.5, 1.0$. A Poisson's ratio of $\nu = 1/3$ and an applied stress value of $1.0\,\text{MPa}$ are assumed for all three configurations. For $\nu = 1/3$, the values of θ and α both equal 60°; see (9) and (10). To study the effect of mesh refinement on the convergence of $r_{\max}$, three meshes of increasing density are considered for each configuration; see Figures 4–6.

The meshes are designed so that nodes of several elements are made to lie along the radial line which makes an angle of θ with the horizontal (60° for $\nu = 1/3$). This line begins at the crack-tip and terminates at the outer boundaries of the cracked plate. It should be noted that according to [Dally and Sanford 1987], a single strain gage is required to be placed at an appropriate location on this line in the direction of α in order to measure the linear strain $\varepsilon_{x'x'}$ (Figure 2). We call this the *gage-line*. The computed strains in the global coordinates (using the finite element analysis) along the gage line are then transformed to
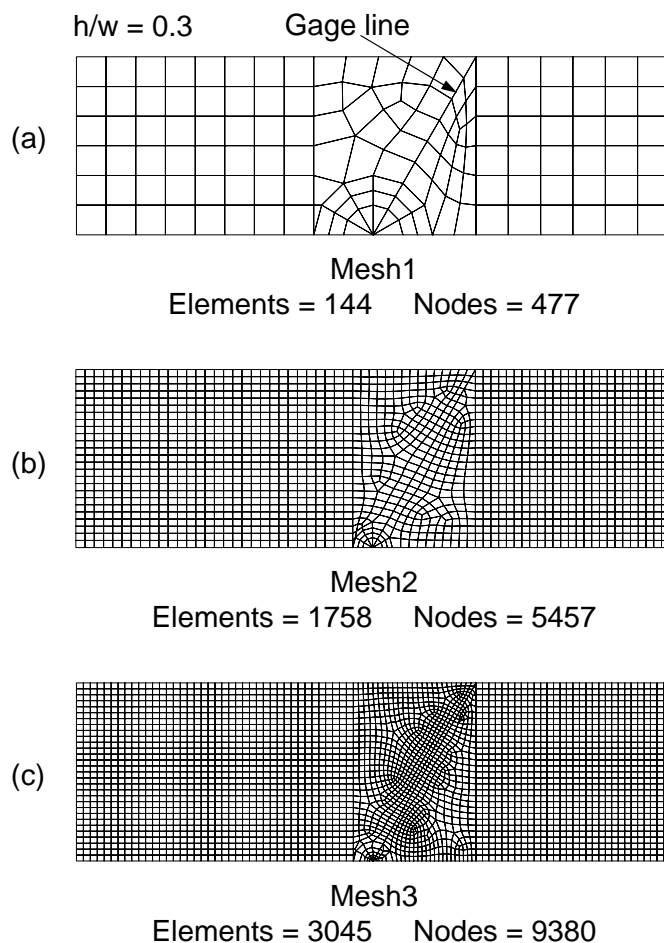
Figure 4. Different finite element meshes used for convergence study of $r_{\max}$ of $a/w = 0.5$ and $h/w = 0.3$ edge cracked configuration.

the linear strain $\varepsilon_{x'x'}$ in the direction defined by $\alpha = 60°$; see (8). The radial distances (r) of each of the nodes on the gage line from the crack tip are then computed.

Figures 7 and 8 show plots of $\log \varepsilon_{x'x'}$ as a function of $\log r$, computed from each of the three meshes of $h/w = 0.3, 0.5, 1.0$. The crack tip point is not plotted, as the radius of this point is zero. It is interesting to notice from all the plots of Figures 7 and 8 that the linear trend in logarithmic axes distinctly exists until a radial distance. This trend can be clearly observed in all the three meshes of each of the h/w value. The results presented in Figures 7 and 8 also strongly confirm that the selection of coefficients (A_0, B_0, A_1) that are retained in the three-parameter strain series (8) appears to be valid. The end point of the linear portion of the plots (Figures 7 and 8) clearly indicates the terminal point of validity of the three-parameter strain series (8) or $r_{\max}$ in accordance with the single gage approach of [Dally and Sanford 1987] — see (13).

Since the $\varepsilon_{x'x'}$ values are obtained numerically, we see that the slope of a line segment between any two data points (Figures 7 and 8) belonging to the fine meshes is close to the theoretical value of -0.5 (13) —
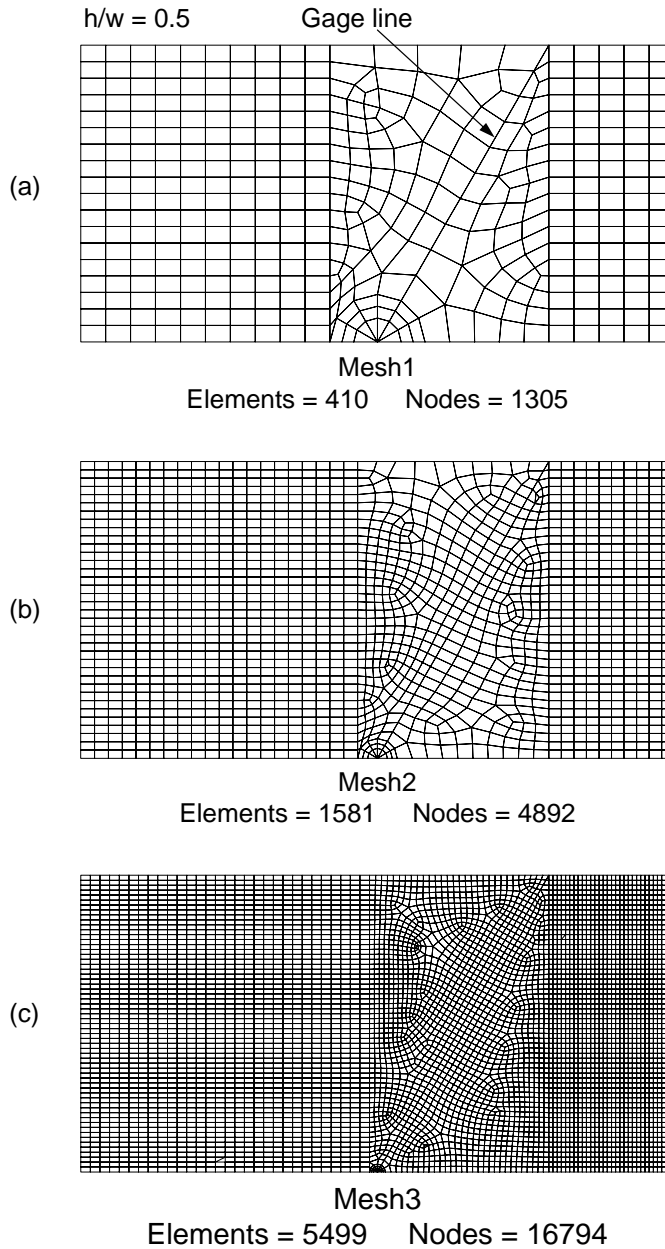
Figure 5. Different finite element meshes used for convergence study of r_{max} of $a/w =$ 0.5 and $h/w = 0.5$ edge cracked configuration.

more so than for coarse meshes. A line of slope -0.5 is included in Figures 7 and 8 for comparison. Thus a reasonably accurate value of r_{max} can be estimated as the terminal point of the straight line portion on logarithmic axes. These terminal points are also indicated in Figures 7 and 8. The precise value of r_{max} is not essential for locating the strain gages, because they do not have to be placed precisely at r_{max}.
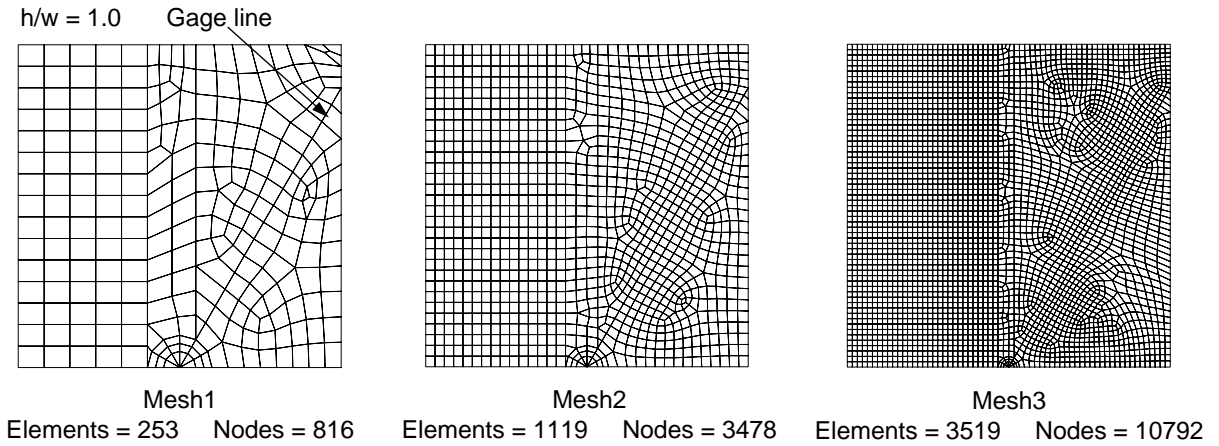
Figure 6. Different finite element meshes used for convergence study of $r_{\max}$ of $a/w = 0.5$ and $h/w = 1.0$ edge cracked configuration.
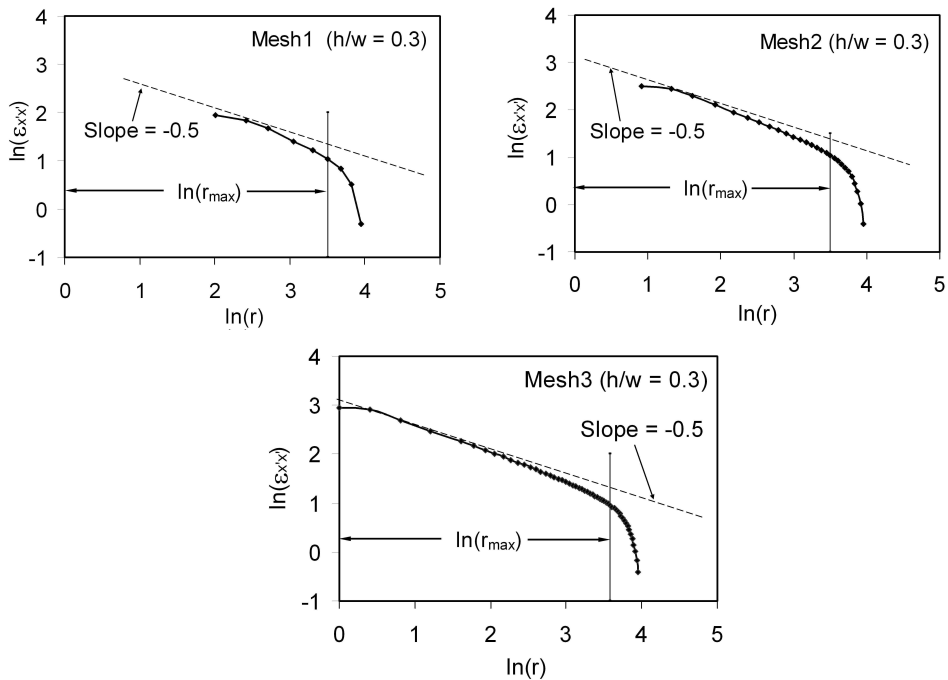
Figure 7. Linear and nonlinear variation of $\ln(\varepsilon_{x'x'})$ with $\ln(r)$ along the gage line for the sequence of meshes ($a/w = 0.5$, $h/w = 0.3$, $v = 1/3$) shown in Figure 4.

Table 1 presents the values of $r_{\max}$ obtained from the graphs of Figures 7 and 8. The convergence of $\log(\varepsilon_{x'x'})$ along the gage line for increasing mesh density of all the configurations is shown in Figure 9 along with the line of slope -0.5. No significant improvement of $\log \varepsilon_{x'x'}$ values along the gage line can be noticed in Figure 9 for any configuration. As a result no noticeable differences in values of $r_{\max}$ can be
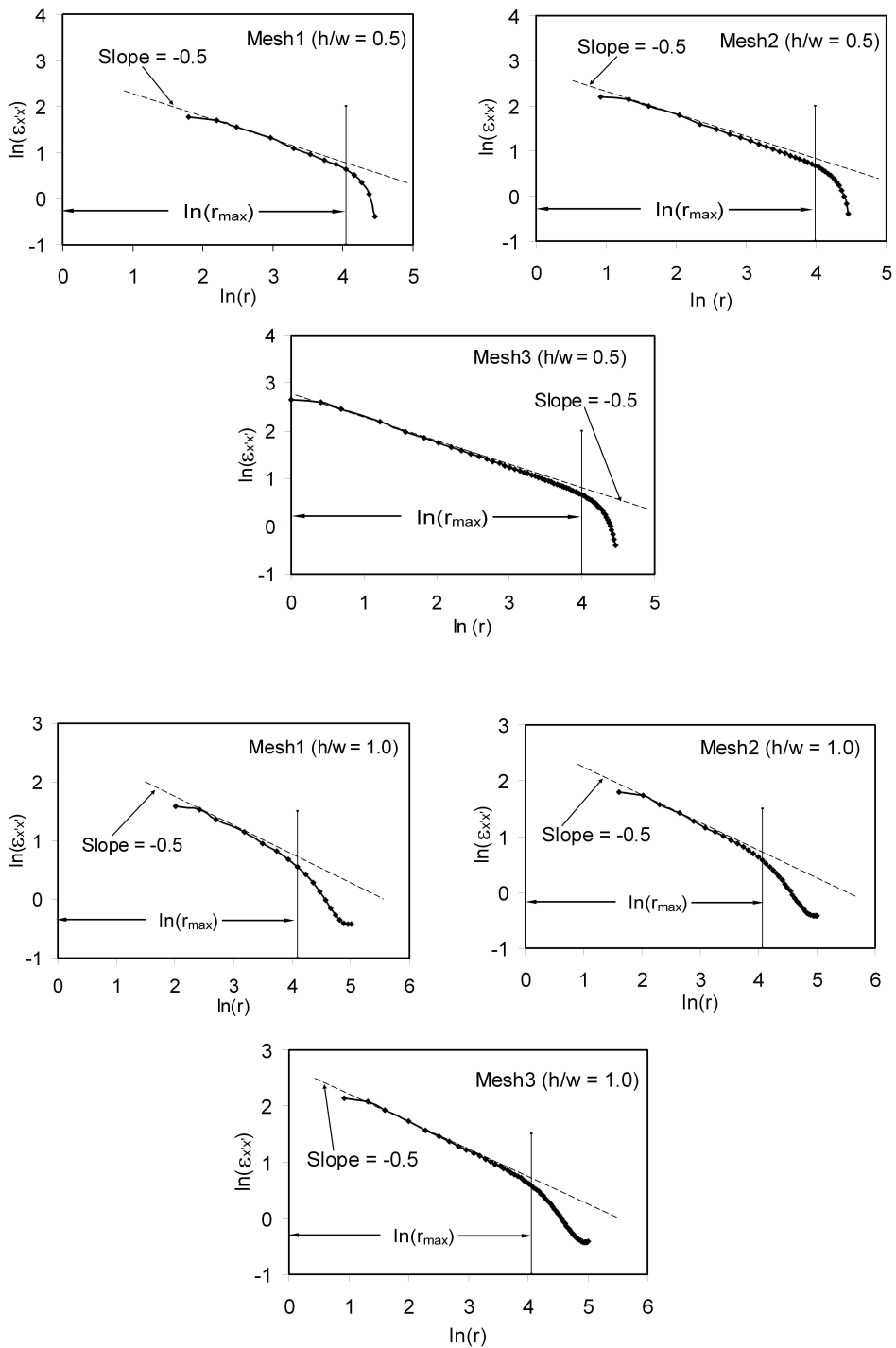
Figure 8. Variation of $\ln(\varepsilon_{x'x'})$ with $\ln(r)$ along the gage line for the sequence of meshes $(a/w = 0.5, h/w = 0.5, \nu = 1/3)$ of Figure 5 (top three graphs) and the sequence of meshes $(a/w = 0.5, h/w = 1.0, \nu = 1/3)$ of Figure 6 (bottom graphs).
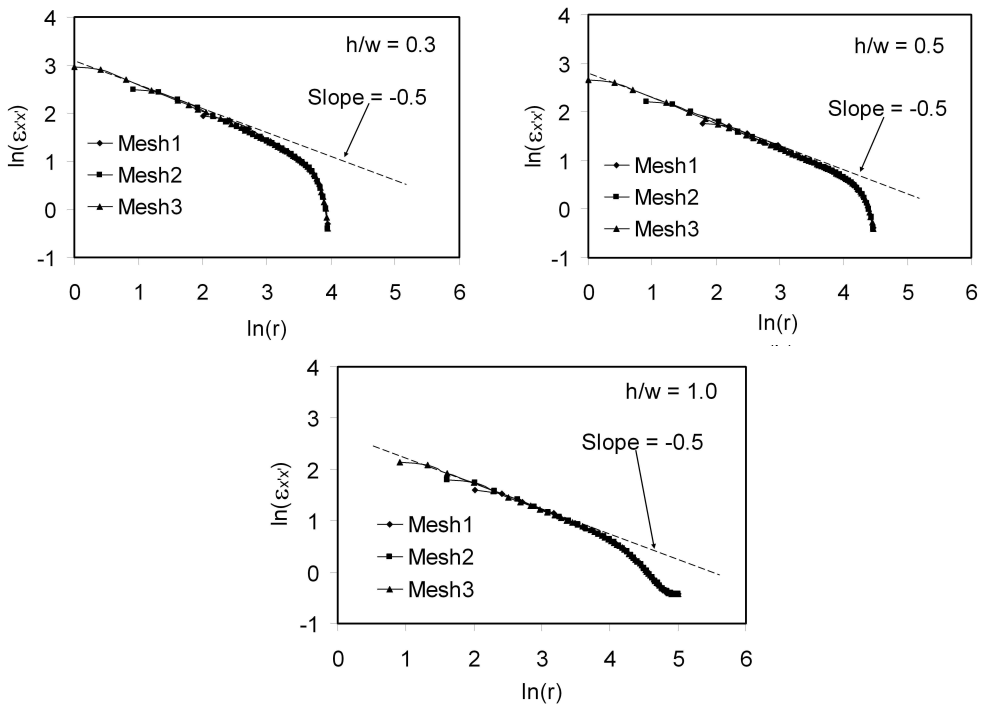
Figure 9. Convergence of $r_{\max}$ with the mesh refinement of various edge cracked configurations, with $a/w = 0.5$.

observed as the meshes are refined. The results presented in Figure 9 and Table 1 lead to the conclusion that a single finite element mesh with a reasonable density appropriate to the given configuration is sufficient to provide a fairly accurate value of $r_{\max}$.

Next, in order to demonstrate the effect of Poisson's ratio on values of $r_{\max}$, two edge cracked plates having $a/w = 0.5$, $h/w = 0.3$ and having different Poisson's ratios ($\nu = 0.25$ and 0.3) is considered. Figure 10 shows corresponding finite element mesh of the domain having $\nu = 0.25$ for determination of $r_{\max}$. It can be noticed from (8) and (10) that, not only the values of θ and α would change because of change in the Poisson's ratio but also the magnitude of $\varepsilon_{x'x'}$ at every point on the gage line. Corresponding to $\nu = 0.25$ the values of θ and α are 73.74° and 63.43° respectively — see (9) and (10). Figure 11 shows the variation of $\varepsilon_{x'x'}$ (and hence $r_{\max}$) with Poisson's ratio on the logarithmic axes. The results obtained

	$h/w = 0.3$		$h/w = 0.5$		$h/w = 1.0$	
	$r_{\max}$ (mm)	$r_{\max}/w$	$r_{\max}$ (mm)	$r_{\max}/w$	$r_{\max}$ (mm)	$r_{\max}/w$
Mesh1	33.5	0.22	56.8	0.38	60.0	0.40
Mesh2	33.2	0.22	54.0	0.36	58.0	0.39
Mesh3	36.0	0.24	55.6	0.37	58.2	0.39

Table 1. Convergence of $r_{\max}$ with the mesh refinement of different edge cracked specimens ($a/w = 0.5$).
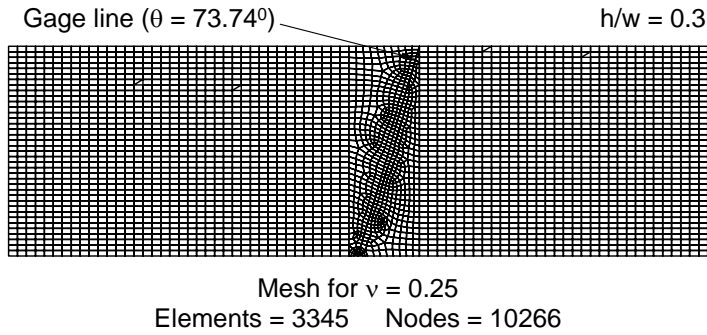
Figure 10. A fine mesh finite idealization of the edge cracked configuration with $a/w = 0.5$, $h/w = 0.3$ (Figure 3) and Poisson's ratio $= 0.25$.
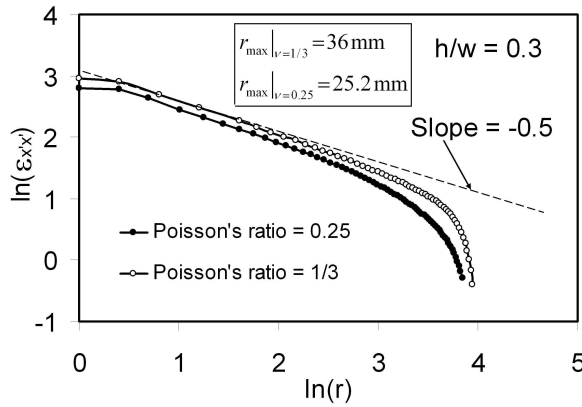
Figure 11. Variation of r_{max} with the Poisson's ratio.

using the meshes in Figure 4(c) and Figure 10 are employed to plot the graphs of Figure 11. These results appear to show that higher is the value of ν, the larger is r_{max}, indicating that the finite element analysis of a single mesh of the experimental configuration with exact material properties can aid in obtaining reasonably accurate values of r_{max} graphically.

Example 2: Dependence of the extent of the three parameter zone on the crack length. The goal of this example is to demonstrate effect of the crack length on the value of r_{max}. For this purpose the problem of edge cracked plate having $h/w = 1.0$ and different values of $a/w = 0.5, 0.6, 0.7, 0.8$ subjected to uniform tensile stress (Figure 3(a)) is chosen. A Poisson's ratio of $\nu = 1/3$ and an applied stress value of 1.0 MPa are assumed for all the configurations. Only one finite element mesh (fine mesh) of each of the above configurations is employed in the analysis. Figure 12 shows fine meshes of the edge cracked plates with $a/w = 0.6, 0.7, 0.8$. The third mesh in Figure 6 is employed for $a/w = 0.5$.

Figure 13 shows the variation of $\log \varepsilon_{x'x'}$ with $\log r$ on the gage line of each configuration. It also shows the extent of validity of the three-parameter zone, that is, the value r_{max} of the edge cracked plate as the crack length is increased. These values of r_{max} are shown in Table 2. The results in this figure and table indicate that the extent of three-parameter zone decreases as the crack length increases. In other words,
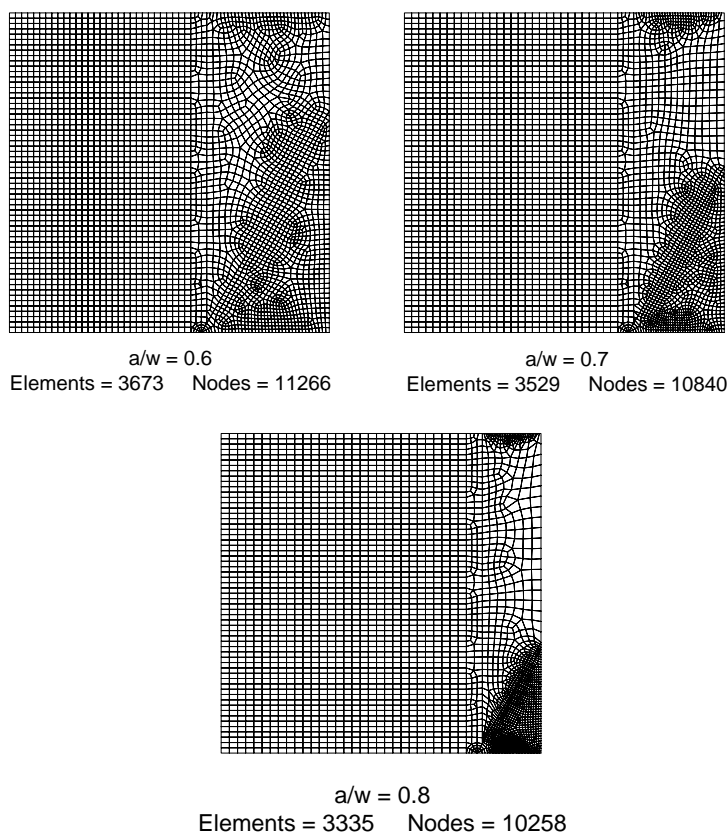
Figure 12. Finite element meshes of edge cracked plates with increasing crack length ($h/w = 1.0$).

as the cracked domain becomes more finite, the $r_{\max}$ value decreases. The same observation can be made from the results of Table 1, and a similar conclusion was reached by Chona et al. [1983] using photoelastic studies, applied to the singular solutions in an effort to identify the singularity-dominated zone.

a/w	$r_{\max}$ (mm)	$r_{\max}/w$
0.5	58.2	0.39
0.6	35.7	0.24
0.7	27.7	0.18
0.8	15.1	0.10

Table 2. Variation of $r_{\max}$ with $a/w (h/w = 1.0)$.
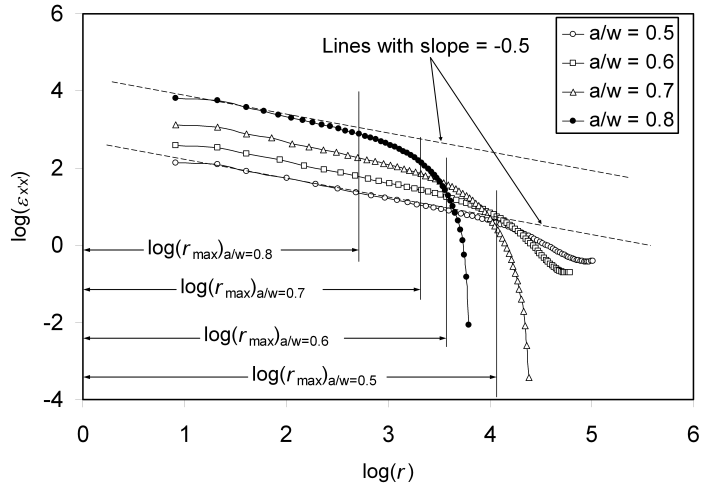
Figure 13. Dependence of the extent of the three-parameter zone on length of the crack.

Conclusions

The present work outlines the theoretical basis for determination of r_{max} in accordance with the single strain gage method of [Dally and Sanford 1987] which in turn can be used to justify the selected radial location of the gages. The present work attempts to propose a method of finding the reasonably accurate r_{max} of a given experimental specimen using the finite element analysis. The numerical examples clearly demonstrate that reasonably accurate values of r_{max} can be determined using the proposed approach. The dependence of r_{max} on the geometry of the specimen and Poisson's ratio is demonstrated.

Acknowledgements

References

[Baik et al. 1995] M. C. Baik, S. H. Choi, J. S. Hawong, and J. D. Kwon, "Determination of stress-intensity factors by the method of caustics in anisotropic materials", *Exp. Mech.* **35**:2 (1995), 137–143.

[Barsoum 1976] R. S. Barsoum, "On the use of isoparametric finite elements in linear fracture mechanics", *Int. J. Numer. Methods Eng.* **10**:1 (1976), 25–37.

[Berger and Dally 1988] J. R. Berger and J. W. Dally, "An overdeterministic approach for measuring K_I using strain gages", *Exp. Mech.* **28**:2 (1988), 142–145.

[Bonesteel et al. 1978] R. M. Bonesteel, D. E. Piper, and A. T. Davinroy, "Compliance and K_I calibration of double cantilever beam (DCB) specimens", *Eng. Fract. Mech.* **10**:2 (1978), 425–428.

[Chan and Chow 1979] W. Y. Chan and C. L. Chow, "Photoelastic stress intensity determination of circular-sector crack in rectangular plate", in *Papers: SESA Spring Meeting* (San Francisco, 1979), Society for Experimental Stress Analysis, Westport, CT, 1979.

[Chona et al. 1983] R. Chona, G. R. Irwin, and R. J. Sanford, "The influence of specimen size and shape on the singularity-dominated zone", pp. 1–23 in *Fracture mechanics: fourteenth symposium, I: Theory and analysis* (Los Angeles, 1981), edited by J. C. Lewis and G. Sines, ASTM Special Technical Publication **791**, ASTM, Philadelphia, 1983.

[Dally and Berger 1993] J. W. Dally and J. R. Berger, "The role of the electrical resistance strain gauge in fracture research", pp. 1–39 in *Experimental techniques in fracture mechanics*, edited by J. S. Epstein, Wiley VCH, New York, 1993.

[Dally and Sanford 1987] J. W. Dally and R. J. Sanford, "Strain-gage methods for measuring the opening-mode stress-intensity factor, K_I", *Exp. Mech.* **27**:4 (1987), 381–388.

[Gdoutos and Theocaris 1978] E. E. Gdoutos and P. S. Theocaris, "A photoelastic determination of mixed-mode stress-intensity factors", *Exp. Mech.* **18**:3 (1978), 87–96.

[Hyde and Warrior 1990] T. H. Hyde and N. A. Warrior, "An improved method for determination of photoelastic stress intensity factors using the Westergaard stress function", *Int. J. Mech. Sci.* **32**:3 (1990), 265–273.

[Kazemi et al. 1989] A. D. A. Kazemi, N. S. Murthy, and N. G. Raju, "Stress intensity factor determination of radially cracked circular rings subjected to tension using photoelastic technique", *Eng. Fract. Mech.* **32**:3 (1989), 403–408.

[Konsta-Gdoutos 1996] M. Konsta-Gdoutos, "Limitations in mixed-mode stress intensity factor evaluation by the method of caustics", *Eng. Fract. Mech.* **55**:3 (1996), 371–382.

[Kuang and Chen 1995] J. H. Kuang and L. S. Chen, "A single strain gage method for K_I measurement", *Eng. Fract. Mech.* **51**:5 (1995), 871–878.

[Lee and Hong 1993] O. S. Lee and S. K. Hong, "Determination of stress intensity factors and J-integrals using the method of caustics", *Eng. Fract. Mech.* **44**:6 (1993), 981–989.

[Marloff et al. 1971] R. H. Marloff, M. M. Leven, T. N. Ringler, and R. L. Johnson, "Photoelastic determination of stress-intensity factors", *Exp. Mech.* **11**:12 (1971), 529–539.

[Newman 1981] J. C. Newman, Jr., "Stress-intensity factors and crack-opening displacements for round compact specimens", *Int. J. Fract.* **17**:6 (1981), 567–578.

[Nurse et al. 1994] A. D. Nurse, E. W. O'Brien, and E. A. Patterson, "Stress intensity factors for cracks at fastener holes", *Fatigue Fract. Eng. Mater. Struct.* **17**:7 (1994), 791–799.

[Rosakis and Ravi-Chandar 1986] A. J. Rosakis and K. Ravi-Chandar, "On crack-tip stress state: an experimental evaluation of three-dimensional effects", *Int. J. Solids Struct.* **22**:2 (1986), 121–134.

[Sanford 1979] R. J. Sanford, "A critical re-examination of the Westergaard method for solving opening-mode crack problems", *Mech. Res. Commun.* **6**:5 (1979), 289–294.

[Sanford 2003] R. J. Sanford, *Principles of fracture mechanics*, Prentice Hall, Upper Saddle River, NJ, 2003.

[Swamy et al. 2008] S. Swamy, M. V. Srikanth, K. S. R. K. Murthy, and P. S. Robi, "Determination of mode I stress intensity factors of complex configurations using strain gages", *J. Mech. Mater. Struct.* **3**:7 (2008), 1239–1255.

[Theocaris 1970] P. S. Theocaris, "Local yielding around a crack tip in Plexiglas", *J. Appl. Mech.* (*ASME*) **37** (1970), 409–415.

[Wei and Zhao 1997] J. Wei and J. H. Zhao, "A two-strain-gage technique for determining mode I stress-intensity factor", *Theor. Appl. Fract. Mech.* **28**:2 (1997), 135–140.

B. KAUSHIK: kauaug18@gmail.com
Tata Motors Limited, Pune, India

K. S. R. K. MURTHY: ksrkm@iitg.ernet.in
Department of Mechanical Engineering, Indian Institute of Technology Guwahati, Guwahati - 781 039, Assam, India

P. S. ROBI: psr@iitg.ernet.in
Department of Aerospace Engineering, Indian Institute of Space Science and Technology, Thiruvananthapuram - 695 022, India

MICROSTRUCTURE-BASED MODELING OF ELASTIC FUNCTIONALLY GRADED MATERIALS: ONE-DIMENSIONAL CASE

ZAHRA SHARIF-KHODAEI AND JAN ZEMAN

Functionally graded materials (FGMs) are two-phase composites with continuously changing microstructure adapted to performance requirements. Traditionally, the overall behavior of FGMs has been determined using local averaging techniques or a given smooth variation of material properties. Although these models are computationally efficient, their validity and accuracy remain questionable, since a link with the underlying microstructure (including its randomness) is not clear. In this paper, we propose a numerical modeling strategy for the linear elastic analysis of FGMs systematically based on a realistic microstructural model. The overall response of FGMs is addressed in the framework of stochastic Hashin–Shtrikman variational principles. To allow for the analysis of finite bodies, recently introduced discretization schemes based on the finite element method and the boundary element method are employed to obtain statistics of local fields. Representative numerical examples are presented to compare the performance and limitations of both schemes. To gain insight into similarities and differences between these methods and to minimize technicalities, the analysis is performed in the one-dimensional setting.

1. Introduction

Generally speaking, the ultimate goal of every design is a product which fully utilizes the properties of the materials used in its construction. This philosophy, in the larger context, naturally leads to the appearance of multiphase composites with microstructure adapted to operation conditions [Petrtýl et al. 1996; Bendsøe and Sigmund 2004; Ray et al. 2005]. Functionally graded materials (FGMs) present one important man-made class of such material systems. Since their introduction in 1984 in Japan as barrier materials for high-temperature components, FGMs have proved to be an attractive choice for numerous applications such as wear resistant coatings, optical fibers, electrical razor blades and biomedical tools [Neubrand and Rodel 1997; Uemura 2003]. To provide a concrete example, consider a microstructure of Al_2O_3/Y-ZrO_2 ceramics (see Figure 1) engineered for the production of all-ceramic hip bearings. In this case, controlled composition and porosity allow us to achieve better long-term performance and hence lower clinical risks when compared to traditional metallic materials [Anné et al. 2006].

As typical of all composites, the analysis of FGMs is complicated by the fact that the explicit discrete modeling of the material microstructure results in a problem which is intractable due to its huge number of degrees of freedom (DOFs) and/or its intrinsic randomness. Models with given smoothly varying material data are often employed as the most straightforward answer to this obstacle. When the spatial nonhomogeneity is assumed to follow a sufficiently simple form, this premise opens the route to very
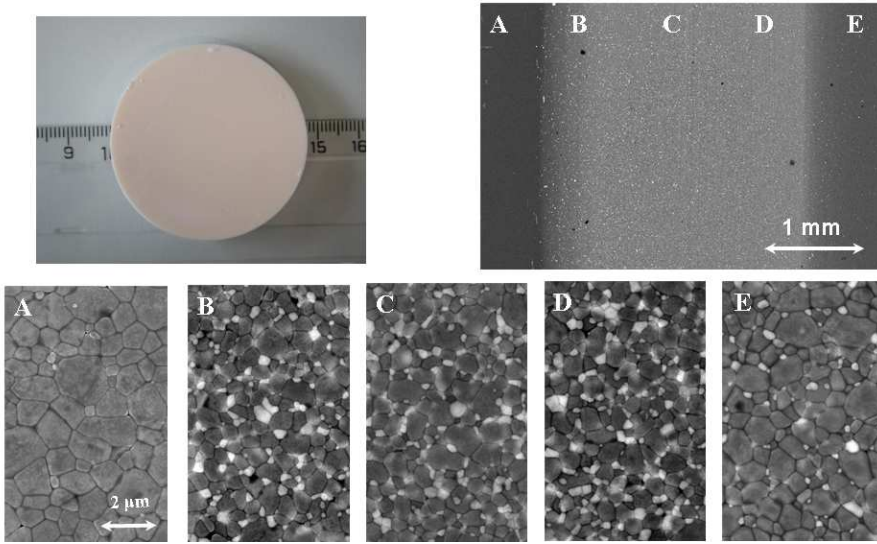
Figure 1. Graded microstructure of Al_2O_3/Y-ZrO_2 ceramics. (Courtesy of J. Vleugels, K.U. Leuven.)

efficient numerical schemes, such as specialized finite elements [Santare and Lambros 2000], boundary element techniques [Sutradhar and Paulino 2004], meshless methods [Ching and Chen 2007], and local integral equations [Sládek et al. 2005]. Thanks to their simplicity, these methods can be rather easily generalized to more complex issues such as coupled thermal-mechanical problems [Noda 1999] or crack propagation [Kandula et al. 2005]. Although this approach is very appealing from the computational point of view, its validity remains rather questionable as it contains no direct link to the underlying heterogeneous microstructure.

One possibility in establishing such a connection is to assert that the FGM locally behaves as a homogeneous composite characterized by a given volume fraction distribution and then use well established local effective media theories; see [Milton 2002; Böhm 2008] for more details. Local averaging techniques have attracted considerable attention due to their simplicity comparable to the previous class of models; see [Markworth et al. 1995; Cho and Ha 2001] for an overview and comparison of various local micromechanical models in the context of FGMs. An exemplary illustration of the capabilities of this modeling paradigm is the work [Goupee and Vel 2006] which provides an efficient algorithm for FGM composition optimization when taking into account coupled thermomechanical effects. Still, despite a substantial improvement in the physical relevance of the model, local averaging methods may lead to inaccurate results. This was demonstrated by systematic studies [Reiter et al. 1997; Reiter and Dvorak 1998], which clearly show that the local averaging technique needs to be adapted to the detailed character of the microstructure in a neighborhood of the point under consideration. When considering the local averaging techniques, however, such information is evidently not available as all the microstructural data was lumped into volume fractions only.

Another appealing approach to FGM modeling is an adaptive discrete modeling of the structure. In order to avoid the fully detailed problem, a simplified model based on, for example, local averaging

techniques is solved first. Then, in regions where the influence of the discreteness of the microstructure is most pronounced, the microstructure with all its details is recovered to obtain an accurate solution. Such a modeling strategy has been, for example, adopted in [Grujicic and Zhang 1998] when using the Voronoi cell finite element method, introduced by Ghosh et al. [1995] or more recently in [Vemaganti and Deshmukh 2006], in the framework of goal oriented modeling. Without a doubt, this approach yields the most accurate results for a given distribution of phases. However, its extension to include the inevitable randomness of the microstructure seems to be an open problem.

The systematic treatment of FGMs as random, statistically nonhomogeneous composites offers, on the other hand, a possibility to apply the machinery of statistical continuum mechanics [Beran 1968; Torquato 2001]. In this framework, overall response of the media is interpreted using the ensemble, rather then spatial, averages of the involved quantities. The first class of methods stems from the description of the material composition by a nonstationary random field. This approach was pioneered by Ferrante and Graham-Brady [2005] and further refined in [Rahman and Chakraborty 2007], where the random field description was applied to the volume fractions of the involved phases and the overall statistics were obtained using local averaging methods. Such a strategy, however, inevitably leads to the same difficulties as in the case of deterministic analysis with a given variation of volume fractions. Alternative methods exploit the tools of mechanics of heterogeneous media. This gives rise to a correct treatment of nonlocal effects when combined with appropriate techniques for estimating the statistics of local fields. Examples of FGM oriented studies include the work of Buryachenko and Rammerstorfer [2001] who employ the multiparticle effective field method or the study by Luciano and Willis [2004] based on the Hashin–Shtrikman energy principles; see also [Buryachenko 2007] for a comprehensive list of references in this field. Both works, however, being analytically based, concentrate on deriving explicit constitutive equations for FGMs and therefore work with infinite bodies neglecting the finite size of the microstructure.

The goal of this paper is to make the first step in formulating a numerical model which is free of the above discussed limitations. The microstructural description is systematically derived from a fully penetrable sphere model introduced by Quintanilla and Torquato [1997], which is briefly reviewed in Section 2. The statistics of local fields then follow from reformulation of the Hashin–Shtrikman (H–S) variational principles introduced, for example, in [Willis 1977; Willis 1981] and summarized in the current context in Section 3 together with the Galerkin scheme allowing us to treat general bodies proposed by Luciano and Willis [2005] or Procházka and Šejnoha [2003]. Section 4 covers the application of the finite element method (FEM) following [Luciano and Willis 2005; Luciano and Willis 2006] and the boundary element method (BEM) in the spirit of [Procházka and Šejnoha 2003]. Finally, based on results of a parametric study executed in Section 5, the comparison of both numerical schemes when applied to FGM modeling is performed in Section 6 together with a discussion of future improvements of the model. In order to make the presentation self-contained and to minimize technicalities, the attention is restricted to an one-dimensional elasticity problem (or, equivalently, to a simple laminate subject to body forces varying in one direction [Luciano and Willis 2001]).

In the following text, we adopt the matrix notation commonly used in the finite element literature. Hence, a, $\boldsymbol{a}$ and $\mathbf{A}$ denote a scalar quantity, a vector (column matrix), and a general matrix, respectively. Other symbols and abbreviations are introduced in the text as needed.

2. Microstructural model

As already indicated, the morphological description adopted in this work is the one-dimensional case of a microstructural model studied in [Quintanilla and Torquato 1997]. A particular realization can be depicted as a collection of N rods of length ℓ distributed within a structure of length L, see Figure 2. The position of the i-th rod is specified by the x coordinate of its *reference point* x_i, which in our case coincides with the midpoint of a rod.
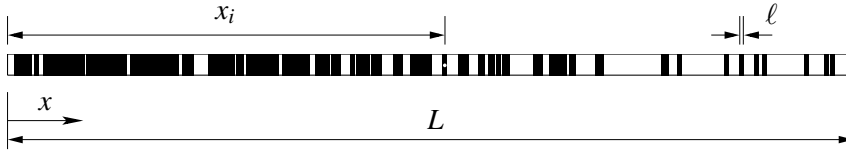
Figure 2. Example of microstructural model realization.

The microstructure gradation is prescribed by an *intensity function* $\rho(x)$, with the product $\rho(x)\,dx$ giving the expected number of reference points in an infinitesimal neighborhood around x. Using the theory of general Poisson processes, the probability of finding exactly m points located in a finite-sized interval I is given by Quintanilla and Torquato [1997]

$$P_m(I) = \frac{\mu_\rho(I)^m}{m!} \exp\bigl(-\mu_\rho(I)\bigr), \quad \text{with} \quad \mu_\rho(I) = \int_I \rho(x)\,dx. \tag{1}$$

Further, to provide a suitable framework for the description of the microstructure related to the model, we attach the symbol α to a particular microstructure realization (see Figure 2) from a sample space $\mathbb{S}$ endowed with a probability measure p. Then, the ensemble average of a random function $f(x, \alpha)$ is defined as[1]

$$\langle f \rangle(x) = \int_{\mathbb{S}} f(x, \alpha) p(\alpha)\,d\alpha.$$

Now, interpret Figure 2 as a distribution of *white* and *black phases*. For a given configuration α, the distribution of a phase r is described by the characteristic function $\chi_r(x; \alpha)$ as

$$\chi_r(x; \alpha) = \begin{cases} 1 \text{ if } x \text{ is located in phase } r, \\ 0 \text{ otherwise,} \end{cases} \tag{2}$$

where $r = 1$ is reserved for the white phase (matrix) while $r = 2$ denotes the black phase (rod). The elementary statistical characterization of the model is provided by the *one-point probability function* S_r, defined as $S_r(x) = \langle \chi_r \rangle(x)$, giving the probability of finding a point x included in the phase r. Recognizing that the probability of locating x in the white phase coincides with the probability that the interval $I(x) = [x - \ell/2, x + \ell/2]$ will not be occupied by any reference point and using (1), we obtain

$$S_1(x) = P_0\bigl(I(x)\bigr) = \exp\left(-\int_{x-\ell/2}^{x+\ell/2} \rho(t)\,dt\right).$$

---

[1]To simplify the exposition, we introduce the following notation: for a real-valued *random* function $f(x, \alpha) : \mathbb{R} \times \mathbb{S} \to \mathbb{R}$, by writing $f(x; \alpha)$ we mean a *deterministic* function of $x \in \mathbb{R}$ related to a given *fixed* realization (that is, $f(x; \alpha) : \mathbb{R} \to \mathbb{R}$). In other words, $f(x; \alpha) := f(x, \beta)|_{\beta=\alpha}$.

The one-point probability function $S_2(x)$ follows from the identity

$$S_1(x) + S_2(x) = 1, \tag{3}$$

which is a direct consequence of the adopted definition of the characteristic function; recall (2).

By analogy, we can introduce the *two-point* probability function S_{rs} as

$$S_{rs}(x, y) = \int_{\mathbb{S}} \chi_r(x, \alpha) \chi_s(y, \alpha) p(\alpha) \, d\alpha,$$

quantifying the probability that a point x will be located in phase r while y stays in the phase s. For $r = s = 1$, the descriptor coincides with the probability that the union of intervals $I(x)$ and $I(y)$ will not be occupied by a reference point, yielding

$$S_{11}(x, y) = P_0\big(I(x) \cup I(y)\big). \tag{4}$$

The remaining functions S_{rs} can be directly expressed from S_{11} by exploiting identity (3). In particular:

$$S_{12}(x, y) = S_1(x) - S_{11}(x, y),$$
$$S_{21}(x, y) = S_1(y) - S_{11}(x, y),$$
$$S_{22}(x, y) = 1 - S_1(x) - S_1(y) + S_{11}(x, y).$$

Finally, to provide a concrete example, consider a piecewise linear intensity function

$$\rho(x) = \begin{cases} \rho_a, & 0 \leq x \leq a, \\ \rho_a + k_\rho(x - a), & a < x \leq b, \\ \rho_b, & b < x \leq L, \\ 0, & \text{otherwise}, \end{cases}$$

where $k_\rho = (\rho_b - \rho_a)/(b - a)$. The corresponding one- and two-point probability functions, evaluated using an adaptive Simpson quadrature [Gander and Gautschi 2000], are shown in Figure 3. Obviously,
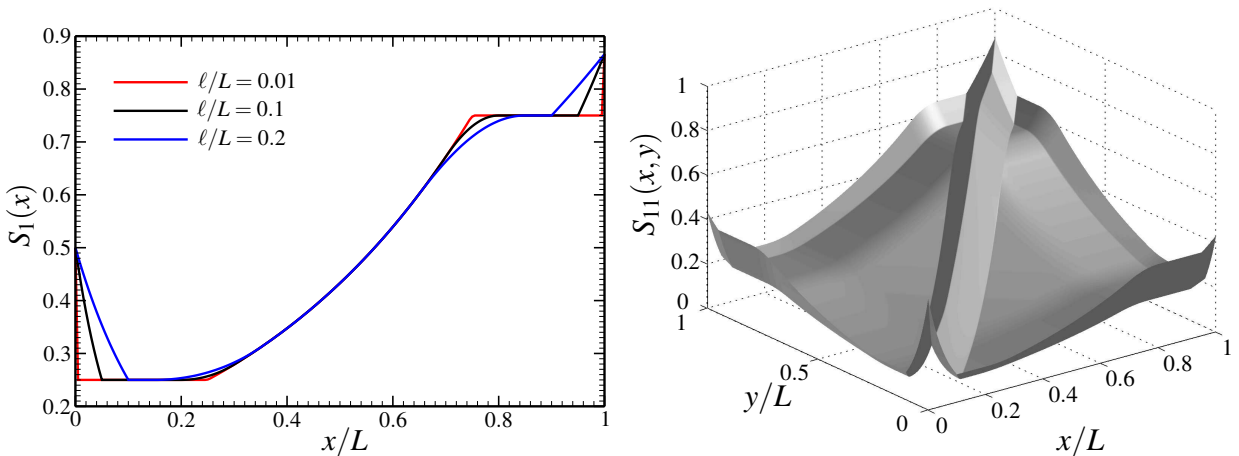
Figure 3. One-point (left) and two-point (right) probability functions for $a = 0.25L$, $b = 0.75L$, $L = 1$ m, $\rho_a = -\log(0.25/\ell)$ and $\rho_b = -\log(0.75/\ell)$. On the right, $\ell = 0.1$.

the shape of the one-point probability function directly follows from the intensity profile (up to some boundary effects due to the extension of ρ by zero outside of Ω and smoothing phenomena with the length scale ℓ demonstrating the "geometrical" size effect present in the model). The two-point probability function then contains further details of the distribution of individual constituents.

3. Hashin–Shtrikman variational principles

The geometrical description introduced provides a solid basis for the formulation of a stochastic model of one-dimensional binary functionally graded bodies. We will concentrate on the simplest case of linear elasticity with deterministic properties of single components.

3.1. *Problem statement.* Consider a bar of cross-sectional area $1\,\mathrm{m}^2$, represented by the interval $\Omega = (0, L)$ with the boundaries $\partial\Omega = \{0, L\}$, fixed at $\partial\Omega^u$, subject to a body force $b(x)$ and tractions $\bar{t}$ at $\partial\Omega^t$ (see Figure 4). For a given realization α, the displacement field $u(x; \alpha)$ follows from the energy minimization problem $u(x; \alpha) = \arg\min_{v(x)\in\mathbb{V}} \Pi(v(x); \alpha)$, where $\arg\min_{x\in X} f(x)$ denotes the minimizer of f on X, $\mathbb{V}$ is the *realization-independent* set of kinematically admissible displacements, v is a test displacement field, and the energy functional Π is defined as

$$\Pi(v(x); \alpha) = \tfrac{1}{2}\int_\Omega \varepsilon(v(x))E(x; \alpha)\varepsilon(v(x))\,\mathrm{d}x - \int_\Omega v(x)b(x)\,\mathrm{d}x - \big(v(x)\bar{t}(x)\big)\Big|_{\partial\Omega^t},$$

with the strain field $\varepsilon(v(x)) = \dfrac{\mathrm{d}v}{\mathrm{d}x}(x)$ and the Young modulus E in the form

$$E(x; \alpha) = \chi_1(x; \alpha)E_1 + \chi_2(x; \alpha)E_2, \tag{5}$$

where E_i denotes the deterministic Young modulus of the i-th phase.

Now, given the probability distribution $p(\alpha)$, the ensemble average of displacement fields follows from the variational problem [Luciano and Willis 2005]:

$$\langle u\rangle(x) = \int_{\mathbb{S}} \left(\arg\min_{v(x, \alpha)\in\mathbb{V}\times\mathbb{S}} \Pi(v(x), \alpha)\right) p(\alpha)\,\mathrm{d}\alpha. \tag{6}$$

In theory, the previous relation fully specifies the distribution of displacement fields. The exact specification of the set $\mathbb{S}$ is, however, very complex and the probability distribution $p(\alpha)$ is generally not known. Therefore, the solution needs to be based on partial geometrical data such as the one- and two-point probability functions introduced in Section 2.

3.2. *Hashin–Shtrikman decomposition.* Following the seminal ideas of Hashin and Shtrikman [1962] and Willis [1977], the solution of the stochastic problem is sought as a superposition of two auxiliary problems, each characterized by constant material data E^0.
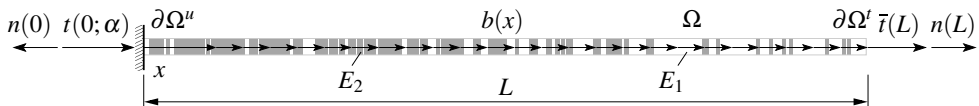
Figure 4. The one-dimensional elasticity problem associated with realization α.
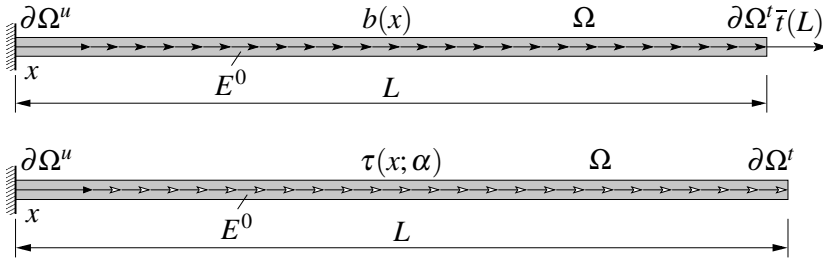
Figure 5. Problem decomposition: top, *deterministic* reference case; bottom, *stochastic* polarization problem.

In the first reference case (Figure 5, top), the homogeneous structure is subject to the body force b and the boundary tractions $\bar{t}$. The second, the polarization problem shown in Figure 5, bottom, corresponds to a homogeneous body loaded by polarization stress τ arising from the stress equivalence conditions $\sigma(x; \alpha) = E(x; \alpha)\varepsilon(x; \alpha) = E^0\varepsilon(x; \alpha) + \tau(x; \alpha)$. The unknown polarization stress now becomes a new variable to be determined as the stationary point of the two-field Hashin–Shtrikman–Willis functional (see [Willis 1977; Procházka and Šejnoha 2004] and [Bittnar and Šejnoha 1996, Chapter 1.8], for example)

$$\big(u(x; \alpha), \tau(x; \alpha)\big) = \arg \min_{v(x) \in \mathbb{V}} \operatorname*{stat}_{\theta(x; \alpha) \in \mathbb{T}(\alpha)} U\big(v(x), \theta(x; \alpha); \alpha\big), \tag{7}$$

where θ denotes an admissible polarization stress from the *realization-dependent* set $\mathbb{T}(\alpha)$, $\arg \operatorname*{stat}_{x \in X} f(x)$ stands for a stationary point of f on X, and a new energy functional U is defined as

$$U\big(v(x), \theta(x; \alpha); \alpha\big) = \frac{1}{2} \int_\Omega \varepsilon\big(v(x)\big) E^0 \varepsilon\big(v(x)\big) \, \mathrm{d}x - \int_\Omega v(x) b(x) \, \mathrm{d}x - \big(v(x)\bar{t}(x)\big)\big|_{\partial\Omega^t}$$
$$+ \int_\Omega \theta(x; \alpha)\varepsilon\big(v(x)\big) \, \mathrm{d}x + \frac{1}{2} \int_\Omega \theta(x; \alpha)\big(E(x; \alpha) - E^0\big)^{-1} \theta(x; \alpha) \, \mathrm{d}x. \tag{8}$$

The minimization with respect to v in (7) can be efficiently performed using the Green's function technique. To that end, we introduce a decomposition of the displacement field

$$u(x; \alpha) = u^0(x) + u^1(x; \alpha), \tag{9}$$

where u^0 solves the reference problem, while u^1 denotes the displacement field due to a test stress polarization field θ. Note that the determination of u^0 is a standard task, which can be generally solved by a suitable numerical technique (see Sections 4.1 and 4.2). By introducing the Green's function of the reference problem satisfying

$$E^0 \frac{\partial^2 G^0}{\partial x^2}(x, y) + \delta(x - y) = 0,$$

with boundary conditions (n denotes the outer normal, recall Figure 4)

$$G^0(x, y) = 0 \text{ for } x \in \partial\Omega^u, \qquad T^0(x, y) = E^0 \frac{\partial G^0(x, y)}{\partial x} n(x) = 0 \text{ for } x \in \partial\Omega^t, \tag{10}$$

we relate the u^1 component and the associated strain field ε^1 to the polarization stresses θ via [Luciano and Willis 2005]

$$
\begin{aligned}
u^1(x; \alpha) &= -\int_\Omega \frac{\partial G^0(x, y)}{\partial y} \theta(y; \alpha) \, \mathrm{d}y = -\int_\Omega \Delta^0(x, y) \theta(y; \alpha) \, \mathrm{d}x, \\
\varepsilon\big(u^1(x; \alpha)\big) &= -\int_\Omega \frac{\partial^2 G^0(x, y)}{\partial x \partial y} \theta(y; \alpha) \, \mathrm{d}y = -\int_\Omega \Gamma^0(x, y) \theta(y; \alpha) \, \mathrm{d}x.
\end{aligned}
\tag{11}
$$

By exploiting the optimality properties of the minimizing displacement $u(x; \alpha)$ and upon exchanging the order of optimization, Equation (8) can be, after some steps described in, for example, [Willis 1981; Luciano and Willis 2005], recast solely in terms of the polarizations

$$
\tau(x; \alpha) = \arg \operatorname*{stat}_{\theta(x;\alpha) \in \mathbb{T}(\alpha)} H\big(\theta(x; \alpha); \alpha\big),
$$

where the *condensed* energy functional is defined as

$$
\begin{aligned}
H\big(\theta(x; \alpha); \alpha\big) &= \min_{v(x) \in \mathbb{V}} U\big(v(x), \theta(x; \alpha); \alpha\big) = \Pi^0(u^0(x)) + \int_\Omega \theta(x; \alpha) \varepsilon\big(u^0(x)\big) \, \mathrm{d}x \\
&\quad - \frac{1}{2} \int \theta(x; \alpha)\big(E(x; \alpha) - E^0\big)^{-1} \theta(x; \alpha) \, \mathrm{d}x - \frac{1}{2} \int_\Omega \int_\Omega \theta(x; \alpha) \Gamma^0(x, y) \theta(y; \alpha) \, \mathrm{d}x \, \mathrm{d}y,
\end{aligned}
$$

with Π^0 denoting the total energy of the reference structure.

With the Hashin–Shtrikman machinery at hand, the stochastic problem introduced by (6) can be solved by repeating the previous arguments in the probabilistic framework. In particular, taking the ensemble average of (9) and (11)$_1$ yields

$$
\langle u \rangle(x) = u^0(x) - \int_\Omega \Delta^0(x, y) \langle \tau \rangle(y) \, \mathrm{d}y,
\tag{12}
$$

where the expectation $\langle \tau \rangle$ is a solution of the variational problem

$$
\langle \tau \rangle(x) = \int_{\mathbb{S}} \Big(\arg \operatorname*{stat}_{\theta(x,\alpha) \in \mathbb{T}(\alpha) \times \mathbb{S}} H(\theta(x, \alpha), \alpha) \Big) p(\alpha) \, \mathrm{d}\alpha.
\tag{13}
$$

Again, due to limited knowledge of the detailed statistical characterization of the phase distribution, the previous variational problem can only be solved approximately. In particular, we postulate the following form of the polarization stresses:

$$
\begin{aligned}
\tau(x, \alpha) &\approx \chi_1(x, \alpha) \tau_1(x) + \chi_2(x, \alpha) \tau_2(x), \\
\theta(x, \alpha) &\approx \chi_1(x, \alpha) \theta_1(x) + \chi_2(x, \alpha) \theta_2(x),
\end{aligned}
$$

where τ_r and θ_r are now the realization-independent polarization stresses related to the r-th phase. Plugging the approximation into (13) leads, after some manipulations detailed in [Willis 1981; Šejnoha and

Zeman 2000], to the variational principle

$$\left(\tau_1(x),\, \tau_2(x)\right) = \arg \operatorname*{stat}_{(\theta_1(x),\theta_2(x))} \Pi^0\left(u^0(x)\right) + \sum_{r=1}^{2} \int_\Omega \theta_r(x) S_r(x)\varepsilon\left(u^0(x)\right) dx$$

$$-\frac{1}{2}\sum_{r=1}^{2}\int_\Omega \theta_r(x)S_r(x)(E_r-E^0)^{-1}\theta_r(x)\,dx - \frac{1}{2}\sum_{r=1}^{2}\sum_{s=1}^{2}\int_\Omega\int_\Omega \theta_r(x)S_{rs}(x,y)\Gamma^0(x,y)\theta_s(y)\,dx\,dy,$$

meaning that the *true* phase polarization stresses τ_r satisfy the optimality conditions ($r = 1, 2$)

$$\int_\Omega \theta_r(x)S_r(x)(E_r-E^0)^{-1}\tau_r(x)\,dx$$

$$+\sum_{s=1}^{2}\int_\Omega\int_\Omega \theta_r(x)S_{rs}(x,y)\Gamma^0(x,y)\tau_s(y)\,dy\,dx = \int_\Omega \theta_r(x)S_r(x)\varepsilon\left(u^0(x)\right)dx, \quad (14)$$

for arbitrary θ_r.

3.3. *Discretization.* Two ingredients are generally needed to convert the conditions (14) to the finite-dimensional system: representation of the reference strain field and the Green's function-related quantities and discretization of the phase polarization stresses. The first step is dealt with in detail in Section 4; now it suffices to consider the approximations $\varepsilon^{0,h_0}(x)$, $\Delta^{0,h_0}(x)$ and $\Gamma^{0,h_0}(x,y)$, where h_0 denotes a parameter related to the discretization of the reference problem.[2]

Next, we reduce (14) to a finite-dimensional format using the standard Galerkin procedure. To that end, we introduce the discretization of the phase polarization stresses

$$\tau_r(x) \approx \mathbf{N}^{\tau h_1}(x)\boldsymbol{d}_r^{\tau h_0 h_1}, \qquad \theta_r(x) \approx \mathbf{N}^{\tau h_1}(x)\boldsymbol{d}_r^{\theta h_1}, \qquad (15)$$

where $\mathbf{N}^{\tau h_1}$ is the matrix of (possibly discontinuous) shape functions controlled by the discretization parameter h_1; $\boldsymbol{d}_r^{\theta h_1}$ and $\boldsymbol{d}_r^{\tau h_0 h_1}$ denote the DOFs of trial and true polarization stresses, the latter related to the discrete Green's function. Introducing the approximations (15) in the variational statement (14) and using the arbitrariness of $\boldsymbol{d}_r^{\theta h_1}$ leads to a system of linear equations

$$\mathbf{K}_r^{\tau h_1}\boldsymbol{d}_r^{\tau h_0 h_1} + \sum_{s=1}^{2}\mathbf{K}_{rs}^{\tau h_0 h_1}\boldsymbol{d}_s^{\tau h_0 h_1} = \boldsymbol{R}_r^{\tau h_0 h_1}, \qquad (16)$$

with the individual terms given by ($r, s = 1, 2$)

$$\mathbf{K}_r^{\tau h_1} = \int_\Omega \mathbf{N}^{\tau h_1}(x)^\mathsf{T} S_r(x)[E_r - E^0]^{-1}\mathbf{N}^{\tau h_1}(x)\,dx, \qquad (17)$$

$$\mathbf{K}_{rs}^{\tau h_0 h_1} = \int_\Omega\int_\Omega \mathbf{N}^{\tau h_1}(x)^\mathsf{T} S_{rs}(x,y)\Gamma^{0,h_0}(x,y)\mathbf{N}^{\tau h_1}(y)\,dx\,dy, \qquad (18)$$

$$\boldsymbol{R}_r^{\tau h_0 h_1} = \int_\Omega \mathbf{N}^{\tau h_1}(x)^\mathsf{T} S_r(x)\varepsilon^{0,h_0}(x)\,dx. \qquad (19)$$

---

[2]To be more precise, the goal is not to obtain accurate estimates of the Green's function-related operators themselves, but rather to approximate the action of the operators; see Section 5.2 for further discussion.

Finally, once the approximate values of phase polarization stresses are available, the elementary statistics of the displacement field follow from the discretized form of (12):

$$\langle u \rangle(x) \approx \langle u \rangle^{h_0 h_1}(x) = u^{0,h_0}(x) - \sum_{r=1}^{2} \left(\int_\Omega \Delta^{0,h_0}(x,y) S_r(y) \mathbf{N}^{\tau h_1}(y) \, \mathrm{d}y \right) \boldsymbol{d}_r^{\tau h_0 h_1}. \tag{20}$$

Note that additional information such as conditional statistics can be extracted from the polarization fields in postprocessing steps similar to (20); see [Luciano and Willis 2005; 2006] for more details.

4. Reference problem and Green's function-related quantities

4.1. *Finite element method.* The solution of the reference problem follows the standard finite element procedures, see for examples [Bittnar and Šejnoha 1996; Krysl 2006]. Nevertheless, we briefly repeat the basic steps of the method for the sake of clarity.[3] The reference displacement u^0 follows from the identity

$$\int_\Omega \varepsilon(v(x)) E^0 \varepsilon(u^0(x)) \, \mathrm{d}x = \int_\Omega v(x) b(x) \, \mathrm{d}x + \left(v(x) \bar{t}(x) \right)\Big|_{\partial \Omega^t}, \tag{21}$$

which should hold for any test function $v \in \mathbb{V}$. Within the conforming finite element approach, the unknown displacement u^0 and the test function v together with the associated strain field are sought in a finite-dimensional subspace $\mathbb{V}^{h_0} \subset \mathbb{V}$

$$u^0(x) \approx u^{0,h_0}(x) = \mathbf{N}^{uh_0}(x) \boldsymbol{d}^{uh_0}, \qquad v(x) \approx v^{h_0}(x) = \mathbf{N}^{uh_0}(x) \boldsymbol{d}^{vh_0}, \tag{22}$$

$$\varepsilon(u^0(x)) \approx \varepsilon(u^{0,h_0}(x)) = \mathbf{B}^{uh_0}(x) \boldsymbol{d}^{uh_0}, \qquad \varepsilon(v(x)) \approx \varepsilon(v^{h_0}(x)) = \mathbf{B}^{uh_0}(x) \boldsymbol{d}^{vh_0}, \tag{23}$$

where $\mathbf{N}^{uh_0}$ is the displacement interpolation matrix and $\mathbf{B}^{uh_0}$ denotes the displacement-to-strain matrix. Using the discretized fields, (21) reduces to the system

$$\mathbf{K}^{uh_0} \boldsymbol{d}^{uh_0} = \boldsymbol{R}^{uh_0}, \tag{24}$$

where

$$\mathbf{K}^{uh_0} = \int_\Omega \mathbf{B}^{uh_0}(x)^\mathsf{T} E^0 \mathbf{B}^{uh_0}(x) \, \mathrm{d}x, \qquad \boldsymbol{R}^{uh_0} = \int_\Omega \mathbf{N}^{uh_0}(x)^\mathsf{T} b(x) \, \mathrm{d}x + \left(\mathbf{N}^{uh_0}(x) \bar{t}(x) \right)\Big|_{\partial \Omega^t}. \tag{25}$$

Solving the system for $\boldsymbol{d}^{uh_0}$ enables us to obtain the ε^{0,h_0} approximation using (23)$_1$.

The discretized version of the Green's function follows from (21) with $\bar{t} = 0$ and $b = \delta(y - x)$ (see (24) and (25)$_2$),

$$G^0(x,y) \approx G^{0,h_0}(x,y) = \mathbf{N}^{uh_0}(x)(\mathbf{K}^{uh_0})^{-1} \mathbf{N}^{uh_0}(y)^\mathsf{T}.$$

The remaining Green's function-related quantities can now be expressed directly from (11) and (11)$_2$, leading to

$$\Delta^0(x,y) \approx \Delta^{0,h_0}(x,y) = \mathbf{N}^{uh_0}(x)(\mathbf{K}^{uh_0})^{-1} \mathbf{B}^{uh_0}(y)^\mathsf{T}, \tag{26}$$

$$\Gamma^0(x,y) \approx \Gamma^{0,h_0}(x,y) = \mathbf{B}^{uh_0}(x)(\mathbf{K}^{uh_0})^{-1} \mathbf{B}^{uh_0}(y)^\mathsf{T}. \tag{27}$$

---

[3]Recall that for simplicity, we assume homogeneous Dirichlet boundary conditions only. The treatment of the nonhomogeneous data can be found in [Luciano and Willis 2005, Appendix A].

4.2. *Boundary element discretization.* Following the standard BEM procedures (see for examples [Bittnar and Šejnoha 1996; Duddeck 2002]), we start from the Betti identity written for the reference problem

$$\int_\Omega \frac{d^2 v}{d\xi^2}(\xi) E^0 u^0(\xi)\, d\xi = \left. \left(n(\xi)\varepsilon(v(\xi)) E^0 u^0(\xi) - v(\xi) t^0(\xi) \right) \right|_{\partial\Omega(\xi)} - \int_\Omega v(\xi) b(\xi)\, d\xi, \qquad (28)$$

and apply the test displacement in the form $v(\xi) = G^{0,\infty}(\xi, x)$, where $G^{0,\infty}$ is the infinite body Green's function defined as the solution of

$$E^0 \frac{\partial^2 G^{0,\infty}(\xi, x)}{\partial\xi^2} + \delta(x - \xi) = 0, G^{0,\infty}(\xi, x) = G^{0,\infty}(x, \xi). \qquad (29)$$

In the one-dimensional setting, this quantity is provided by [Luciano and Willis 2001, Equation (13)]

$$G^{0,\infty}(x, \xi) = -\frac{1}{2E^0}|x - \xi|,$$

and the integral identity (28), written for any $x \in \Omega$, receives the form

$$u^{0,h_0}(x) = \left. \left(G^{0,\infty}(x, \xi) t^{0,h_0}(\xi) - T^{0,\infty}(x, \xi) u^{0,h_0}(\xi) \right) \right|_{\partial\Omega(\xi)} + \int_\Omega G^{0,\infty}(x, \xi) b(\xi)\, d\xi, \qquad (30)$$

where the tractions $T^{0,\infty}(x, \xi)$ are defined analogously to $(10)_2$ as

$$T^{0,\infty}(x, \xi) = E^0 \frac{\partial G^{0,\infty}(x, \xi)}{\partial\xi} n(\xi) = \left(H(x - \xi) - \tfrac{1}{2} \right) n(\xi), \quad \text{for} \quad \xi \in \partial\Omega, \qquad (31)$$

and H denotes the Heaviside function. Imposing the consistency with boundary data for $x \to 0_+$ and $x \to L_-$ yields the system of two linear equations

$$E^0 u^{0,h_0}(L) - E^0 u^{0,h_0}(0) - L t^{0,h_0}(L) = \int_\Omega \xi b(\xi)\, d\xi, \qquad (32)$$

$$E^0 u^{0,h_0}(L) - E^0 u^{0,h_0}(0) - L t^{0,h_0}(0) = \int_\Omega (L - \xi) b(\xi)\, d\xi. \qquad (33)$$

Since one component of the pair (u^{0,h_0}, t^{0,h_0}) is always specified on $\partial\Omega$ and $\partial\Omega^u \neq \varnothing$, the previous system uniquely determines the unknown boundary data (that is, u^{0,h_0} on $\partial\Omega^t$ and t^{0,h_0} on $\partial\Omega^u$), needed to evaluate (30).[4]

Making use of the identity $2E^0 \partial_x G^{0,\infty}(x, \xi) = 1 - 2H(x - \xi)$, the associated strain field can be expressed as

$$\varepsilon^{0,h_0}(x) = \left. \left(\frac{\partial G^{0,\infty}(x, \xi)}{\partial x} t^{0,h_0}(\xi) \right) \right|_{\partial\Omega(\xi)} + \int_\Omega \frac{\partial G^{0,\infty}(x, \xi)}{\partial x} b(\xi)\, d\xi$$

$$= \frac{1}{2E^0} \left(t^{0,h_0}(L) - t^{0,h_0}(0) - \int_0^x b(\xi)\, d\xi + \int_x^L b(\xi)\, d\xi \right). \qquad (34)$$

---

[4]It can be verified that (30) now provides the exact *one-dimensional* displacement field rather than an approximate one. Nevertheless, to keep the following discussion valid in the multidimensional setting and consistent with Section 4.1, we keep the index "h_0" in the sequel.

Analogously to the finite element treatment, the expression for the finite-body Green's function starts from (28) with $b = \delta(y - \xi)$ and boundary data (10). Following the specific form of (30) (and allowing for a slight inconsistency in notation), we introduce a decomposition of the Green's function into the discretization-independent infinite-body part and the discretization-dependent boundary contribution $G^0(x, y) \approx G^{0,\infty}(x, y) + G^{0,h_0}(x, y)$, where the boundary part, written for $x \in \Omega$ and $y \in \Omega$, assumes the form

$$G^{0,h_0}(x, y) = \left(G^{0,\infty}(x, \xi) T^{0,h_0}(\xi, y) - T^{0,\infty}(x, \xi) G^{0,h_0}(\xi, y) \right) \Big|_{\partial\Omega(\xi)},$$

with the boundary displacements G^{0,h_0} and tractions T^{0,h_0} at $\xi \in \partial\Omega$ due to a unit impulse at y determined from a linear system (compare with (32) and (33))

$$E^0 G^{0,h_0}(L, y) - E^0 G^{0,h_0}(0, y) - L T^{0,h_0}(L, y) = y, \tag{35}$$

$$E^0 G^{0,h_0}(L, y) - E^0 G^{0,h_0}(0, y) - L T^{0,h_0}(0, y) = L - y. \tag{36}$$

The expression for Δ^0 is derived following an analogous procedure. We exploit the infinite-body–boundary split $\Delta^0(x, y) \approx \Delta^{0,\infty}(x, y) + \Delta^{0,h_0}(x, y)$, and obtain the first part directly from the definition (11)

$$\Delta^{0,\infty}(x, y) = \frac{\partial G^{0,\infty}(x, y)}{\partial y} = \frac{1}{2E^0} \left(2H(x - y) - 1 \right).$$

The boundary-dependent part now follows from

$$\Delta^{0,h_0}(x, y) = \left(G^{0,\infty}(x, \xi) \frac{\partial T^{0,h_0}(\xi, y)}{\partial y} - T^{0,\infty}(x, \xi) \frac{\partial G^{0,h_0}(\xi, y)}{\partial y} \right) \Big|_{\partial\Omega(\xi)},$$

with the y-sensitivities of the boundary data evaluated from (35)–(36) as

$$E^0 \frac{\partial G^{0,h_0}(L, y)}{\partial y} - E^0 \frac{\partial G^{0,h_0}(0, y)}{\partial y} - L \frac{\partial T^{0,h_0}(L, y)}{\partial y} = 1, \tag{37}$$

$$E^0 \frac{\partial G^{0,h_0}(L, y)}{\partial y} - E^0 \frac{\partial G^{0,h_0}(0, y)}{\partial y} - L \frac{\partial T^{0,h_0}(0, y)}{\partial y} = -1. \tag{38}$$

The BEM-based approach is completed by approximating the Γ^0 function. In particular, we get

$$\Gamma^0(x, y) \approx \Gamma^{0,\infty}(x, y) + \Gamma^{0,h_0}(x, y), \tag{39}$$

$$\Gamma^{0,\infty}(x, y) = \frac{\partial \Delta^{0,\infty}(x, y)}{\partial x} = \frac{1}{E^0} \delta(x - y), \tag{40}$$

$$\Gamma^{0,h_0}(x, y) = \frac{\partial \Delta^{0,h_0}(x, y)}{\partial x} = \left(\frac{G^{0,\infty}(x, \xi)}{\partial x} \frac{\partial T^{0,h_0}(\xi, y)}{\partial y} \right) \Big|_{\partial\Omega(\xi)}$$

$$= \frac{1}{2E^0} \left(\frac{\partial T^{0,h_0}(L, y)}{\partial y} - \frac{\partial T^{0,h_0}(0, y)}{\partial y} \right). \tag{41}$$

Finally note that the previous procedure can be directly translated to multidimensional and/or vectorial cases; see [Procházka and Šejnoha 2003, Section 3] for more details.

5. Numerical examples

Before getting to the heart of the matter, we start by converting the relations (16)–(20) to the fully discrete format by replacing the integrals by a numerical quadrature and selecting a specific form of shape functions $\mathbf{N}^{\tau h_1}$. To that end, we introduce a set of integration points $\{\zeta_1, \zeta_2, \ldots, \zeta_{N_\zeta}\}$ as well as associated integration weights $\{w_1, w_2, \ldots, w_{N_\zeta}\}$ and evaluate the components of the system matrix and right-hand side vector as

$$\mathbf{K}_r^{\tau h_1} \approx \sum_{i=1}^{N_\zeta} w_i \mathbf{N}^{\tau h_1}(\zeta_i)^\top S_r(\zeta_i)[E_r - E^0]^{-1} \mathbf{N}^{\tau h_1}(\zeta_i), \tag{42}$$

$$\mathbf{K}_{rs}^{\tau h_0 h_1} \approx \sum_{i=1}^{N_\zeta} \sum_{j=1}^{N_\zeta} w_i w_j \mathbf{N}^{\tau h_1}(\zeta_i)^\top S_{rs}(\zeta_i, \zeta_j) \Gamma^{0,h_0}(\zeta_i, \zeta_j) \mathbf{N}^{\tau h_1}(\zeta_j)$$
$$+ \int_\Omega \int_\Omega \mathbf{N}^{\tau h_1}(x)^\top S_{rs}(x, y) \Gamma^{0,\infty}(x, y) \mathbf{N}^{\tau h_1}(y)\, \mathrm{d}x\, \mathrm{d}y, \tag{43}$$

$$\boldsymbol{R}_r^{\tau h_0 h_1} \approx \sum_{i=1}^{N_\zeta} \mathbf{N}^{\tau h_1}(\zeta_i)^\top S_r(\zeta_i) \varepsilon^{0,h_0}(\zeta_i), \tag{44}$$

$$\langle u \rangle^{h_0 h_1}(x) \approx u^{0,h_0}(x) - \sum_{r=1}^{2} \sum_{i=1}^{N_\zeta} w_i \Delta^{0,h_0}(x, \zeta_i) S_r(\zeta_i) \mathbf{N}^{\tau h_1}(\zeta_i) \boldsymbol{d}_r^{\tau h_0 h_1}$$
$$- \sum_{r=1}^{2} \left(\int_\Omega \Delta^{0,\infty}(x, y) S_r(y) \mathbf{N}^{\tau h_1}(y)\, \mathrm{d}y \right) \boldsymbol{d}_r^{\tau h_0 h_1}, \tag{45}$$

with the convention $\Gamma^{0,\infty} = \Delta^{0,\infty} \equiv 0$ for the FEM-based approximation of the polarization problem. The basis functions and integration schemes employed below, based on a uniform partitioning of Ω into N_e cells Ω_e of length $h_1 = L/N_e$, are defined by Figure 6. In particular, the specification of the polarization stress in terms of $\mathbb{P}_0$ shape functions requires $2N_e$ DOFs (meaning one DOF per cell and phase), while the $\mathbb{P}_1$ and $\mathbb{P}_{-1}$ discretizations are parametrized using $2(N_e + 1)$ or $4N_e$ values, respectively.
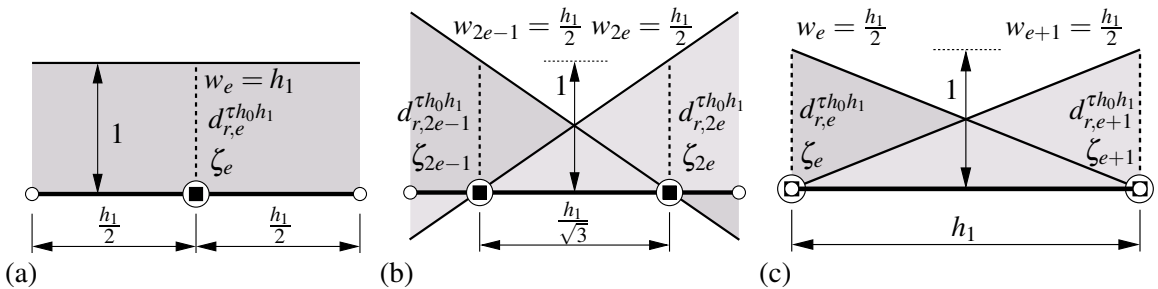
Figure 6. Choice of shape functions and integration points related to the e-th cell: (a) piecewise-constant basis functions ($\mathbb{P}_0$) and the Gauss–Legendre quadrature of order 1 (GL$_1$), (b) piecewise-linear discontinuous basis functions ($\mathbb{P}_{-1}$) and the Gauss–Legendre quadrature of order 2 (GL$_2$), and (c) piecewise linear continuous basis functions ($\mathbb{P}_1$) and Newton–Cotes quadrature of order 1 (NC$_1$). ∘ represent cell nodes, ○ degrees of freedom, and ■ integration points.

Note that the BEM-related infinite-body contributions appearing in (43) and (45) are still kept explicit, as they are available in the closed form and can be treated separately. In the present case, action of the $\Gamma^{0,\infty}$ operator is local—recall (41)—while the quantities related to $\Delta^{0,\infty}$ are evaluated at cell nodal points and linearly interpolated to the interior of a cell to account for the discontinuity of the integrand.

To summarize, the following factors significantly influence the accuracy of the discrete Hashin–Shtrikman scheme:

- approximation of the Green's function of the comparison body,
- the basis functions and numerical quadrature used to discretize the polarization problem,
- the Young's modulus of the reference body E^0,
- contrast of the Young moduli of individual phases (E_2/E_1),
- the characteristic size of the microstructure with respect to the analyzed domain (ℓ/L).

All these aspects are studied in detail in the rest of this section. Two representative examples of structures subject to a uniform body force b and homogeneous mixed and Dirichlet boundary data are considered, see Figure 7,

$$\text{statically determinate structure: } u(0,\alpha) = 0, \quad t(L,\alpha) = 0, \tag{46}$$

$$\text{statically indeterminate structure: } u(0,\alpha) = 0, \quad u(L,\alpha) = 0. \tag{47}$$

In both cases, the heterogeneity distribution is quantified according to the model introduced in Section 2 with the one- and two-point probability functions plotted in Figure 3. Moreover, taking advantage of the one-dimensional setting, we systematically compare the obtained numerical results against reliable reference values determined by extensive Monte Carlo (MC) simulations, introduced next.

5.1. *Direct simulation results.* For the purpose of the following discussion, the reference values of the average displacement fields $\langle u \rangle_{\text{MC}}(x)$ together with the 99.9% interval estimates $[\langle u_- \rangle_{\text{MC}}(x), \langle u_+ \rangle_{\text{MC}}(x)]$ are understood as the piecewise linear interpolants of discrete data sampled by the MC procedure described in detail in the Appendix. In addition, the homogenized displacement field $u_{\text{H}}(x)$, corresponding to a deterministic structure with the position-dependent elastic modulus

$$\frac{1}{E_{\text{H}}(x)} = \frac{S_1(x)}{E_1} + \frac{S_2(x)}{E_2}, \tag{48}$$

is introduced to assess the performance of the local averaging approach. Figure 7 stores several representative results plotted using dimensionless quantities.

As apparent from Figure 7, the obtained statistics of overall response exhibit rather narrow confidence intervals, implying the reliability and accuracy of the MC estimates. For the statically determinate structure, the locally homogenized solution coincides with the ensemble average of the displacement fields, as demonstrated by the overlap of the simulation results with the homogenized data. The converse is true (with the 99.9% confidence) for the statically indeterminate case, where these two results can be visually distinguished from each other. The mismatch (which increases with increasing E_2/E_1 or ℓ/L) clearly demonstrates that even in the one-dimensional setting local averaging may lead to incorrect values when treating nonhomogeneous random media. These results are consistent with the fact that
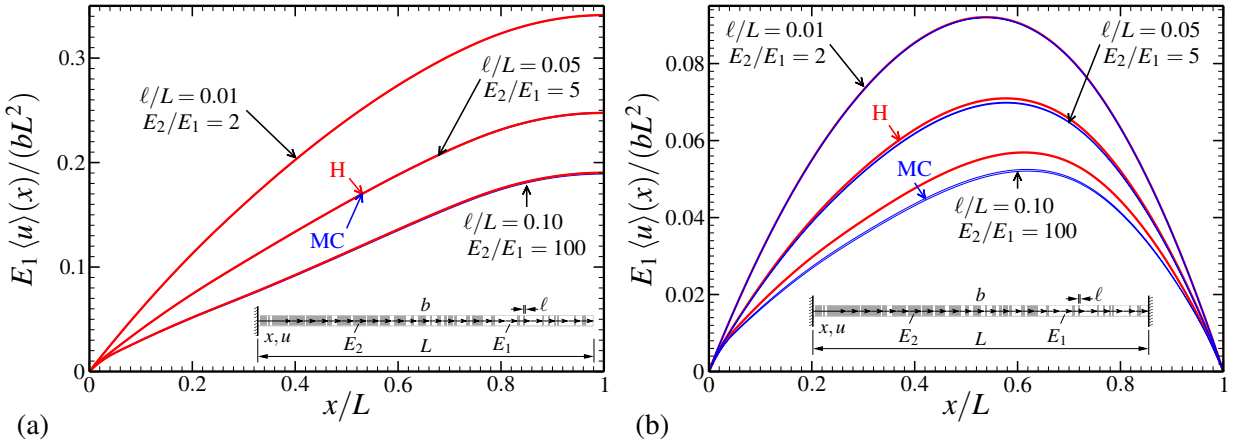
Figure 7. Reference MC solution; (a) statically determinate and (b) indeterminate problems; MC results correspond to 99.9% confidence interval estimates, H refers to homogenized solution.

in the statically determinate case, the stress field $\sigma(x, \alpha)$ is independent of α as follows from the one-dimensional equilibrium equations $\partial_x \sigma(x, \alpha) + b(x) = 0$ and the deterministic value of the traction at $x = L$ due to the boundary condition provided by (46)$_2$. In the latter case, however, the traction value as well as the stress field become configuration-dependent. Such an effect does not appear in the classical homogenization setting, where for $\ell/L \to 0$ the harmonic average is known to represent the homogenized solution exactly [Murat and Tartar 1997]. This result naturally justifies the application of approaches based on higher-order statistics to FGMs, with the H–S method being the most prominent example.

5.2. *Effect of the Green's function approximation.* In order to illustrate the effect of the approximate Green's function, we restrict our attention to the statistically determinate structure and employ the standard piecewise linear basis functions $\mathbf{N}^{uh_0}$ to evaluate the Γ^{0,h_0} function in the FEM setting using (27). Figure 8 allows us to perform the qualitative assessment of the results for different choices of basis functions, integration schemes, and discretization parameters h_0.

Evidently, a suitable choice of discretization parameter h_0 is far from straightforward. From all the possibilities presented in Figure 8a, only the combinations $h_1 = h_0$ with the $\mathbb{P}_0/\text{GL}_1$ discretization of the polarization problem and $h_1 = 2h_0$ with the $\mathbb{P}_{-1}/\text{GL}_2$ scheme are capable of reproducing the homogenized solution, while all the remaining possibilities lead to inaccurate results often accompanied by an oscillatory response. On the other hand, the h_0-independent BEM-based solutions show correct response for all discretizations of the polarization problem (and are virtually independent of the scheme used due to the sufficiently low value of the h_1 parameter, see Section 5.5).

To shed a light on such phenomena, consider the FEM approximation of the Γ^{0,h_0} function plotted in Figure 9a. The piecewise linear basis functions used to express the reference displacements imply the piecewise constant values of $\Gamma^{0,h_0}(x, y)$ approximating the exact expression $\frac{1}{E^0}\delta(x - y)$, see (39). As pointed out by Luciano and Willis [2006], however, the accuracy of the HS scheme is governed by the correct reproduction of the *action* of the $\Gamma^0(x, y)$ operator rather than the local values. In the present

context, it follows from (44) that such a requirement is equivalent to the accurate representation of the $\Gamma^0(x, y)$ operator action for x coinciding with the integration points related to the selected numerical quadrature. It can be verified that this condition is satisfied only for the two aforementioned discretizations of the reference problem. In particular, for the $\mathbb{P}_0/\mathrm{GL}_1$ combination we obtain (see Figures 9a and 10a)

$$\int_{\Omega_e} \Gamma^0(\zeta_e, \xi)\tau_r(\xi)\, \mathrm{d}\xi \approx w_e \Gamma^{0,h_0}(\zeta_e, \zeta_e) d_{e,r}^{\tau h_0 h_1} = h_1 \frac{1}{E^0 h_0} d_{e,r}^{\tau h_0 h_1} = \frac{d_{e,r}^{\tau h_0 h_1}}{E^0},$$

meaning that the numerical scheme reproduces the action of Γ^0 exactly.
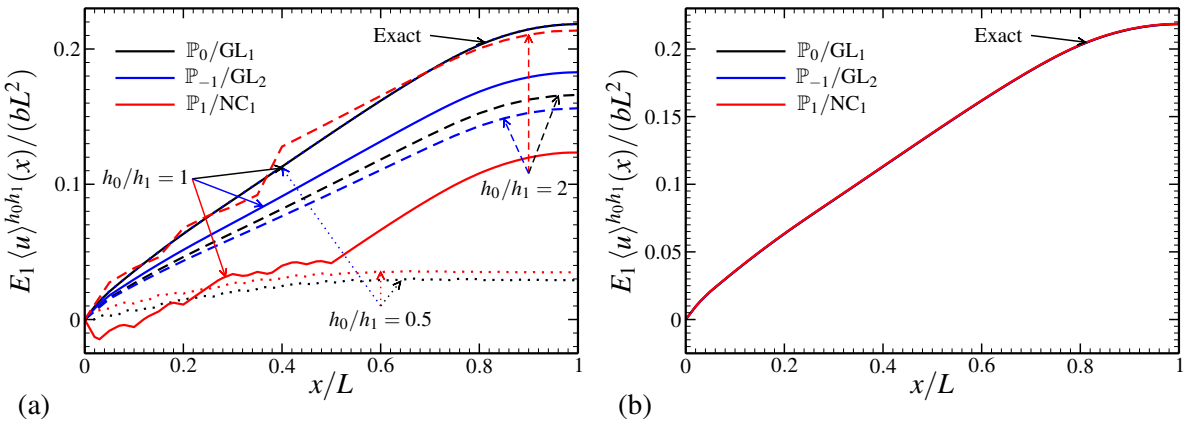
Figure 8. Influence of the approximate Green's function for the statically determinate problem: (a) FEM-based solution, and (b) BEM-based solution. $E_2/E_1 = 10$, $E^0/E_1 = 5$, $\ell/L = 0.1$, and $h_1/\ell = 0.25$.
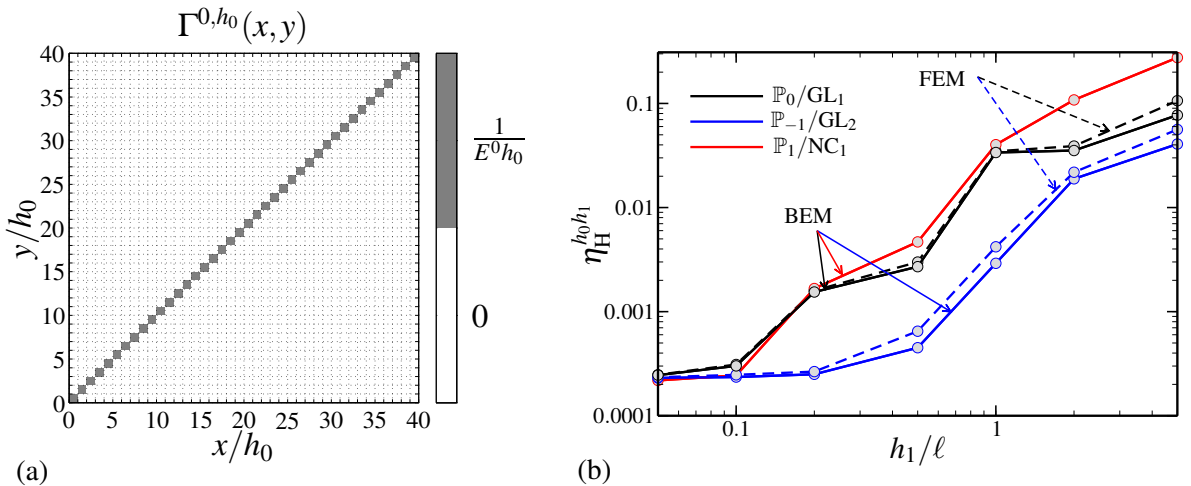
Figure 9. (a) Finite element approximation of the Green's function and (b) convergence rates of FEM vs. BEM; $E_2/E_1 = 10$, $E^0/E_1 = 5$, and $\ell/L = 0.1$.
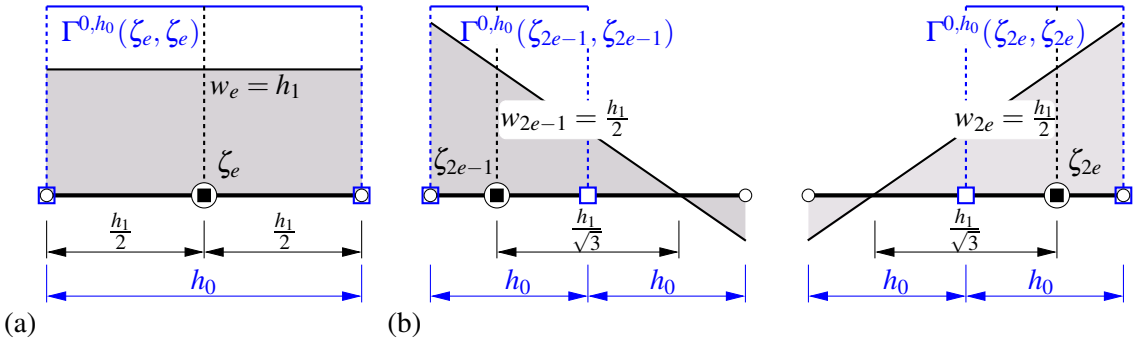
Figure 10. Valid combinations of the discretized Green's function and the polarization stresses: (a) $\mathbb{P}_0/\text{GL}_1$ and (b) $\mathbb{P}_{-1}/\text{GL}_2$; $\square$ are finite element nodes.

Using Figures 9a and 10b, we find the analysis of the $\mathbb{P}_{-1}/\text{GL}_2$ discretization completely analogous:

$$
\int_{\Omega_e} \Gamma^0(\zeta_{2e-1}, \xi)\tau_r(\xi)\, d\xi \approx w_{2e-1}\Gamma^{0,h_0}(\zeta_{2e-1}, \zeta_{2e-1})d_{2e-1,r}^{\tau h_0 h_1} = \frac{h_1}{2}\frac{1}{E^0 h_0}d_{2e-1,r}^{\tau h_0 h_1} = \frac{d_{2e-1,r}^{\tau h_0 h_1}}{E^0},
$$

$$
\int_{\Omega_e} \Gamma^0(\zeta_{2e}, \xi)\tau_r(\xi)\, d\xi \approx w_{2e}\Gamma^{0,h_0}(\zeta_{2e}, \zeta_{2e})d_{2e,r}^{\tau h_0 h_1} = \frac{d_{2e,r}^{\tau h_0 h_1}}{E^0},
$$

which explains the good performance of the particular discretization scheme.

To allow for the quantitative comparison, we exploit the fact that the exact solution is available for the statically determinate case and introduce a relative L_2 error measure

$$
\eta_{\text{H}}^{h_0 h_1} = \frac{\left\| \langle u \rangle^{h_0 h_1}(x) - u_{\text{H}}(x) \right\|_{L_2(\Omega)}}{\left\| u_{\text{H}}(x) \right\|_{L_2(\Omega)}}. \tag{49}
$$

The resulting convergence rates of the FEM- and BEM-based approaches are shown in Figure 10b with the integrals in (49) evaluated using an adaptive Simpson quadrature [Gander and Gautschi 2000] with a relative accuracy of 10^{-6}. Clearly, the performance of the BEM-based scheme is slightly superior to the (properly tuned) FEM approach. By a sufficient resolution of the reference problem, however, both approaches become comparable. Moreover, the results confirm the good performance of the $\mathbb{P}_0$ and $\mathbb{P}_1$ schemes when compared to the $\mathbb{P}_{-1}$ discretization, which requires about twice the number of DOFs of the former schemes for the same cell dimensions h_1 (recall Figure 6). Similar conclusions can also be drawn for the statically indeterminate case. Therefore, in view of the above comments, we concentrate on the BEM approach in the sequel and limit the choice of basis functions to $\mathbb{P}_0$ and $\mathbb{P}_1$ only.

5.3. *Influence of the integration scheme and basis functions.* Thus far, we have investigated the combination of the *polarization* numerical quadratures and shape functions, for which the location of integration points coincides with the position of DOFs. Figure 11 shows the convergence plots for the relevant basis function/integration scheme pairs. To address also the statically determinate case, the relative error is

now related to the MC data, leading to the definition

$$\eta_{\mathrm{MC}}^{h_0 h_1} = \frac{\left\| \langle u \rangle^{h_0 h_1}(x) - \langle u \rangle_{\mathrm{MC}}(x) \right\|_{L_2(\Omega)}}{\left\| \langle u \rangle_{\mathrm{MC}}(x) \right\|_{L_2(\Omega)}}. \tag{50}$$

In addition, two comparative values are introduced: the relative error of the homogenized solution H (determined by (50) with $\langle u \rangle^{h_0 h_1}$ replaced by u_{H}) and the relative error associated with the $\langle u_- \rangle_{\mathrm{MC}}$ or $\langle u_+ \rangle_{\mathrm{MC}}$ function, appearing as the interval estimate (IE) line.

For the statistically determinate structure, the observed behavior is rather similar to the one reported in Section 5.2. In particular, Figure 11a confirms that the H–S solution quickly reaches an accuracy comparable with the confidence intervals (indicated by the grey area) and eventually converges to the homogenized solution, with the exception of the $\mathbb{P}_1/\mathrm{GL}_1$ combination resulting in a singular system matrix (16). Moreover, the superiority of the GL_2 quadrature over the lower-order scheme is evident; the proper representation of spatial statistics seems to be more important than smoothness of the polarization shape functions.

Figure 11b shows the results for the statically indeterminate case. With 99.9% confidence, the results *quantitatively* demonstrate that the homogenized solution differs from the MC data. The H–S solution gives an error of about 50% of the value of the homogenized solution, but ceases to attain the accuracy set by the confidence interval. It should be kept in mind that the H–S result actually delivers an estimate pertinent to the fixed value of parameter E^0 and *all* random one-dimensional media characterized by the two-point statistics (4).

5.4. *Influence of the reference media and phase contrast.* Having identified the intrinsic limitation of the H–S approach, we proceed with the last free parameter of the method: the choice of the reference medium. To that end, we introduce the parameterization of the Young modulus

$$E^0 = (1 - \omega)E_1 + \omega E_2.$$
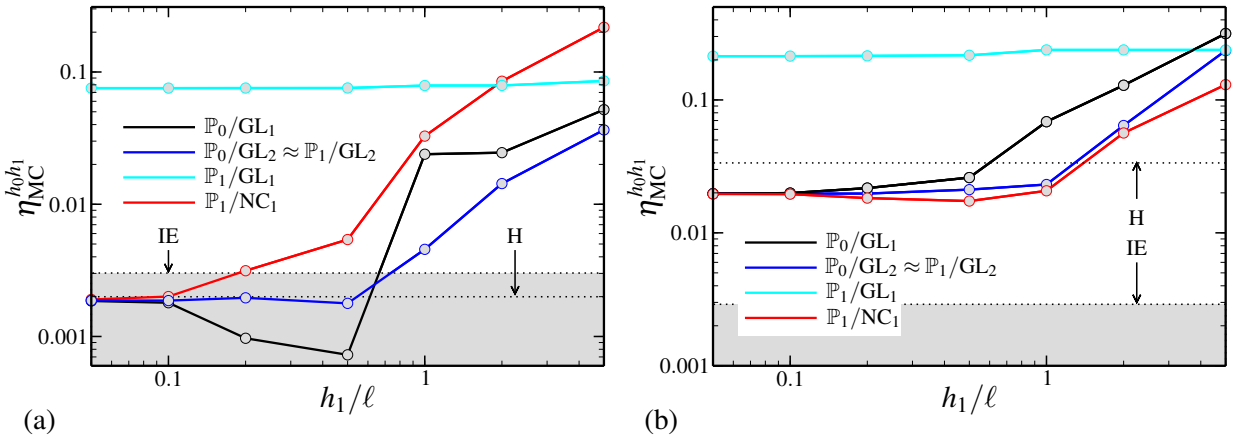
Figure 11. Influence of the choice of numerical discretization: (a) statically determinate and (b) indeterminate structures; $E_2/E_1 = 5$, $\ell/L = 0.1$, $E^0/E_1 = 3$, and IE denotes the error associated with the 99.9% confidence interval estimate.
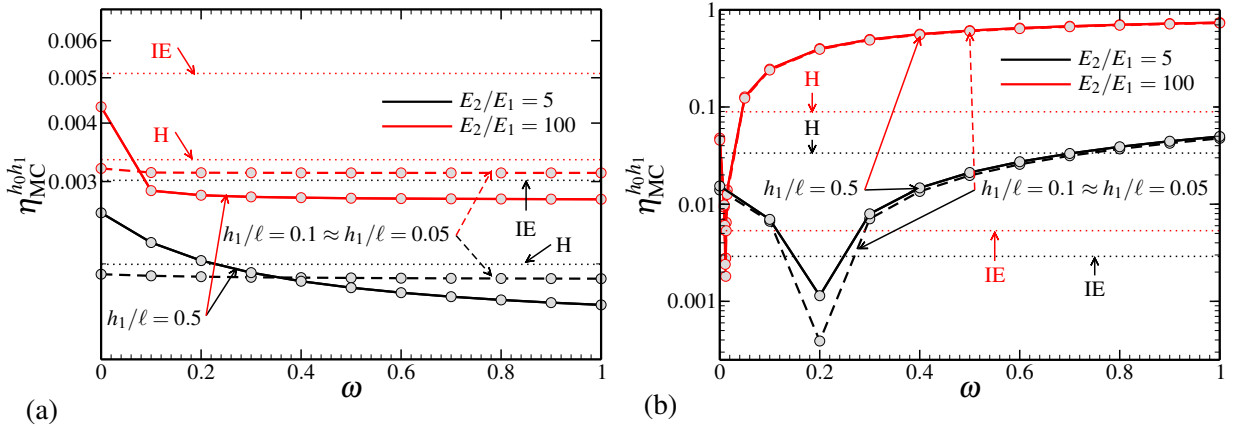
Figure 12. Influence of the choice of the reference media: (a) statically determinate and (b) indeterminate structures; $\ell/L = 0.1$, and $\mathbb{P}_0/\mathrm{GL}_2$ discretization.

Note that for the phases indexed such that $E_1 < E_2$, $\omega = 0$ and $\omega = 1$ correspond to the rigorous lower and upper bounds on the ensemble average of the energy stored in the structure and, consequently, to the positive- or negative-definite system matrix [Procházka and Šejnoha 2004; Luciano and Willis 2005]. The intermediate values lead to energetic variational estimates and to a symmetric indefinite system matrix. Figure 12 illuminates the effect of ω, plotted for two representative contrasts of the phase moduli and h_1/ℓ ratios.

In the first case, see Figure 12a, the choice of the reference media has almost negligible effect on the H–S solution error; the slight influence observed for the coarse discretization completely disappears upon cell refinement. This is not very surprising, as the homogenized solution depends on the first-order statistics only—recall (48)—and therefore can be retained by the discrete H–S method (up to controllable errors) for any choice of E^0. Results for the statically indeterminate structure, on the other hand, show a significant sensitivity to the value of ω. By a proper adjustment of the reference medium, the error can be reduced by an order of magnitude and can eventually reach the accuracy of extensive MC sampling. With increasing phase moduli contrast, however, the range of such ω values rapidly decreases; for $E_2/E_1 = 100$ one needs to satisfy $9 \cdot 10^{-4} \lesssim \omega \lesssim 1.5 \cdot 10^{-3}$ in order to recover the MC results. It is noteworthy that these values agree rather well with the particular choice of reference media used by Matouš [2003] when modeling composites with a high phase contrast using the methodology proposed by Dvorak and Srinivas [1999].

5.5. *Influence of microstructure size.* Finally, we investigate the influence of the microstructure size. Figure 13 summarizes the obtained results for a moderate phase contrast and the optimal setting of the H–S method identified in the previous sections. A similar conclusion can be reached for both case studies: for all three ℓ/L values, the H–S method is capable of reaching an accuracy of MC confidence intervals for the cell length h_1 approximately equal to half of the microscopic length scale ℓ. In other words, keeping the same number of DOFs as used to discretize the polarization problem, the accuracy of the method increases with the increasing ℓ/L ratio, which is exactly an opposite trend to that of the classical deterministic homogenization.
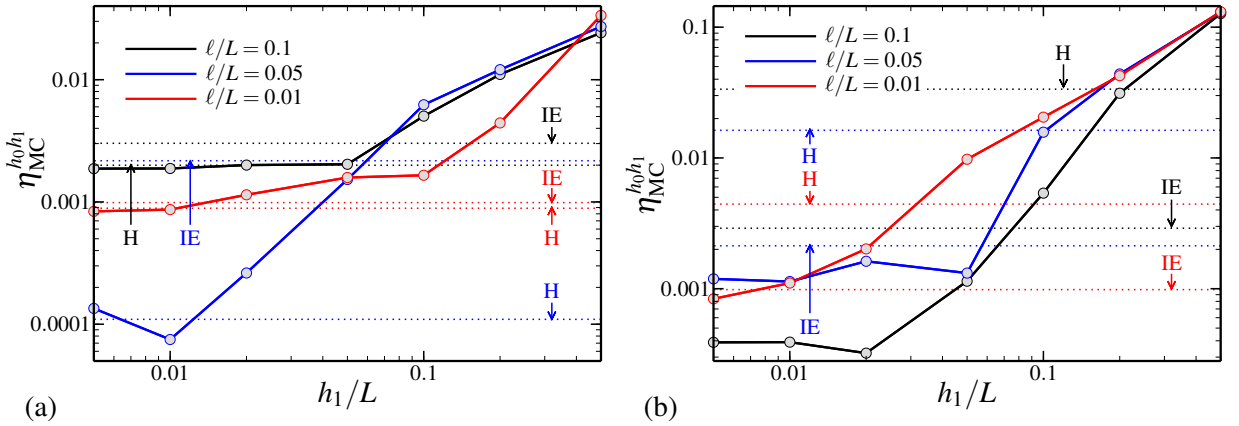
Figure 13. Influence of microstructure size: (a) statically determinate and (b) indeterminate structures; $E_2/E_1 = 5$, $\omega = 0.2$, $\ell/L = 0.05$, and $\mathbb{P}_0/\mathrm{GL}_2$ discretization.

6. Conclusions

In the present work, the predictive capacities of numerical methods based on the Hashin–Shtrikman–Willis variational principles, when applied to a specific model of functionally graded materials, have been systematically assessed. By restricting attention to the one-dimensional setting, an extensive parametric study has been executed and the results of numerical schemes have been verified against reliable large-scale Monte Carlo (MC) simulations. On the basis of the obtained data, we are justified in stating that:

- The Hashin–Shtrikman based numerical method, when set up properly, is capable of delivering results with accuracy comparable to detailed MC simulations and, consequently, of outperforming local averaging schemes.

- When applying the finite element method (FEM) to the solution of reference problem, the employed discretization has to be compatible with the numerics used to solve the polarization problem. If this condition is satisfied, the additional FEM-induced errors quickly become irrelevant.

- For the discretization of the reference problem, it appears to be advantageous to combine a low order (discontinuous) approximation of the polarization stresses with a higher order quadrature scheme to concisely capture the heterogeneity distribution.

- The correct choice of the reference medium has the potential to substantially decrease the error. Unfortunately, apart from [Dvorak and Srinivas 1999], we fail to give any a priori estimates of the optimal value for statistically nonhomogeneous structures.

- For accurate results, the characteristic cell size should be around 2–5 times smaller than the typical dimensions of the constituents.

The bottleneck in the current implementation is the solution of system (16), since it leads to a fully populated system matrix. Fortunately, as illustrated by Figure 14, the conditioning of the polarization problem seems to be dominated by the phase contrast rather than the discretization of the reference problem, which opens the way to efficient iterative techniques.
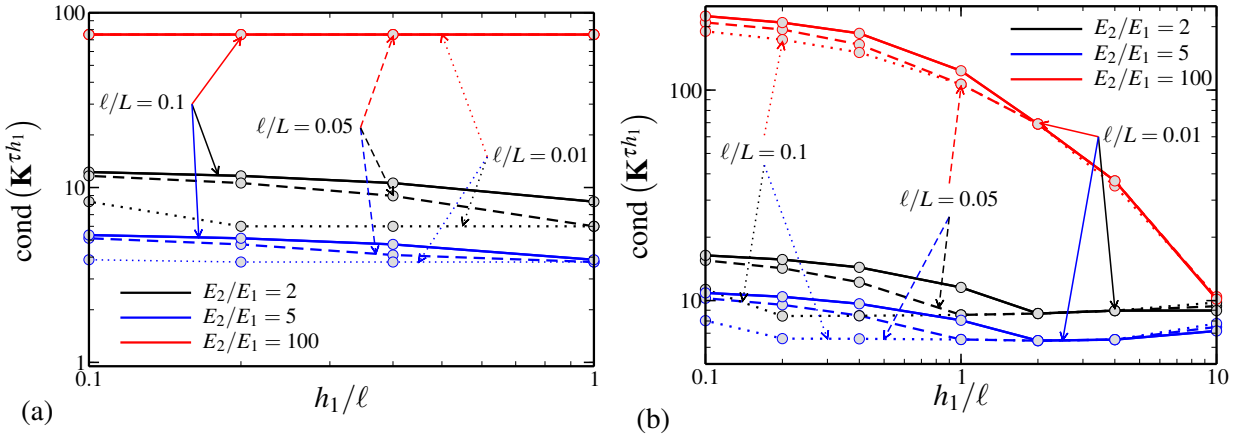
Figure 14. Sensitivity of conditioning of system matrix of the polarization problem: (a) statically determinate and (b) indeterminate structures; $\ell/L = 0.05$, $\omega = 0.2$, $\mathbb{P}_0/\mathrm{GL}_2$ scheme, and the condition number is estimated using the algorithm from [Higham and Tisseur 2000].

The next extension of the method would involve generalization to a multidimensional setting. For the FEM-based treatment, the key aspect remains a more rigorous analysis of the combined effect of the discretized Γ^0 operator, basis functions and integration scheme employed for the polarization problem. The multidimensional BEM approach, on the other hand, requires a careful treatment of the singularities of the Green's function-related quantities [Procházka and Šejnoha 2003] which are suppressed in the current one-dimensional setting. Such work will be reported separately in our future publications.

Acknowledgments

Appendix: Overview of the simulation procedure

A crude MC method is employed to estimate the statistics of the local fields. In particular, given a number of simulations N_α, sampling points $0 = y_0 < y_1 < \ldots < y_{N_s} = L$, and an upper bound on the intensity $\rho^* \geq \sup_{x \in [0,L]} \rho(x)$, the following steps are repeated for $\alpha = 1, 2, \ldots, N_\alpha$:

Microstructure generation: Construction of a microstructural sample is based on a two-step procedure proposed for general Poisson processes in [Stoyan et al. 1987, Section 2.6]. First, the number of reference points $N_p^*(\alpha)$ is determined by simulating a Poisson random variable with mean $\rho^* L$. The coordinates of the reference points $z_1^*(\alpha), z_2^*(\alpha), \ldots, z_{N_p^*(\alpha)}^*(\alpha)$ then follow from a realization of $N_p^*(\alpha)$ independent random variables uniformly distributed on a closed interval $[0, L]$. Second, each point in the set is deleted with a probability $1 - \rho(z_p^*(\alpha))/\rho^*$, leading to a (relabeled) sequence of $N_p(\alpha)$ particle centers $z_p(\alpha)$.

Solution of the one-dimensional problem: With the microstructure realization fixed, the displacement of sampling points is computed by the recursion

$$u_{\mathrm{MC}}(y_s; \alpha) = u_{\mathrm{MC}}(y_{s-1}; \alpha) + \int_{y_{s-1}}^{y_s} \frac{t(0; \alpha) - \int_0^x b(\xi) \, \mathrm{d}\xi}{E(x; \alpha)} \, \mathrm{d}x, \tag{A.1}$$

where the Young modulus is provided by (5) with the characteristic function χ_1 defined as

$$\chi_1(x; \alpha) = 1 \quad \Leftrightarrow \quad \min_{p=1,2,\ldots,N_p(\alpha)} \left| x - z_p(\alpha) \right| > \frac{\ell}{2},$$

and the boundary data $u(0; \alpha)$ and $t(0; \alpha)$ determined from a generalization of the system of boundary equations (32)–(33).

After completing the sampling phase, the first- and second-order local statistics are assessed using the unbiased values

$$\langle u \rangle_{\mathrm{MC}}(y_s) \approx \frac{1}{N_\alpha} \sum_{\alpha=1}^{N_\alpha} u_{\mathrm{MC}}(y_s; \alpha), \qquad \sigma_{\mathrm{MC}}^2(y_s) \approx \frac{1}{N_\alpha - 1} \sum_{\alpha=1}^{N_\alpha} \left(\langle u_{\mathrm{MC}} \rangle(y_s) - u_{\mathrm{MC}}(y_s; \alpha) \right)^2,$$

to arrive at the γ-confidence interval estimates [Rektorys 1994, Section 34.8]

$$\langle u \rangle(y_s) \in \left[\langle u_- \rangle_{\mathrm{MC}}(y_s), \langle u_+ \rangle_{\mathrm{MC}}(y_s) \right]$$
$$= \left[\langle u \rangle_{\mathrm{MC}}(y_s) - t_{(1+\gamma)/2, N_\alpha - 1} \frac{\sigma_{\mathrm{MC}}(y_s)}{\sqrt{N_\alpha}}, \langle u \rangle_{\mathrm{MC}}(y_s) + t_{(1+\gamma)/2, N_\alpha - 1} \frac{\sigma_{\mathrm{MC}}(y_s)}{\sqrt{N_\alpha}} \right],$$

where $t_{\beta,n}$ denotes the inverse of the Student's t distribution function for value β and n DOFs.

The reference results reported in Section 5 correspond to the values obtained for $N_\alpha = 100{,}000$ simulations, confidence level $\gamma = 99.9\%$, 101 equidistant sampling points, and with the integral (A.1) evaluated with an adaptive Simpson quadrature [Gander and Gautschi 2000] with the relative tolerance set to 10^{-6}.

References

[Anné et al. 2006] G. Anné, S. Hecht-Mijic, H. Richter, O. van der Biest, and J. Vleugels, "Strength and residual stresses of functionally graded Al$_2$O$_3$/ZrO$_2$ discs prepared by electrophoretic deposition", *Scr. Mater.* **54**:12 (2006), 2053–2056.

[Bendsøe and Sigmund 2004] M. P. Bendsøe and O. Sigmund, *Topology optimization: theory, methods and applications*, 2nd ed., Springer, Berlin, 2004.

[Beran 1968] M. J. Beran, *Statistical continuum theories*, Monographs in Statistical Physics and Thermodynamics **9**, Interscience, New York, 1968.

[Bittnar and Šejnoha 1996] Z. Bittnar and J. Šejnoha, *Numerical methods in structural mechanics*, ASCE/Thomas Telford, New York/London, 1996.

[Böhm 2008] H. J. Böhm, "A short introduction to basic aspects of continuum micromechanics", ILSB Report 206, Institute of Lightweight Design and Structural Biomechanics, Vienna University of Technology, 2008, Available at http://www.ilsb.tuwien.ac.at/links/downloads/cdlfmdrep03.pdf.

[Buryachenko 2007] V. A. Buryachenko, *Micromechanics of heterogeneous materials*, Springer, New York, 2007.

[Buryachenko and Rammerstorfer 2001] V. A. Buryachenko and F. G. Rammerstorfer, "Local effective thermoelastic properties of graded random structure matrix composites", *Arch. Appl. Mech.* **71**:4–5 (2001), 249–272.

[Ching and Chen 2007] H. K. Ching and J. K. Chen, "Thermal stress analysis of functionally graded composites with temperature-dependent material properties", *J. Mech. Mater. Struct.* **2**:4 (2007), 633–653.

[Cho and Ha 2001] J. R. Cho and D. Y. Ha, "Averaging and finite-element discretization approaches in the numerical analysis of functionally graded materials", *Mater. Sci. Eng. A* **302**:2 (2001), 187–196.

[Duddeck 2002] F. M. E. Duddeck, *Fourier BEM: generalization of boundary element methods by Fourier transform*, Lecture Notes in Applied Mechanics **5**, Springer, Berlin, 2002.

[Dvorak and Srinivas 1999] G. J. Dvorak and M. V. Srinivas, "New estimates of overall properties of heterogeneous solids", *J. Mech. Phys. Solids* **47**:4 (1999), 899–920.

[Ferrante and Graham-Brady 2005] F. J. Ferrante and L. L. Graham-Brady, "Stochastic simulation of non-Gaussian/non-stationary properties in a functionally graded plate", *Comput. Methods Appl. Mech. Eng.* **194**:12–16 (2005), 1675–1692.

[Gander and Gautschi 2000] W. Gander and W. Gautschi, "Adaptive quadrature: revisited", *BIT* **40**:1 (2000), 84–101.

[Ghosh et al. 1995] S. Ghosh, K. Lee, and S. Moorthy, "Multiple scale analysis of heterogeneous elastic structures using homogenization theory and Voronoi cell finite element method", *Int. J. Solids Struct.* **32**:1 (1995), 27–62.

[Goupee and Vel 2006] A. J. Goupee and S. S. Vel, "Two-dimensional optimization of material composition of functionally graded materials using meshless analyses and a genetic algorithm", *Comput. Methods Appl. Mech. Eng.* **195**:44–47 (2006), 5926–5948.

[Grujicic and Zhang 1998] M. Grujicic and Y. Zhang, "Determination of effective elastic properties of functionally graded materials using Voronoi cell finite element method", *Mater. Sci. Eng. A* **251**:1–2 (1998), 64–76.

[Hashin and Shtrikman 1962] Z. Hashin and S. Shtrikman, "On some variational principles in anisotropic and nonhomogeneous elasticity", *J. Mech. Phys. Solids* **10**:4 (1962), 335–342.

[Higham and Tisseur 2000] N. J. Higham and F. Tisseur, "A block algorithm for matrix 1-norm estimation, with an application to 1-norm pseudospectra", *SIAM J. Matrix Anal. Appl.* **21**:4 (2000), 1185–1201.

[Kandula et al. 2005] S. S. V. Kandula, J. Abanto-Bueno, P. H. Geubelle, and J. Lambros, "Cohesive modeling of dynamic fracture in functionally graded materials", *Int. J. Fract.* **132**:3 (2005), 275–296.

[Krysl 2006] P. Krysl, *A pragmatic introduction to the Finite Element Method for thermal and stress analysis*, World Scientific, Singapore, 2006.

[Luciano and Willis 2001] R. Luciano and J. R. Willis, "Non-local constitutive response of a random laminate subjected to configuration-dependent body force", *J. Mech. Phys. Solids* **49**:2 (2001), 431–444.

[Luciano and Willis 2004] R. Luciano and J. R. Willis, "Non-local constitutive equations for functionally graded materials", *Mech. Mater.* **36**:12 (2004), 1195–1206.

[Luciano and Willis 2005] R. Luciano and J. R. Willis, "FE analysis of stress and strain fields in finite random composite bodies", *J. Mech. Phys. Solids* **53**:7 (2005), 1505–1522.

[Luciano and Willis 2006] R. Luciano and J. R. Willis, "Hashin–Shtrikman based FE analysis of the elastic behaviour of finite random composite bodies", *Int. J. Fract.* **137**:1–4 (2006), 261–273.

[Markworth et al. 1995] A. J. Markworth, K. S. Ramesh, and W. P. Parks, Jr., "Modeling studies applied to functionally graded materials", *J. Mater. Sci.* **30**:9 (1995), 2183–2193.

[Matouš 2003] K. Matouš, "Damage evolution in particulate composite materials", *Int. J. Solids Struct.* **40**:6 (2003), 1489–1503.

[Milton 2002] G. W. Milton, *The theory of composites*, Cambridge Monographs on Applied and Computational Mathematics **6**, Cambridge, Cambridge, 2002.

[Murat and Tartar 1997] F. Murat and L. Tartar, "Calculus of variations and homogenization", pp. 139–173 in *Topics in mathematic modelling of composite materials*, edited by A. Cherkaev and R. V. Kohn, Progress in Nonlinear Differential Equations and Their Applications **31**, Birkhäuser, Boston, 1997.

[Neubrand and Rodel 1997] A. Neubrand and J. Rodel, "Gradient materials: an overview of a novel concept", *Z. Metallkd.* **88**:5 (1997), 358–371.

[Noda 1999] N. Noda, "Thermal stresses in functionally graded materials", *J. Therm. Stresses* **22**:4–5 (1999), 477–512.

[Petrtýl et al. 1996] M. Petrtýl, J. Heřt, and P. Fiala, "Spatial organization of the haversian bone in man", *J. Biomech.* **29**:2 (1996), 161–167.

[Procházka and Šejnoha 2003] P. Procházka and J. Šejnoha, "A BEM formulation for homogenization of composites with randomly distributed fibers", *Eng. Anal. Bound. Elem.* **27**:2 (2003), 137–144.

[Procházka and Šejnoha 2004] P. Procházka and J. Šejnoha, "Extended Hashin–Shtrikman variational principles", *Appl. Math.* **49**:4 (2004), 357–372.

[Quintanilla and Torquato 1997] J. Quintanilla and S. Torquato, "Microstructure functions for a model of statistically inhomogeneous random media", *Phys. Rev. E* **55**:2 (1997), 1558–1565.

[Rahman and Chakraborty 2007] S. Rahman and A. Chakraborty, "A stochastic micromechanical model for elastic properties of functionally graded materials", *Mech. Mater.* **39**:6 (2007), 548–563.

[Ray et al. 2005] A. K. Ray, S. Mondal, S. K. Das, and P. Ramachandrarao, "Bamboo: a functionally graded composite-correlation between microstructure and mechanical strength", *J. Mater. Sci.* **40**:19 (2005), 5249–5253.

[Reiter and Dvorak 1998] T. Reiter and G. J. Dvorak, "Micromechanical models for graded composite materials, II: Thermomechanical loading", *J. Mech. Phys. Solids* **46**:9 (1998), 1655–1673.

[Reiter et al. 1997] T. Reiter, G. J. Dvorak, and V. Tvergaard, "Micromechanical models for graded composite materials", *J. Mech. Phys. Solids* **45**:8 (1997), 1281–1302.

[Rektorys 1994] K. Rektorys, *Survey of applicable mathematics*, vol. II, 2nd ed., Mathematics and its Applications **281**, Kluwer, Dordrecht, 1994.

[Santare and Lambros 2000] M. H. Santare and J. Lambros, "Use of graded finite elements to model the behavior of nonhomogeneous materials", *J. Appl. Mech.* (*ASME*) **67**:4 (2000), 819–822.

[Šejnoha and Zeman 2000] M. Šejnoha and J. Zeman, *Micromechanical analysis of random composites*, Habilitation thesis, Faculty of Civil Engineering, Czech Technical University in Prague, 2000, Available at http://mech.fsv.cvut.cz/~sejnom/download/hab.pdf.

[Sládek et al. 2005] V. Sládek, J. Sládek, and C. Zhang, "Domain element local integral equation method for potential problems in anisotropic and functionally graded materials", *Comput. Mech.* **37**:1 (2005), 78–85.

[Stoyan et al. 1987] D. Stoyan, W. S. Kendall, and J. Mecke, *Stochastic geometry and its applications*, Akademie-Verlag, Berlin, 1987.

[Sutradhar and Paulino 2004] A. Sutradhar and G. H. Paulino, "The simple boundary element method for transient heat conduction in functionally graded materials", *Comput. Methods Appl. Mech. Eng.* **193**:42–44 (2004), 4511–4539.

[Torquato 2001] S. Torquato, *Random heterogeneous materials: microstructure and macroscopic properties*, Springer, New York, 2001.

[Uemura 2003] S. Uemura, "The activities of FGM on new application", *Mater. Sci. Forum* **423–425** (2003), 1–10.

[Vemaganti and Deshmukh 2006] K. Vemaganti and P. Deshmukh, "An adaptive global-local approach to modeling functionally graded materials", *Comput. Methods Appl. Mech. Eng.* **195**:33–36 (2006), 4230–4243.

[Willis 1977] J. R. Willis, "Bounds and self-consistent estimates for the overall properties of anisotropic composites", *J. Mech. Phys. Solids* **25**:3 (1977), 185–202.

[Willis 1981] J. R. Willis, "Variational and related methods for the overall properties of composites", pp. 1–78 in *Advances in applied mechanics*, vol. 21, edited by C.-S. Yih, Academic Press, New York, 1981.

ZAHRA SHARIF-KHODAEI: zahra.sharif@gmail.com
Faculty of Civil Engineering, Department of Mechanics, Czech Technical University in Prague, Thakurova 7, Prague 6, 166 29, Czech Republic

and

Department of Aeronautics, Imperial College London, Prince Consort Road, London SW7 2AZ, Great Britain

JAN ZEMAN: zemanj@cml.fsv.cvut.cz
Faculty of Civil Engineering, Department of Mechanics, Czech Technical University in Prague, Thakurova 7, Prague 6, 166 29, Czech Republic
http://mech.fsv.cvut.cz/~zemanj

RECONSIDERING THE BOUNDARY CONDITIONS FOR A DYNAMIC, TRANSIENT MODE I CRACK PROBLEM

TANYA L. LEISE, JAY R. WALTON AND YULIYA GORB

A careful examination of a dynamic mode I crack problem leads to the conclusion that the commonly used boundary conditions do not always hold in the case of an applied crack face loading, so that a modification is required to satisfy the equations. In particular, a transient compressive stress wave travels along the crack faces, moving outward from the loading region on the crack face. This does not occur in the quasistatic or steady state problems, and is a special feature of the transient dynamic problem that is important during the time interval immediately following the application of crack face loading. We demonstrate why the usual boundary conditions lead to a prediction of crack face interpenetration, and then examine how to modify the boundary condition for a semi-infinite crack with a cohesive zone. Numerical simulations illustrate the resulting approach.

1. Introductory remarks

The subject of the present contribution is unsteady, dynamic crack propagation in brittle polymers. The subject has received considerable attention in the literature, mostly focused upon experimental and numerical studies with comparatively few results obtained via analytical methods. Analytical solutions to select canonical fracture boundary value problems have an important role to play in gaining a deep understanding of the physical processes involved in dynamic fracture of polymeric materials and their numerical simulation. However, constructing analytical solutions to such boundary values, even subject to various simplifying idealizations, presents many technical obstacles.

There is a growing literature devoted to constructing analytical solutions to dynamic fracture boundary value problems in the context of either linear elasticity or viscoelasticity. Broberg [1999] and Freund [1990] give extensive accounts of these developments prior to 2000. Analytical solutions for dynamic steady (constant crack speed) crack growth in linear viscoelastic materials have been constructed for both mode III (antiplane shear) [Herrmann and Walton 1989; Walton 1987] and mode I (planar opening) [Walton 1990; Herrmann and Walton 1994] fracture conditions.

For dynamic, unsteady crack growth, the catalog of analytical solutions in the literature is much smaller, and almost entirely confined to mode III cracks in elastic material, two exceptions being a paper by Saraikin and Slepyan [1979], which points the way to solving dynamically accelerating mode I cracks in elastic material but does not explicitly exhibit a full solution for general loading, and those by Walton and Leise [2003; 2004] which consider a mode III accelerating crack in a linear viscoelastic material.

A number of analytical solutions for dynamic, accelerating mode III crack problems in the setting of linear elasticity have been constructed, both without a cohesive zone [Walton and Herrmann 1992; Leise and Walton 2001b; 2001a] and with a cohesive zone [Costanzo and Walton 1997; 1998]. The subject of the present contribution is to generalize this work to the setting of mode I fracture with a cohesive zone exhibiting nonlinear constitutive behavior modeling an infinitesimally thin evolving craze field in front of an accelerating crack tip. In future work, we will show how this approach can be generalized to a cohesive zone with nonlinear, time dependent constitutive behavior.

2. Mode I crack problem

Consider an infinite, isotropic, homogeneous elastic body with a planar crack along the xz-plane for $x < \ell(t)$ under mode I conditions, where $x = \ell(t)$ locates the crack tip. We can reduce the problem to the xy-plane since the displacement and stress are independent of z, and we can restrict attention to the upper half-plane $y > 0$ if we apply a crack face loading symmetric with respect to the xz-plane. The goal is to determine the crack face displacement due to a time-dependent loading, which we accomplish by adapting the method of Saraikin and Slepyan [1979; 2002] to obtain a boundary integral equation relating the stress and displacement along the x-axis for $t > 0$.

Let $u_k(x, y, t)$ denote the displacement and $\sigma_{ij}(x, y, t)$ the components of the Cauchy stress tensor. The equations of motion in the context of plane strain are

$$\rho \ddot{u}_1 = (2\mu + \lambda)u_{1,11} + \mu u_{1,22} + (\mu + \lambda)u_{2,12},$$
$$\rho \ddot{u}_2 = (2\mu + \lambda)u_{2,22} + \mu u_{2,11} + (\mu + \lambda)u_{1,12},$$

while the relevant constitutive relations are

$$\sigma_{12} = \mu(u_{1,2} + u_{2,1}), \ \sigma_{22} = \lambda u_{1,1} + (2\mu + \lambda)u_{2,2}.$$

The initial conditions are

$$u_i(x, y, 0) = 0 \quad \text{and} \quad \dot{u}_i(x, y, 0) = 0,$$

and we assume $\sigma_{ij} \to 0$ as $x^2 + y^2 \to \infty$. The mode I assumption is that $\sigma_{12}(x, 0, t) = 0$, for all x and t. The classical crack problem assumes a known loading on the crack faces:

$$\sigma_{22}(x, 0, t) = \Lambda(x, t) \quad \text{for } x < \ell(t).$$

Note that this implies that off the support of $\Lambda(x, t)$, the crack faces are stress free.

The classical crack tip model has $u_2(x, 0, t) = 0$ for $x > \ell(t)$ and a square root singularity in the stress σ_{22} at the crack tip. Alternatively, one can insert a cohesive zone to the right of the crack tip and impose a law such as $\sigma_{22}(x, 0, t) = F(u_2(x, 0, t))$ in the cohesive zone (thereby eliminating the crack tip singularity in the stress). One can then use a critical crack opening displacement criterion to determine the crack tip position: when the displacement at the edge of the cohesive zone reaches the critical value δ_c, the material can no longer support stress and the crack extends. The function F should then satisfy $F(u) \geq 0$, $F(0) = 0$, and $F(\delta_c) = 0$.

We show below that this classical crack model (whether a sharp crack model or a cohesive zone model) can exhibit a logical inconsistency by predicting crack surface interpenetration.

3. Integral equation derivation

Defining Fourier and Laplace transforms (as used in [Saraikin and Slepyan 1979]) via

$$\hat{f}(p, y, t) = \int_{-\infty}^{\infty} e^{ipx} f(x, y, t)dx,$$

$$\hat{\hat{f}}(p, y, s) = \int_{0}^{\infty} e^{-st} \hat{f}(p, y, t)dt,$$

the transformed equations of motion become (assuming the initial conditions of $u_k(x, y, 0) = 0$ and $\dot{u}_k(x, y, 0) = 0$ for $k = 1, 2$)

$$\rho s^2 \hat{\hat{u}}_1 = -p^2(2\mu + \lambda)\hat{\hat{u}}_1 + \mu \frac{\partial^2}{\partial y^2}\hat{\hat{u}}_1 - ip(\mu + \lambda)\frac{\partial}{\partial y}\hat{\hat{u}}_2, \tag{3-1}$$

$$\rho s^2 \hat{\hat{u}}_2 = (2\mu + \lambda)\frac{\partial^2}{\partial y^2}\hat{\hat{u}}_2 - p^2 \mu \hat{\hat{u}}_2 - ip(\mu + \lambda)\frac{\partial}{\partial y}\hat{\hat{u}}_1, \tag{3-2}$$

and the constitutive relations become

$$\hat{\hat{\sigma}}_{12} = \mu\left(\frac{\partial}{\partial y}\hat{\hat{u}}_1 - ip\hat{\hat{u}}_2\right), \tag{3-3}$$

$$\hat{\hat{\sigma}}_{22} = -ip\lambda\hat{\hat{u}}_1 + (2\mu + \lambda)\frac{\partial}{\partial y}\hat{\hat{u}}_2. \tag{3-4}$$

The general solutions of equations (3-1) and (3-2) that vanish as $y \to \infty$ are

$$\hat{\hat{u}}_1 = A_1(p, s)e^{-\alpha(p,s)y} + B_1(p, s)e^{-\beta(p,s)y}, \tag{3-5}$$

$$\hat{\hat{u}}_2 = A_2(p, s)e^{-\alpha(p,s)y} + B_2(p, s)e^{-\beta(p,s)y}, \tag{3-6}$$

where $\alpha A_1 = ip A_2$, $-ip B_1 = \beta B_2$, and

$$\alpha(p, s) = \sqrt{p^2 + s^2/c_L^2},$$

$$\beta(p, s) = \sqrt{p^2 + s^2/c_S^2}.$$

Here

$$c_L = \sqrt{\frac{2\mu + \lambda}{\rho}}$$

is the longitudinal wave speed and $c_S = \sqrt{\mu/\rho}$ is the shear wave speed. The functions $\alpha(p, s)$ and $\beta(p, s)$ are decomposed into square roots of linear functions, e.g., $\alpha(p, s) = \sqrt{ip + s/c_L}\sqrt{-ip + s/c_L}$, taken with positive real part (branch cut for $\sqrt{\zeta}$ is taken along negative real axis in the z-plane). Substituting (3-5)–(3-6) into (3-3)–(3-4) and taking the limit $y \to 0$ yields

$$\hat{\hat{\sigma}}_{12}(p, 0, s) = \frac{\rho s^2 \alpha(p, s)}{p^2 - \alpha(p, s)\beta(p, s)}\hat{\hat{u}}_1(p, 0, s) - ip\left(2\mu + \frac{\rho s^2}{p^2 - \alpha(p, s)\beta(p, s)}\right)\hat{\hat{u}}_2(p, 0, s),$$

$$\hat{\hat{\sigma}}_{22}(p, 0, s) = ip\left(2\mu + \frac{\rho s^2}{p^2 - \alpha(p, s)\beta(p, s)}\right)\hat{\hat{u}}_1(p, 0, s) + \frac{\rho s^2 \beta(p, s)}{p^2 - \alpha(p, s)\beta(p, s)}\hat{\hat{u}}_2(p, 0, s).$$

The plane strain problem can be simplified to a single equation by assuming that there is no shear surface traction, $\sigma_{12}(x, 0, t) = 0$ for all x. This assumption leads to the relation

$$\hat{\bar{\sigma}}(p, s) = \frac{\mu^2 R(p, s)}{\rho s^2 \alpha(p, s)} \hat{\bar{u}}(p, s),   \tag{3-7}$$

where $\sigma(x, t) = \sigma_{22}(x, 0, t)$ and $u(x, t) = u_2(x, 0, t)$. The Rayleigh function $R(p, s)$ is defined by

$$R(p, s) = 4p^2 \alpha(p, s)\beta(p, s) - (2p^2 + s^2/c_S^2)^2.$$

Note that the Rayleigh function $R(p, s)$ has zeros only at $p = \pm is/c_R$. Define the transfer function $\hat{\bar{S}}$ to be

$$\hat{\bar{S}}(p, s) = \frac{\rho s^2 \alpha(p, s)}{\mu^2 R(p, s)},$$

and let $\hat{\bar{P}} = 1/\hat{\bar{S}}$. These transfer functions can be decomposed as

$$\hat{\bar{P}}(p, s) = \hat{\bar{P}}_+(p, s)\hat{\bar{P}}_-(p, s) \quad \text{and} \quad \hat{\bar{S}}(p, s) = \hat{\bar{S}}_+(p, s)\hat{\bar{S}}_-(p, s)$$

in such a manner that the functions $S_\pm(x, t)$ and $P_\pm(x, t)$ satisfy the following conditions:

$$S_+(x, t) = P_+(x, t) = 0 \quad \text{whenever } x > c_L t \text{ or } x < 0,   \tag{3-8}$$

$$S_-(x, t) = P_-(x, t) = 0 \quad \text{whenever } x < -c_L t \text{ or } x > 0.   \tag{3-9}$$

This leads to the integral equation (as derived in [Saraikin and Slepyan 1979]):

$$S_+ ** \sigma = P_- ** u,   \tag{3-10}$$

where double asterisks refer to convolution with respect to both x and t:

$$f ** g(x, t) = \int_0^t \int_{-\infty}^\infty f(x - r, t - s)g(r, s)\, dr\, ds.$$

We use a slightly different factorization than [Saraikin and Slepyan 1979] (in which the goal was to restrict the support of these functions in order to derive the stress intensity factor). The original decomposition in [Saraikin and Slepyan 1979] and the one given below differ only by a factor of s, effectively removing a time derivative from the expression for S_+ and thereby easing numerical computations involving that function. We do not need the stress intensity factor here, since we consider a cohesive zone, so the changes to the support properties of $S_\pm$ due to this slight difference do not pose a difficulty for us. This small alteration to the factorization is solely to reduce the complexity of the computations of the stress and displacement expressions (which involve convolutions with S_+ and a related function T_- defined below).

We decompose the transfer function $\hat{\bar{S}}(p, s)$ as follows:

$$\hat{\bar{S}}_+ = \frac{\sqrt{as - ip}}{s(cs - ip)} D_+(ip/s), \qquad \hat{\bar{S}}_- = -\frac{b^2 s \sqrt{as + ip}}{2\mu(b^2 - a^2)(cs + ip)} D_-(ip/s),$$

where $a = \dfrac{1}{c_L}$, $b = \dfrac{1}{c_S}$, $c = \dfrac{1}{c_R}$, and

$$D_{\pm}(ip/s) = 1 + \int_a^b \frac{F_1(u)du}{u \mp ip/s}, \qquad F_1(u) = \gamma(u) \exp[\aleph(u)],$$

$$\gamma(u) = \frac{4}{\pi} \frac{u^2\sqrt{b^2-u^2}\sqrt{u^2-a^2}}{\sqrt{(b^2-2u^2)^4 + 16u^4(b^2-u^2)(u^2-a^2)}}, \qquad \aleph(u) = \frac{1}{\pi}P.V. \int_a^b \varphi(\alpha)\frac{d\alpha}{\alpha-u},$$

$$\varphi(\alpha) = \tan^{-1} \frac{4\alpha^2\sqrt{b^2-\alpha^2}\sqrt{\alpha^2-a^2}}{(b^2-2\alpha^2)^2} = \sin^{-1} \frac{4\alpha^2\sqrt{b^2-\alpha^2}\sqrt{\alpha^2-a^2}}{\sqrt{(b^2-2\alpha^2)^4 + 16\alpha^4(b^2-\alpha^2)(\alpha^2-a^2)}}.$$

The reciprocal of $D_{\pm}(ip/s)$ is given by

$$D_{\pm}^{-1}(ip/s) = 1 + \int_a^b \frac{F_2(u)du}{u \mp ip/s}, \quad \text{where} \quad F_2(u) = -\gamma(u)\exp[-\aleph(u)].$$

4. Crack face interpenetration

We now carefully examine the integral equation $S_+ ** \sigma = T_- ** Du = D(T_- ** u)$, where T_- is defined as

$$P_- = D \circ T_- \quad \text{and} \quad D = \left(c\frac{\partial}{\partial t} - \frac{\partial}{\partial x}\right).$$

Examination of the functions S_+ and T_- yields some unexpected results. The basic definitions are

$$G_1(s) = 1 - H(b-s)\int_s^b F_1(u)\sqrt{\frac{u-a}{u-s}}\frac{du}{c-u},$$

$$G_2(s) = 1 + H(b-s)\int_s^b F_2(u)\frac{du}{\sqrt{u-a}\sqrt{u-s}},$$

$$S_+(x,t) = \frac{H(x)}{\sqrt{\pi x}}H(t-ax)\left[G_1(t/x) - H(c-t/x)B\sqrt{\frac{c-a}{c-t/x}}\right], \tag{4-1}$$

$$T_-(x,t) = -\frac{2\mu(b^2-a^2)}{b^2}\left[\frac{H(-x)}{\sqrt{-\pi x}}H(t+ax)G_2(-t/x)\right],$$

where

$$B = G_1(a) = 1 - \int_a^b F_1(u)\frac{du}{c-u}.$$

See Figures 1 and 2 for graphs of $G_1(s) - H(c-s)B\sqrt{(c-a)/(c-s)}$ and $G_2(s)$.

Suppose $(b/a)^2 \geq 2$, corresponding to a nonnegative Poisson ratio λ. The numerical results shown in Figures 1 and 2 indicate that the function $T_-(x,t)$ is always negative for $-c_Lt < x < 0$, while $S_+(x,t)$ changes sign: $S_+(x,t) < 0$ for $c_Rt < x < c_Lt$, $\lim_{t/x \to c^-} S_+(x,t) = -\infty$ due to the term involving $1/\sqrt{c-t/x}$, and $S_+(x,t) > 0$ for $0 < x < c_Rt$.

Consider the following scenario. Suppose the loading $\sigma_-(x,t) = \Lambda(x,t)$ has support on a fixed interval $(-d-L, -d)$, on which it is always negative, and further suppose that the cohesive zone has
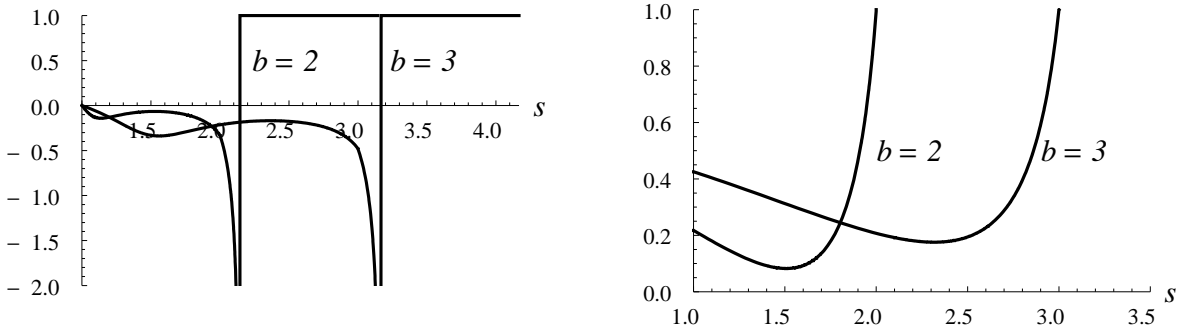
Figure 1. Graph of $G_1(s) - H(c-s)B\sqrt{(c-a)/(c-s)}$ on the left and of $G_2(s)$ on the right for $a = 1$, $b = 2.0, 3.0$, and $c \approx 2.14, 3.17$, respectively. The function $G_1(s) - H(c-s)B\sqrt{(c-a)/(c-s)}$ involves a square root singularity and sign switch at $s = c = 1/c_R$. while $G_2(s)$ is always positive.
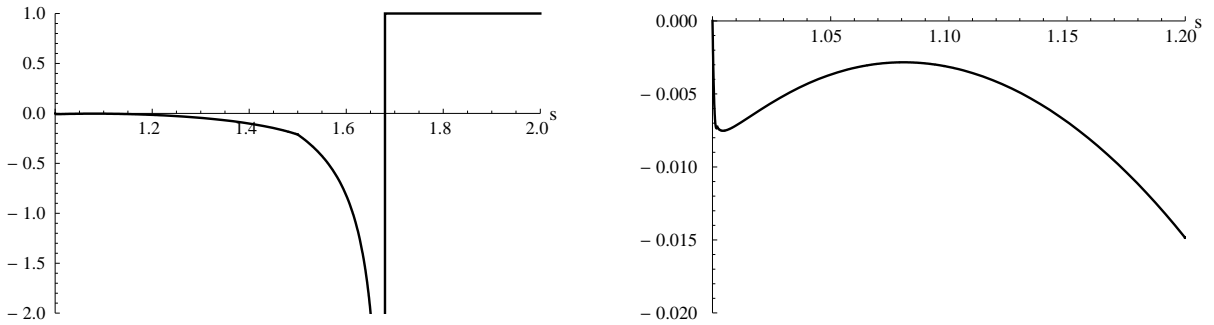
Figure 2. Graphs of $G_1(s) - H(c-s)B\sqrt{(c-a)/(c-s)}$ for $a = 1$, $b = 1.5$, and $c \approx$ 1.68, showing that even for values of b close to $a\sqrt{2}$ this function remains negative on the interval (a, c).

not yet begun opening (implying zero stress on the unloaded crack faces and to the right of the crack tip). Let R be the region in the xt-plane defined by

$$-d + c_R t < x < -d + c_L t \quad \text{and} \quad t > 0.$$

If $(x, t) \in R$, then S_+ is negative on the domain involved in the convolution $(S_+ ** \Lambda)(x, t)$ and so this convolution will be positive. See Figure 3. The integral equation relating stress and displacement is

$$S_+ ** \Lambda = D(T_- ** u);$$

integrate both sides with respect to Rayleigh characteristic to remove the derivative D. If $(x, t) \in R$, then this integral is along a line segment contained within R. Hence the integral of $S_+ ** \sigma$ will be positive if $(x, t) \in R$. Since T_- is nonpositive, the integral equation implies that the displacement must be negative on some portion of the crack face. See Figure 4 for a simulation showing that this negative displacement appears in the context of a cohesive zone as well.
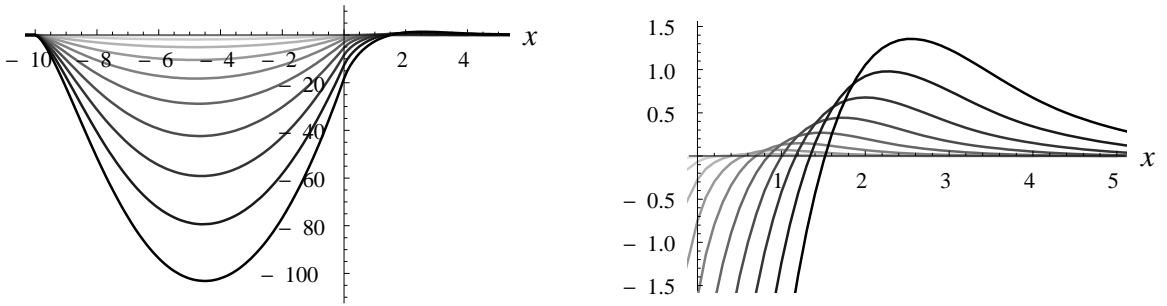
Figure 3. Graph of $S_+(x, t)$ convolved with the loading (with $L = 10$) on the crack face, where $b = 2$. Profiles of $(S_+ ** \Lambda)(x, t)$ are shown for times $t = 1, 2, \ldots, 10$ (in dimensionless units). This convolution is usually negative, but at the extreme right is positive, as only the region where S_+ is negative is involved in the convolution for these values.

5. Implications

This reasoning implies that we cannot assume zero stress on the unloaded ("free") portion of the crack faces. This would mean that other solution methods for mode I fracture that explicitly assume zero stress on the unloaded portion of the crack faces are also missing the small compressive stress occurring behind the longitudinal wave front. That is, we are not free to specify *a priori* the stress on the entire crack face and the parts of the boundary where displacement is zero, contrary to common assumption.
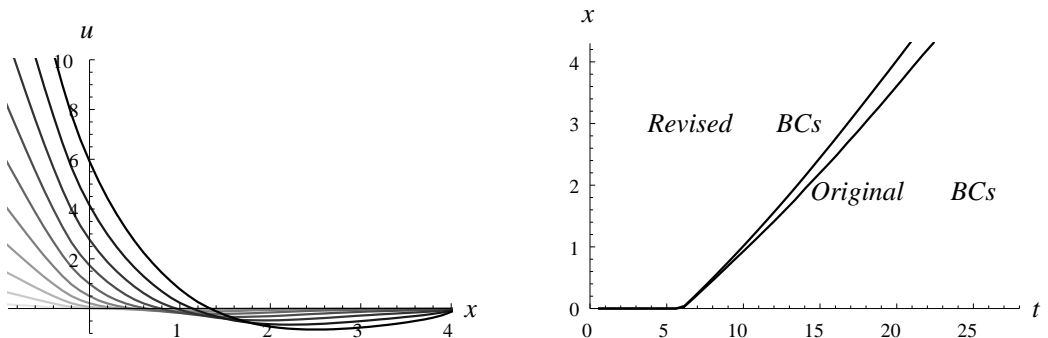
Figure 4. Example with $b = 2$, showing negative displacements from integral equation calculations under the assumption that the unloaded crack faces and the region to the right of the cohesive zone will be stress-free. The graph on the left shows the displacement profiles at times $t = 1, 2, \ldots, 10$ (in dimensionless units), where the crack tip begins accelerating at $t \approx 6.1$. While these negative displacements are very small compared to those in the loading interval, they do have a significant effect in preventing the crack faces from properly opening and so significantly impact transient crack tip calculations, as shown in the graph on the right of the crack tip position $x = \ell(t)$.

If the loading is changing — cycling, for example — the resulting boundary values could be quite complicated and involve multiple regions where the stress must be computed. The problem becomes similar to a crack closure problem, for which stresses on the crack faces must be computed.

6. Modification of the boundary conditions

Since negative displacement doesn't make physical sense, the boundary conditions must be modified. We can't assume that the stress is always zero on the part of the crack face where the applied load is zero (or in the region to the right of a cohesive zone). There can be a small compressive stress traveling at the longitudinal wave speed that must be calculated as part of the solution (as depicted in Figure 5). Perhaps this is due to the point on the crack face where the displacement first equals zero acting as a pivot: the crack face to the left of the pivot is pushed up and so the crack face to the right tends to be pressed down. This compressive stress wave will continue along the boundary, moving out from the applied loading interval in both positive and negative directions.

Consider the integral equation (3-10) in the case that the loading increases in strength over time on a loading interval $[-d - L, -d]$, where the right end is a nonzero distance from the crack tip. Let $\Lambda(x, t)$ represent the crack face loading and u_- the crack face displacement. Let u_+ represent the cohesive zone displacement, so that $\sigma_+ = F(u_+)$ is the cohesive stress. Regions of compressive stress will travel out from the left and right edges of the loading interval on the crack face with speed c_L. Let the curve $x = r(t)$ mark the front edge of the region of compressive stress traveling to the right; this also marks where the displacement becomes zero. Note that $r(0) = -d < \ell(0)$, so $x = r(t)$ begins to the left of the crack tip path $x = \ell(t)$ and typically crosses it. Let σ_r represent the stress in the region $r(t) < x < c_L t$. For $x > -d - L$, the integral equation (3-10) expands to

$$S_+ ** F(u_+) + S_+ ** \sigma_r + S_+ ** \Lambda = P_- ** u_+ + P_- ** u_-. \qquad (6\text{-}1)$$

This can be used to solve for the displacements u_+ and u_-. We also need to calculate σ_r. Fortunately,
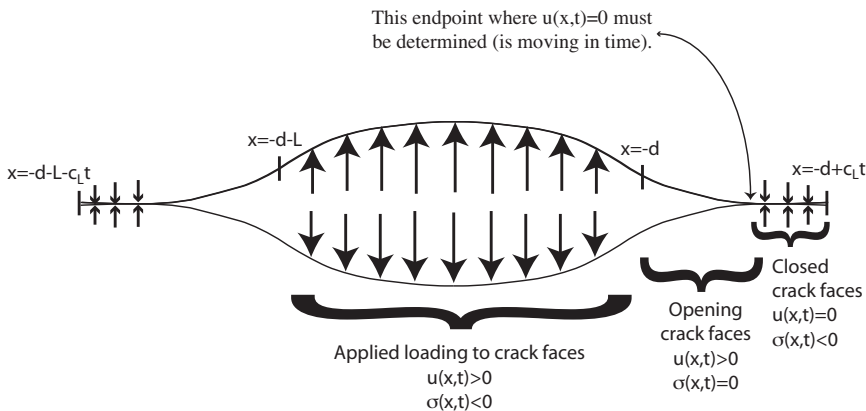
Figure 5. New scheme with a compressive stress in front of the opening portion of the crack faces. The curve $x = r(t)$ where the opening displacement becomes zero and the compressive stresses for $x > r(t)$ must be determined.

the $T_- ** u_\pm$ terms in this case drop out, so the integral equation reduces to

$$S_+ ** \sigma_r = -S_+ ** F(u_+) - S_+ ** \Lambda, \tag{6-2}$$

for $x > r(t)$.

7. Numerical methods

We discretize using a grid in characteristic coordinates $\eta = t + ax$ and $\xi = t - ax$, after nondimension-alizing the integral equations (length with respect to δ_c, time with respect to $a\delta_c$, and stress with respect to μ, where δ_c is the critical crack opening displacement). In the simulations shown in the figures, we implicitly refer to the dimensionless slownesses $a = 1$, $b = c_L/c_S$, and $c = c_L/c_R$. We use continuous piecewise linear approximations of the displacement (using triangles) and continuous piecewise quadratic approximations of the stress on quadrilaterals. This is compatible with the various convolution domains, including on the crack face and in the cohesive zone.

The basic process is to step with respect to increasing values of ξ. For each ξ value, we find nodal values of the displacement and stress for increasing values of η on the grid. There are three cases:

(1) Solve (6-1) for $u_-(x, t)$ if $x < \min\{\ell(t), r(t)\}$.
(2) Solve (6-1) for $u_+(x, t)$ if $\ell(t) < x < r(t)$.
(3) Solve (6-2) for $\sigma_r(x, t)$ if $r(t) < x < c_L t$.

In each case, all the required values in the integral equation will be known from previous steps.

The computations are done efficiently by precomputing all needed convolutions on two prototype triangles and a quadrilateral. These can then be used repeatedly to avoid redundant integrations. These precomputed convolution values scale with the step size, so this lengthy set of computations only needs to be done once.

For examples of simulations, see Figures 6 and 7. In these examples, $\Lambda(x, t) = 0.08t(x+d)(x+d+L)$ on $[-d - L, -d]$ and equals zero otherwise, where $d = 0.2$ and $L = 10$ (all in dimensionless units). The
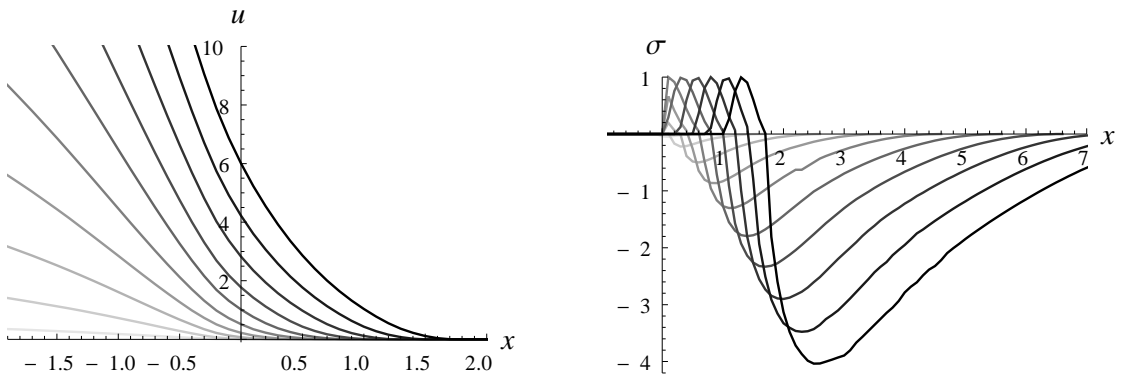
Figure 6. Example of a simulation using the revised scheme. Profiles of the displacement u and stress σ for times $t = 1, 2, \ldots, 10$, all in dimensionless units. See Section 7 for modeling details. The stress equals zero at the crack tip, is positive within the cohesive zone, and negative in the region to the right of the cohesive zone.
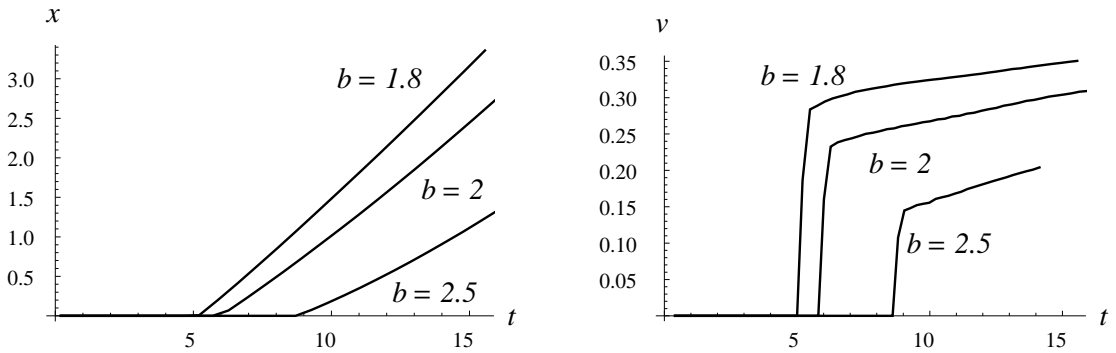
Figure 7. Comparison of crack tip paths and speeds for different ratios $b = c_L/c_S$, using dimensionless units.

crack tip is initially located at $x = 0$, and begins to run once the opening displacement equals 1 at the crack tip position (which is the left edge of the cohesive zone). The crack propagates according to a critical crack opening displacement criterion. The cohesive zone law in dimensionless units is $F(u) = 6.75u(1 - u)^2$ (maximum cohesive stress equals 1). The right edge path $r(t)$ is determined by calculating the value of η at which the displacement will first equal zero for the current value of ξ. We use step size $\triangle \xi = \triangle \eta = 0.1$ in all simulations.

8. Concluding remarks

The problem considered is that of the unsteady, dynamic propagation of a semi-infinite, pure mode I crack in a brittle polymer. The bulk material is modeled as an infinite, homogeneous, isotropic linearly elastic body with a crack with a cohesive zone ahead of the advancing crack tip. The cohesive zone constitutive behavior is modeled through a nonlinear elastic-like response relation incorporating an evolving damage parameter. It was shown that the classical crack paradigm that assumes zero stress outside the loading interval and cohesive zone must be modified in this unsteady, dynamic mode I setting since it predicts zones of crack face interpenetration in a neighborhood of the crack tip (Figure 4). Consequently, the classical crack/cohesive zone model must be generalized to include a contact/slip zone between the fully opened crack and the cohesive zone (Figure 5). The extent of the contact/slip zone must be determined as part of the boundary value problem solution by imposition of the requirement that the displacement discontinuity across the fracture plane (the crack opening displacement) must be everywhere nonnegative. This effect is not seen in dynamic steady-state or transient quasistatic analyses or in the transient dynamic mode III case; it follows from properties of the Dirichlet-to-Neumann map appropriate for transient, dynamic mode I fracture problems.

References

[Broberg 1999] K. B. Broberg, *Cracks and fracture*, Academic Press, San Diego, CA, 1999.

[Costanzo and Walton 1997] F. Costanzo and J. R. Walton, "A study of dynamic crack growth in elastic materials using a cohesive zone model", *Int. J. Eng. Sci.* **35**:12-13 (1997), 1085–1114.

[Costanzo and Walton 1998] F. Costanzo and J. R. Walton, "Numerical simulations of a dynamically propagating crack with a nonlinear cohesive zone", *Int. J. Fract.* **91**:4 (1998), 373–389.

[Freund 1990] L. B. Freund, *Dynamic fracture mechanics*, Cambridge, Cambridge, 1990.

[Herrmann and Walton 1989] J. M. Herrmann and J. R. Walton, "On the energy release rate for dynamic transient anti-plane shear crack propagation in a general linear viscoelastic body", *J. Mech. Phys. Solids* **37**:5 (1989), 619–645.

[Herrmann and Walton 1994] J. M. Herrmann and J. R. Walton, "The energy release rate for transient dynamic mode I crack propagation in a general linearly viscoelastic body", *Quart. Appl. Math.* **52**:2 (1994), 201–228.

[Leise and Walton 2001a] T. L. Leise and J. R. Walton, "A general method for solving dynamically accelerating multiple co-linear cracks", *Int. J. Fract.* **111**:1 (2001), 1–16.

[Leise and Walton 2001b] T. L. Leise and J. R. Walton, "Dynamically accelerating cracks, II: A finite length mode III crack in elastic material", *Quart. Appl. Math.* **59**:4 (2001), 601–614.

[Leise and Walton 2004] T. L. Leise and J. R. Walton, "An analytical and numerical study of a dynamically accelerating semi-infinite crack in a linear viscoelastic material", *Int. J. Fract.* **127**:2 (2004), 101–117.

[Saraikin and Slepyan 1979] V. A. Saraikin and L. I. Slepyan, "Plane problem of the dynamics of a crack in an elastic solid", *Mech. Solids* **14**:4 (1979), 46–62.

[Slepyan 2002] L. I. Slepyan, *Models and phenomena in fracture mechanics*, Springer, Berlin, 2002.

[Walton 1987] J. R. Walton, "The dynamic, energy release rate for a steadily propagating anti-plane shear crack in a linearly viscoelastic body", *J. Appl. Mech.* (*ASME*) **54**:3 (1987), 635–641.

[Walton 1990] J. R. Walton, "The dynamic energy release rate for a steadily propagating mode I crack in an infinite, linearly viscoelastic body", *J. Appl. Mech.* (*ASME*) **57**:2 (1990), 343–353.

[Walton and Herrmann 1992] J. R. Walton and J. M. Herrmann, "A new method for solving dynamically accelerating crack problems, I: The case of a semi-infinite mode III crack in elastic material revisited", *Quart. Appl. Math.* **50**:2 (1992), 373–387.

[Walton and Leise 2003] J. R. Walton and T. L. Leise, "A method for solving dynamically accelerating crack problems in linear viscoelasticity", *SIAM J. Appl. Math.* **64**:1 (2003), 94–107.

TANYA L. LEISE: tleise@amherst.edu
Amherst College, Department of Mathematics and Computer Science, Amherst, MA 01002, United States

JAY R. WALTON: jwalton@math.tamu.edu
Texas A & M University, Department of Mathematics, College Station, TX 77843-3368, United States

YULIYA GORB: gorb@math.tamu.edu
Texas A & M University, Department of Mathematics, College Station, TX 77843-3368, United States

SUBMISSION GUIDELINES

ORIGINALITY

Authors may submit manuscripts in PDF format on-line. Submission of a manuscript acknowledges that the manuscript is *original and has neither previously, nor simultaneously, in whole or in part, been submitted elsewhere.* Information regarding the preparation of manuscripts is provided below. Correspondence by email is requested for convenience and speed. For further information, write to:

Marie-Louise Steele
Division of Mechanics and Computation
Durand Building, Room 262
Stanford University
Stanford CA 94305

LANGUAGE

Manuscripts must be in English. A brief abstract of about 150 words or less must be included. The abstract should be self-contained and not make any reference to the bibliography. Also required are keywords and subject classification for the article, and, for each author, postal address, affiliation (if appropriate), and email address if available. A home-page URL is optional.

FORMAT

Authors are encouraged to use LaTeX and the standard article class, but submissions in other varieties of TeX, and, exceptionally in other formats, are acceptable. Electronic submissions are strongly encouraged in PDF format only; after the refereeing process we will ask you to submit all source material.

REFERENCES

Bibliographical references should be listed alphabetically at the end of the paper and include the title of the article. All references in the bibliography should be cited in the text. The use of BIBTeX is preferred but not required. Tags will be converted to the house format (see a current issue for examples), however, in the manuscript, the citation should be by first author's last name and year of publication, e.g. "as shown by Kramer, et al. (1994)". Links will be provided to all literature with known web locations and authors are encoraged to provide their own links on top of the ones provided by the editorial process.

FIGURES

Figures prepared electronically should be submitted in Encapsulated PostScript (EPS) or in a form that can be converted to EPS, such as GnuPlot, Maple, or Mathematica. Many drawing tools such as Adobe Illustrator and Aldus FreeHand can produce EPS output. Figures containing bitmaps should be generated at the highest possible resolution. If there is doubt whether a particular figure is in an acceptable format, the authors should check with production by sending an email to:

production@mathscipub.org

Each figure should be captioned and numbered so that it can float. Small figures occupying no more than three lines of vertical space can be kept in the text ("the curve looks like this:"). It is acceptable to submit a manuscript with all figures at the end, if their placement is specified in the text by means of comments such as "Place Figure 1 here". The same considerations apply to tables.

WHITE SPACE

Forced line breaks or page breaks should not be inserted in the document. There is no point in your trying to optimize line and page breaks in the original manuscript. The manuscript will be reformatted to use the journal's preferred fonts and layout.

PROOFS

Page proofs will be made available to authors (or to the designated corresponding author) at a web site in PDF format. Failure to acknowledge the receipt of proofs or to return corrections within the requested deadline may cause publication to be postponed.